Formulation Development, Pharmacokinetic and Pharmacodynamic Assessments of a Combination regimen of Paclitaxel and Calcipotriol in a Kras^{G12D} Mouse Model of Pancreatic Ductal Adenocarcinoma

by

Victor R. Lincha

A Dissertation Submitted to the Department of Pharmacological and Pharmaceutical Sciences

College of Pharmacy, University of Houston

In Partial Fulfillment of the Requirements for the Degree of

Doctor of Philosophy in Pharmaceutics

Chair of Committee: Dr. Diana S-L Chow

Committee Member: Dr. Chun Li

Committee Member: Dr. Romi Ghose

Committee Member: Dr. Niranjan Rao

Committee Member: Dr. Xinli Liu

University of Houston

April 2020

Acknowledgements

This dissertation is dedicated to God, the author and finisher of my faith, and to all those who trained, encouraged and supported my journey in graduate school. I am very appreciative of my advisor Dr. Diana S-L Chow and co-advisor Dr. Chun Li for their support-both material and immaterial without which this project would not have been possible. I also acknowledge my committee members, Dr. Romi Ghose, Dr. Xinli Liu and Dr. Niranjan Rao for the commitment you have shown to ensuring my training was a success. Your comments and feedback helped shape my research.

I express my profound gratitude to Dr. Jun Zhao, whose work laid the foundation for this project, and also to my lab members at both University of Houston and MD Anderson Cancer Center for their support.

Finally, I am thankful to my family for their prayers, encouragement and support.

Abstract

Pancreatic ductal adenocarcinoma (PDAC) is a human health challenge whose solution remains elusive. Advancement in our understanding of PDAC has uncovered significant stroma-tumor crosstalk, the disruption of which may improve treatment outcome. Genetic deletion of stroma has led to increased T-cell and chemotherapy infiltration into the tumor bed, but these approaches are characterized by complete stroma depletion which leads to more aggressive PDAC phenotypes. An alternative strategy that maintains a balance between stroma depletion and excess was pursued. In this study, a pharmacological approach using the synthetic vitamin D analog calcipotriol (Cal) to achieve stroma reprogramming while simultaneously delivering a chemotherapeutic agent, paclitaxel (PTX), into the tumor was pursued. To facilitate the studies, an LC-MS/MS method with improved sensitivity was developed to simultaneously measure Cal and PTX in biological samples. To improve the efficacy and safety profiles of Cal and PTX, a polymeric micellar drug delivery system (MDDS) was developed and optimized using the response surface methodology to reduce free Cal exposure as well as facilitate tumor accumulation of both agents. Pharmacokinetic (PK) and biodistribution studies confirmed the MDDS extended the half-lives of both Cal and PTX, reduced systemic exposure of Cal and facilitated tumor accumulation of Cal and PTX.

A potential drug-drug interaction (DDI) between Cal and PTX was discovered. Co-administering Cal and PTX resulted in increased clearance of Cal but decreased PTX clearance. The involvement of transporters is speculated.

Significant differential PK of Cal between healthy and tumor bearing mice was observed, but less so for PTX. Cal elimination half-life in healthy mice was at least 16 times longer

than that in the diseased mice. Cal clearance was also > 5 times faster in the diseased mice compared to the healthy ones. Unsurprisingly, this resulted in a significantly diminished exposure in the diseased mice. A reduction in PTX exposure and an increase in clearance was observed in the diseased mice. PTX clearance was 1.5x faster and exposure (AUC_{last}) 1.5x lower in the diseased animals compared to the healthy ones. While the potential clinical impact of these differences is unknown, the combination regimen remained effective at the doses tested.

Population PK analyses revealed the diseased status to be a significant covariate of Cal PK. Increased expression of CYP24A1 in the diseased mice was postulated to be the underlying factor for the PK difference. Further, a population PK approach was used to understand the metabolic profile of Cal and its major metabolites MC1046 and MC1080. The analyses showed that although Cal is metabolized to MC1046 by CYP24A1, this clearance pathway only accounted for 23% of the total Cal clearance. CYP24A1-mediated Cal metabolism to metabolites other than MC1046, or the involvement of other enzymes in the metabolism of Cal could not be ruled out. Moreover, the analyses suggested that the immediate metabolite of Cal, MC1046, was predominantly further metabolized by another enzyme which accounted for 94% of MC1046 elimination.

In vivo, it was demonstrated that the micellar formulation of Cal and PTX had no negative impact on the body weights of mice, as well as the markers of liver and kidney functions. Additionally, this combination regimen deactivated the PDAC stroma and inhibited tumor cell proliferation that led to the extended survival of diseased animals. Overall, the study demonstrated the potential merits of micellar co-delivery of Cal and PTX for PDAC treatment which warrants further development.

List of Tables

Table 1. Key clinical studies investigating adjuvant therapy in PDAC 7

Table 2. Palliative chemotherapy in PDAC (Abbassi and Schmid, 2019). 9

Table 3. Antibodies used for immunohistochemical staining 24

Table 4. Source and analyte-dependent parameters for Cal, PTX and their internal standards on the mass spectrometer 31

Table 5. Intra- and inter-day precision and accuracy of Cal and PTX in whole blood 57

Table 6. Intra- and inter-day precision and accuracy of Cal and PTX in plasma 58

Table 7. Internal-standard normalized matrix effects and recovery of Cal and PTX in whole blood (A) and plasma (B) 60

Table 8. Non-IS normalized matrix effects and recovery of Cal and PTX in whole blood and plasma..... 61

Table 9. Storage, process and freeze-thaw stability of Cal and PTX in whole blood..... 62

Table 10. Pharmacokinetic parameters of Cal and PTX after treatments of combination and single agent alone..... 66

Table 11. Formulation values of independent factors and measured response variables 70

Table 12. Equations for best-fit models and summary statistics for micelle size and 2-hr PTX release at pH 6 and 7.4 71

Table 13. Tabular summary of model diagnostics for formulation optimization at pH 6. 79

Table 14. Tabular summary of model diagnostics for formulation optimization at pH 7.4 87

Table 15. Tabular summary of model diagnostics for formulation size optimization..... 95

Table 16. Model-predicted and observed outputs for PTX in optimal M-Cal/PTX..... 97

Table 17. Tabular summary of model diagnostics for Cal encapsulation optimization . 106

Table 20. Population PK parameters for Cal and its metabolites 124

Table 21. Demographics of animals used for population PK modeling 127

Table 22. Population PK parameters for calcipotriol 130

Table 23. Population PK parameters of PTX 134

List of Figures

Figure 1. Tumor-stroma crosstalk in immune evasion (Yao et al., 2020) 5

Figure 2. Therapeutic targets and drugs in development for PDAC (Abbassi and Schmid, 2019) 13

Figure 3A. Structure of paclitaxel and it's mechanism of action 17

Figure 3B. Structures of Cal and its major metabolites 19

Figure 4. MS/MS Spectra of Cal (A), Cal-D4 (B), PTX (C) and PTX-D5 (D) with chemical structures and assignment of the main fragment ions 49

Figure 5. Representative chromatograms of Cal and PTX 53

Figure 6. Calibration curves of Cal (A) and PTX (B) in rat whole blood 55

Figure 7. Calibration curves for Cal (A) and PTX (B) in rat plasma 56

Figure 8. Concentration-time profiles of (A) Cal and (B) PTX in whole blood for alone and combination groups 65

Figure 9. Polymer synthesis and formulation of Cal and PTX loaded micelles (M-Cal/PTX) 68

Figure 10. Surface map (A) and diagnostic plots (B-M) for CCD model used for formulation optimization at pH 6 78

Figure 11. Surface map (A) and diagnostic plots (B-M) for CCD model used for formulation optimization at pH 7.4 86

Figure 12. Surface map (A) and diagnostic plots (B-M) for CCD model used for formulation size optimization 94

Figure 13. Drug release profiles of Cal and PTX from optimal M-Cal/PTX 97

Figure 14. 1H-NMR spectrum of poly(OEG-MA)40-b-poly[HEMA-g-(ε-caprolactone)7]20 (polymer 2) (A) TEM (B) images of M-Cal/PTX at a scale of 500 nm and at 25,000X magnification 98
Figure 15. Effects of ratios of Cal and PTX on their encapsulation efficiencies. 99
Figure 16. Surface map (A) and diagnostic plots (B-L) for CCD model used for the optimization of Cal encapsulation efficiency. 105
Figure 17. Storage stability of optimal M-Cal/PTX as measured by encapsulation efficiency (EE) and size at 4°C (A) and at -80°C (B)..... 108
Figure 18. Polydispersity index (PDI) of M-Cal/PTX during short term (A) and long term (B) storage 108
Figure 19. Mean Concentration-time profiles of Cal/PTX and M-Cal/PTX after a single IV bolus dose of 0.5 mg/kg Cal and 5 mg/kg PTX in healthy mice 109
Figure 20. Comparative concentration-time profiles of Cal (A) and PTX (B) in healthy and diseased mice 111
Figure 21. Biodistribution of Cal M-Cal/PTX and Cal/PTX in a Kras mouse model of PDAC 113
Figure 22. Biodistribution of PTX from M-Cal/PTX and Cal/PTX in a Kras mouse model of PDAC 114
Figure 23. Comparative biodistribution of Cal and PTX across different formulations of Cal and PTX 116
Figure 24. Concentration time profiles for formulated and unformulated Cal and its metabolites (A), formulated Cal and its metabolites (B), unformulated Cal and its

metabolites (C), formulated and unformulated Cal (D), formulated and unformulated MC1046 (E), formulated and unformulated MC1080 (F). 119
Figure 25. Observed vs PRED/IPRED for all analytes (A), Observed vs PRED/IPRED plotted by analyte (B, C), Residual vs PRED and WRES vs PRED (D), histogram of WRES (E) and theoretical vs observed quantiles for the WRES (F). 124
Figure 26. Model-predicted individual Clearance of Cal (A) and MC1046 (B) 125
Figure 27. Model-predicted clearance for MC1080 (A) and the fraction of Cal and MC1040 elimination by CYP-mediated mechanism (B) 126
Figure 28. Concentration-time profiles of Cal and PTX 128
Figure 29. Two-compartment for Cal population PK modeling 129
Figure 30. Observed vs PRED (A), Observed vs IPRED (B), NPDE vs PRED (C), theoretical vs observed quantiles for the WRES (D) and histogram of residuals (E) for Cal population PK model 134
Figure 31. Observed vs PRED (A), Observed vs IPRED (B), WRES vs PRED (C), theoretical vs observed quantiles for the WRES (D) and histogram of residuals (E) for PTX population PK model 138
Figure 32. Schematic dosing scheme for the evaluation of short-term benefit of M-Cal/PTX in a mouse model of PDAC 139
Figure 33. T2-MRI Measurements of PDAC tumors in sham (A) and M-Cal/PTX groups (B) 141
Figure 34. Change in tumor volumes with M-Cal/PTX (Red) and sham treatments (Blue) 142

Figure 35. Treatment effects on circulating stroma markers TIMP1 (A), TSP2 (B) and MMP7 (C) 144
Figure 36. Effects of treatment on tumor α-SMA 146
Figure 37. Effects of treatment on tumor Ki67 148
Figure 38. Effects of treatment on COL1A1 149
Figure 39. Body weight change with treatment 150
Figure 40. Treatment effect on organ specific toxicity including Albumin (A), ALP (B), ALT(C), ASP (D), BUN (E), Globulin (F) and total protein (G) 153
Figure 41. Kaplan-Meier survival curves for mice survival after various treatments 155
Figure 42. Relationship between baseline tumor size and inter-subject variation of tumor growth rate (A), tumor growth inhibition rate (B), resistance (C) as well as treatment assignment with tumor growth rate (D), tumor growth inhibition rate (E), resistance (F) 157
Figure 43. Goodness of fit plots for PDAC tumor growth model 158
Figure 44. Conditional weighted residual vs population prediction (A), individual conditional weighted residual vs individual prediction (B), conditional weighted residual vs time (C) and individual conditional weighted residual vs time (D). 159
Figure 45. Time to tumor growth (A), tumor size change at week 1 (TR1, B) and 2 (TR2, B) for sham (0) and M-Cal/PTX (1) groups. 160
Figure 46. Mean model-predicted tumor progression between sham (0) and M-Cal/PTX (1) groups. 161
Figure 47. Relation between AUC and circulating TIMP1 levels in mouse blood 162
Figure 48: Metabolism of vitamin D_3. Modified from (Schlingmann et al., 2011) 172

Figure 49. Graphical abstract for the proposed mechanism of action of M-Cal/PTX.... 182

Figure S1: Eta-matrix for Calcipotriol Parent-metabolites model..... 210

Figure S2. Eta-matrix for Cal population PK model 213

Figure S3: Eta-matrix for PTX population PK model..... 215

Figure S4. Overlaid observed, population predicted and individual predicted values for tumor growth model 218

List of Abbreviations

λ	Tumor resistance to treatment
5-FU	5-Fluorouracil
ABC	ATP Binding Cassette
ABX	Abraxane
ACN	Acetonitrile
ADEX	Aberrantly differentiated endocrine exocrine
ALP	Alkaline phosphatase
ALT	Alanine transferase
ANOVA	Analysis of variance
apCAF	Antigen-presenting CAF
AST	Aspartate aminotransferase
AUC	Area under concentration-time curve
BCRP	Breast cancer resistance protein
BRCA	Breast Cancer Associated gene
BUN	Blood urea nitrogen
CA19-9	Carbohydrate antigen 19-9
CAF	Cancer associated fibroblast
Cal	Calcipotriol
CCD	Central composite design
CD	Cyclin dependent
CD44	Cluster of Differentiation 44
CDKN2A	Cyclin-dependent kinase inhibitor 2A

CE	Collision energy
CEA	Carcinoembryonic antigen
CL	Clearance
Cmax	Maximum drug concentration
COL1A1	Collagen 1A1
CPL	Caprolactone
Crem-Cal/PTX	Cremophor formulation of calcipotriol and paclitaxel
CSCs	Cancer stem cells
CTL	Cytotoxic T lymphocyte
CTL	Cytotoxic T lymphocyte
CuBr	Copper bromide
CV	Coefficients of variation
CXP	Cell exit potential
CYP	Cytochrome P450
DLS	Dynamic light scattering
DNA	Deoxyribonucleic acid
DOE	Design of experiments
DP	Declustering potential
ECM	Extracellular matrix
EE	Encapsulation efficiency
EGFR	Epithelial growth factor receptor
ELISA	Enzyme-linked immunosorbent assays
EP	Entrance potential

ESI	Electrospray ionization
ETA	Inter-individual variation
ETS	Early tumor shrinkage
$FAP\alpha^{+}$	Fibroblast activation protein-α-positive
FGF/FGFR	Fibroblast growth factor/receptor
FOLFIRINOX	Folic acid, fluorouracil, irinotecan, oxaliplatin
HA	Hyaluronic acid
HABP1	Hyaluronan-binding protein 1
HEMA	Hydroxyethyl methacrylate
HER2	Human epidermal growth factor receptor
HRP	Horse radish peroxidase
IACUC	Institutional Animal Care and Use Committee
iCAF	Inflammatory CAF
Ig	Immunoglobulin
IGF/IGFR	Insulin-like growth factor receptor
IHC	Immunohistochemistry
IL-1	Interleukin-1
IND	Investigational new drug enabling
IPRED	Individual prediction
IS	Internal standard
IV	Intravenous
JAK/STATs	Janus tyrosine kinase and activators of transcription
$K_2S_2O_8$	Potassium persulfate

KD	Tumor growth inhibition rate
KL	Tumor growth rate
KRAS	Ki-ras2 Kirsten rat sarcoma viral oncogene homolog
LC-MS/MS	Liquid chromatography-tandem mass spectrometer
LIF	Leukemia inhibitory factor
LLOQ	Lower limit of quantification
LV	Leucovorin
M-Cal/PTX	Micelle formulated calcipotriol and paclitaxel
MeOH	Methanol
mFOLFIRINOX	Modified FOLFIRINOX
MMP	Matrix metalloproteinase
MMP7	Matrix metalloproteinase
MMR	Mismatch repair gene mutation
MRI	Magnetic resonance imaging
MRP1	Multidrug resistance-associated protein 1
MRT	Mean residence time
MSH2	DNA mismatch repair protein Msh2
MUC	Mucin
MULT1	MutL homolog 1
myCAF	Myofibroblast CAF
Na EDTA	Sodium ethylenediaminetetraacetic acid
nab-Paclitaxel	Nano-albumin bound paclitaxel
$NaHCO_3$	Sodium bicarbonate

NCA	Non-compartmental analyses
NIH	National institute of health
NOTCH	Notch homolog 1, translocation-associated
NPDE	Normalized prediction distribution error
OBS	Observed
OEG-MA-500	Methacrylate-grafted oligoethylene glycol
OFF	Oxaliplatin, folinic acid, 5-fluorouracil
OFV	Objective function value
OS	Overall survival
PanIN	Pancreatic intraepithelial neoplasia
PD-L1	Programmed cell death protein 1
PD-L1	Programmed death ligand
PDAC	Pancreatic ductal adenocarcinoma
PDI	Polydispersity index
PEG	Polyethylene glycol
Pgp-1	P-glycoprotein-1
PI3K/AKT	Phosphatidylinositol 3-kinase and protein kinase B
PK	Pharmacokinetic
PLCγ/PKC	Phospholipase C gama and protein kinase C
PO	Oral administration
PRED	Population prediction
PSC	Pancreatic stellate cells
PTX	Paclitaxel

Q1	Parent ion
Q3	Product ion
QC	Quality control
Ras/MAP	Ras-mitogen activated protein kinase
Rb	Rabbit
RPPA	Reversed-phase protein array
RSD	Relative standard deviation
RTKs	Receptor tyrosine kinases
SD	Standard deviation
SHH	Sonic hedgehog
SMA	Smooth muscle actin
SMAD4	Mothers against decapentaplegic homolog 4
SPARC	Secreted protein acidic and rich in cysteine
$t_{1/2}$	Elimination half-life
TEA	Triethyl amine
TEMED	Tetramethylethylenediamine
TGFb	Transforming growth factor beta
THF	Tetrahydrofuran
TIMP1	TIMP metallopeptidase inhibitor 1
TME	Tumor microenvironment
TNF-α	Tumor necrosis factor
TP53	Tumor protein 53
Tregs	Regulatory T cell

TSP2	Thrombospondin-2
TTG	Time to tumor growth
TVTHETA	Typical value of the parameter
ULOQ	Upper limit of quantification
US FDA	United States food and drugs authority
V1	Central volume of distribution
V2	Peripheral volume of distribution
VDR	Vitamin D receptor
V_{ss}	Volume of distribution at steady state
WB	Western blot
Wnt	Wingless-related integration site
WRES	Weighted residuals
XL	Crosslinking density
y_0	Tumor size at baseline

Table of Contents

Acknowledgements ii

Abstract iii

List of Tables v

List of Figures vii

List of Abbreviations xii

Chapter 1. Introduction 1

1.1 Hallmark and statistics of PDAC 1

1.2. The genomic map and evolution of PDAC 1

1.3. Stromal heterogeneity and the role of the stroma in PDAC progression 2

1.4 Fluid dynamics and interstitial pressure in PDAC 4

1.5 Immune Evasion in PDAC 4

1.6 Treatment paradigms for PDAC 6

1.7 Targets and therapeutic developments in PDAC 10

1.7.1 Molecular targets in PDAC 11

1.8 Role of Vitamin D in stroma reprogramming 14

1.9 Potential biomarkers for PDAC 15

1.10 Paclitaxel: Clinical pharmacology and mechanism of action 16

1.11 Calcipotriol: Clinical pharmacology and mechanism of action 18

Chapter 2. Basis for this Research, Hypothesis, Objectives, and Specific Aims 20

2.1 Basis for this research 20

2.2 Hypothesis 21

2.2.1 A dual-functional drug delivery system loaded with Cal and PTX will facilitate pharmacological stroma reprogramming and overcome resistance to chemotherapy ... 21
2.3 Objectives ... 22
2.4 Specific Aims ... 23
2.4.1 Specific Aim 1 ... 23
2.4.2 Specific Aim 2 ... 23
2.4.3 Specific Aim 3 ... 23
Chapter 3. Materials and Methods ... 24
3.1 Materials ... 24
3.1.1 Chemicals and Materials ... 24
3.1.2 Supplies ... 26
3.1.3 Equipment ... 27
3.1.4 Software ... 29
3.2 Methods ... 29
3.2.1 UPLC-MS/MS assay for simultaneous quantifications of Cal and PTX in biological samples ... 29
3.2.1.1 Chromatographic and mass spectrometry conditions ... 29
3.2.1.2 Preparation of calibration standards and quality control samples ... 31
3.2.1.3 Sample preparation and extraction ... 32
3.2.3 Method Validation ... 33
3.2.3.1 Specificity and endogenous interference on analyte retention times ... 33
3.2.3.2 Assay linearity ... 34
3.2.3.3 Assay accuracy and precision ... 34

3.2.3.4 Recovery and matrix effects 34
3.2.3.5 Sample stability 35
3.2.4 Pharmacokinetic and drug-drug interaction studies 35
3.2.5 Polymer synthesis 36
3.2.5.1 Polymer reaction initiator, 2-(benzyloxycarbonyl amino) ethyl 2-bromo-isobutyrate (Compound 1) 36
3.2.5.2 Poly[oligo(ethylene glycol) monomethyl ether methacrylate)$_{40}$-b-poly(2-hydroxyethyl methacrylate)$_{20}$ (Polymer 1) 37
3.2.5.3 Poly(OEG-MA)$_{40}$-b-poly[HEMA-g-(ε-caprolactone)$_6$]$_{20}$ (Polymer 2) 37
3.2.5.4 Poly(OEG-MA)$_{40}$-b-poly[HEMA-g-(acryloyloxy ε-caprolactone)$_6$]$_{20}$-(Polymer 3) . 38
3.2.5.4 Preparation of micelles loaded with Cal and PTX (M-Cal/PTX) 38
3.2.5.5 Micelle optimization using central composite design (CCD) 39
3.2.5.6 Characterization of M-Cal/PTX 39
3.2.5.6.1 Cal and PTX encapsulation efficiency 39
3.2.5.6.2 Morphology and size determination of M-Cal/PTX 40
3.2.5.6.3 Drug release of polymeric micelles 40
3.2.5.6.4 Storage stability of M-Cal/PTX 41
3.2.5.7 Development of Kras^{G12D} mouse model of PDAC 41
3.2.5.8 Pharmacokinetics and biodistribution of M-Cal/PTX 41
3.2.5.9 T2-weighted magnetic resonance imaging 42
3.2.5.10 Immunohistochemical staining 42
3.2.5.11 Reverse phase protein array 43
3.2.5.12 Enzyme-linked immunosorbent assay (ELISA) 44

3.2.5.12.1 Mouse matrix metalloproteinase-7 (MMP-7) ELISA 44
3.2.5.12.2 Mouse thrombospondin-2 (TSP-2) ELISA 45
3.2.5.12.3 TIMP Metallopeptidase Inhibitor 1 (TIMP1) ELISA 46
3.2.6 Statistical analysis 46
Chapter 4. Results 47
4.1 MS/MS fragmentation 47
4.1.1 Cal, PTX, Cal-d4, Cal-D5 parent to daughter ions 47
4.1.2 Retention times of analytes 49
4.1.3. LLOQ and linearity 54
4.1.4. Precision and accuracy 56
4.1.5 Matrix effects and recovery 58
4.1.6 Sample stability 61
4.1.7 Drug-drug interaction study 62
4.2 Development of an optimal M-Cal/PTX using CCD 67
4.2.1 Synthesis of a micellar-based polymeric drug delivery system. 67
4.2.2 Optimizing the micellar formulation with PTX as the model drug 68
4.2.3 Selection of an optimal drug delivery system and validation of the CCD with Cal and PTX 96
4.3 Characterization of optimal M-Cal/PTX 97
4.3.1 NMR and TEM analyses 98
4.3.2 Encapsulation efficiency of optimal M-Cal/PTX 99
4.3.2 Polydispersity index and zeta potential of optimal M-Cal/PTX 107
4.3.3 Storage stability at 4^{o}C and 80^{o}C 107

4.3.4 Pharmacokinetic and biodistribution of optimal M-Cal/PTX in healthy mice and an orthotopic $Kras^{G12D}$ mouse model of pancreatic cancer 109
4.3.4.1 Comparative PK between formulated and unformulated Cal and PTX in healthy mice 109
4.3.4.2 Comparative PK for M-Cal/PTX between healthy and diseased mice 110
4.3.4.3 Biodistribution of M-Cal/PTX in Kras mouse model of PDAC 112
4.3.5. Simultaneous population PK modeling of Cal and it's metabolites MC1046 and MC1080 116
4.3.5.1 Pharmacokinetics of Cal and metabolites 116
4.3.5.2 Simultaneous modeling of Cal, MC1040 and MC1080 120
4.3.5.3 Posthoc comparison of PK parameters between formulated and unformulated Cal 124
4.3.6 Population PK modeling of formulated and unformulated Cal in healthy and diseased mice 127
4.3.6.1 Concentration-time profiles of Cal and PTX 127
4.3.6.2 Population PK modeling of Cal 129
4.3.6.2.1 Model fits and diagnostic plots for Cal population PK model 131
4.3.6.3 Population PK modeling of PTX 134
4.3.6.3.1 Model fits and diagnostic plots for PTX population PK model 135
4.3.7 Short-term efficacy and safety studies of M-Cal/PTX in an orthotopic $Kras^{*}$ mouse model of PDAC 138
4.3.7.1 M-Cal/PTX and blank micelles (sham) effects on tumor volume 139
4.3.7.3 M-Cal/PTX effects on circulating markers of stroma activity 142

4.3.7.4 Effects of treatment on alpha-smooth muscle actin (α-SMA) 145
4.3.7.5 Effects of treatment on the cell proliferation marker Ki67 inhibition 146
4.3.7.6 Effects of treatment on the matrix protein collagen 148
4.3.7.7 Effects of treatment on body weight 150
4.3.7.8 Effects of treatment on markers of organ health 151
4.3.7.9 Reverse phase protein array (RPPA) 154
4.3.7.10 Survival studies 154
4.3.8 A tumor growth inhibition model to describe tumor progression 155
4.3.8.1 Base model and covariate assessment 156
4.3.8.2 Tumor growth model fits and diagnostic plots 157
4.3.9 Exposure-response model to describe Cal effects on tumor stroma deactivation 161
Chapter 5. Discussion and Conclusion 163
5.1. UPLC-MS/MS Assay for simultaneous quantifications of Cal and PTX in biomatrices 163
5.2 Conclusion of UPLC-MS/MS assay 165
5.3 A design of experiment approach facilitates the development of micelles with pre-specified characteristics 165
5.3.1 Summary of formulation optimization using central composite design 167
5.4 A potential drug-drug interaction between Cal and PTX is possible 168
5.4.1 Conclusion of Cal and PTX DDI study 169
5.5 Micelle formulated Cal and PTX (M-Cal/PTX) reduced Cal exposure and extended the half-lives 169
5.5.1 Conclusion of Cal and PTX PK in formulated and unformulated groups. 170

5.6 Cal PK is substantially different in healthy vs diseased mice while PTX is essentially the same 171
5.6.1 Summary of Cal and PTX in healthy vs diseased mice 173
5.7 Cal to MC1046 conversion accounts for only a quarter of circulating Cal 173
5.7.1 Summary of Calcipotriol metabolic profile 174
5.8 The micellar formulation facilitates tumor accumulation of Cal and PTX 174
5.8.1 Summary of M-Cal/PTX distribution 175
5.9 M-Cal/PTX showed better treatment benefits, as well as reduced impact on body weight change 175
5.9.1 Exploratory reverse phase protein array 179
5.9.2 Summary of efficacy and safety studies 179
6.0 Study conclusions 180
References 183

Chapter 1. Introduction

1.1 Hallmark and statistics of PDAC

Pancreatic ductal adenocarcinoma (PDAC) is one of the most lethal human cancers and is projected to be the second leading killer by 2030 (Rahib et al., 2014). It is distinguished from other cancer types by a robust desmoplastic stroma, which contributes to an immunosuppressive tumor microenvironment and poses a physical barrier to tumor infiltration by cytotoxic T lymphocytes (CTLs) (Anderson et al., 2017; Fukunaga et al., 2004). The 5-year survival rate of PDAC remains abysmal but has steadily increased from 5% to 10% owing largely to the improvement in adjuvant and neoadjuvant therapies (Yao et al., 2020). Surgery, radiation and chemotherapy remain options for patients, but these are rarely curative.

1.2. The genomic map and evolution of PDAC

PDAC is characterized by several signature oncogenic mutations; the most predominant one, which is present in about 90% of cases, is the oncogenic mutations of *KRAS.* Inactivated TP53, SMAD4 and CDKN2A tumor suppressors are also frequent mutations observed (Ying et al., 2016). More recent sequencing efforts have discovered several recurrent genetic events in PDAC with low frequency. These mutations/alterations commonly belong to well-studied pathways including RAS signaling, TGFb pathway, cell cycle control, WNT and NOTCH signaling, epigenetic regulation, and DNA damage repair (Ying et al., 2016).

Some of these mutations are therapeutically actionable targets. Indeed, the recent uptick in overall survival in PDAC patients is largely due to the targeting of some of these mutations in specific subsets of patients. Examples include small molecule $KRAS^{G12C}$ -

targeting small molecule inhibitors which is present in about 1.5% of PDAC patients. Early results from clinical studies suggest the treatment benefit in PDAC (Canon et al., 2019). Phylogenetic modeling of mutations in PDAC uncovered that the development of PDAC from PanIN to metastatic lesions could take years (Makohon-Moore et al., 2018). This critical finding presents a long window within which PDAC could be detected, but that has yet to be taken advantage of.

1.3. Stromal heterogeneity and the role of the stroma in PDAC progression

A prominent defining characteristic of PDAC is the presence of a profuse desmoplastic stroma which can make up about 90% of overall tumor volume. Subgroup analyses have uncovered two distinct stromal subgroups- normal and activated (Moffitt et al., 2015). The normal subtype takes the forms of myofibroblast or pancreatic stellate cells. On the other hand, the activated subtype which is associated with worse prognosis assumes inflammatory phenotypes (Moffitt et al., 2015). These subtypes and their association with disease prognosis underscores the importance of stromal heterogeneity in defining PDAC biology. The role of cancer-associated fibroblasts, the main driver for the stroma desmoplasia remains a topic of debate. Encasing the stroma is the extracellular matrix (ECM) which is made up of a variety of cellular material including collagen, integrin, laminin, fibronectin, glycosaminoglycan, matrix metalloproteinase (MMP), and secreted protein acidic and rich in cysteine (SPARC)(Hidalgo, 2011). Under normal physiology, pancreatic stellate cells, a subset of cancer associated fibroblast (CAFs) maintain lipid turnover in the ECM (Apte et al., 1998; Phillips et al., 2003). In health, these nestin-positive cells remain quiescent with high levels of vitamin A and low levels of ECM component production (Apte et al., 1998). In this state, ECM preserves cellular polarity, proliferation,

and migration while inhibiting dysplasia (Tod et al., 2013). At the onset of pancreatic injury, pancreatic stellate cells (PSCs) lose their morphology as well as cytoplasmic lipid droplets and begin to express alpha smooth muscle actin ($\alpha - SMA$), a fibroblast activation biomarker. Activated PSCs are characterized by dysregulated integrin subunits which aid carcinogenesis (Bi et al., 2014). Persistent PSC activation results in the formation of a physical mass in the ECM due to the deposition of matrix proteins like hyaluronan and glycosaminoglycan which are synthesized in copious amounts (Whatcott et al., 2011). Binding of hyaluronan to its receptor, CD44 is reported to aid cancer-cell survival and growth. The exact role of CAFs in pancreatic cancer development and progression is not completely understood and seemingly contradictory. CAFs are regulated by transforming growth factor β (TGF-β) and other proteins such as tumor necrosis factor (TNF-α) and sonic hedgehog (De Wever et al., 2004; Von Ahrens et al., 2017). The role of TGF-β on cancer growth is dependent on the state of physiology. It initially plays a tumor-suppressive role but becomes pro-tumorigenic as cancer progresses (Bierie and Moses, 2006; Tod et al., 2013). Recent studies have uncovered significant CAF heterogeneity in PDAC. These studies have led to 3 classifications of CAFs- myofibroblast ("myCAF), inflammatory fibroblast ("iCAF) and antigen-presenting fibroblast ("apCAF) in human and animal samples (Elyada et al., 2019). These CAF subsets are dynamic but their proximity to tumor cells and the paracrine factors they release are major determinants of their phenotypes (Biffi et al., 2020). Dense collagen deposition is driven by myCAFs which are induced by TGF-β from neighboring tumor cells. These myofibroblasts are thought to inhibit tumor growth. On the other hand, iCAFs which are formed from IL-1 activation of distal CAFs by leukemia inhibitory factor (LIF) are thought to have a tumor-promoting role

mediated by autocrine or paracrine mechanisms (Biffi et al., 2020; Norton et al., 2020). The polar, opposite roles of myCAF and iCAF potentially explains the seemingly contradictory role of CAFs in PDAC.

1.4 Fluid dynamics and interstitial pressure in PDAC

The high concentration of matrix proteins including hyaluronan and glycosaminoglycan together with large gel-fluid phase leads to a high interstitial pressure in the tumor microenvironment (TME) often characterized by vascular collapse (Dufort et al., 2016). This pressure, together with the physical mass created by the deposited matrix proteins have been identified as primary sources of treatment resistance in PDAC. Despite the recognition of tissue pressure involvement in the treatment failure, the sources of pressure most relevant to impaired solute delivery in PDAC and other cancer solid tumors is poorly understood (Brace, 1981). Recent work has led to proposals implicating the hyaluronan-rich and somewhat immobile gel-fluid phase as the inducer of vascular collapse and inadequate delivery of oxygen and nutrients, eventually leading to the treatment resistance in PDAC (Dufort et al., 2016).

1.5 Immune Evasion in PDAC

PDAC is recognized as a cold tumor with low T cell infilitrate and average neoantigen presence in the tumor bed (Balachandran et al., 2017; Balli et al., 2017). As such, the neoantigen number together with the abundance of $CD8^+$ T cell infiltration are key determinants of anti-tumor immunity and long-term survival in PDAC (Balachandran et al., 2017). The TME, which includes the stroma compartment is implicated as the driver for immune-quiscence in PDAC. Copious ECM deposition by activated CAFs creates a physical barrier that excludes cytotoxic T lymphocytes infiltration into the tumor bed. Other

components of TME with immune-suppressive roles include endothelial cells, subsets of myeloid cells and suppressive B cells among others (Anderson et al., 2017). These immunosuppressive cells are recruited when PDAC cells release cytokines, and the suppressive cells function to inhibit effector T cells (**Figure. 1**).

Directly, PDAC cells also promote stromal fibroblast reaction by producing ligands such as SHH.Together with some of the immune filtrates, the activated fibroblasts enhance tumor growth while inhibiting the anti-tumorigenic effector T cells (Anderson et al., 2017). Additinally, the nutrient-depleted TME also contributes to the immunosupresive TME. Metabolic changes including the depletion of glucose, arginine and tryptophan deprive the effector T cells of critical nutrients while the accoumulation of lactate and kynurenine creates an environment less-conducive for effector T cell function (**Figure. 1**)

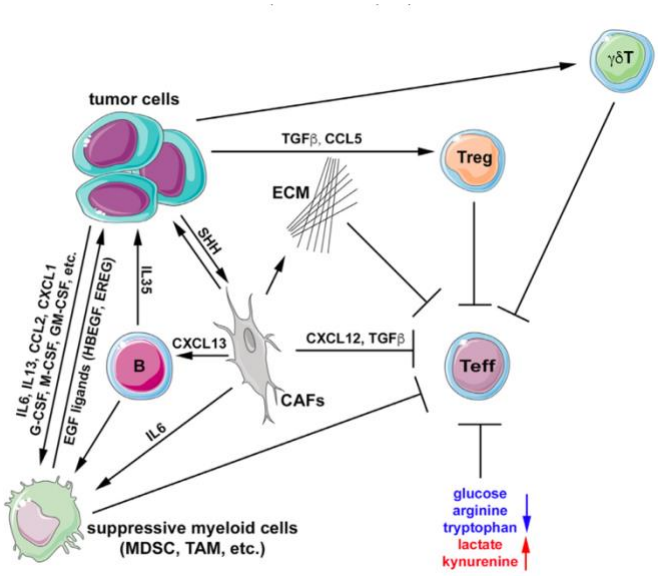

Figure 1. Tumor-stroma crosstalk in immune evasion (Yao et al., 2020)

1.6 Treatment paradigms for PDAC

PDAC is treatment-refractory with only 15% of tumors presented as resectable, hence adjuvant and additive chemotherapy is often required (Abbassi and Schmid, 2019). Options for adjuvant therapy remain limited and recent studies have produced inconsistent results. Results from the CONK-001 trial comparing adjuvant treatment with gemcitabine versus observation has produced mixed results. Although adjuvant treatment with gemcitabine resulted in an improvement of disease-free survival (13.4 vs. 6.7 months), the difference in overall survival between the two arms was minimal, as summarized in **Table 1** (Oettle et al., 2013)**.** Nonetheless, this treatment remained the standard of care for a few years due to the lack of better options. Additional studies comparing adjuvant treatment with gemcitabine versus 5-FU/folinic acid did not result in benefit to the patients (Moore et al., 2012)**.** The use of gemcitabine/capecitabine versus gemcitabine alone as adjuvant therapy was investigated in the ESPAC-4 trial (**Table 1**) but the combination treatment resulted in minimal benefit with significant toxicity. Therefore, this combination is only recommended in patients with good performance status after surgery. By far, the most promising adjuvant therapy till date involves the use of FOLFIRINOX. In the PRODIGE 24 trial comparing adjuvant chemotherapy with modified FOLFIRINOX (mFOLFIRINOX) versus gemcitabine, the use of mFOLFIRINOX resulted in 8.8 months of disease-free survival compared with the comparator arm's 5.2 months. More importantly, these robust disease-free results translated into an equally impressive increase in median overall survival as summarized in **Table 1.** However, the inclusion criteria for this study were very strict, only enrolling patients with good performance status. Therefore, mFOLFIRINOX treatment is only considered standard of care for patients in

relatively good health, while gemcitabine remains the standard of care for patients in relatively poor health (Abbassi and Schmid, 2019). An emerging interesting option for adjuvant therapy is an oral 5-FU pro-drug, S-1, which achieved a 5-year overall survival of 44.1% when compared with gemcitabine alone (24.4%). More importantly, subjects in the S-1 group did not experience increased safety events making S-1 a viable option. However, this study was conducted in subjects of Asian descent; hence, it is unknown if the results will be replicated in other populations (Uesaka et al., 2016).

Table 1. Key clinical studies investigating adjuvant therapy in PDAC

Trial	n	Randomization	Overall survival, months	P
CONKO-001	368	Gemcitabine vs. observation	22.1 vs 20.1 Long term observation 22.8 vs 20.2	0.06 0.01
ESPAC-1	541	Radiochemotherapy (5-FU, 20 Gy) vs no radiochemotherapy vs. observation	15.5 vs 16.1 19.7 vs 14.0	0.024 0.0005
ESPAC-4	732	Gemcitabine/capecitabine vs gemcitabine	28.0 vs. 25.5	0.032
JASPAC 01	385	Gemcitabine vs S-1	25.2 vs. 45.5	0.005
PRODIGE 24	493	mFOLFIRINOX vs gemcitabine	54.4 vs. 35.0	0.003

In recent times, neoadjuvant therapies have been used to improve response in resectable tumors, and also form the basis for selection of patients for surgical treatment of advanced PDAC (Abbassi and Schmid, 2019). Currently, in the neoadjuvant setting, FOLFIRINOX or a combination of gemcitabine and nano-albumin bound paclitaxel are the standard preparative regimens widely used before surgery (Dhir et al., 2018; Janssen et al., 2019; Okada et al., 2017; Schwarz et al., 2018; Wolfe et al., 2020). These neoadjuvant

therapies have been shown to help increase resectable rate while decreasing the rate of relapse. Additionally, neoadjuvant therapy before resection in PDAC has led to an increase in disease-free survival in about 10-20% of cases (Mokdad et al., 2017). Arguments in favor of widespread adoption of neoadjuvant therapy in PDAC derives support from the observations that only about 50% of PDAC patients are deemed eligible to receive chemotherapy post-surgery due to poor health; on the contrary, before surgery most patients are healthy enough to receive chemotherapy. Thus, not only does neoadjuvant therapy expose patients early to treatment, but it also increases the pool of candidates for chemotherapy (Abbassi and Schmid, 2019). Finally, neoadjuvant therapy has been put forward as a means of candidate selection for resection because patients who fail chemotherapy are unlikely to benefit from surgery due to disease progression (Abbassi and Schmid, 2019).

The use of chemotherapy in the palliatve setting is widespread because most PDAC patients present at an advanced stage. Additionally, most subjects that previously underwent resection will receive chemotherapy at some points due to relapse (Abbassi and Schmid, 2019). FOLFIRINOX or gemcitabine plus nab-paclitaxel are the current first line options for use of chemotherapy as palliative treatment in PDAC. The PRODIGE-4-ACCORD trial compared FOLFIRINOX with gemcitabine in subjects with good health status and found FOLFIRINOX improved overall survival by 4.3 months compared with gemcitabine with a response rate of 31.65% in the FOLFIRINOX cohort far superior to the response rate of 9.4% in the gemcitabine cohort (Vaccaro et al., 2011). Other studies evaluating palliative regimens for PDAC are summarized in **Table 2**. The choice of FOLFIRINOX or gemcitabine/nab-paclitaxel is based on among other factors, patient

health status and age. The combination regimen of gemcitabine and nab-paclitaxel is preferred when the patient has a relatively reduced health status and is over the age of 70. This combinatiom is preferred in this popoulation of patients because of its better safety profile when compared to FOLIRINOX which is administered to subjects under the age of 76 who are in good health condition and without contradicting comobidities. Substantial toxicity associated with FOLFIRINOX has led to the development of a modified FOLFIRINOX dosing regimen, called mFOLFIRINOX. A phase II clinical study showed mFOLFIRINOX, as first-line therapy in locally advanced and metastatic PDAC, resulted in an overall survival of 10.2 months with a response rate of 35.1% (Dahan et al., 2018).

Table 2. Palliative chemotherapy in PDAC (Abbassi and Schmid, 2019).

Trial	n	Randomization	Overall survival, months	p, HR
First line				
PRODIGE-4-ACCORD 11	342	FOLFIRINOX vs. gemcitabine	11.1 vs. 6.8	<0.001, 0.57
MPACT	861	gemcitabine/nab-paclitaxel vs. gemcitabine	8.5 vs. 6.7	<0.001, 0.72
(Moore et al., 2007)	569	gemcitabine/erlotinib vs. gemcitabine	6.24 vs. 5.91	<0.001, 0.82
(Haas et al., 2018)	569	gemcitabine/erlotinib in rash-positive patients vs. FOLFIRINOX	10.1 vs. 10.6	
(Burris et al., 1997)	126	gemcitabine vs. 5-FU	5.65 vs. 4.4.1	0.0025
Second line				
CONKO-003	168	OFF vs. 5-FU	5.9 vs. 3.3	0.01
Second/third line				
NAPOLI-1	417	liposomal irinotecan/5-FU/LV vs. 5-FU/LV	6.1 vs. 4.2	0.012

Half of PDAC patients initially administered first line treatment will be in condition to receive second line treatment if disease progresses. In administering second line therapy, the patient's age, prior treatment history, health status and side effects are considered when making a determination for the choice of second line treatment. When FOLFIRINOX treatment is precluded due to the reasons previously discussed, gemcitabine-based treatments become the standard of care. The combination of gemcitabine and nab-paclitaxel in patients with slightly reduced health condition has been shown to improve overall survival and objective response rate (Portal et al., 2015). Patients who failed gemcitabine combination treatments as second line therapy are candidates for either 5-FU (5-fluorouracil) based treatments or the OFF (oxaliplatin, folinic acid, 5-FU) regimen. In the CONKO-003 trial, the OFF regimen was compared with 5-FU/leucovorin and was shown to provide benefit as summrized in **Table 2** (Pelzer et al., 2011).

The options for third line therapy in PDAC are limited and only a small percentage of patients are in a condition to receive the third line chemotherapy after failing two prior lines of therapy (Abbassi and Schmid, 2019). Currently, only the NAPOLI-1 trial (**Table 2**) which evaluated liposomal irinotecan/5-FU/LV vs. 5-FU/LV included patients who had failed two prior therapies. Liposomal irinotecan/5-FU/LV remains the only validated third line option for PDAC (Collisson et al., 2011).

1.7 Targets and therapeutic developments in PDAC

Although four molecular subtypes of PDAC with highly divergent genetic and biological characteristics have been identified, the DNA repair pathway remains the only validated clinically relevant target (Lai et al., 2019). The four PDAC subtypes identified thus far are

squamous, pancreatic progenitor, immunogenic and aberrantly differentiated endocrine exocrine (ADEX).

1.7.1 Molecular targets in PDAC

These are often molecular receptor proteins controlling downtsream oncogenic signaling cascades. The receptor tyrosine kinases (RTKs) activate oncogenic pathways including Ras/MAPK, PI3K/AKT, PLCγ/PKC, and JAK/STATs. These genes are frequently observed to be upregulated in PDAC and are asociated with poor prognosis (Ebrahimi et al., 2017). Other RTKs that are implicated in PDAC include epithelial growth factor receptor (EGFR) which is associated with aggressive tumor types and higher refractory rates after surgery (Polireddy and Chen, 2016), the fibroblast growth factor/receptor (FGF/FGFR) and the insulin-like growth factor receptor (IGF/IGFR) are often associated with shorter survival (Kang et al., 2019, Polireddy and Chen, 2016). Other pathways that have received recent attention are Wnt/beta-catenin and NOTCH signaling pathways (Sahin et al., 2016; Sano et al., 2016). A well-studied pathway implicated in the development and progression of PDAC is the hedgehog (Hh) pathway (Niyaz et al., 2020; Van Mackelenbergh et al., 2019). In healthy pancreas, Shh exists at low levels but disregulated Shh signaling is implicated in tumorigenesis where siginificatly elevated activity of Shh is often observed (Niyaz et al., 2020)

Targeting tumor suppressor genes also remains an area of active research. These genes encode proteins which control cell proliferation, and loss of function usually results in abberant cell growth (Lai et al., 2019). The tumor suppressive proteins TP53 and SMAD4 have been studied in the context of PDAC treatment. The extensive PDAC heterogeneity is often associated with lack of TP53 activity, a mutation that occurs in 50-75% of PDAC

cases (Lai et al., 2019). Half of PDAC patients present mutations in the SMAD4 gene, a TGF inducer which influences tumor-stroma interaction (Polireddy and Chen, 2016).

Other therapeutic targets that continue to garner interest are the DNA repair factors, especially germline mutations of the breast cancer genes (BRAC1/2) (Pihlak et al., 2017) and mismatch repair gene mutation (MMR)(Macherla et al., 2018). Studies showed PDAC patients with BRCA2 mutations have a life-time risk of up to 10 times more than the general population, while those with BRCA1 have about a 3-fold higher risk (Iqbal et al., 2012). The ECM plays a vital role in tumor growth, metastasis and chemoresistance and constitutes the bulk of the tumor volume (Van Mackelenbergh et al., 2019). Unsurprisingly, attention has been directed to the ECM in the hope of finding therapeutic targets within the microenvironment. Cancer-associated fibroblasts (CAFs) in particular have received a significant attention. As discussed previously, activated CAFs lead to upregulated levels of matrix proteins such as α-smooth muscle actin (αSMA) and secretory CAFs. While CAFs promote stiffness, hypoxia and avascularization, secretory CAF contribute to overall tumor aggresiveness and chemotherapy resistance (Awaji and Singh, 2019; Erdogan and Webb, 2017). Hyaluronic acid (HA) within the tumor microenvironment has also been targeted. In normal physiology, HA functions to maintain tissue structure and malleability (Wong et al., 2017). Elevated levels of HA is common in PDAC which increases the interstitial fluid pressure leading to chemoresistance (Huang and Brekken, 2019).

Finally, cancer stem cells (CSCs) have emerged as targets for PDAC treatment. These cells express surface markers like CD24, CD44 and CD133 (Hou et al., 2019). Cancer stem cells are particularly resistant to chemotherapy in the non-dividing G0-state and form the basis of tumor relapse in late stage chemotherapy. The mechanisms of drug

resistance by CSCs is largely unknown but may be mediated by ATP Binding Cassette (ABC) drug transporters and detoxifying enzymes (Polireddy and Chen, 2016).

Evidence suggests CSCs are low expressors of T-cell activation co-stimulatory molecules and high expressers of T-cell inhibitory molecules including PD-L1, which enables these cells to evade immune surveillance (Hou et al., 2019). Other targets that are being pursued are summarized in **Figure 2**.

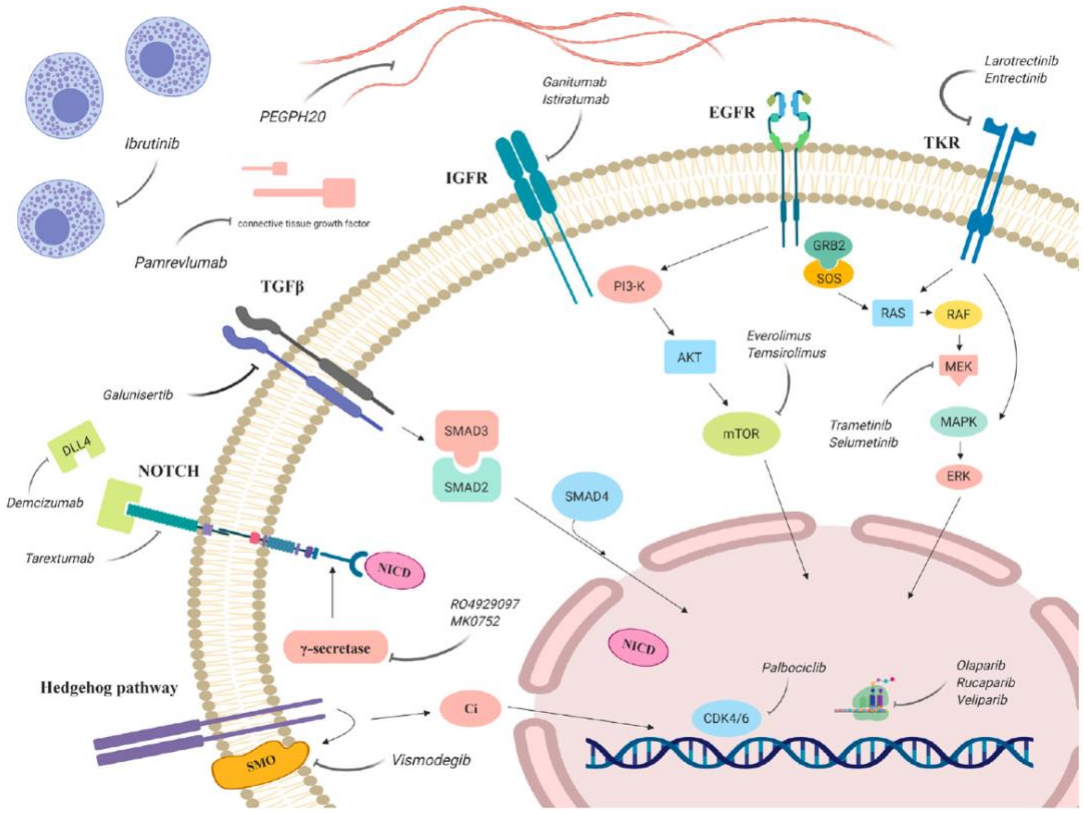

Figure 2. Therapeutic targets and drugs in development for PDAC (Abbassi and Schmid, 2019).

1.8 Role of Vitamin D in stroma reprogramming

It is well-established that the dense ECM associated with PDAC forms a physical barrier that obstructs chemotherapy and vasculature within the tumor bed (Olive et al., 2009). New ideas to overcome this stromal impedance have been proposed (Jacobetz et al., 2013; Provenzano et al., 2012). Deregulated vitamin D is implicated in several cancer types including PDAC. Vitamin D functions in a variaty of physiologic and pathologic processes (Norman, 2008; Rosen et al., 2012). Active vitamin D, 1,25-dihydroxyvitamin D_3 [$1,25(OH)_2D_3$] is formed through the hydroxylation of the precursor 25-dihydroxyvitamin [$25(OH)_2D_3$] by the hydroxylase 25-Hydroxyvitamin D_3 1α-hydroxylase (CYP27B1) (Townsend et al., 2005). Active vitamin D and $25(OH)_2D_3$ bind the vitamin D receptor (VDR) in the promoter region of vitamin D target genes (Pike and Meyer, 2010). One of such target genes of vitamin D is 1,25-dihydroxyvitamin-D_3 24-hydroxylase (*CYP24A1*) which is often overpressed in cancers including PDAC. Studies to delineate the association between PDAC and circulating $25(OH)_2D_3$ have yielded inconsistent results. While some studies found increased risk for PDAC among subjects with high $25(OH)_2D_3$ (Stolzenberg-Solomon et al., 2010, 2006), separate analyses found no such association (Stolzenberg-Solomon et al., 2009). Nonetheless, active vitamin D has the potential to affect the endocrine immune system (Jacobetz et al., 2013) and is implicated in the regulation of cell proliferation and apoptosis (Hobaus et al., 2012).

Transcriptomic analyses of PSCs revealed high levels of VDR (Sherman et al., 2014) previously not thought to be expressed in exocrine pancreas (Zeitz et al., 2003). Induction of VDR led to a reduction in the levels of α-SMA and significant lipid droplet formation supporting the idea that activated PSCs could be controlled in a signal dependent manner.

Against this backdrop, VDR induction has been proposed to be a means to deactivate PSCs.

1.9 Potential biomarkers for PDAC

Progression from tumor initiation to advanced PDAC may take a long time, sometimes decades but most patients have advanced disease at diagnosis (Yachida et al., 2010). The reasons for late diagnosis include non-specifc PDAC symtomatology as well as the lack of clinically useful circulating biomarkers (Korc, 2007). Late diagnosis is strongly correlated with poor outcomes; hence, there is a renewed push to find circulating biomarkers which are specific to PDAC and could help diagnose the disease early.

Till date, the only FDA approved PDAC-relevant serum biomarker routinely used in clinical setting is the carbohydrate antigen (CA) 19-9 (Ducreux et al., 2015). However, this biomarker lacks the sensitivity and specificity required to be useful for PDAC diagnosis (Goonetilleke and Siriwardena, 2007). Additionally, elevated levels of CA19-9 is observed in pancreatitis and benign disease as well as in other diseases of the gastrointestinal system. Distinguishing these different states with CA19-9 is difficult (Duffy et al., 2009). Further complications arise from the observed racial and sex variations in CA19-9 expression levels. Even worse, 20% of Lewis-antigen negative population do not express CA19-9 making this biomarker unreliable for PDAC diagnosis, or for monitoring the treatment response (Tempero et al., 2013). The advancement of proteomics has led to the discovery of several markers that may be of clinical relevance in PDAC (Sun et al., 2011), but most of these have not been further evaluated for the diagnostic or prognostic value in the context of PDAC (Brand et al., 2011; Capello et al., 2013; Chan et al., 2014). Desirable tumor biomarkers bear the hallmarks of being minimall invasive and

reproducible. To this end, peripheral blood is a good source for circulating proteins that have the potential to be used as tumor biomarkers in PDAC (Whitney et al., 2003). A recent study found circulating plasma protein biomarkers that were predictive of tumor stage and survival (Ren et al., 2014). Circulating levels of interleukin (IL)-6, IL-8, carcinoembryonic antigen (CEA), and hypoxia-inducible factor 1-alpha were of high prognostic value while the levels of IL-8, CEA and mucin (MUC)-1 were good indicators of metastatic potential. From this same study, a correlation was found between receptor tyrosine-protein kinase erbB-2 (HER2) levels and overall survival. Subjects with elevated HER2 leves treated with erlotinib had a better repsonse compared with placebo suggesting HER2 as a potential drug reponse predictor (Ren et al., 2014). Increasingly, biomarker panels have been shown to have predictive and prognostgic value. In a clinical study, the soluble stroma makers TIMP1, MMP7, and TSP2 were shown to be good biomarkers for the treatment response, outperforming CA19-9 (Resovi et al., 2018).

1.10 Paclitaxel: Clinical pharmacology and mechanism of action

Paclitaxel, PTX (**Figure 3A**) is a diterpenoid of natural origin that was first shown in late 1970s to act on microtubule assembly (Schiff et al., 1979). Due to the limited solubility of PTX, early developments used a combination of cremophor and ethanol which resulted in significany side effects including hypersensitivity. Major side efffects attributable to PTX include neutropenia and peripheral neuropathies (Rowinsky et al., 1993). PTX is a potent inhibitor of cell replication and migration with cell arrest occuring in the G2/M phase of the cell cycle (Schiff and Horwitz, 1980). Within the cell, an equilibrium exists between soluble tubulin and the microtuble polymer but this equilibrium is shifted towards the latter by PTX, thereby reducing the concentration of tubulin required to make microtubules. (Schiff and

Horwitz, 1981). Microtubules are involved in mitosis and other processes like cell shape maintenance, motility and intracellular trafficking of organelles and macromolecules, but PTX disrupts the ability of microtubules to perform these functions (Yvon et al., 1999). PTX has broad antineoplastic activity and is approved for the treatment of metastatic carcinoma of the ovaries and breast. Due to the toxicity associated with the cremophor formulation of PTX, a nano-albumin bound formulation (Abraxane) was developed and is approved in combination with gemcitabine for the treatment of PDAC.

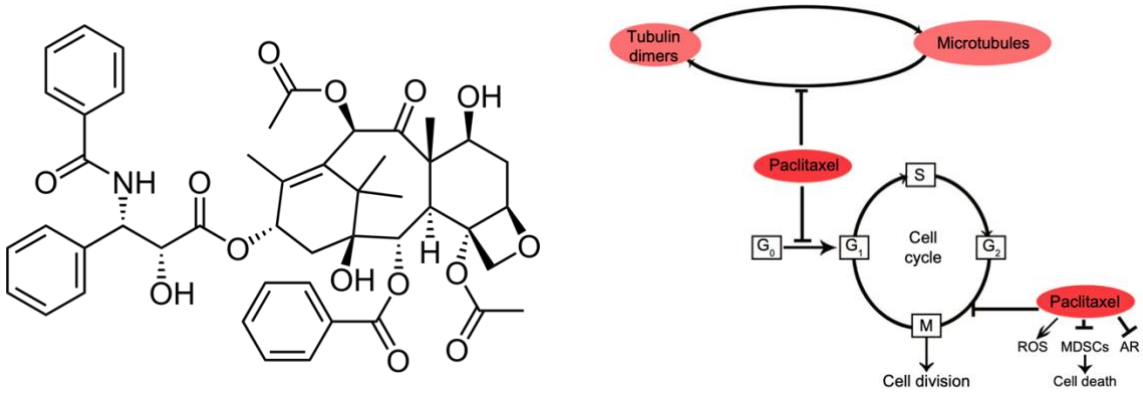

Figure 3A. Structure of paclitaxel and it's mechanism of action

PTX has non-linear pharmacokinetics (PK) which is highly dependent on the schedule of administration; PTX peak plasma concentrations and exposure disproportionately increase with increasing dosing with saturation attained by high-doses infused over a short period of time. PTX follows biphasic (Wiernik et al., 1987) or triphasic (Huizing et al., 1993) dispositions after administration. PTX is extensively distributed following intravenous administration, despite being highly bound to albimun (89%)(Rowinsky et al., 1992). PTX

is primarily eliminated through hepatic metabolism and biliary excretion with 12% excreted in urine unchanged (Huizing et al., 1993). PTX is metabolized by the liver isoenzymes CYP2C8 and CYP3A4, and thus liable to drug-drug interaction with drugs that inhibit or induce these enzymes (Monsarrat et al., 1997).

1.11 Calcipotriol: Clinical pharmacology and mechanism of action

Calcipotriol (Cal) is a structural analogue of 1α, 25-dihydroxycholecalciferol ($1,25(OH)_2D_3$), the active metabolite of vitamin D_3 (**Figure 3B**). Cal induces cell differentiation and inhibits proliferation of cells expressing the VDR (Binderup and Bramm, 1988). The pharmacological profiles of Cal and the active metabolite of vitamin D_3 are similar, but 100-200 times less potent in the metabolite effect on calcium metabolism (Binderup and Bramm, 1988). The minimized hypercalcemia inducing property of Cal has generated interested in using this agent to treat proliferative disorders. Cal is therefore a safe and effective therapy indicated for the topical treatment of psoriasis (KRAGBALLE et al., 1988). *In vivo*, Cal is less potent than its active vitamin, D_3, in its affinity for serum proteins including the vitamin D binding protein. The decreased affinity of Cal for the vitamin D binding protein leads to a decreased capacity for the transport of Cal and has been suggested as the reason for its reduced hypercalcemia induction.

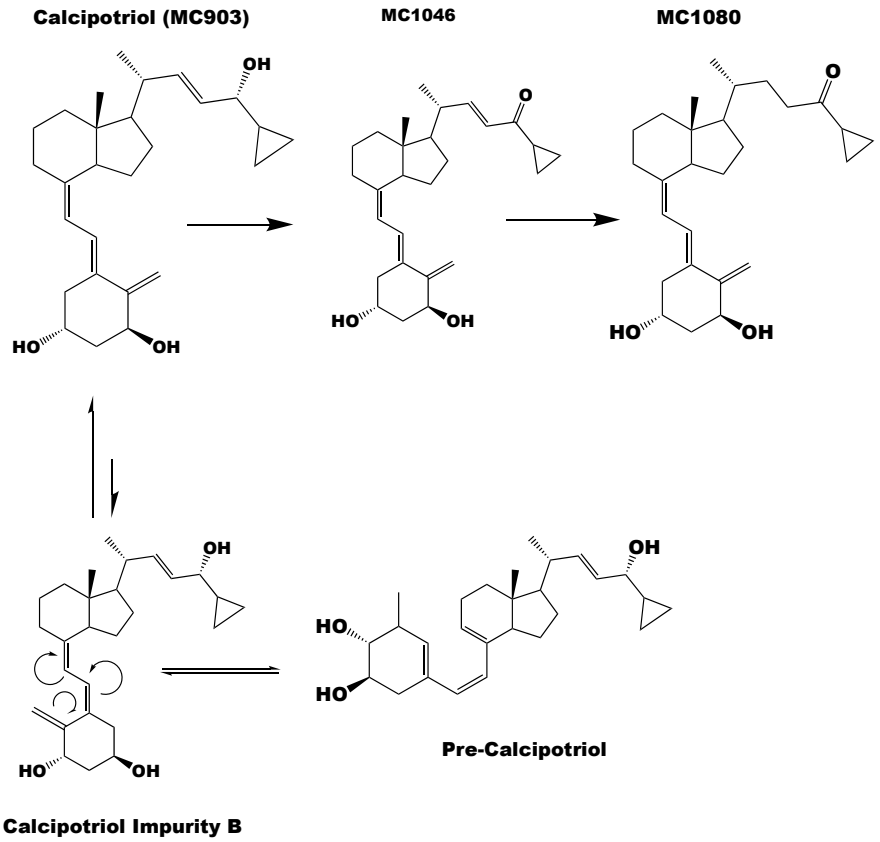

Figure 3B. Structures of Cal and its major metabolites

Cal has two major metabolites that are less active-MC1080 and MC1046 (Masudata et al., 1994). Both metabolites have lower affinities for VDR, compared to the parent Cal (Masudata et al., 1994). The half-life of Cal in rats is 4 min after IV administration and 0.6 h after oral administration (Knutson et al., 1997). The relatively rapid elimination of Cal, compared to active vitamin D ($t_{1/2}$ = 13 min) has been proposed as another reason why Cal has reduced hypercalcemic effect.

Chapter 2. Basis for this Research, Hypothesis, Objectives, and Specific Aims

2.1 Basis for this research

PDAC is refractory to treatments and one of the most lethal human cancers (Rahib et al., 2014). It is distinguished from other cancer types by a robust desmoplastic stroma, which contributes to an immunosuppressive tumor microenvironment and poses a physical barrier to tumor infiltration by cytotoxic T lymphocytes (Anderson et al., 2017; Fukunaga et al., 2004; Joyce and Fearon, 2015; Puré and Lo, 2016). Blockade of the immune checkpoint protein programmed cell death-1 (PD-1) has produced durable response in subsets of patients in several tumor types; however, the efficacy of PD-1 blockade in PDAC patients has been limited (Brahmer et al., 2012; Royal et al., 2010). Although significant progress has been made, an effective treatment for PDAC remains an unmet medical need. Innovative therapies that modulate the PDAC stroma to promote CTL infiltration and overcome resistance to chemotherapy, and PD-1 inhibitors are needed. Recent studies on modulation of the PDAC stroma have generated mixed results. The efficacy of anti-PD-L1 was enhanced by genetically depleting fibroblast activation protein-α-positive ($FAP\alpha^+$) CAFs (Feig et al., 2013). The antitumor activity of another immune checkpoint blockade antibody, anti-CTLA-4, was enhanced by depletion of α-smooth muscle actin-positive (αSMA^+) CAFs. However, the extensive depletion of CAFs in the PDAC stroma also led to infiltration by immunosuppressive regulatory T cells (Tregs), depletion of type-I collagen, and induction of aggressive tumor phenotypes (Lee et al., 2014; Özdemir et al., 2014; Rhim et al., 2014). Treatment with PEGylated hyaluronidase degraded hyaluronic acid (HA) in the PDAC stroma, improved the intratumoral delivery of

chemotherapy drugs, and may allow more effective tumor infiltration by CTLs (Guo et al., 2017; Provenzano et al., 2012)

This approach, however, is limited to patients with high tumor levels of HA (Hingorani et al., 2016). These studies demonstrate that it is feasible to enhance immune checkpoint blockade in PDAC by stromal modulation. The challenge, however, is to identify a strategy that can simultaneously enhance the infiltration and activity of CTLs, alleviate immunosuppression, and maintain the tumor-restraining collagenous matrix of PDAC. While significant efforts have been made to use genetic approaches to achieve the stroma modulation, pharmacological means to obtain similar outcomes have been under-explored.

2.2 Hypothesis

2.2.1 A dual-functional drug delivery system loaded with Cal and PTX will facilitate pharmacological stroma reprogramming and overcome resistance to chemotherapy

In vitro and transplantation studies demonstrate the merits of stroma-depleting therapy in combination with chemotherapy for treatment of PDAC. However, the failure of this treatment approach in clinical trials have led to renewed efforts to understand the exact nature of the association between the stroma and cancer cells (Andersen et al., 2013). The overwhelming and very convincing conclusion from *in vitro* and transplantation models is that stromal elements can enhance cancer cell proliferation and invasion (Hwang et al., 2008) and contribute to immune suppression, promoting tumor growth and survival (Hanahan and Weinberg, 2011). However, genetic deletion of the signaling molecule that drives PSC transformation failed to corroborate *in vitro* findings. In fact, the

cancer cells assumed very aggressive phenotypes, suggesting a tumor-restrictive role of the entire stroma, or at least some parts. Attention has therefore been redirected to developing therapies that restrain but do not ablate the stroma (Rhim et al., 2014). Sherman et. al., achieved stromal balance by activating the highly abundant vitamin D receptor in the stroma with Cal, a synthetic analogue of vitamin D. When they co-administered Cal with gemcitabine, an anticancer drug, they observed a marked increase in gemcitabine levels in the tumor and a significant extension of the survival time of tumor bearing mice.

Unfortunately, while the combination treatment improved antitumor effect and survival, the animals suffered severe Cal toxicity. This toxicity is likely related to the activation of the vitamin D receptor in undesired places. To obtain the desired therapeutic effect, large doses of Cal given at high frequency are required to enhance antitumor effect of gemcitabine. We postulated that an extended-release formulation of Cal would enable sustained delivery of Cal and dramatically reduce the free drug concentrations of Cal in circulation. The well-controlled size of our formulation will enable it to take advantage of the leaky tumor vasculature and accumulate in tumor, where the bulk of drugs will be released. Additionally, by co-formulating Cal with PTX, we can simultaneously attack the stromal and cancer cells to extend the survival in tumor-bearing mice.

2.3 Objectives

a) To develop an extended-release co-formulation of Cal and PTX to treat PDAC in mice

b) To assess the pharmacokinetics (PK) and pharmacodynamics (efficacy) of this combination regimen in an orthotopic $Kras^{G12D}$ mouse model of PDAC.

2.4 Specific Aims

2.4.1 Specific Aim 1

Develop and validate a liquid chromatography-tandem mass spectrometer (LC-MS/MS) assay to simultaneously monitor the concentrations of Cal. and PTX in whole blood, plasma and tissue.

2.4.2 Specific Aim 2

Develop an optimal polymeric micellar co-formulation for delivery of Cal and PTX using the Design of Experiment (DOE) Method, and validate the formulation performance

2.4.3 Specific Aim 3

Characterize the PK and biodistribution of Cal and PTX, and assess the therapeutic merits of the co-formulated Cal and PTX in immune-competent orthotopic mouse models of PDAC

Chapter 3. Materials and Methods

3.1 Materials

3.1.1 Chemicals and Materials

- **Table 3. Antibodies used for immunohistochemical staining**

Target	Host	Source and Catalog Number	Application
CD31	Rb	Abcam, 28364	IHC
Hyaluronan-binding protein 1 (HABP1)	Rb	Novus Biological, NBP1-89790	IHC
Ki67 (human specific)	Rb	Cell Signaling, #9027	IHC
Ki67 (mouse specific)	Rb	Cell Signaling, #12202	IHC
α-Smooth muscle actin	Rb	Abcam, ab5694	IHC, WB

- Cal (purity >98%) was purchased from Cayman Chemical Company (Ann Arbor, MI, USA) and PTX (purity >99.5%) was purchased from LC laboratories (Woburn, MA. USA).
- The internal standards (IS), deuterated Cal (Cal-D4, purity > 99%), and deuterated PTX (PTX D5, purity >98%) were purchased from CRO laboratories Inc. (Dallas, TX, USA).
- Abraxane® was purchased from Abraxis Bioscience, LLC (Los Angeles, CA, USA).
- Biotinylated anti-rabbit or anti-goat IgG (Vector Laboratories, CA) and streptavidin-conjugated horseradish peroxidase (DAKO, CA) were used for visualization of stained tissue slides
- Mouse matrix metalloproteinase 7 (MMP-7) and thrombospondin-2 (TSP-2) ELISA

kits were purchased from MyBiosource (San Diego, CA, USA).

- Mouse TIMP Metallopeptidase Inhibitor 1 (TMIP1) ELISA kit was purchased from Abcam (Cambridge, UK).
- Poly (ethylene glycol) methyl ether methacrylate (purity 100%), 2-hydroxyethyl methacrylate (purity > 99%), anhydrous toluene (purity 99.8%), triethylamine (>99%), hexane (purity > 98.5%), Tin(II) 2-ethylhexanoate (purity 92.5-100%), potassium persulfate (purity >99%), Cbz-N-ethanolamine (purity 98%), anhydrous methanol (purity 99.8%), tetrahydrofuran (purity 99.9%), tetramethylethylenediamine (purity 99.5%), ethyl acetate (purity 99.8%), anhydrous $MgSO_4$ (purity > 99.5) were purchased from Sigma-Aldrich (Saint Louis, MO, USA).
- Acryloyl chloride (purity 96%) and copper (I) bromide (purity 99.998%) were purchased from Alfa Aesar (Haverhill, MA, USA).
- 2,2-dipyridyl was purchased from Acros Organics B.V.B.A (Fair Lawn, NJ, USA).
- Buprenorphine was purchased from Abraxis Pharmaceutical Products (Schaumburg, IL, USA).
- Suture needle and sutures were purchased from Ethicon Inc. (Sommerville, NJ, USA).
- Blank rat and mouse whole blood (in Na EDTA) and plasma were purchased from Innovative Research (Novi, MI. USA) to prepare standard curves for LC-MS/MS assay.
- LC-MS grade water, methanol, hexane, isopropyl alcohol and dichloromethane were purchased from EMD Millipore Corporation (Billerica, MA. USA).

- Eight-week-old cannulated male Sprague-Dawley rats weighing 200-250 g C57BL/6 mice weighing approximately 20 g were supplied by Envigo RMS, Inc (Indianapolis, IN, USA).
- Eight-week-old C57BL/6 female mice (Taconic Biosciences, Rensselaer, NY) were used for PDAC model development

3.1.2 Supplies

- 9 mm wide opening 2 ml amber glass vials (Fisher Scientific, Pittsburgh, PA, USA) were used to protect the photosensitive Cal from light and to hold inserts containing samples for LC-MS/MS analysis.
- Biotix microcentrifuge tubes of 2 ml (VWR International, Radnor, PA, USA) were used for extraction of Cal and PTX.
- Centrifuge tubes (15 and 50 ml) with printed graduations and flat caps (VWR International, Radnor, PA, USA) were for solvent mixing and storage.
- Kinetex C18 column (1.7 μm, 100 x 2.10 mm, Phenomenex. Torrance, CA, USA) was used for the LC separation of Cal and PTX.
- Pipettes (VWR International, Radnor, PA, USA) of the ranges 0.5-10, 10-100, 20-200, 100-1000 µl were used to deliver blood and solvent quantities accurately
- Pipette tips (VWR International, Radnor, PA, USA) of various ranges (1-200, 100-1250 µl) were attached to the pipettes to deliver blood and solvent quantities accurately.
- Polypropylene conical inserts with spring (VWR International, Radnor, PA, USA) were used in conjunction with amber glass vials to enable accurate LC-MS

injection and minimize sample loss in this study that involves limited quantities in sampling.

- Polypropylene microcentrifuge tubes of 1.7 ml (VWR International, Radnor, PA, USA) were used during sample preparation.
- Pre-assembled black 9 mm screw caps with slit (Chrom Tech, Inc., Apple Valley, MN, USA) were used with the amber vials to hold and protect samples during LC-MS/MS analysis.

3.1.3 Equipment

- Air dryer/Nitrogen evaporator (N-EVAP 116, Organomation Associates, Inc., Berlin, MA, USA) was used for drying the extracted samples during the extraction process.
- AMT Imaging System (Advanced Microscopy Techniques Corp., Danvers, MA) was used to take digital images
- API 5500-Qtrap triple quadrupole mass spectrometer (Applied Biosystem/AB SCIEX, Framingham, MA, USA) equipped with a TurboIonSpray™ ion source was used as the mass detector in LC-MS/MS analysis
- Balance (Model ME54TE, NewClassic MF, Mettler Toledo International Inc., Columbus, OH, USA) with sensitivity of 0.1 mg was used to weigh samples
- Centrifuge, Microfuge 22R, speed up to 21920x g (Beckman Coulter, Inc., Brea, CA, USA) was used to

  centrifuge samples during the extraction process
- Compact Digital Microplate Shaker (Thermo Fischer, Waltham, MA, USA) was used for shaking samples to extract Cal and PTX.

- ZetaPlus®, Dynamic Light Scattering System (Brookhaven instruments, Holtsville, NY) was used to measure solution-state particle size and polydispersity index.
- Microdialyzer (Cat # 66110, with molecular weight cut-off ~ 3500, Thermo Scientific, Rockford, IL) was used for the drug release study.
- MyFuge mini centrifuge (model C1008-C, G-force 2000 x g, Benchmark Scientific, Inc., Sayreville, NJ, USA) was used to spin down blood samples spiked with Cal and PTX after vortexing.
- SpectraMax plate reader (model M5e, Molecular Devices, San Jose, CA, USA) was used to read plates during ELISA ssay.
- A bead mill homogenizer (Model: Storm BBY24M) and bead lysis kits (Navy RINO screw cap tubes) were purchased from Next Advantage (Troy, NY. USA)
- Transmission electron microscopy (JEOL USA, Inc., Peabody, MA) was used to measure dried-state particle size.
- Ultrahigh performance liquid chromatography system (model ExionLC AC, SCIEX ExionLC™, Framingham, MA, USA) was used for the chromatographic separation in LC-MS/MS analysis
- Vortex-Genie 2 (Scientific Industries, Inc., Bohemia, NY, USA) was used for vortexing and mixing samples during sample preparation
- Zeiss Axio Observer.Z1 fluorescence microscope(Model Apotome 3, Carl Zeiss Meditec, Inc, Hacienda, CA, USA) was used for visualizing the stained slides.

3.1.4 Software

- Analyst 1.7.0 LC-MS/MS acquisition software (SCIEX, Framingham, MA, USA) was used to control both the LC system and the mass spectrometer instrument and used to perform peak integration and quantification of samples.
- Design Expert Software 8 (StatEase, Minneapolis, MN) was used for statistical modeling and the generation of surface response plots.
- GraphPad Prism 8 (GraphPad Software, San Diego, CA, USA) was used for graph plotting and statistical analyses.
- NIH ImageJ analysis software (http://rsb.info.nih.gov/nih-image/) was used for image quantification with the same threshold for each stain
- NONMEM 7.4 and PdxPOP 5.2.2 (ICON Clinical Research, LLC, North Wales, PA, USA) were used for population PK modeling and analysis.
- Phoenix 8.0 (Certara USA, Inc., Princeton, NJ, USA) was used to perform non-compartmental analysis
- R Studio 3.5.1 or later (The R Foundation for Statistical Computing) was used for data manipulation, visualization and post-processing.

3.2 Methods

3.2.1 UPLC-MS/MS assay for simultaneous quantifications of Cal and PTX in biological samples

3.2.1.1 Chromatographic and mass spectrometry conditions

Cal and PTX were analyzed by a UPLC-MS/MS system consisting of a Waters Acquity™ Ultra-pressure liquid chromatography (Milford, MA. USA) coupled with API 5500-Qtrap

triple quadrupole mass spectrometer (Applied Biosystem/AB SCIEX, Foster City, CA. USA) equipped with an electrospray ionization (ESI) source in the positive mode. Chromatographic separation was achieved using Kinetex C18 column (1.7 μm, 100 x 2.10 mm, Phenomenex. Torrance, CA, USA) under isocratic elution conditions. The method had a runtime of 3.5 min at a flow rate of 0.4 mL/min. The column and autosampler were set to 40 ^{O}C and 10^{O}C, respectively, and the injection volume was 10 μL. A mobile phase consisting of ammonium acetate (pH 6.51; 5 mM)-methanol (15:85, v/v) was used. Ionization of Cal, PTX and their respective isotope-labelled internal standards, Cal-D4 and PTX-D5, was achieved with electrospray ionization in the positive mode. The transition states for multiple reaction monitoring (MRM) on the mass spectrometer are summarized in **Table 4**.

Table 4. Source and analyte-dependent parameters for Cal, PTX and their internal standards on the mass spectrometer

Ion source-dependent parameters						
Ion Spray Voltage (V)	Temperature (^{o}C)	Collision gas	Curtain gas (psi)	Ion source gas 1 (psi)	Ion source gas 2 (psi)	
4500	500	Medium	20	30	70	
Analyte-dependent parameters						
Analyte	Q1 (m/z) Da	Q3 (m/z)	DP (V)	EP (V)	CE (V)	CXP (V)
Cal	395.4	105.1	70	5	30	10
Cal-D4	399.2	283.9	70	5	30	10
PTX	854.2	286.1	70	5	30	10
PTX-D5	859.2	291.2	70	5	30	10

Parent ion (Q1), Product ion (Q3), declustering potential (DP), entrance potential (EP), collision energy (CE) and cell exit potential (CXP) for analytes and internal standards

3.2.1.2 Preparation of calibration standards and quality control samples

For the stock solutions, 1 mg/mL of Cal, Cal-D4, PTX and PTX-D5 were prepared in 100% methanol. Working solutions were prepared from the stock with concentrations ranging from 0.5-500 ng/mL by serial dilutions in a solution of equal parts of water and methanol (1:1, v/v). All the stock solutions were stored at -20^{O}C. Prior to use, the solutions were allowed to thaw to room temperature by leaving them on the work bench for 10 min while protected from light.

For the preparation of calibration standards in different biological matrices, working solutions were diluted in 18 μL of the appropriate matrix (whole blood, plasma or tissue homogenate sample) with a linear range of 0.5 – 500 ng/mL for the analytes. The lowest concentrations of Cal and PTX from which a signal to noise ratio of at least 5 was obtained and set as the lower limit of quantification (LLOQ), in accordance with the 2018 US FDA Guide to Bioanalytical Method Development and Validation. Five quality control (QC) levels were used for the method development and validation. These were the LLOQ (0.5 ng/mL), low QC (2.5 ng/mL), medium QC (25 ng/mL), high QC (400 ng/mL) and ULOQ (500 ng/mL). Cal and PTX were normalized by 50 ng/mL of their respective internal standards.

3.2.1.3 Sample preparation and extraction

To 18 μL of blank rat/mouse whole blood or plasma, 2 μL of respective Cal and PTX were added and vortexed for 30 s to obtain the working concentrations of 0.5, 1, 10, 50, 100, 250, and 500 ng/mL. A liquid-liquid analyte extraction method was employed. To extract the analytes from plasma or whole blood, 100 μL of water-MeOH (1:1, v/v) solvent containing IS (50 ng/mL each of PTX-D5 and Cal-D4) was added to 20 μL of analyte-spiked plasma or whole blood and thoroughly mixed by vortexing for 30 s. Afterwards, the spiked sample was centrifuged at 15,000 x g for 15 min at 4^{O}C. The supernatant obtained after centrifugation was carefully transferred with a pipette into a clean 1.5 mL Eppendorf tube. To the supernatant (80-90 μL), 200 μL of hexane-dichloromethane-isopropyl alcohol (150:15:5, v/v/v) was added and vortexed for 30 s to ensure mixing. This mixture was allowed to shake for 15 min at a speed of 450 rpm on the ThermoFischer Compact Digital Microplate Shaker (Waltham, MA, USA), then centrifuged at 15,000 x g for 15 min with the

centrifuge temperature maintained at 4^{O}C. The clear upper organic layer was harvested with a clean pipette, dried under gentle air and finally reconstituted with 60 μL methanol-water-ammonium formate (1 mM)-ammonium acetate (5 mM) (500: 500: 2: 2, v/v/v/v) (pH 6.87).

For tissues, small pieces were taken from different areas of the tissue mass and weighed accurately. To the tissues, 1 mL of deionized water was added and vortexed for 5 min at 4°C with a bead mill homogenizer. A portion of the homogenate (100 μL) was transferred into 2 mL tube to which 500 μL of water-methanol (1:1 v/v) containing 5 ng/mL IS (each of Cal-D4 and PTX-D5) was added and vortexed for a minute. Just as was done for whole blood and plasma samples, the tissue mixture was shaken for 15 min at a speed of 450 rpm and subsequently centrifuged. The supernatant was transferred into a clean 1.5 mL tube, air-dried and then reconstituted with 100 μL of methanol-water-ammonium formate (1 mM)-ammonium acetate (5 mM) (500: 500: 2: 2, v/v/v/v) (pH 6.87).

The concentrations in tissue were normalized by the weight of tissue used.

3.2.3 Method Validation

Validation of the method was performed in accordance with the 2018 US FDA Guidelines of Bioanalytical and Method Validation: Guidance for Industry.

Specificity, linearity, accuracy and precision, extraction efficiency, matrix effects and stability were evaluated. For analyte recovery and matrix effects, IS-normalized and non-IS-normalized were evaluated.

3.2.3.1 Specificity and endogenous interference on analyte retention times

To evaluate the impact of endogenous substances on retention time and signal intensity, a series of concentrations of both analytes in the standard solution of water-MeOH (1:1,

v/v) and from spiked whole blood and plasma samples were injected. Endogenous interference was evaluated by comparing chromatograms from the standard samples to those obtained from whole blood and plasma-processed samples. In addition, the specificity was evaluated by comparing chromatograms from spiked whole blood and plasma with extracted blank whole blood and plasma.

3.2.3.2 Assay linearity

The linear range was tested at 0.5 – 500 ng/mL for both Cal and PTX, and the degree of fitness was described by a correlation coefficient of at least 99%. A weighting factor of 1/x was used for both Cal and PTX

3.2.3.3 Assay accuracy and precision

Accuracy and precision were evaluated at 5 QC levels (LLOQ, LQC, MQC, HQC and ULOQ). For inter-day accuracy and precision, 6 samples of each QC level were analyzed for 3 runs over a 3-day period. For intra-day precision and accuracy, 6 samples of each QC were analyzed for 3 runs (N=18) over a 24-hour period. Accuracy was evaluated as the ratio of calculated to nominal concentrations, and precision was evaluated as the relative standard deviation (RSD) of the calculated value. Accuracy was deemed acceptable if it was within ±15% deviation of LQC, MQC, HQC, ULOQ and ±20% for LLOQ. Similarly, the acceptable precision was ±15% for all QC levels, except ±20% for LLOQ.

3.2.3.4 Recovery and matrix effects

To evaluate the recovery of Cal and PTX, the peak area ratios of non-IS normalized pre-extraction spiked whole blood/plasma to post-extraction spiked whole blood/plasma were compared, as well as IS-normalized pre-extraction spiked whole blood/plasma to post-

extraction spiked whole blood/plasma. Matrix effects was similarly evaluated by comparing peak area ratios of IS-normalized and non-normalized post-extraction spiked whole blood or plasma to analytes in standard solutions

3.2.3.5 Sample stability

The stability of Cal and PTX under different stress conditions were evaluated including freeze-thaw, 2-week storage and sample processing at room temperature at 5 QC levels to evaluate how resilient the analytes were to multiple freeze-thaw cycles, spiked whole blood or plasma stored at -20^{o}C was subjected to 3 freeze-thaw cycles. Samples were frozen at -20^{o}C and thawed at room temperature for a total of three cycles before analyte extraction. Sample processing stability was evaluated by re-injecting spiked plasma and whole blood samples kept in the autosampler at 10^{o}C for 10 hours. For storage stability, spiked whole blood and plasma were stored at -20^{o}C for two weeks. A 2 week-stability test was chosen because samples from experiments were expected to be processed within this time frame. These were compared to measurements from freshly prepared samples. Each stability test was performed with 6 replicates, from which the coefficients of variation (% CV) were calculated

3.2.4 Pharmacokinetic and drug-drug interaction studies

Male Sprague Dawley rats (8-week-old, 200-250 g) were randomly divided into 3 groups of 3 and allowed to acclimatize for 3 days after delivery. The rats were allowed free access to chow and water. All experiments were approved by the Institutional Animal Care and Use Committee (IACUC) (Protocol number 15-023) of the University of Houston. Rats were intravenously administered 1 mg/kg of either Cal, PTX or in a combination of both dissolved in 10% dimethyl acetamide solution. Blood samples were drawn at pre-

determined time points (5 min, 10 min, 15 min, 20 min, 30 min, 45 min, 1 hr, 2 h, 4 h, 6 h, 12 h and 24 h) post dose. After each blood draw of 200 µL an equal volume of heparinized saline was injected back into the animals through the cannula. Half volume of the drawn blood (100 µL) was stored at -20^{o}C and the remaining 100 µL was transferred into a new tube and centrifuged at 2,000 x g for 15 min to harvest plasma. The plasma was also stored at -20^{o}C until quantification. Samples were protected from light at all times to protect the highly photosensitive Cal. All blood samples were processed within 2 weeks of collection using the process described in **3.2.1.3.** The concentrations of Cal and PTX in whole blood and plasma were measured with the developed and validated LC-MS/MS assay. Concentration-time profiles were subsequently constructed. Non-compartmental PK analyses were performed using Phoenix® WinNonlin 8.0, to derive relevant PK parameters.

3.2.5 Polymer synthesis

3.2.5.1 Polymer reaction initiator, 2-(benzyloxycarbonyl amino) ethyl 2-bromo-isobutyrate (Compound 1)

Cbz-N-ethanolamine 3 g (15.36 mmol) was dissolved in 20 mL of ethyl acetate in a round bottom flask and stirred vigorously with cooling in an ice bath for 1 hr. Triethylamine (2.35 mL) was directly added into the mixture in the round bottom flask. 2-Bromoisobutyryl bromide (3 mL, 165.1 mmol) in 5 mL of ethyl acetate was slowly added in dropwise under vigorous stirring. A cloudy product resulted. More ethyl acetate (up to 50 mL) was added when reaction mixture was too viscous. The ethyl acetate solution was subsequently washed with saturated $NaHCO_3$, 5% HCl, and double-distilled water. Once separated, the aqueous phase (bottom layer) was discarded, and the product was dried with anhydrous

$MgSO_4$ and condensed in vacuo at 35°C. The resulting viscous oil was stored at 4°C (Compound 1).

3.2.5.2 Poly[oligo(ethylene glycol) monomethyl ether methacrylate)$_{40}$-b-poly(2-hydroxyethyl methacrylate)$_{20}$ (Polymer 1)

The synthetic schemes described in this manuscript are adaptations of the atomic radicalization polymerization reactions described by Matyjaszewski and Xia ((Matyjaszewski and Xia, 2001). Into a round-bottom flask was added Compound 1 (0.17 g, 70.2 µmol), oligo ethylene glycol methyl methacrylate (OEG_{20}-MA, MW ~ 500, 10 g, 20 mmol), 2,2'-bipyridine, BPy (0.16 g, 1.02 mmol), and 5 mL of anhydrous methanol. The flask was flushed with anhydrous argon for 20 min and immersed in a 55°C oil bath. CuBr (0.072 g, 0.5 mmol) was quickly added under argon protection, and the reaction was allowed to proceed for 30 min. A separate mixture of 2-hydroxyethyl methacrylate (1.2 mL, 2.1 mmol) in 3.7 mL of de-oxygenized methanol was added into the reaction mixture. The polymerization continued for 18 h at 55°C and then stopped by exposure to open air for at least 4 h. After a dilution step with ethyl acetate, the reaction was passed through a basic aluminum column to remove the CuBr catalyst and condensed in vacuo at 45°C to give **Polymer 1.**

3.2.5.3 Poly(OEG-MA)$_{40}$-b-poly[HEMA-g-(ε-caprolactone)$_6$]$_{20}$ (Polymer 2)

Polymer 1 (2.5 g, 0.11 mmol) was dried azeotropically by distillation with toluene at 140°C and allowed to cool for 1 hr. Anhydrous ε-caprolactone (CPL, 1.48 mL, 13.14 mmol) and tin (II) 2-ethylhexanoate [$Sn(Oct)_2$, (0.015 g, 0.04 mmol)] were added. The flask was flushed with anhydrous argon and allowed to run overnight under N_2 gas at 110°C. The polymerization mixture was precipitated in hexane and kept at -20°C for 4 h. Once fully

precipitated, the product was filtered and dried under N_2 gas for 1 h to obtain 3.8 g of **Polymer 2**

3.2.5.4 Poly(OEG-MA)$_{40}$-b-poly[HEMA-g-(acryloyloxy ε-caprolactone)$_6$]$_{20}$-(Polymer 3)

To 1 g of **Polymer 2**, 8 mL of tetrahydrofuran (THF) was added, and polymer thoroughly dissolved on an ice bath. To this mixture, 70.5 µL of triethyl amine (TEA) was added while stirring. To the stirring mixture, 38.3 µL of acryloyl chloride (0.46 mmol) in 2 mL THF was added dropwise. The mixture reacted for 45 min, then was centrifuged at 6,000 g for 10 min after which the supernatant was collected (10 mL) (Polymer 3)

3.2.5.4 Preparation of micelles loaded with Cal and PTX (M-Cal/PTX)

To 5 mg of PTX and 1 mg of Cal, 2 mL of **Polymer 3** in THF was added and vortexed to ensure the drugs were completely dissolved. The initial drug loading ratio of 5:1 PTX to Cal ratio was chosen after optimization with response surface methodology. Different ratios of PTX and Cal by weight were evaluated with encapsulation efficiency as the readout. We observed a 5:1 ratio of PTX to Cal yielded satisfactory encapsulation efficiencies (> 90% for PTX and > 65% for Cal). To the resulting mixture, 10 µL of tetramethylethylenediamine (TEMED) was added. While vortexing, 4 mL of distilled water was added and vigorously vortexed for 1 min. The organic solvent (THF) was removed in vacuo to leave concentrated micelles (4 mL). Potassium persulfate, $K_2S_2O_8$ (10 mg) was added and then stirred for 1 hr. The loaded micelle (M-Cal/PTX) was dialyzed to remove unencapsulated drugs. Subsequently it was centrifuged at 10,000 g for 10 min, and supernatant collected to obtain a final PTX to Cal ratio of ~ 10:1. The freshly prepared micelles were stored at 4^{o}C for short-term period of 6 weeks. For long-term storage (>3 months), the micelles were stored at -80 ^{o}C using 5% sucrose as a cryoprotectant.

3.2.5.5 Micelle optimization using central composite design (CCD)

To obtain micelles with size <100 nm and extended drug release properties, CCD was employed to tune formulation parameters, namely, the number of repeating units of methacrylate-grafted oligoethylene glycol (OEG-MA-500, 13.2 – 46.8 units), CPL (4.3–7.6 units) and crosslinking density (XL, 7.9-92%). To simplify the model and reduce the number of parameters to be optimized, the number of repeating units of 2-hydroxyethyl methacrylate was kept constant (20-HEMA) based on preliminary studies. A full factorial design was used to generate models using Design Expert Software v8 (StatEase, Minneapolis, MN) for statistical modeling and the generation of surface response plots. The independent factors of OEG-MA-500, CPL and XL, and their effects on the micelle size, and 2-hr accumulative drug release at pH 6 and pH 7.4 were coded at 5 levels as −α, −1, 0, +1, +α, with 0 as the central point (**Table 11**).

3.2.5.6 Characterization of M-Cal/PTX

The size, morphology, zeta potential, drug loading and release properties of M-Cal/PTX preparations were characterized. Particle size and zeta potential were measured with a dynamic light scattering system on ZetaPlus® particle sizer (Brookhaven Instruments Corp., Holtsville, NY). The methods for drug encapsulation efficiency (EE), size, morphology and release evaluations are described in sections **3.2.5.6.1 to 3.2.5.6.4**

3.2.5.6.1 Cal and PTX encapsulation efficiency

Drug loading efficiency was evaluated by modifying a published protocol (Zhao et al., 2018a). Briefly, micelles were dissolved in methanol and vortexed at high speed, followed by a 5 min sonication to release encapsulated drugs. After centrifugation at 10,000 g for 30 min, the supernatant containing released drugs was collected and analyzed on Waters

Acquity™ Ultra-high-pressure liquid chromatography (UPLC, Milford, MA. USA). Chromatographic separation was achieved using Kinetex C18 column (1.7 μm, 100 x 2.10 mm, Phenomenex. Torrance, CA, USA) under isocratic elution conditions with a total runtime of 3.5 min at a flow rate of 0.4 mL/min. The detection wavelengths for Cal and PTX were 210 nm and 227 nm respectively. The column and autosampler temperatures were 40°C and 10°C, respectively, and the injection volume was 10 μL. The composition of the mobile phase was ammonium acetate solution (5 mM)-methanol (15:85, v/v). Encapsulation efficiency (EE) was computed according to the formula

EE (%) = (Amounts of Cal and PTX recovered after dialysis) / (Amounts Cal and PTX added in micelles) x 100%

3.2.5.6.2 Morphology and size determination of M-Cal/PTX

The dried state visualization of particle size and morphology of Cal and PTX-loaded micelles were examined on a transmission electron microscopy (JEOL USA, Inc., Peabody, MA) according to the method described in Zhao et al., 2018b, with digital images collected on the AMT Imaging System (Advanced Microscopy Techniques Corp., Danvers, MA). To also determine the range of particle size distribution in the native solution state we used the Dynamic Light Scattering System (Brookhaven instruments, Holtsville, NY).

3.2.5.6.3 Drug release of polymeric micelles

To determine the drug release profiles, polymeric micelles containing 1.2 mg/mL PTX and 0.17 mg/mL Cal were diluted in the appropriate matrix (PBS at pH 7.4 or sodium acetate at pH 6, and mouse serum) and added to a microdialyzer (molecular weight cut-off ~ 3500, Thermo Scientific, Rockford, IL). The microdialyzers were incubated in PBS (pH 7.4), sodium acetate buffer (pH 6.0) or mouse plasma in a 37°C water bath with agitation.

Aliquots (30 µL) were taken at predefined times from the microdialyzer. The samples were centrifuged at 6,000 g for 5 min and 10 µL of the supernatant was retrieved and analyzed for Cal and PTX concentrations using UPLC method in **3.2.5.6.1**

3.2.5.6.4 Storage stability of M-Cal/PTX

The storage stability of M-Cal/PTX was evaluated by storing the formulation at 4°C for 6 weeks. The stability was evaluated by measuring the changes in micelle size and encapsulation efficiency**.**

3.2.5.7 Development of $Kras^{G12D}$ mouse model of PDAC

All animal studies were approved by the Institutional Animal Care and Use Committees (IACUC) of UT-M.D. Anderson Cancer Center and University of Houston. Kras* murine pancreatic cancer cells with a doxycycline-inducible mutation of *KRAS*^{G12D} were cultured and the Kras* murine PDAC model was developed according to a previously published protocol (Zhao et al., 2018b). Eight-weeks old C57BL/6 female mice (Taconic Biosciences, Rensselaer, NY) were injected with Kras* cells into the pancreas head under isoflurane anesthesia after a small opening was made in the abdomen to expose the pancreas. A 27-gauge needle was used for precise injection of 5×10^5 Kras* cells. Mice were administered buprenorphine twice a day for the first 3 days to ease pain and allowed to completely heal before study initiation (10-14 days).

3.2.5.8 Pharmacokinetics and biodistribution of M-Cal/PTX

Mice with palpable pancreatic tumors of diameter 5 mm were recruited and randomized into two study groups. The mice were each administered an intravenous bolus of M-Cal/PTX (N=3) at doses of 5 mg/kg PTX and 0.5 mg/kg Cal or the non-formulated drugs (N=3) at the equivalent doses. Blood samples were collected at pre-determined time

points, …. and the mice were euthanized 24 hours post dose. Tumor and liver tissues were collected for simultaneous quantifications of Cal and PTX concentrations, using the developed and validated tandem UHPLC-MS/MS assay referenced in **3.2.1**

3.2.5.9 T2-weighted magnetic resonance imaging

Tumor size was measured using respiration-gated T_2-MRI on a Biospec USR70/30 system (Bruker Biospin MRI, Billerica, MA) equipped with a 7-T magnet. The following parameters were used: TE/TR = 38/2000 ms; BW = 101010.10 Hz; Rare = 8; averages = 3; matrix size = 256 × 192; field of view = 4 cm × 3 cm; slick thickness = 0.75 mm; slice gap = 0.25 mm. Images were processed using Bruker Biospin software (version 2.10). Tumor size was measured at the largest tumor cross-section of axial images. The tumor size was quantified using NIH ImageJ analysis software (http://rsb.info.nih.gov/nih-image/).

3.2.5.10 Immunohistochemical staining

Harvested tumors were fixed in formalin, embedded in paraffin then cut into pieces of approximately 4-μm in thickness for storage at room temperature until further analysis. The sections were subsequently deparaffinized, rehydrated, and subjected to antigen retrieval for 30 min in 95 °C 10 mM citrate buffer (pH 6). The slides were allowed to cool to room temperature. Next, the slides were blocked in tris-buffered saline (pH 7.4) supplemented with 0.1% Tween-20 and 10% goat or donkey serum. The primary antibodies were incubated overnight at 4 °C. For visualization, the slides were washed and incubated with biotinylated anti-rabbit or anti-goat IgG secondary antibody (Vector Laboratories, CA, USA) and incubated at room temperature for 30 min. The choice of anti-rabbit or anti-goat IgG secondary antibody depended on the source of the primary

antibody. Subsequently, the secondary antibodies were washed off and the slides re-incubated in streptavidin-conjugated horseradish peroxidase (DAKO, CA, USA) at room temperature for 30 min. A positive reaction was detected by exposure to 3,3′-diaminebenzidine (DAB) for 20-30 s. Slides were counterstained with hematoxylin and visualized under a brightfield microscope at 100x or 200Å~ magnification. All the images acquired on the microscope were quantified using NIH ImageJ analysis software (http://rsb.info.nih.gov/nih-image/), keeping the threshold constant across stains.

3.2.5.11 Reverse phase protein array

Harvested tumors were flash-frozen in liquid nitrogen and quickly transferred into -80 ^{o}C freezer. The reversed-phase protein array (RPPA) analysis was performed in the Functional Proteomics RPPA Core Facility at the University of Texas MD Anderson Cancer Center. The tumor tissues were lysed with RPPA lysis buffer and then serially diluted in five 2-fold dilutions. Next, the samples were printed on nitrocellulose-coated slides using an Aushon Biosystem 2470 arrayer (Billerica, MA). The slides were subsequently probed with validated primary antibodies, followed by the complementary biotinylated secondary antibodies for visualization. The signals were amplified using a Cytomation-catalyzed system of Avidin−biotinylated peroxidase (Vectastain Elite ABC kit from Vector Lab, Burlingame, CA). The amplification system recognizes and binds to secondary antibodies and facilitates the tyramide-biotin conjugation reaction to produce insoluble biotinylated phenols. A secondary streptavidin conjugated HRP and DAB colorimetric reaction was used to visualize the amplified signals. Next, the slides were scanned and quantified with Array-Pro Analyzer software (Media Cybernetics, Rockville, MD) to generate spot intensity (level 1 data). With SuperCurve GUI, an R package, relative

protein levels were estimated. The signal intensities and relative amounts of protein in the log2 scale were plotted on the y- and x-axes, respectively, using a nonparametric, monotone increasing B-spline model. Additionally, the raw data was adjusted with control spots to correct for spatial bias. The slides underwent quality control where those with at least 0.8 score on a 0-1 scale were deemed to have sufficient quality and used for further analysis (level 2 data). A median-centered approach was used to correct protein measurements for loading (level 3 data) and samples with extremely low protein levels were excluded.

3.2.5.12 Enzyme-linked immunosorbent assay (ELISA)

Whole blood samples were carefully collected into non-heparinized tubes and allowed to clot for 30 min at room temperature. The samples were centrifuged at 1,000 g for 15 min. The supernatant (serum) was collected and stored at -20 ^{o}C for later analysis.

3.2.5.12.1 Mouse matrix metalloproteinase-7 (MMP-7) ELISA

A 100 μL volume of mouse serum or sample diluent was measured into blank wells pre-coated with MMP-7 antibodies. A similar volume of previously prepared MMP-7 standards was measured into blank wells. The plate was covered with an adhesive strip and incubated at 37 ^{o}C for 1 hr. Next, the wells were decanted through inversion without washing. A working solution of the concentrated biotin conjugate antibody (100X) was prepared 15 min before use according to the manufacturer's instructions. A 100 μL volume of biotin conjugated antibody diluent was added to the blank well, and to the sample wells an equal volume of biotin conjugated antibody working solution. The plate was covered with a new adhesive strip and incubated at 37 ^{o}C for 1 hour. A working solution of streptavidin-horseradish peroxidase was prepared 15 minutes before use. After

incubation, each well was washed with 350 μL of wash buffer for a total of three washes. Streptavidin-horseradish peroxidase diluent was added to the blank well, and to the others 100 μL of streptavidin-horseradish peroxidase working solution. The plate was covered with a new adhesive strip and allowed to incubate at 37 °C for 30 min. After incubation, the wash step was repeated for a total of 5 washes. To each well, 50 μL of TMB solution was added at 37 °C under light protection for 20 minutes. Subsequently, the reaction was stopped with a 50 μL volume of a stop solution and the optical density of each well was determined using a microplate reader set at 450 nm within 5 minutes after adding the stop solution.

3.2.5.12.2 Mouse thrombospondin-2 (TSP-2) ELISA

All reagents were allowed to reach room temperature and mixed thoroughly before use.

A 100 μL volume of standard, blank or sample was added to new wells. The plate was covered with an adhesive strip and incubated at 37 °C for 2 hr. The liquids were removed from each well through inversion without washing. To each well, 100 μL of a working solution of detection reagent A was added. The plate was covered with a new strip and allowed to incubate at 37 °C for 1 hr. Subsequently, each well was aspirated and washed with the wash buffer (400 μL/wash) for a total of 3 washes. The wash buffer was completed removed and after the last wash the plate was blotted. Next, 100 μL of a working solution of detection reagent B was added to each well, covered and incubated at 37 °C for 1 hr. The aspiration and wash step were repeated for a total of 5 washes. Next, 90 μL of substrate solution was added to each well, covered and allowed to incubate at 37 °C for

20 min while protected from light. After incubation, 50 μL of stop solution was added, and the optical density was measured within 5 minutes on a microplate reader set at 450 nm.

3.2.5.12.3 TIMP Metallopeptidase Inhibitor 1 (TIMP1) ELISA

All materials and reagents were allowed to equilibrate to room temperature prior to use. The reagents, working standards and samples were prepared according to the manufacturer's instructions.

A 50 μL volume of standard or sample was added to the empty wells. Next, 50 μL of antibody cocktail was added to each well. The plate was sealed and then incubated for 1 hr at room temperature on a plate shaker set to 450 rpm. After incubation each well was washed with 350 μL of 1X wash buffer per wash for a total of 3 washes. Complete removal of the wash buffer was ensured by decanting and blotting the plate against clean absorbent-paper. Next, 100 μL of TMB substrate was added to each well and incubated for 10 min in the dark on a plate shaker set to 450 rpm. Subsequently, 100 μL of a stop solution was added to each reaction well. The contents of the plate were mixed thoroughly by shaking on the plate shaker for 1 min, and the optical density was measured on a plate reader with a wavelength set at 450 nm.

3.2.6 Statistical analysis

Data were evaluated using Student's t-test or 1-way analysis of variance (ANOVA) followed by post hoc Tukey test for multiple comparisons. The statistical significance was evaluated at $p < 0.05$.

Chapter 4. Results

4.1 MS/MS fragmentation

4.1.1 Cal, PTX, Cal-d4, Cal-D5 parent to daughter ions

In choosing the parent-daughter pairs for analyte quantifications, daughter ions with the highest signal intensities were considered first. Although the 395.4 →133.1 m/z for Cal had the highest signal, this pair produced chromatograms with a high baseline, making Cal quantifications at low concentrations unreliable. The 395.4 → 105.1 m/z for Cal was therefore chosen to monitor and quantify Cal (Fig. 4A). For Cal-D4, 399.2 → 283.9 m/z was chosen because this pair was very stable and could be reliably used for Cal normalization (Fig. 4B). PTX was monitored and quantified with 854.2 → 286.1 m/z (Fig. 4C) and 859.2 → 291.2 m/z for PTX-D5 (Fig. 4D)

A.

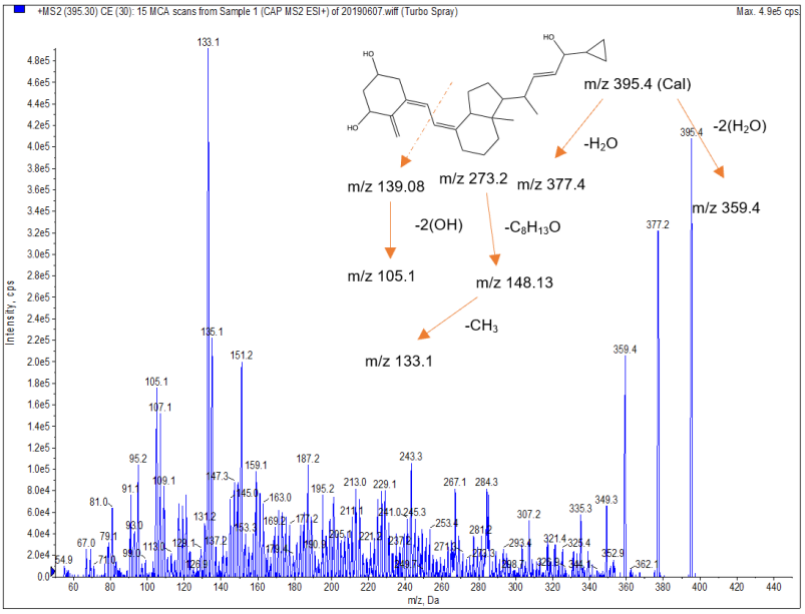

B.

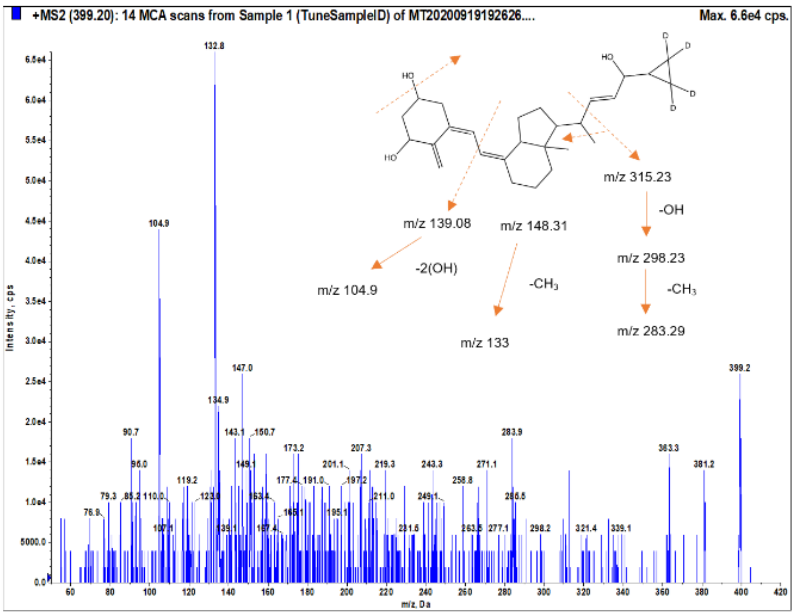
+MS2 (399.20): 14 MCA scans from Sample 1 (TuneSampleID) of MT20200919192626....
Max. 6.6e4 cps.
Intensity, cps
m/z, Da
m/z 315.23
-OH
m/z 298.23
-CH3
m/z 283.29
m/z 139.08
-2(OH)
m/z 104.9
m/z 148.31
-CH3
m/z 133

C.

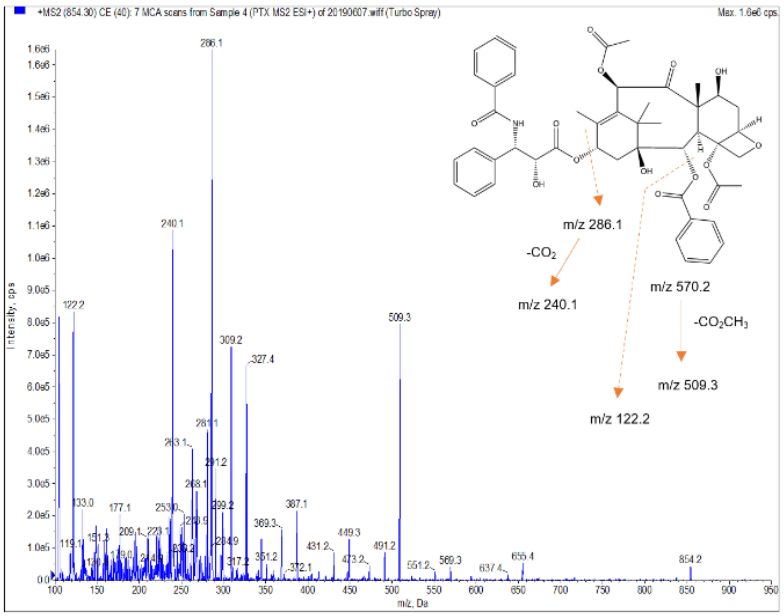
+MS2 (854.30) CE (40): 7 MCA scans from Sample 4 (PTX MS2 ESI+) of 20190607.wiff (Turbo Spray)
Max. 1.6e6 cps.
Intensity, cps
m/z, Da
m/z 286.1
-CO2
m/z 240.1
m/z 570.2
-CO2CH3
m/z 509.3
m/z 122.2

D.

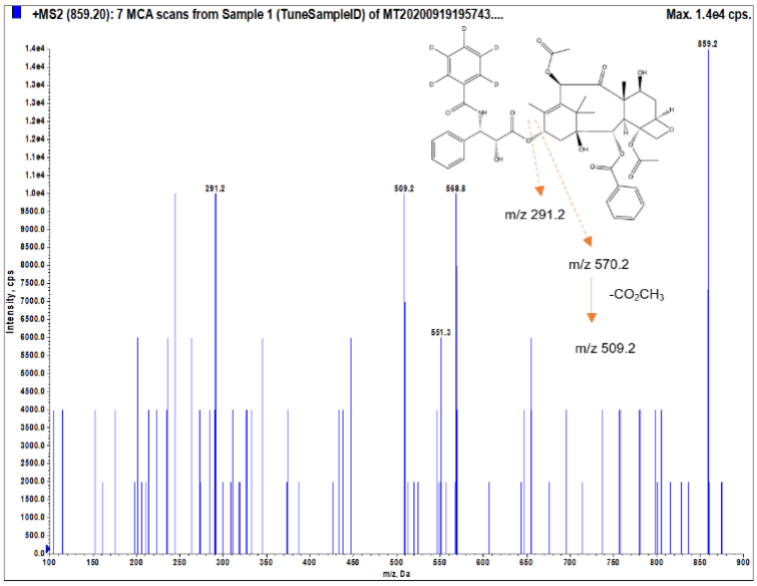

Figure 4. MS/MS Spectra of Cal (A), Cal-D4 (B), PTX (C) and PTX-D5 (D) with chemical structures and assignment of the main fragment ions

4.1.2 Retention times of analytes

The retention times of Cal and PTX were 1.03 and 0.66 min, respectively. Blank and pre-extraction spiked rat whole blood was used to determine assay specificity as shown in **Figure 5.**

A.

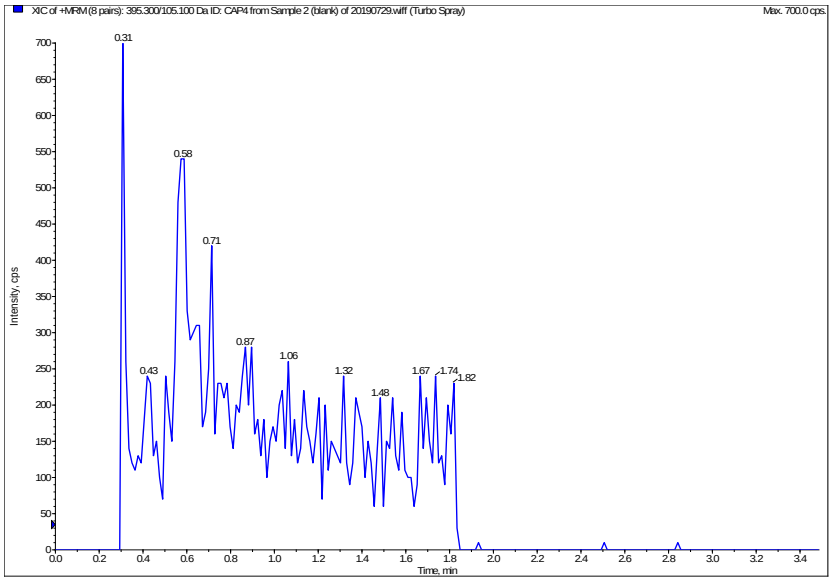
XIC of +MRM (8 pairs): 395.300/105.100 Da ID: CAP4 from Sample 2 (blank) of 20190729.wiff (Turbo Spray)
Max. 700.0 cps.
Intensity, cps
Time, min
0.31
0.58
0.71
0.43
0.87
1.06
1.32
1.48
1.67
1.74
1.82

B.

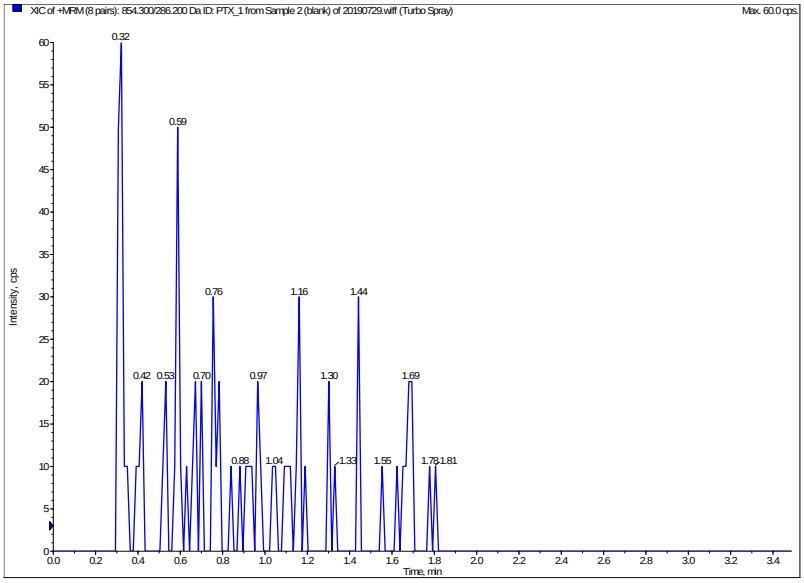
XIC of +MRM (8 pairs): 854.300/286.200 Da ID: PTX_1 from Sample 2 (blank) of 20190729.wiff (Turbo Spray)
Max. 60.0 cps.
Intensity, cps
Time, min
0.32
0.59
0.76
1.16
1.44
0.42
0.53
0.70
0.97
1.30
1.69
0.88
1.04
1.33
1.55
1.78
1.81

C.

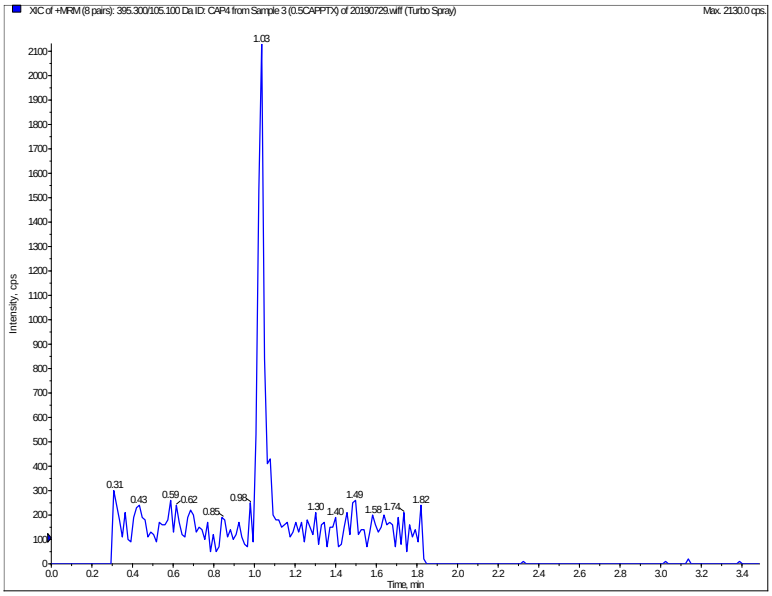
XIC of +MRM (8 pairs): 395.300/105.100 Da ID: CAP4 from Sample 3 (0.5CAPPTX) of 20190729.wiff (Turbo Spray)
Max. 2130.0 cps.
Intensity, cps
Time, min
1.03
0.31
0.43
0.59
0.62
0.85
0.98
1.30
1.40
1.49
1.58
1.74
1.82

D.

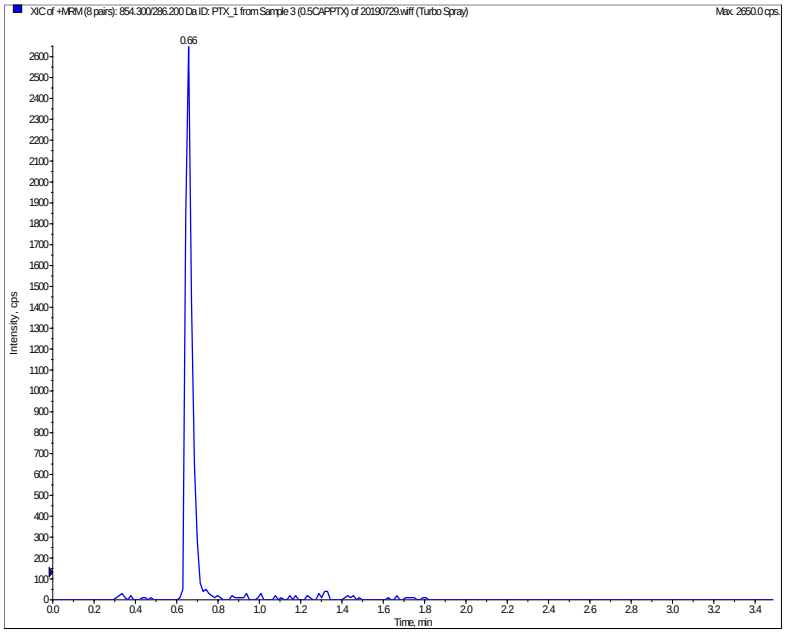
XIC of +MRM (8 pairs): 854.300/286.200 Da ID: PTX_1 from Sample 3 (0.5CAPPTX) of 20190729.wiff (Turbo Spray)
Max. 2650.0 cps.
Intensity, cps
Time, min
0.66

E.

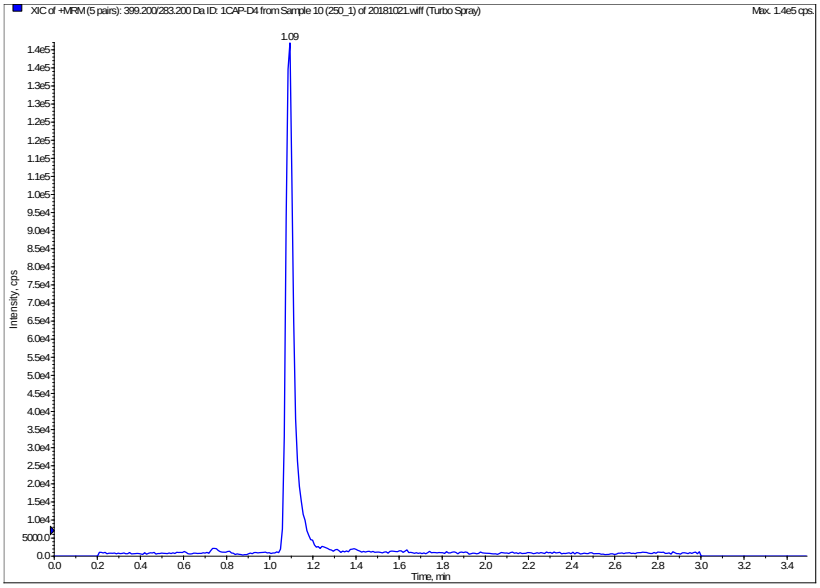
XIC of +MRM (5 pairs): 399.200/283.200 Da ID: 1CAP-D4 from Sample 10 (250_1) of 20181021.wiff (Turbo Spray)
Max. 1.4e5 cps.
1.09
Intensity, cps
Time, min

F.

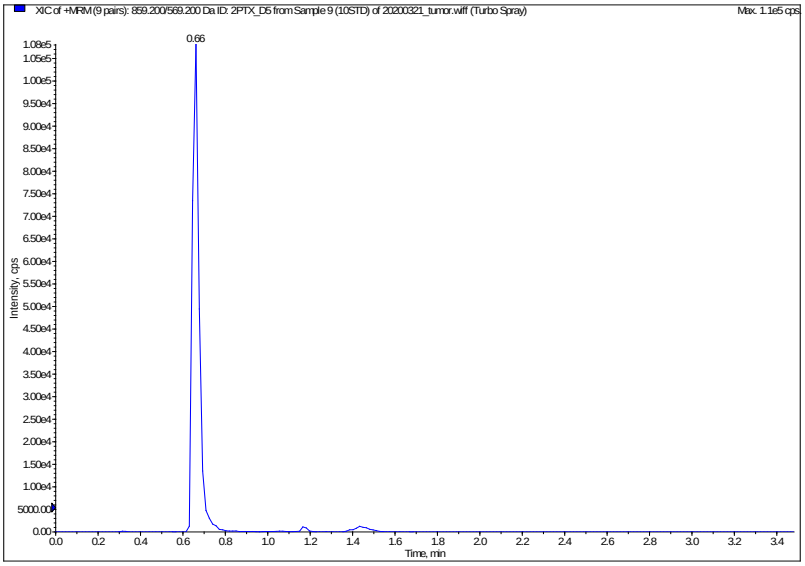
XIC of +MRM (9 pairs): 859.200/569.200 Da ID: 2PTX_D5 from Sample 9 (10STD) of 20200321_tumor.wiff (Turbo Spray)
Max. 1.1e5 cps
0.66
Intensity, cps
Time, min

G.

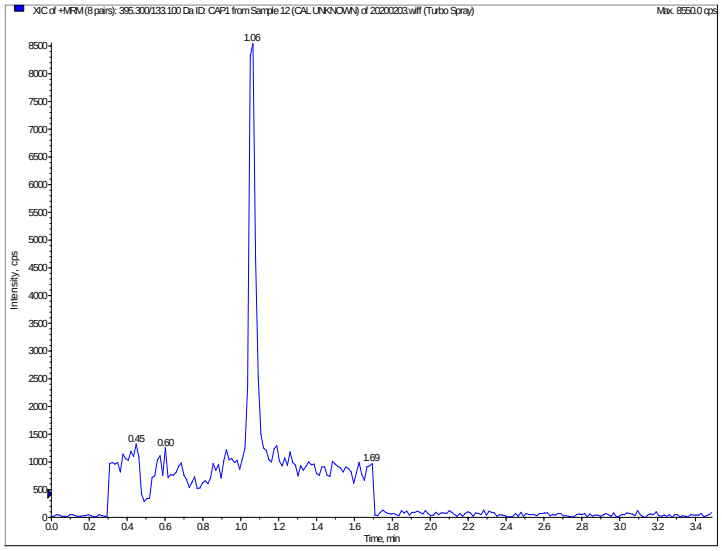

H.

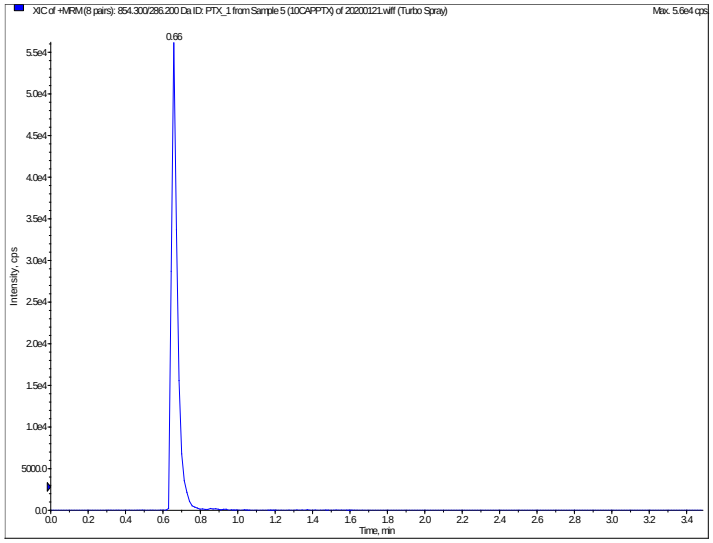

Figure 5. Representative chromatograms of Cal and PTX. Extracted whole blood blanks (A, B) Cal LLOQ (C) PTX LLOQ (D) and IS, 100 ng/mL Cal-D4 (E), 100 mg/mL PTX-D5 (F), Cal from a whole blood study sample (G) and PTX from whole blood study sample (H)

4.1.3. LLOQ and linearity

The LLOQ for Cal and PTX in whole blood is 0.5 ng/mL with signal to noise ratio of >10, far exceeding the requirements by the US FDA. The linear ranges for Cal and PTX in whole blood (**Fig. 6**) and plasma (**Fig. 7**) were 0.5 ng/mL - 500 ng/mL with coefficients of correlation of at least 0.99.

A.

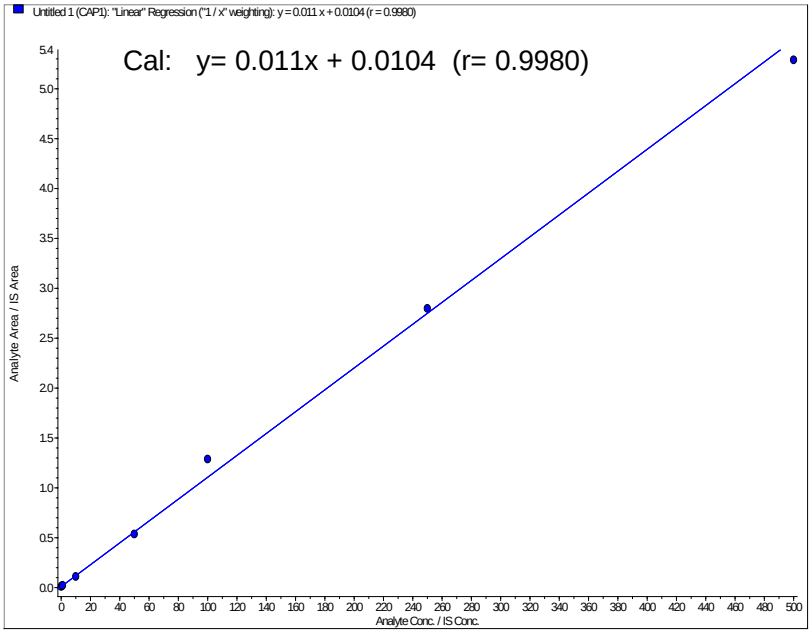

B.

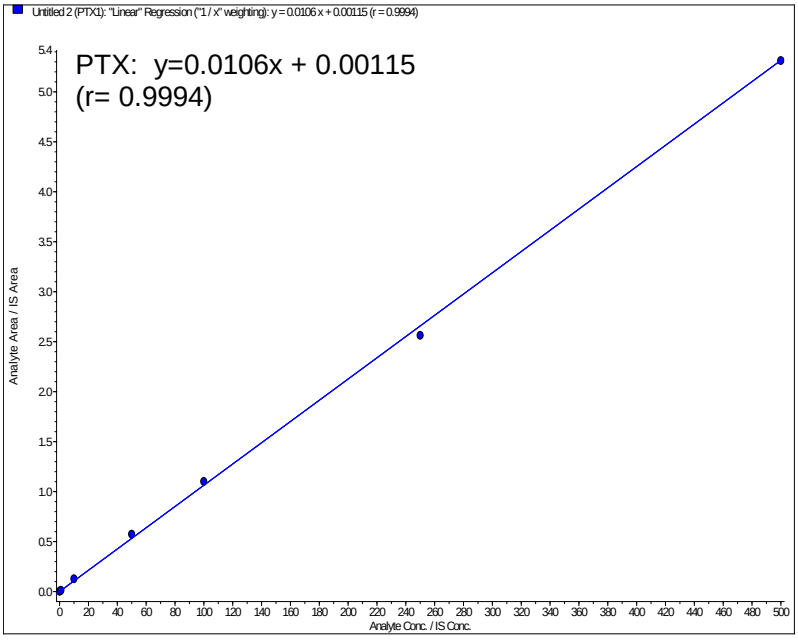

Figure 6. Calibration curves of Cal (A) and PTX (B) in rat whole blood

A.

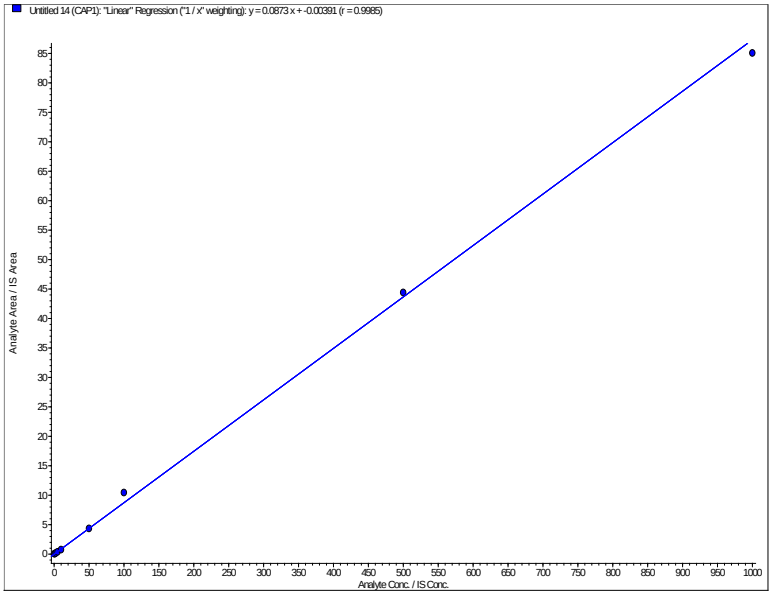

B.

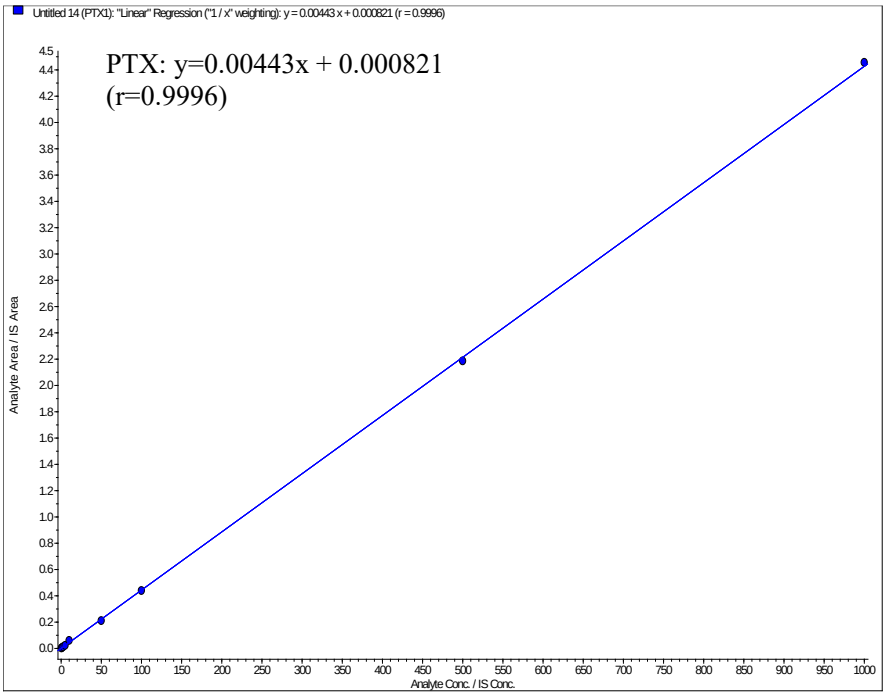

Figure 7. Calibration curves for Cal (A) and PTX (B) in rat plasma

4.1.4. Precision and accuracy

For whole blood samples, the intra-day accuracy was 90.5 – 105.0%, and precision of 3.09 – 10.7% for Cal. The accuracy and precision for PTX were 93.7 – 105.0% and 2.71 -10.7% , respectively. The corresponding inter-day precision in whole blood was 5.20-8.70% for Cal and 3.65 – 9.70 % for PTX. The inter-day accuracy for Cal and PTX were 96.6 – 102.0% and 98.2 – 101.0 % respectively **(Table 5).**

Table 5. Intra- and inter-day precision and accuracy of Cal and PTX in whole blood

Intra-day (N=6)							Inter-day (N=18)	
Cal								
QC level	Day 1		Day 2		Day 3			
(ng/mL)	Precision	Accuracy	Precision	Accuracy	Precision	Accuracy	Precison	Accuracy
	(%)	(%)	(%)	(%)	(%)	(%)	(%)	(%)
0.5	9.44	93.7	5.95	98.1	10.7	103.8	8.70	101.0
2.5	5.75	105.0	4.70	99.6	8.28	102.0	6.83	99.5
25	6.94	95.5	7.92	90.5	7.85	94.3	6.84	96.6
400	3.57	102.0	6.42	102.0	8.91	100.0	5.91	102.0
500	3.09	98.3	5.25	99.1	4.95	102.0	5.20	99.3
PTX								
0.5	10.5	102.0	8.94	93.7	7.62	94.6	9.70	98.5
2.5	6.90	99.2	5.58	97.7	8.90	99.9	7.16	98.2
25	5.96	99.1	10.7	104.0	7.10	105.0	7.63	101.0
400	5.04	99.7	3.80	102.0	3.53	102.0	4.35	101.0
500	3.87	100.0	2.71	97.8	3.08	97.9	3.65	99.30

For plasma samples, the intra-day accuracy was 93.4-107.0%, and precision of 4.23 – 13.9% for Cal. The accuracy and precision for PTX were 101.0-105.0% and 1.12-6.44% respectively. The corresponding inter-day precision in plasma was 9.22- 12.9% for Cal and 4.62 – 6.33 % for PTX. The inter-day accuracy for Cal and PTX were 99.9- 104.0 and 101.0 – 103.0 % respectively (**Table 6**).

Table 6. Intra- and inter-day precision and accuracy of Cal and PTX in plasma

Intra-day (N=6)							Inter-day (N=18)	
Cal								
	Day 1		Day 2		Day 3			
QC level	Precision	Accuracy	Precision	Accuracy	Precision	Accuracy	Precision	Accuracy
ng/mL	(%)	(%)	(%)	(%)	(%)	(%)	(%)	(%)
2.5	13.9	103.0	12.6	93.4	5.91	99.8	12.9	104.0
25	6.86	95.6	7.71	99.7	5.35	96.2	7.42	99.9
500	11.4	105.0	5.82	101.0	4.23	107.0	9.22	101.0
PTX								
2.5	6.44	102.0	1.42	101.0	4.28	103.0	4.62	101.0
25	3.98	104.0	2.02	105.0	4.13	104.0	5.43	103.0
500	1.68	104.0	1.12	101.0	1.43	101.0	6.33	103.0

4.1.5 Matrix effects and recovery

Adequate analyte recovery from biological matrices and reduced effects of endogenous substances are critical for reliable quantifications of Cal and PTX concentrations. For these studies, the internal standards were added post extraction in order to eliminate IS recovery/matrix effects as confounding factors. Results for IS-normalized recoveries and matrix effects of Cal and PTX in whole blood are reported in **Table 7A** and in **Table 7B** for plasma. Additionally, non-IS normalized recoveries and matrix effects are presented in **Tables 8.**

Other extraction procedures, such as protein precipitation were explored, but the highest analyte recoveries and reduced matrix effects were attained with the liquid-liquid extraction procedure. In choosing the solvents for extraction, careful consideration was given to the physicochemical properties of Cal and PTX (both very hydrophobic), as well as matrix components. An initial solvent mixture of methanol and water allowed efficient

extraction of the hydrophobic analytes but also the water-soluble components in the blood. A further purification step was achieved with a mixture of hexane, isopropyl alcohol and dichloromethane in an optimal ratio as **3:2:1:3** by volume**.** Initially, several solvents and solvent mixtures were explored including acetonitrile (ACN), ethyl acetate-isopropyl alcohol (1:1 v/v), hexane-dichloromethane (1:1 v/v) and a previously described hexane dichloromethane-isopropyl alcohol (300:150:15 v/v/v) for Cal extraction (Li et al., 2013). Although the hexane-dichloromethane-isopropyl alcohol combination yielded acceptable recovery, the peak shapes were not optimal, especially at low Cal and PTX concentrations. Additional solvent ratio tuning was explored with different solvent ratios, and a dichloromethane content of between 15-25% by volume and isopopropyl alcohol content of 5-15% yielded desirable analyte recoveries, and optimal peak shapes. The final solvent mixture was therefore hexane dichloromethane-isopropyl alcohol (150:15:5 v/v/v). This solvent mixture was critical to separating the hydrophobic agents from the water-soluble components of the blood to attain a clean sample.

Sufficient sample purity is crucial for accurate concentration measurement and maintain the extended column lifespan.

Table 7. Internal-standard normalized matrix effects and recovery of Cal and PTX in whole blood (A) and plasma (B)

A.

Cal						
QC level (ng/mL)	Recovery (%)	SD (N=6)	%CV	Matrix Effects (%)	SD (N=6)	%CV
0.5	90.2	0.05	12.3	94.6	0.01	10.6
2.5	112.0	0.19	9.63	92.2	0.11	9.72
25	109.0	0.93	8.41	103.0	1.49	15.1
400	103.0	51.4	14.2	111.0	24.2	12.3
500	96.2	47.2	11.1	105.0	21.9	9.43
PTX						
0.5	104.0	0.04	12.3	85.7	0.05	11.2
2.5	92.5	0.09	6.21	110.0	0.18	9.85
25	103.0	1.34	12.3	110.0	0.92	4.69
400	104.0	23.9	7.54	96.2	13.2	3.64
500	96.6	23.2	5.31	103.0	13.4	3.06

B.

Cal						
QC level (ng/mL)	Recovery (%)	SD (N=4)	% CV	Matrix Effects (%)	SD (N=4)	% CV
0.5	109.0	0.02	9.87	86.9	0.07	15.5
2.5	104.0	0.11	8.07	96.4	0.21	9.47
25	93.8	1.05	7.49	103.0	1.74	8.06
400	93.8	24.8	9.22	99.9	17.4	7.40
500	106.0	25.3	7.12	99.1	18.31	6.41
PTX						
0.5	108.0	0.04	17.9	105.0	0.03	16.0
2.5	92.4	0.16	9.46	102.0	0.07	8.88
25	100.0	1.14	9.34	104.0	1.64	9.72
400	97.2	18.2	6.96	111.0	13.8	5.63
500	102.0	17.1	6.02	92.7	14.8	4.66

Table 8. Non-IS normalized matrix effects and recovery of Cal and PTX in whole blood and plasma

Cal Non-IS normalized recovery and matrix effects (whole blood)						
QC level (ng/mL)	Recovery (%)	SD (N=6)	%CV	Matrix Effects (%)	SD (N=6)	%CV
0.5	87.2	0.04	15.4	88.4	0.03	8.67
2.5	94.8	0.27	12.4	90.7	0.23	10.2
25	99.2	1.23	9.73	98.5	2.23	17.4
400	101.4	44.5	11.9	89.9	30.4	15.1
500	94.5	50.5	20.7	97.1	22.7	6.63
PTX Non-IS normalized recovery and matrix effects (whole blood)						
0.5	92.7	0.03	19.4	86.3	0.02	13.54
2.5	89.6	1.02	8.45	99.8	0.21	7.32
25	90.1	2.23	18.4	95.2	1.23	3.05
400	97.4	24.7	9.32	96.9	16.5	2.64
500	95.3	39.4	4.33	89.5	11.4	2.21
Cal Non-IS normalized recovery and matrix effects (plasma)						
QC level (ng/mL)	Recovery (%)	SD (N=4)	% CV	Matrix Effects (%)	SD (N=4)	% CV
0.5	94.5	0.01	5.32	92.4	0.05	10.3
2.5	98.7	0.21	12.4	96.9	0.37	7.34
25	99.7	0.99	13.2	99.5	2.34	6.06
400	96.4	15.4	8.43	93.4	14.5	7.60
500	96.3	20.7	6.56	99.4	10.3	5.33
PTX Non-IS normalized recovery and matrix effects (plasma)						
0.5	95.3	0.02	11.4	93.5	0.01	9.04
2.5	92.4	0.12	7.43	100.2	0.05	6.33
25	98.5	1.42	8.46	97.2	2.34	5.34
400	98.2	12.4	5.77	98.1	12.5	7.22
500	96.6	15.4	4.65	95.4	16.4	6.73

4.1.6 Sample stability

Storage, process and freeze-thaw stabilities of Cal and PTX in whole blood was evaluated and presented in **Table 9**. After two weeks of storage of spiked whole blood samples at 20 ^{o}C, Cal and PTX stabilities were within 90.53-110.32% of nominal values at all QC

levels. Similarly, processing the samples at room temperature for 10 hr had no significant impact on the stabilites as corroborated by the stabilities within 91.92-111.24% of nominal concentrations. Because the samples get frozen in storage and then thawed before processing, we evaluated the impact of hree freeze-thaw cycles on analyte stabilites. Concentrations of Cal and PTX remained between 96.91-105.63% of baseline concentrations. These results confirm that under the described conditions, the integrities of Cal and PTX remain largely unperturbed. These stabilties were evaluated in whole blood but not plasma because whole blood is the matrix of interest for future studies.

Table 9. Storage, process and freeze-thaw stability of Cal and PTX in whole blood

	Two-weeks storage		Process		Freeze-thaw	
Cal						
QC level (ng/mL)	Stability (%)	% CV (N=6)	Stability (%)	% CV (N=6)	Stability (%)	% CV (N=6)
0.5	98.3	7.32	111.0	9.21	104.0	11.1
2.5	103.0	6.62	92.2	10.2	96.9	9.84
25	102.0	3.44	103.0	7.97	105.0	13.6
400	90.5	8.68	91.9	6.43	106.0	8.79
500	109.0	7.26	107.0	5.84	101.0	7.71
PTX						
0.5	95.4	7.66	93.2	6.65	99.7	8.10
2.5	96.2	6.88	101.0	5.45	98.3	5.65
25	110.0	4.10	106.0	3.11	99.4	2.21
400	93.3	4.21	103.0	6.78	102.0	1.91
500	105.0	3.68	97.5	3.56	101.0	1.31

4.1.7 Drug-drug interaction study

Male Sprague Dawley rats (N=9) were randomly assigned into 3 groups (N=3 each), to receive a single I.V bolus dose of Cal, PTX, or a combination of Cal/PTX dissolved in 10% dimethyl acetamide at 1 mg/kg of each drug. Blood samples were taken at predetermined

time points for whole blood and plasma samples for analyte quantifications. The concentrations of Cal and PTX were measured using the above described, validated UPLC-MS/MS assay, and PK profiles were constructed (**Figure 8**). Partially validated and incompletely described Cal assays exist in literature; however, these assays are not sensitive enough to monitor Cal concentrations 2 hr post single IV dose of 1 mg/kg. Additionally, these assays use sample volumes of up to 100 µL, a luxury that cannot be afforded when working with small animals like mice. Measuring Cal over an extended period after administration is particularly challenging because of its short half-life. We aimed to develop the assay to overcome these limitations, by careful optimization of analyte and source parameters, as well as efficient sample extraction. With only 20 µL of whole blood, Cal concentrations could be monitored up to 24 hours after a single dose of 1 mg/kg (**Figure. 8A**). Due to the presence of three hydroxy groups in Cal, monitoring this analyte in the negative ionization mode appears reasonable. However, while developing this assay, it was recognized that the ionization in the negative mode presented instability problems, and yielded a high baseline, espcially for Cal. A positive ESI resolved these issues.

The PK analysis was performed using Phoenix® WinNonlin (8.0) to characterize the impact of combination treatment on the derived PK parmaters of the individual agents (**Table 10**). The mean exposure ($AUC_{0\rightarrow\infty}$) and C_{max} of Cal was decreased in the combination group, resulting from an increase in total clearance (CL) while the elimination half-life ($t_{1/2}$) was essentially the same between the groups. These observations held true in both whole blood and plasma samples. The $AUC_{0\rightarrow\infty}$ and C_{max} of PTX were higher in combination with Cal than those in PTX alone treatment group in both whole blood and plasma samples,

due to the decreased CL. PTX showed marginally increased $t_{1/2}$ in the combination groups but this was not statistically significant. For PTX in whole blood samples, the exposure ($AUC_{0\rightarrow\infty}$) and C_{max} were 5-7 times higher than those in plasma for both single and co-treatment groups, suggesting a significant binding of PTX to blood cells. On the other hand, Cal profiles did not show difference between whole blood and plasma, suggesting no significant distribution to blood cells. This PK study revealed, for the first time, a potential drug-drug interaction between Cal and PTX. Co-adminstration of PTX and Cal resulted in an increase in PTX exposure and a decrease in Cal exposure.

A.

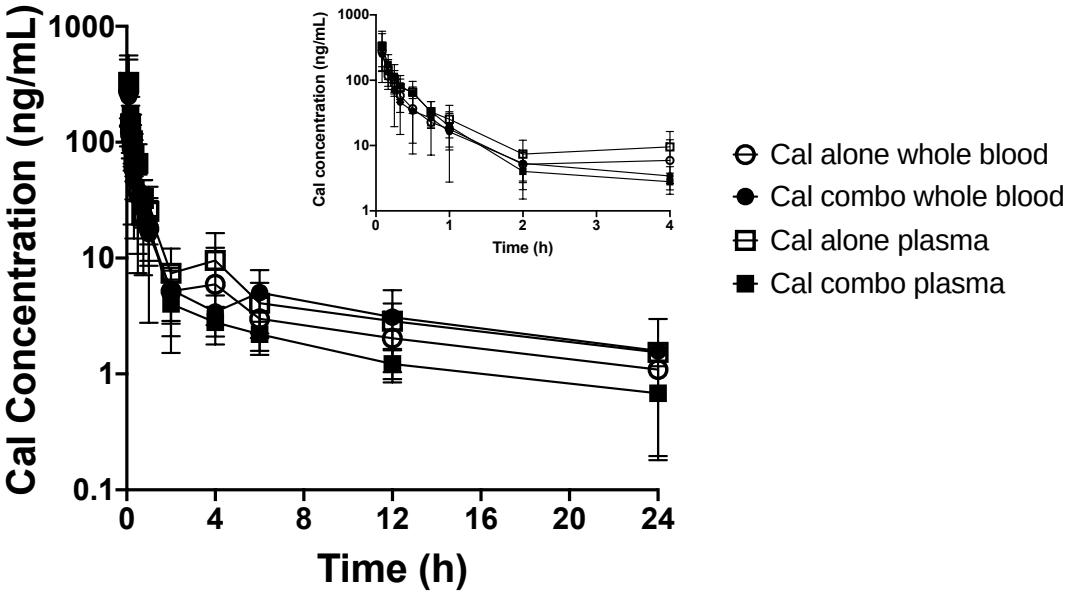

B.

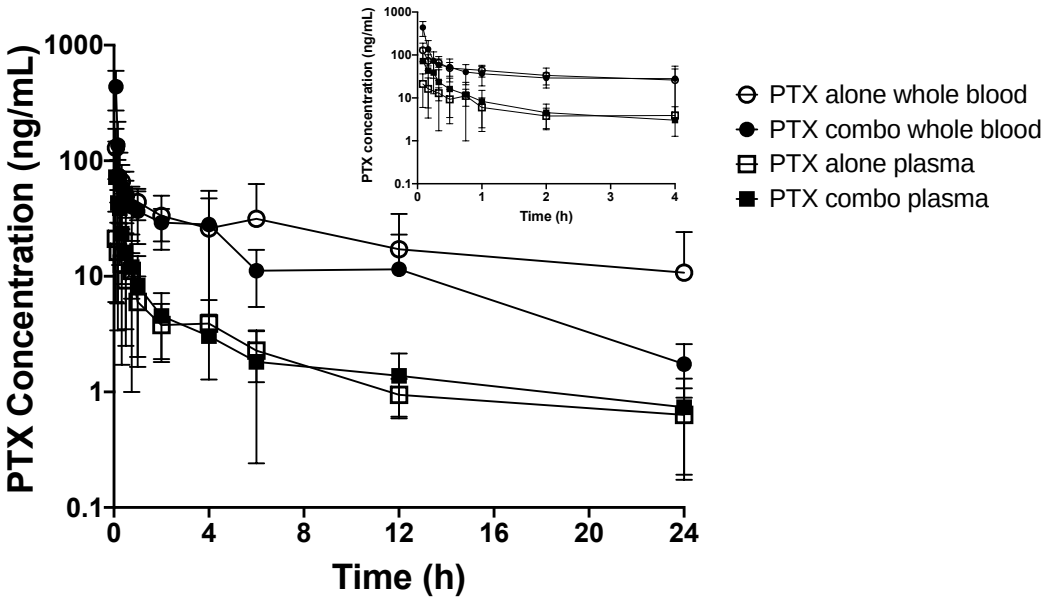

Figure 8. Concentration-time profiles of (A) Cal and (B) PTX in whole blood for alone and combination groups. Data represents mean ± S.D (N=3)

Table 10. Pharmacokinetic parameters of Cal and PTX after treatments of combination and single agent alone

Cal					
Whole blood (N=3)				Plasma (N=3)	
		Alone	Combination	Alone	Combination
Parameter	Units	Mean (%CV)	Mean (%CV)	Mean (%CV)	Mean (%CV)
AUC	h*ng/mL	117.0 (19.8)	102.0 (27.7)	15.4x10 (40.8)	11.8x10 (22.08)
CL	mL/h/kg	$87.6x10^2$(17.8)	$10.2\ x10^{3*}$(25.4)	$75.3x10^2$ (50.6)	$96.7x10^{2*}$ (20.7)
C_{max}	ng/mL	92.5x10 (62.5)	$68.7x10^{*}$ (48.4)	$11.5x10^2$ (72.8)	$66.4x10^{*}$ (77.2)
$t_{1/2}$	hr	0.58 (24.1)	0.52 (67.3)	0.67 (40.0)	0.51 (39.4)
PTX					
Whole blood (N=3)				Plasma (N=3)	
		Alone	Combination	Alone	Combination
Parameter	Units	Mean (%CV)	Mean (%CV)	Mean (%CV)	Mean (%CV)
AUC	h*ng/mL	$13.4x10^{\Delta}$ (40.4)	$17.6x10^{*\#}$ (34.9)	27.1 (33.3)	28.9 (62.0)
CL	mL/h/kg	$14.9x10^{3\,\Delta}$(21.1)	$10.9x10^{3\#}$ (31.8)	$40.2x10^3$ (37.7)	$40.3x10^3$(47.9)
C_{max}	ng/mL	$12.4x10^{\Delta}$ (11.6)	$18.1x10^{*\#}$ (21.1)	17.0 (65.2)	31.1 (57.9)
$t_{1/2}$	hr	1.62 (30.8)	1.90 (45.7)	1.50 (20.7)	1.73 (42.9)

Student's t test was used for comparison between groups with significance set at $p < 0.05$ for N=3 in each group.

*significant difference between alone vs. combination group;

$^{\Delta}$ significant difference between alone in whole blood vs. alone in plasma

$^{\#}$significant difference between combination group in whole blood vs. combination group in plasma

4.2 Development of an optimal M-Cal/PTX using CCD

Adequate exposure of the tumor to drug is essential for efficacy. However, PDAC is characterized by the presence of a “physical wall” formed by the dense stroma action. A pharmacological approach to reprogram the stroma requires a drug delivery vehicle to deliver sufficient amounts of drugs to the tumor bed.

4.2.1 Synthesis of a micellar-based polymeric drug delivery system.

An effective drug micelle-based drug delivery system must be able to carry sufficient drug payload and remain relatively stable in circulation and be released at the desired site of action. An adaption of the atomic radical polymerization reaction, initially described by (Matyjaszewski and Xia, 2001) was employed (**Figure 9)**

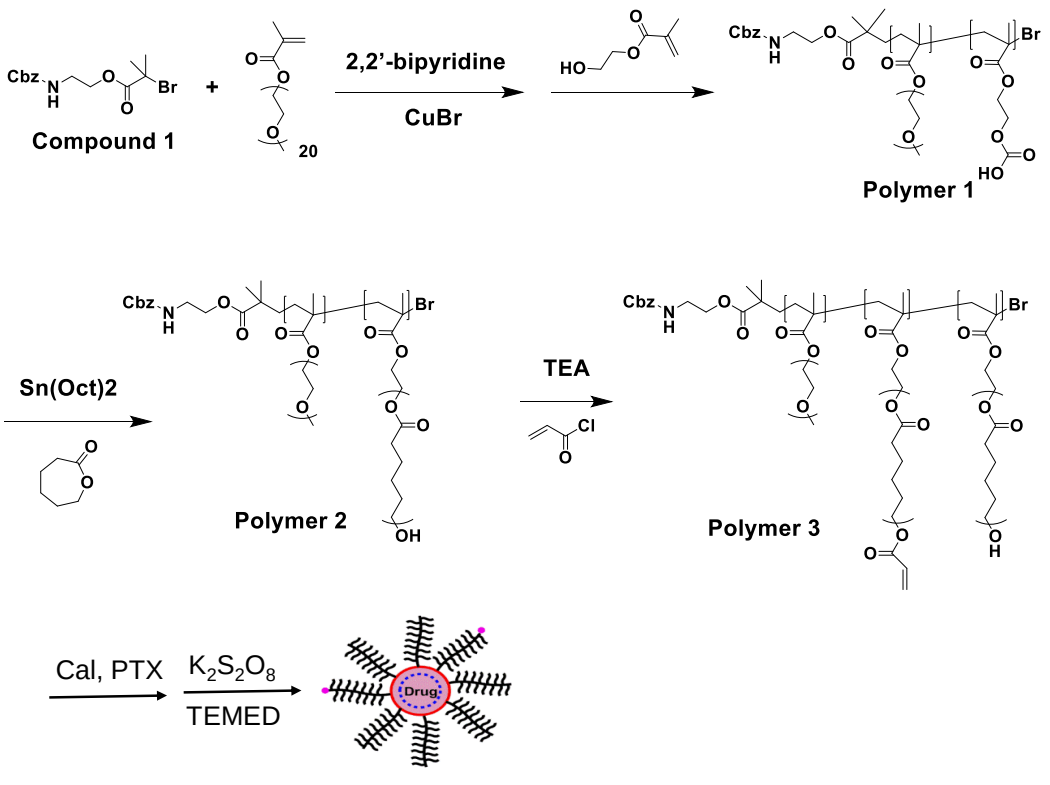

Figure 9. Polymer synthesis and formulation of Cal and PTX loaded micelles (M-Cal/PTX). TEA, trimethylamine; TEMED, tetramethylethylenediamine.

4.2.2 Optimizing the micellar formulation with PTX as the model drug

The effects of the number of units of OEG-MA-500, CPL, and XL (%) on the size and 2 hr drug release kinetics of PTX were studied using 20 experimental runs (**Table 11**). PTX was chosen as the model drug for CCD formulation optimization, because PTX (MW= 853.9 g/mol, logP= 3.52, water solubility= 0.0056 mg/mL) and Cal (MW= 412.6 g/mol, logP=4.3, water solubility=0.0135 mg/mL) have similar physicochemical properties, making extrapolation from PTX to Cal feasible. Economic consideration was another factor for not using large amounts of Cal in the process of formulation optimization, but validating with Cal in the optimized formulation. Micelle size from the experimental runs ranged between 16.6-100 nm, cumulative 2-hr PTX release at pH 6 and 7.4 were 17.7-115.4% and 6.6- 100 %, respectively, depending on the formulation compositions. The formulation variable-dependent drug release characteristics were best described by a linear model for pH 6 and, and a quadratic model for the release characteristics for pH 7.4. A log-transformed linear model best described the impacts of formulation variables on the micelle size, as summarized in **Table 12.**

Surface response maps **(Figure 10A)** corroborated the mathematical models and showed that the extent of drug release decreased with increasing amount of PEGMA 500 at pH 6. Several diagnostic plots were assessed for model suitability and are presented in **Figures B-M.** At pH 7.4, drug release decreased with increasing PEGMA500 while drug release increased with increasing CPL. The response-surface

map and model diagnostics are shown in **Figure 11.**

The response surface map showed micelle size had an inverse relationship with both PEGMA500 and CL (**Figure 12A**) with acceptable model diagnostics (**Figures 12B-M**). The normal percentage probability vs externally studentized residuals residual plot is a test for the normality of the residual. The residuals fell directly on or were close to the diagonal line signifying the model met the assumption of residual normality (**Figure 12B**). The relative weight of observations used for predictions were also tested by plotting the externally studentized residual vs predicted (**Figure 12C**) and also vs run (**Figure 12D**). these graphs did not reveal any trends in the residuals and most residuals were within the acceptable +/- 2 standard deviation range. The actual vs predicted plot also showed the model had a decent fit (**Figure 12E**). This was corroborated by the residual vs lambda plot (**Figure 12F**). The blue line which represents the model was between the two red lines which represent the margin of acceptability. The green line reflects an ideal or perfect model. Models within the limits of acceptability are considered fit for purpose. Again, the externally studentized residuals were plotted against the PEGMA500 (**Figure 12G**), CL (**Figure 12H**) and XL (**Figure 12I**). The residuals showed no model misspecification.

The influence of observations on model predictions were tested. The Cook's distance (**Figure 12J**), leverage (**Figure 12K**), DFFITS (**Figure 12L**) and DFBETAS (**Figure 12M**) were plotted against the run number. The farther an observation is from the line of unity the more influential the observation on the prediction. Influential observations are those whose omission from the model significantly impacts the prediction. Generally, these are not desired because they could bias the model. The plots showed that most observations were within the acceptable limits. The model diagnostics are also summarized in **Table**

13. These same diagnostics were used to qualify the model for drug release and pH 6 and micelle size. For succinctness, they will not be repeated.

Table 11. Formulation values of independent factors and measured response variables

	Factor 1	Factor 2	Factor 3	Response 1		Response 2		Response 3	
Run	PEGMA-500	CPL	XL	2-hr release at pH 6 (%)		2-hr release at pH 7.4 (%)		size (nm)	
units	No. of units	No. of units	%	Mean (%)	SD	Mean (%)	SD	Mean (%)	SD
1	20	5	25	65.4	2.2	30.9	32.0	21.7	16.9
2	30	6	50	66.3	1.1	39.1	33.9	24.7	20.6
3	30	6	50	70.0	3.1	41.0	34.4	26.1	20.3
4	40	7	25	19.9	2.2	15.7	12.0	9.9	7.0
5	30	7.6	50	112.5	2.2	54.9	55.3	37.5	30.5
6	40	7	75	14.2	2.0	30.4	39.1	23.8	19.4
7	40	5	25	83.1	2.6	36.9	41.5	27.0	21.2
8	46.8	6	50	19.1	1.5	23.5	24.5	16.5	13.0
9	30	6	50	68.7	1.7	40.1	34.6	25.5	20.8
10	30	6	7.9	97.4	2.3	35.9	53.3	30.5	25.9
11	30	4.3	50	106.5	3.3	53.3	51.7	36.1	28.4
12	30	6	50	65.4	1.3	38.9	33.4	24.6	20.3
13	30	6	92	65.4	0.5	52.6	47.1	33.4	28.6
14	20	5	75	96.8	2.6	58.1	49.3	36.7	29.9
15	13.2	6	50	115.5	4.5	56.7	55.8	39.0	29.9
16	40	5	75	60.3	2.5	45.9	38.3	28.9	23.2
17	20	7	75	58.2	1.8	45.0	38.4	28.4	23.3
18	20	7	25	34.0	1.1	20.0	17.0	12.7	10.2
19	30	6	50	67.0	2.0	39.7	33.7	25.1	20.2
20	30	6	50	69.6	2.6	40.7	34.5	25.9	20.5

Table 12. Equations for best-fit models and summary statistics for micelle size and 2-hr PTX release at pH 6 and 7.4

Response variables	Model equations in terms of coded factors	R^2	p value
2-hr PTX release at pH 6	47.49 - 19.77 x PEGMA-500 + 16.83 x CPL	0.62	0.0035
2-hr PTX release at pH 7.4	48.34 - 19.70 xPEGMA-500 + 11.19 x CPL + 2.97 x XL -13.96 x PEGMA-500 x CPL + 11.26 x CPL^2 - 8.26x XL^2	0.83	0.0004
Micelle size	1.72 - 0.13 x PEGMA-500 - 0.11 x CPL + 0.10 x XL	0.60	0.0262

A.

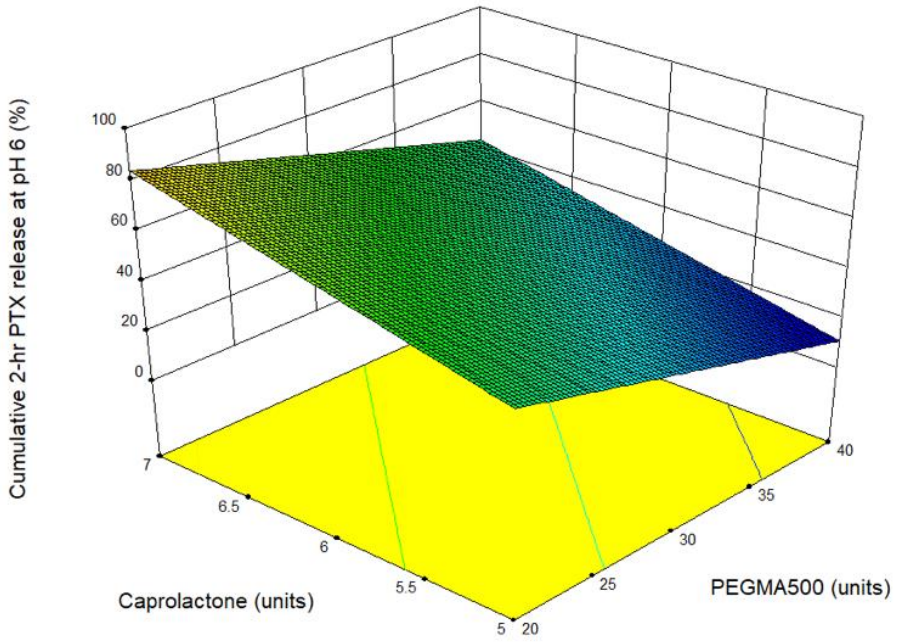

B

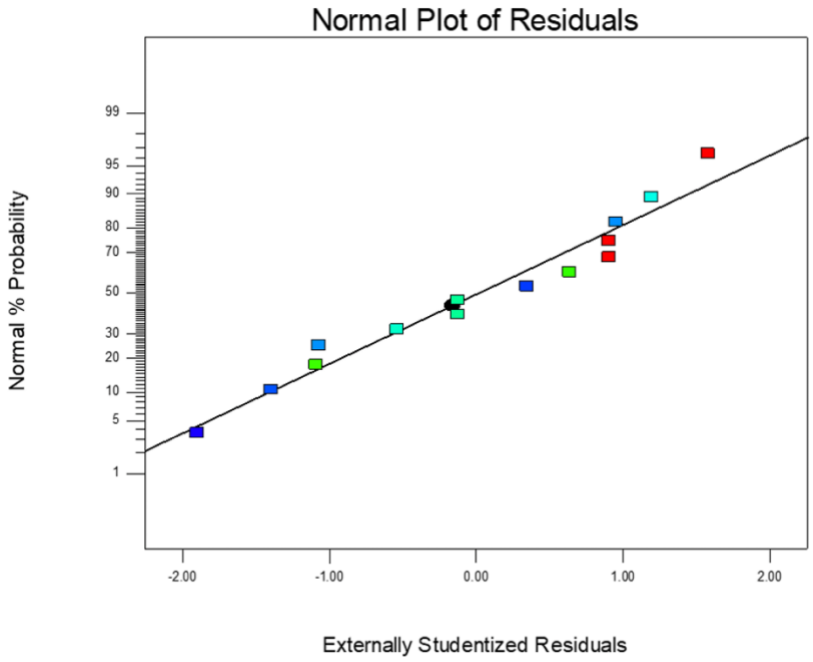
Normal Plot of Residuals
Normal % Probability
99
95
90
80
70
50
30
20
10
5
1
-2.00
-1.00
0.00
1.00
2.00
Externally Studentized Residuals

C.

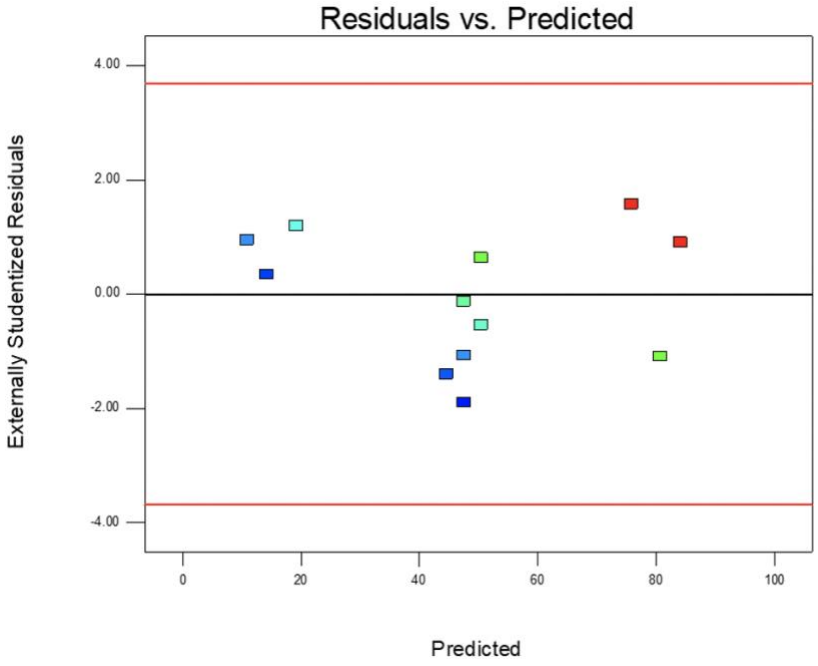
Residuals vs. Predicted
Externally Studentized Residuals
4.00
2.00
0.00
-2.00
-4.00
0
20
40
60
80
100
Predicted

D.

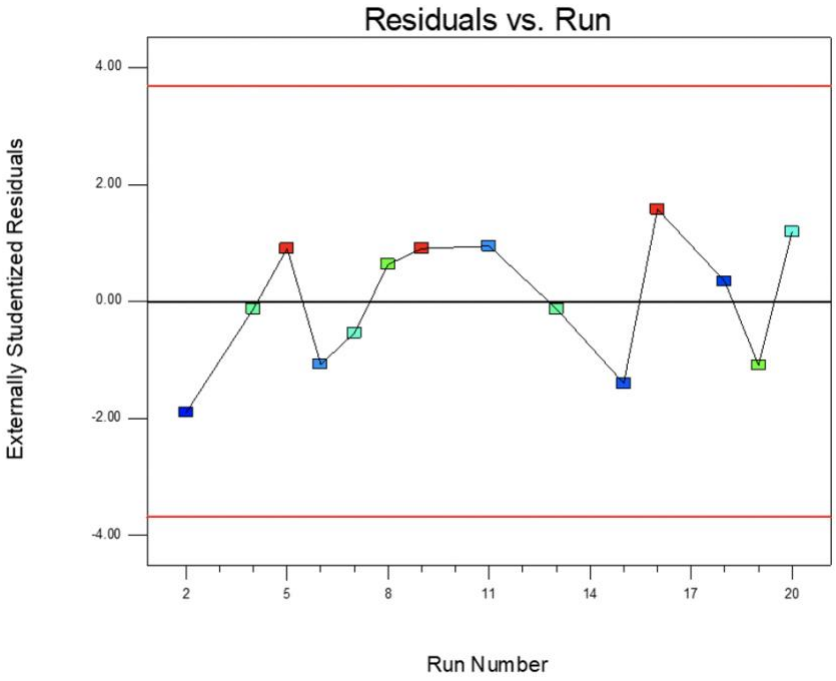
Residuals vs. Run
Externally Studentized Residuals
4.00
2.00
0.00
-2.00
-4.00
2
5
8
11
14
17
20
Run Number

E.

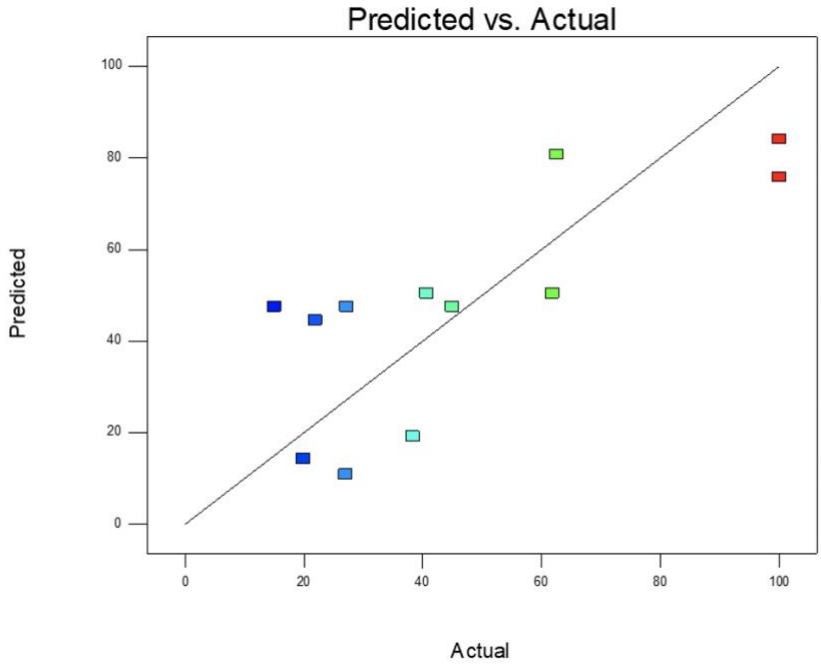
Predicted vs. Actual
Predicted
100
80
60
40
20
0
0
20
40
60
80
100
Actual

F.

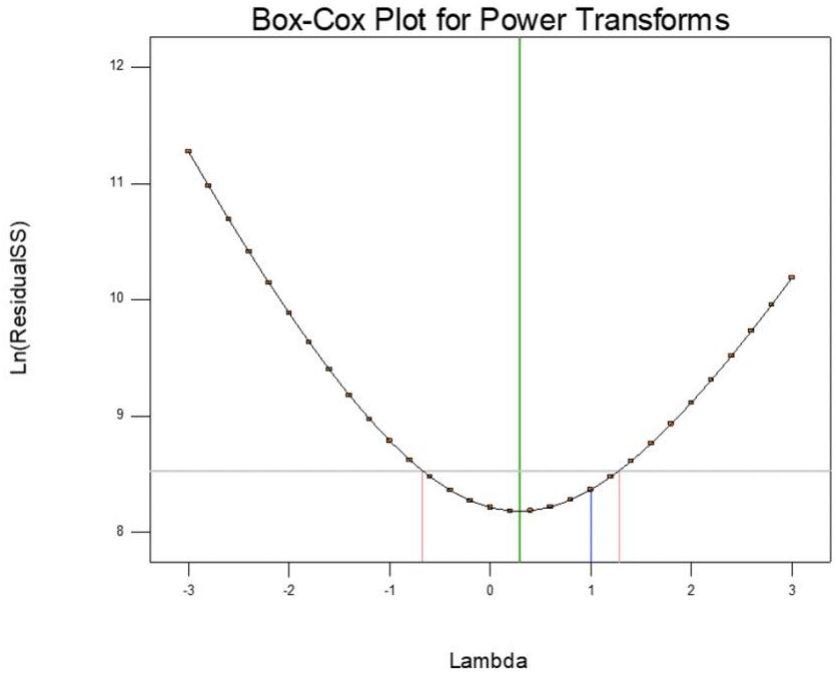
Box-Cox Plot for Power Transforms
Ln(ResidualSS)
12
11
10
9
8
-3
-2
-1
0
1
2
3
Lambda

G.

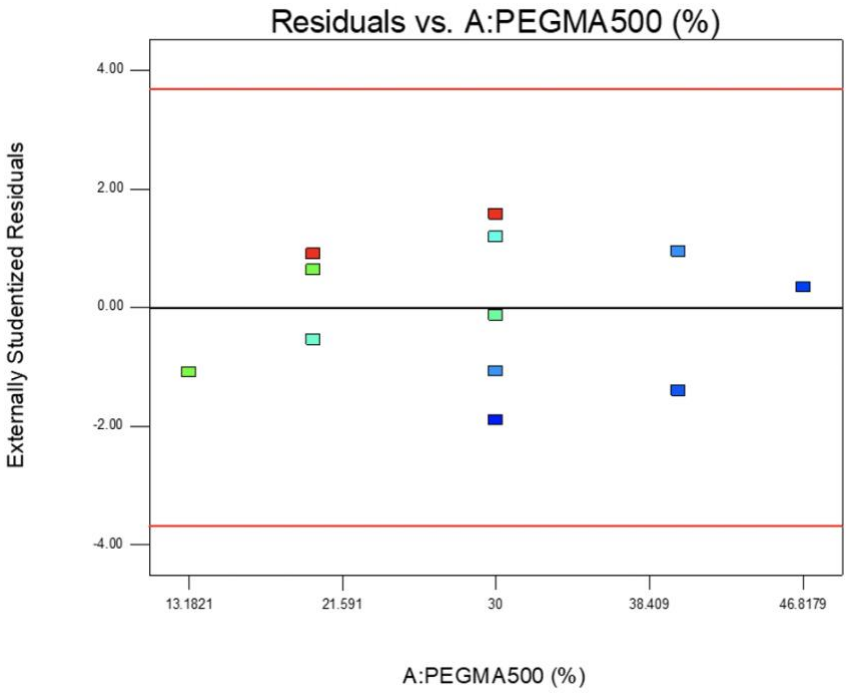
Residuals vs. A:PEGMA500 (%)
Externally Studentized Residuals
4.00
2.00
0.00
-2.00
-4.00
13.1821
21.591
30
38.409
46.8179
A:PEGMA500 (%)

H.

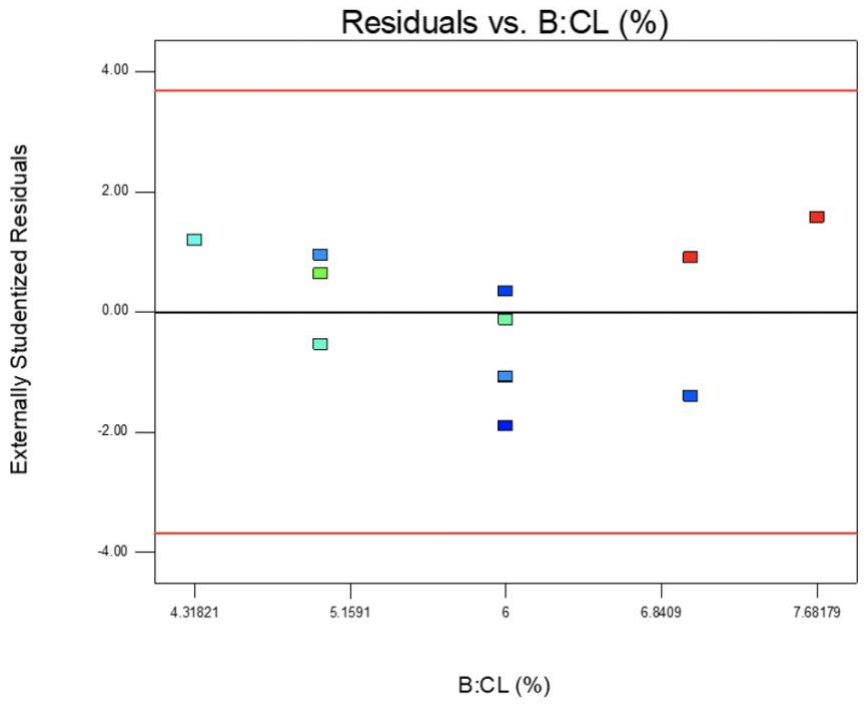
Residuals vs. B:CL (%)
Externally Studentized Residuals
4.00
2.00
0.00
-2.00
-4.00
4.31821
5.1591
6
6.8409
7.68179
B:CL (%)

I.

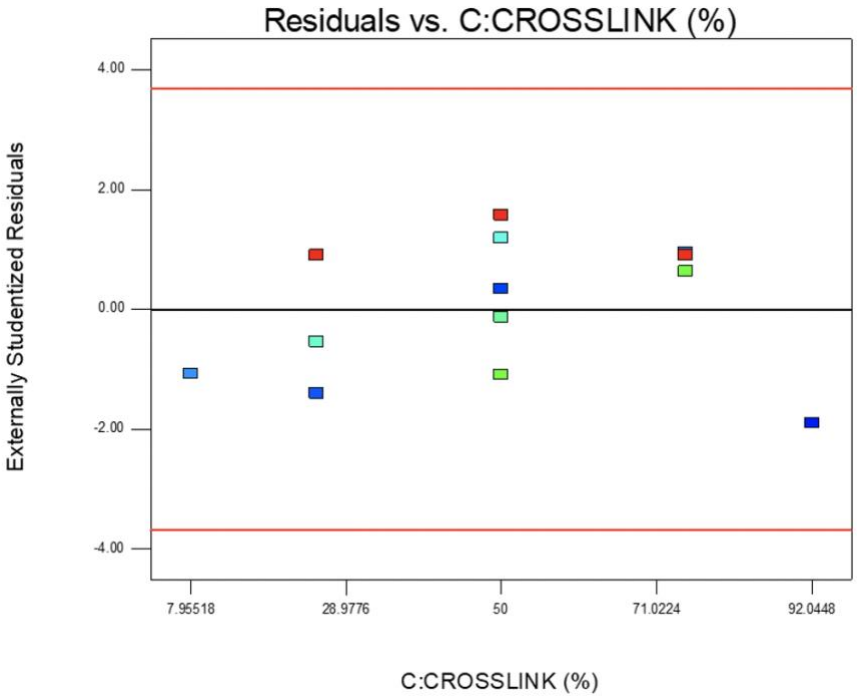
Residuals vs. C:CROSSLINK (%)
Externally Studentized Residuals
4.00
2.00
0.00
-2.00
-4.00
7.95518
28.9776
50
71.0224
92.0448
C:CROSSLINK (%)

J.

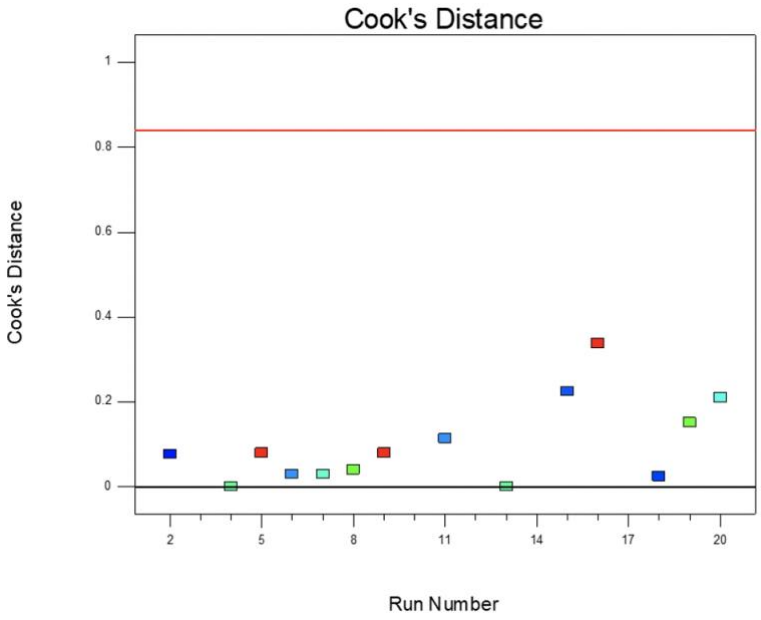
Cook's Distance
Cook's Distance
1
0.8
0.6
0.4
0.2
0
2
5
8
11
14
17
20
Run Number

K.

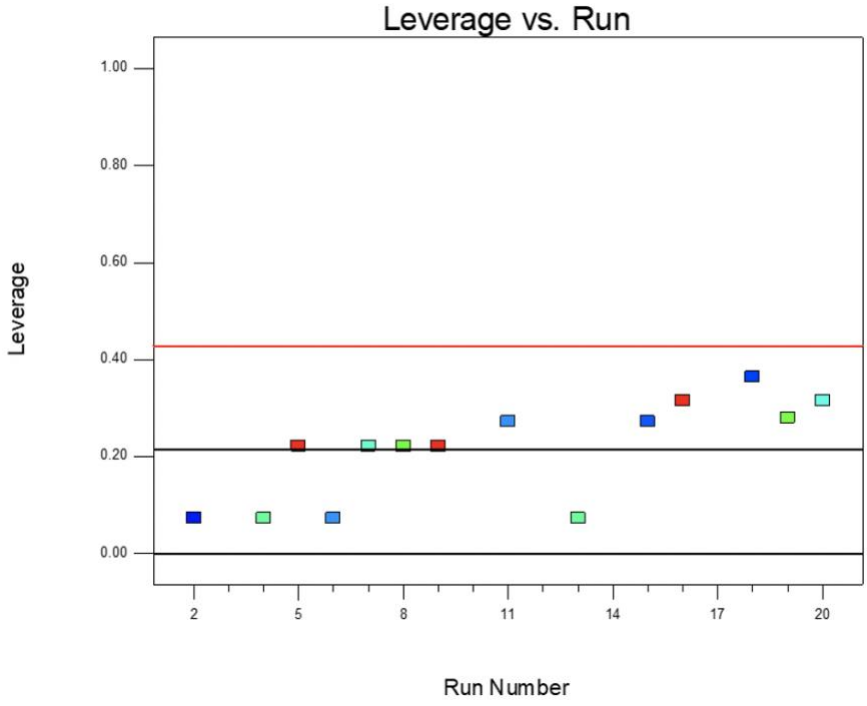
Leverage vs. Run
Leverage
1.00
0.80
0.60
0.40
0.20
0.00
2
5
8
11
14
17
20
Run Number

L.

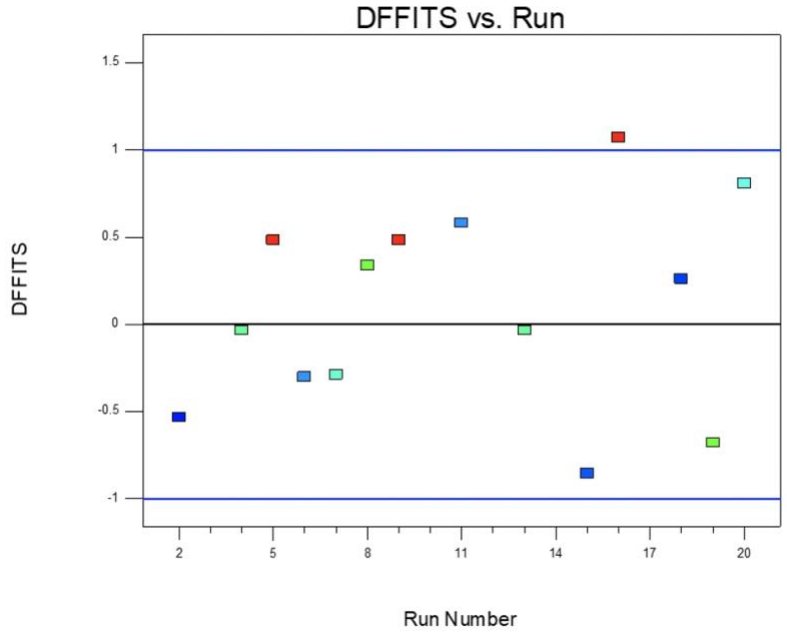
DFFITS vs. Run
DFFITS
1.5
1
0.5
0
-0.5
-1
2
5
8
11
14
17
20
Run Number

M.

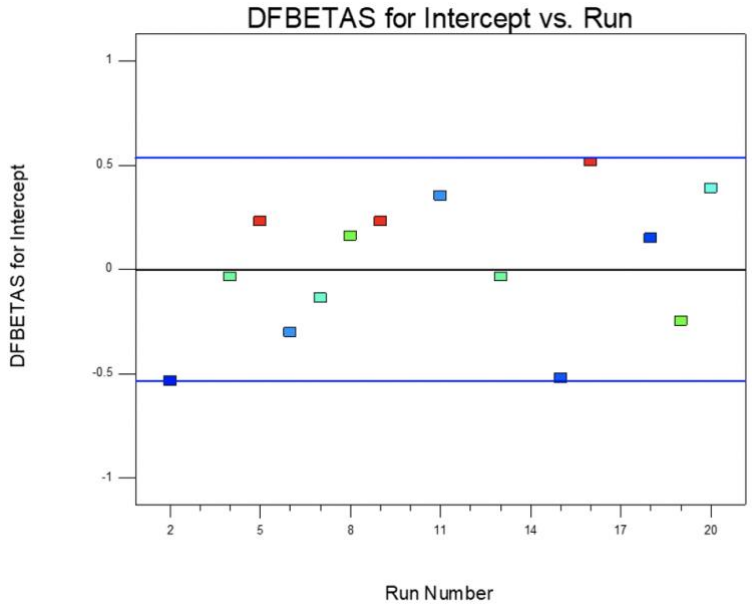
DFBETAS for Intercept vs. Run
DFBETAS for Intercept
1
0.5
0
-0.5
-1
2
5
8
11
14
17
20
Run Number

Figure 10. Surface map (A) and diagnostic plots (B-M) for CCD model used for formulation optimization at pH 6.

Table 13. Tabular summary of model diagnostics for formulation optimization at pH 6.

Response	1	2-hr REL @pH6			Transform:	None			
Diagnostics Case Statistics									
					Internally	Externally		Influence on	
Run	Actual	Predicted			Studentized	Studentized	Cook's	Fitted Value	Standard
Order	Value	Value	Residual	Leverage	Residual	Residual	Distance	DFFITS	Order
2	15.00	47.49	-32.49	0.073	-1.708	-1.900	0.077	-0.534	14
18	19.90	14.24	5.66	0.364	0.359	0.344	0.025	0.261	10
15	21.90	44.55	-22.65	0.272	-1.344	-1.401	0.225	-0.857	4
11	27.00	10.89	16.11	0.272	0.955	0.951	0.114	0.582	6
6	27.20	47.49	-20.29	0.073	-1.067	-1.074	0.030	-0.302	13
20	38.30	19.19	19.11	0.316	1.169	1.191	0.210	0.810	11
7	40.70	50.43	-9.73	0.222	-0.558	-0.540	0.030	-0.288	1
4	45.00	47.49	-2.49	0.073	-0.131	-0.125	0.000	-0.035	20
13	45.00	47.49	-2.49	0.073	-0.131	-0.125	0.000	-0.035	15
8	61.80	50.43	11.37	0.222	0.652	0.634	0.040	0.339	5
19	62.60	80.74	-18.14	0.280	-1.081	-1.091	0.151	-0.680	9
5	100.00	84.09	15.91	0.222	0.913	0.905	0.079	0.483	3
9	100.00	84.09	15.91	0.222	0.913	0.905	0.079	0.483	7
16	100.00	75.79	24.21	0.316	1.481	1.578	0.338	1.073 *	12

*Exceeds limit

A.

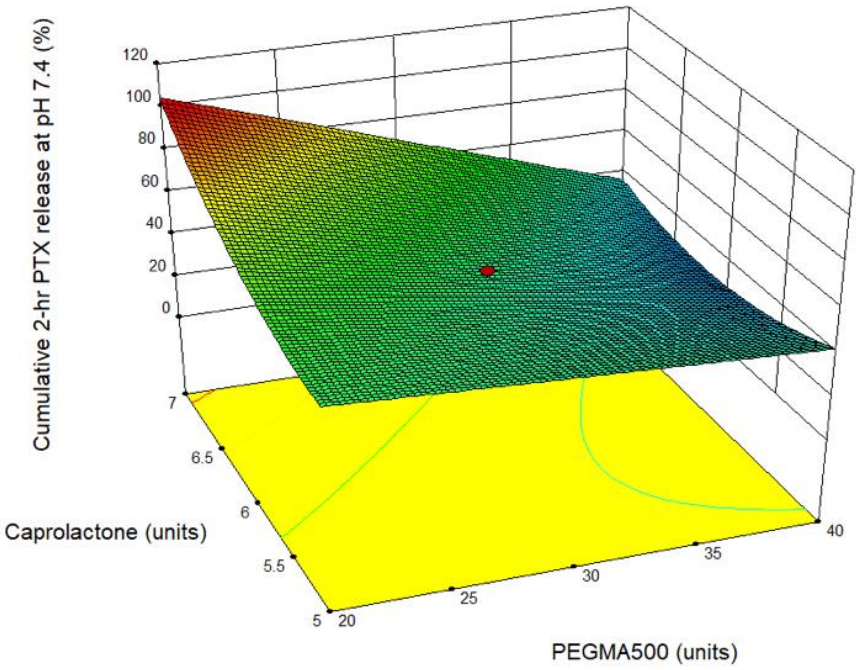
Cumulative 2-hr PTX release at pH 7.4 (%)
120
100
80
60
40
20
0
Caprolactone (units)
7
6.5
6
5.5
5
PEGMA500 (units)
20
25
30
35
40

B.

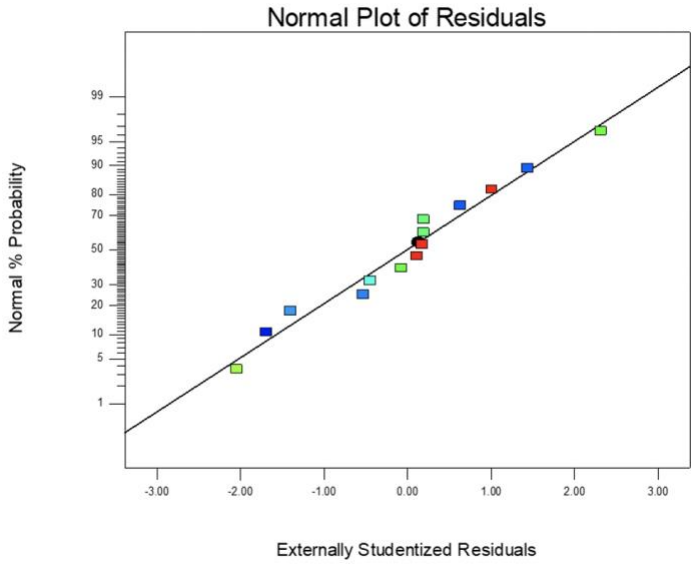
Normal Plot of Residuals
Normal % Probability
99
95
90
80
70
50
30
20
10
5
1
-3.00
-2.00
-1.00
0.00
1.00
2.00
3.00
Externally Studentized Residuals

C.

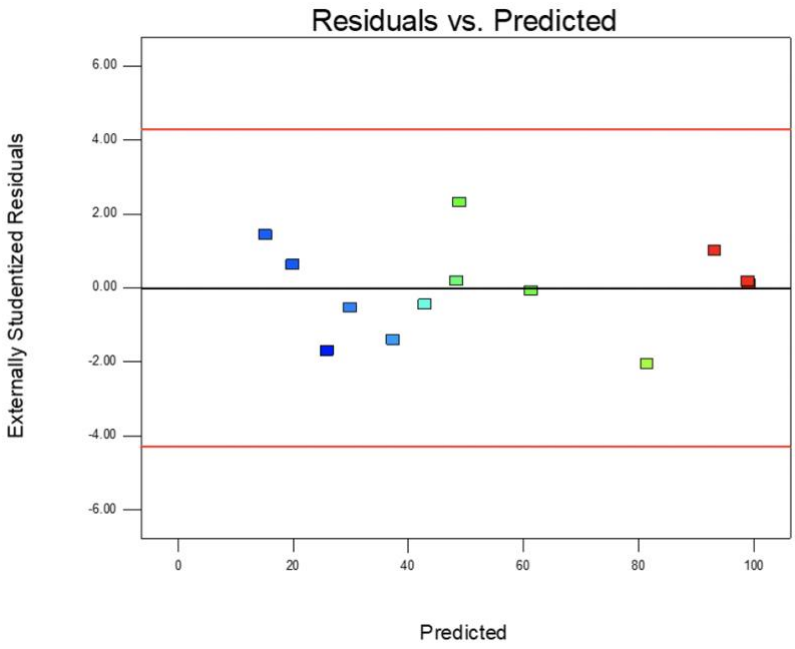
Residuals vs. Predicted
Externally Studentized Residuals
6.00
4.00
2.00
0.00
-2.00
-4.00
-6.00
0
20
40
60
80
100
Predicted

D.

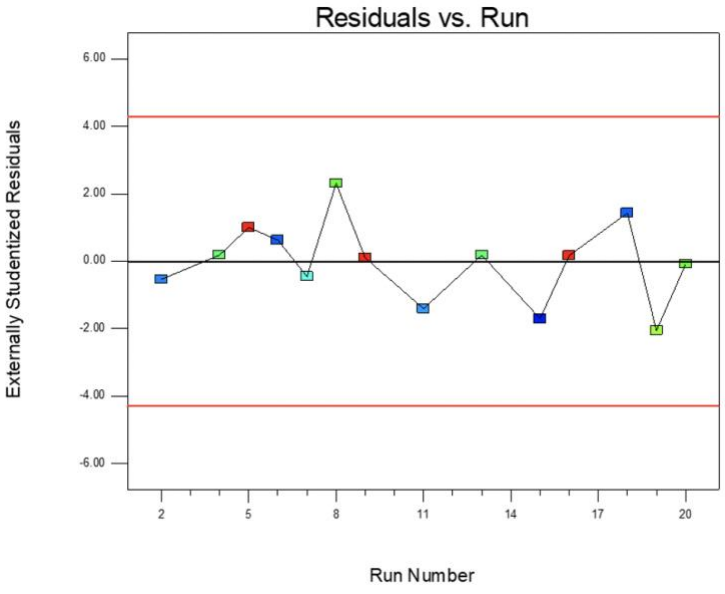
Residuals vs. Run
Externally Studentized Residuals
6.00
4.00
2.00
0.00
-2.00
-4.00
-6.00
2
5
8
11
14
17
20
Run Number

E.

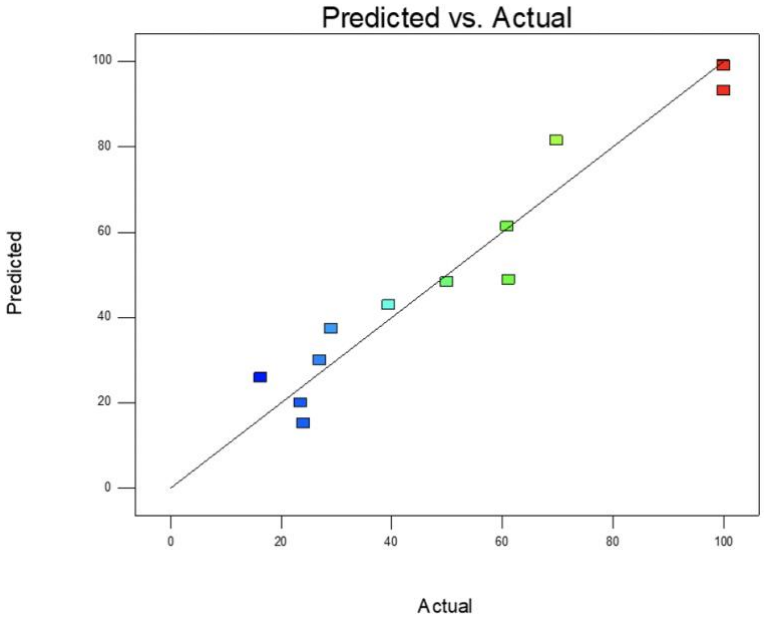
Predicted vs. Actual
Predicted
Actual
0
20
40
60
80
100

F.

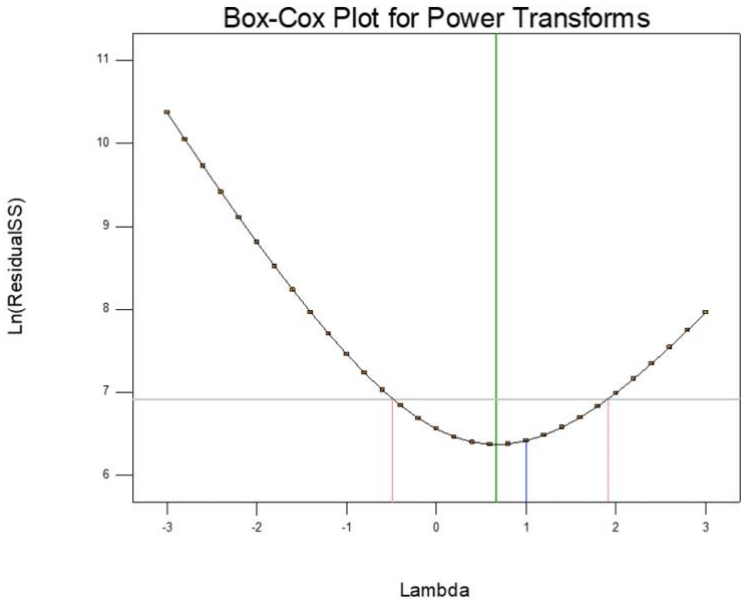
Box-Cox Plot for Power Transforms
Ln(ResidualSS)
Lambda
6
7
8
9
10
11
-3
-2
-1
0
1
2
3

G.

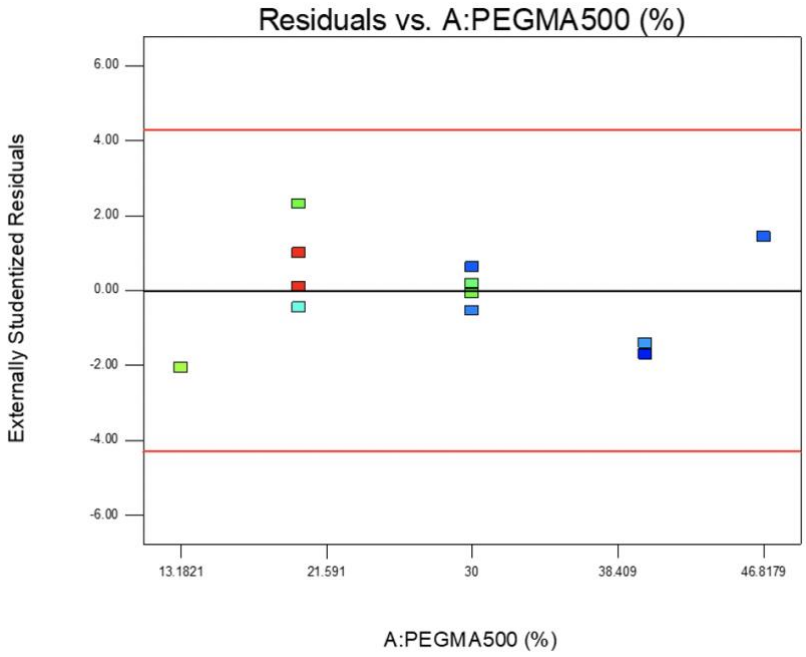
Residuals vs. A:PEGMA500 (%)
Externally Studentized Residuals
6.00
4.00
2.00
0.00
-2.00
-4.00
-6.00
13.1821
21.591
30
38.409
46.8179
A:PEGMA500 (%)

H.

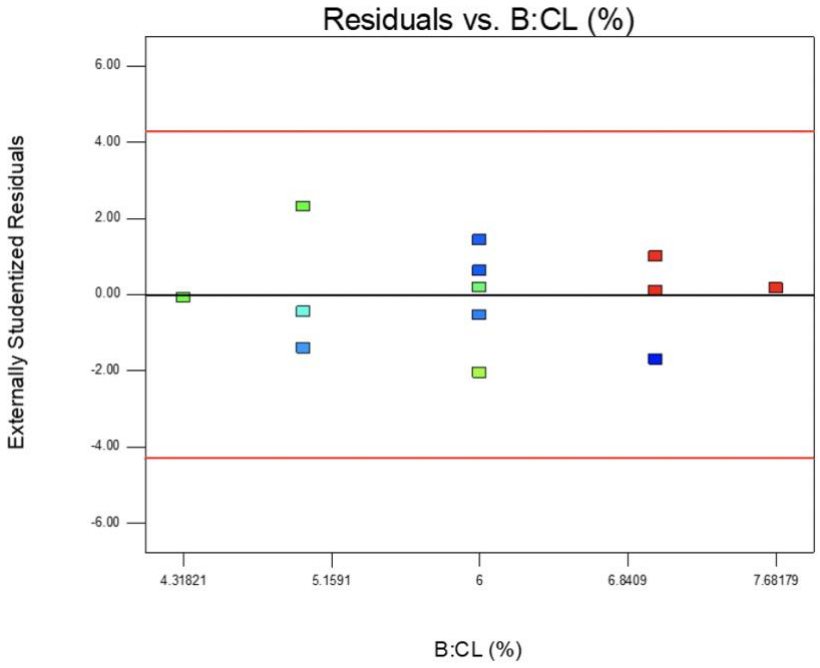
Residuals vs. B:CL (%)
Externally Studentized Residuals
6.00
4.00
2.00
0.00
-2.00
-4.00
-6.00
4.31821
5.1591
6
6.8409
7.68179
B:CL (%)

I.

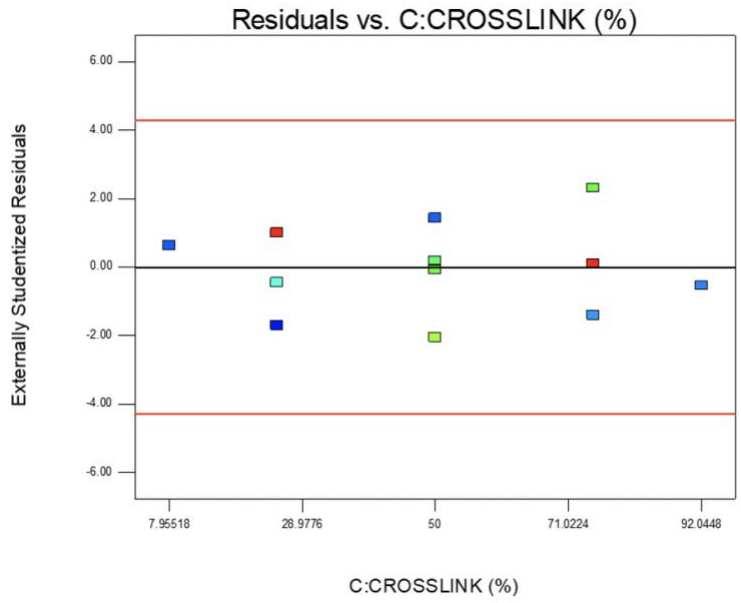
Residuals vs. C:CROSSLINK (%)
Externally Studentized Residuals
6.00
4.00
2.00
0.00
-2.00
-4.00
-6.00
7.95518
28.9776
50
71.0224
92.0448
C:CROSSLINK (%)

J.

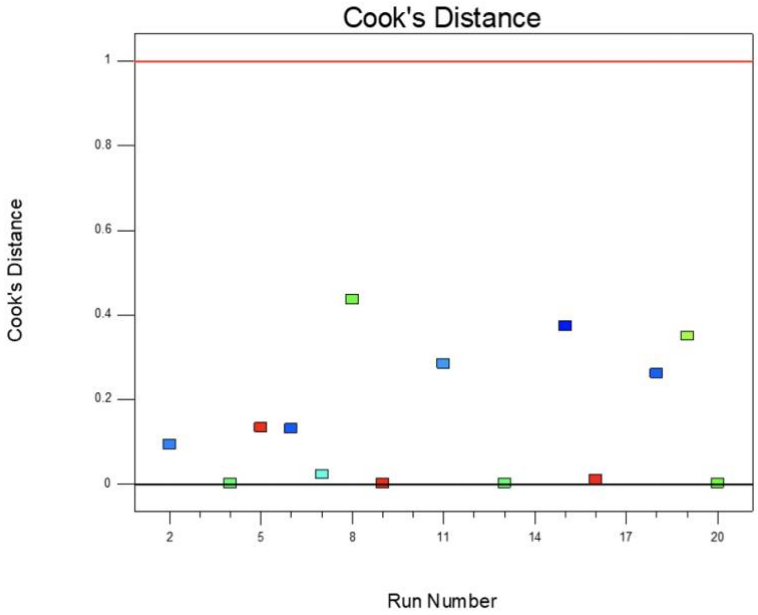
Cook's Distance
Cook's Distance
1
0.8
0.6
0.4
0.2
0
2
5
8
11
14
17
20
Run Number

K.

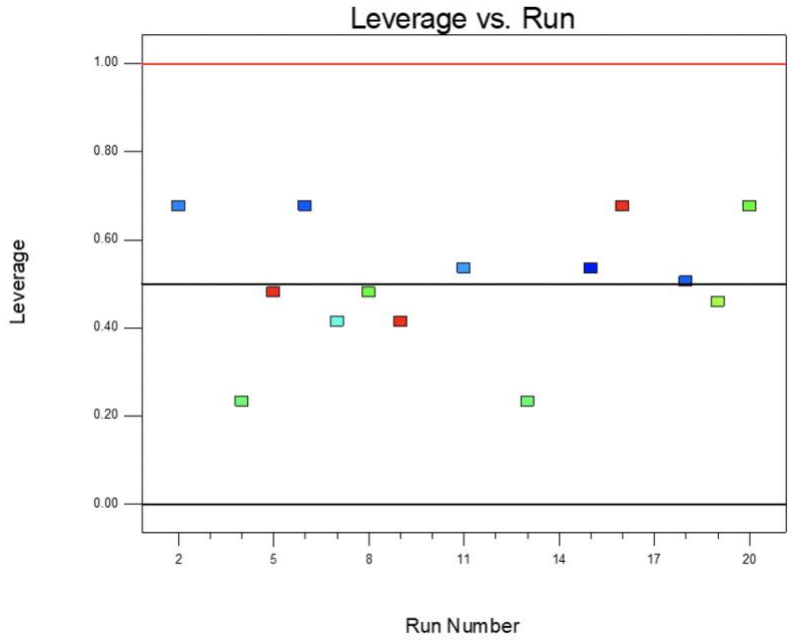
Leverage vs. Run
Leverage
1.00
0.80
0.60
0.40
0.20
0.00
2
5
8
11
14
17
20
Run Number

L.

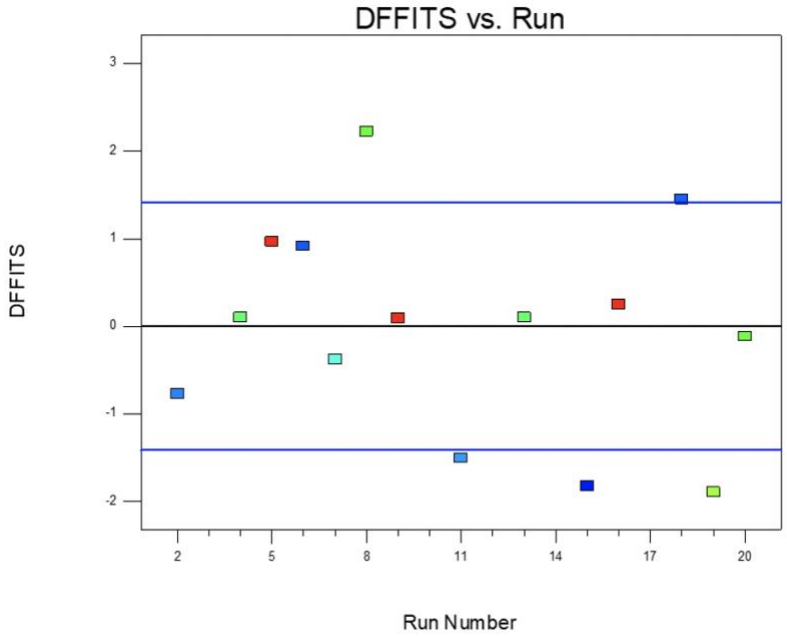
DFFITS vs. Run
DFFITS
3
2
1
0
-1
-2
2
5
8
11
14
17
20
Run Number

M.

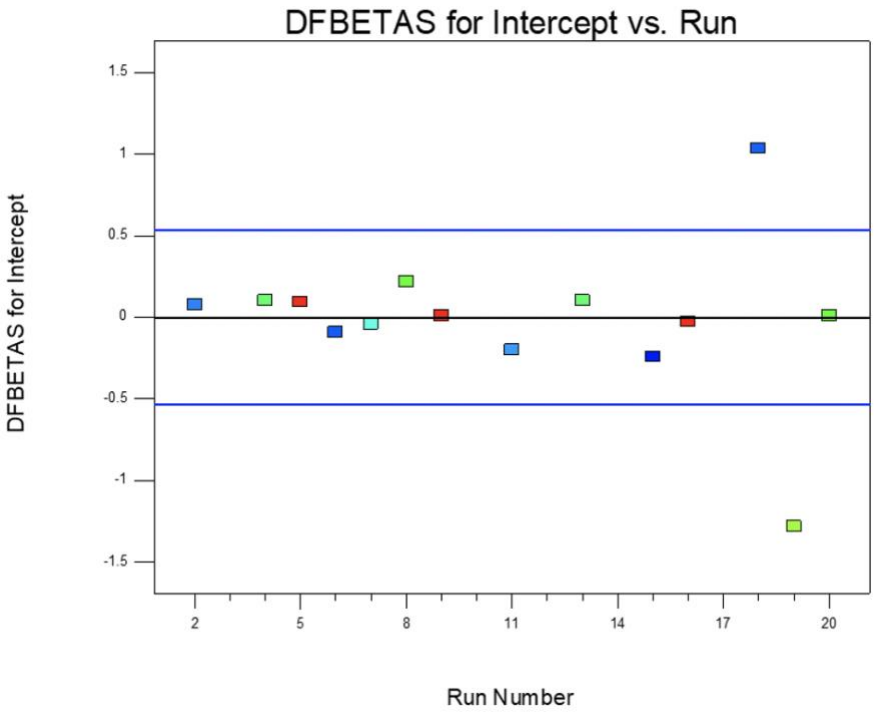

Figure 11. Surface map (A) and diagnostic plots (B-M) for CCD model used for formulation optimization at pH 7.4

Table 14. Tabular summary of model diagnostics for formulation optimization at pH 7.4

Response	2	2-hr REL@ pH 7.4			Transform:	None			
Diagnostics Case Statistics									
					Internally	Externally		Influence on	
Run	Actual	Predicted			Studentized	Studentized	Cook's	Fitted Value	Standard
Order	Value	Value	Residual	Leverage	Residual	Residual	Distance	DFFITS	Order
15	16.30	25.90	-9.60	0.536	-1.506	-1.696	0.374	-1.821 *	4
6	23.50	19.98	3.52	0.677	0.662	0.633	0.131	0.916	13
18	24.00	15.21	8.79	0.506	1.338	1.436	0.262	1.453 *	10
2	27.00	29.98	-2.98	0.677	-0.560	-0.531	0.094	-0.768	14
11	29.00	37.38	-8.38	0.536	-1.315	-1.402	0.285	-1.506 *	6
7	39.50	42.91	-3.41	0.414	-0.477	-0.449	0.023	-0.377	1
4	50.00	48.34	1.66	0.233	0.203	0.188	0.002	0.104	20
13	50.00	48.34	1.66	0.233	0.203	0.188	0.002	0.104	15
20	60.90	61.35	-0.45	0.677	-0.086	-0.079	0.002	-0.115	11
8	61.10	48.86	12.24	0.481	1.817	2.314	0.436	2.226 *	5
19	69.80	81.47	-11.67	0.460	-1.698	-2.050	0.350	-1.890 *	9
5	100.00	93.22	6.78	0.481	1.006	1.007	0.134	0.969	3
9	100.00	99.17	0.83	0.414	0.117	0.108	0.001	0.091	7
16	100.00	99.01	0.99	0.677	0.187	0.174	0.010	0.251	12

*Exceeds limit

A.

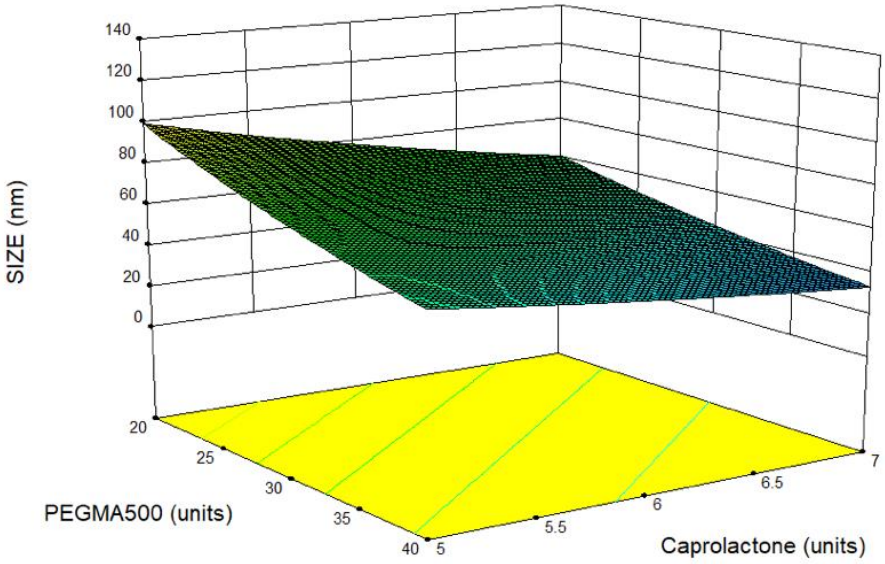
SIZE (nm)
140
120
100
80
60
40
20
0
20
25
30
35
40
PEGMA500 (units)
5
5.5
6
6.5
7
Caprolactone (units)

B.

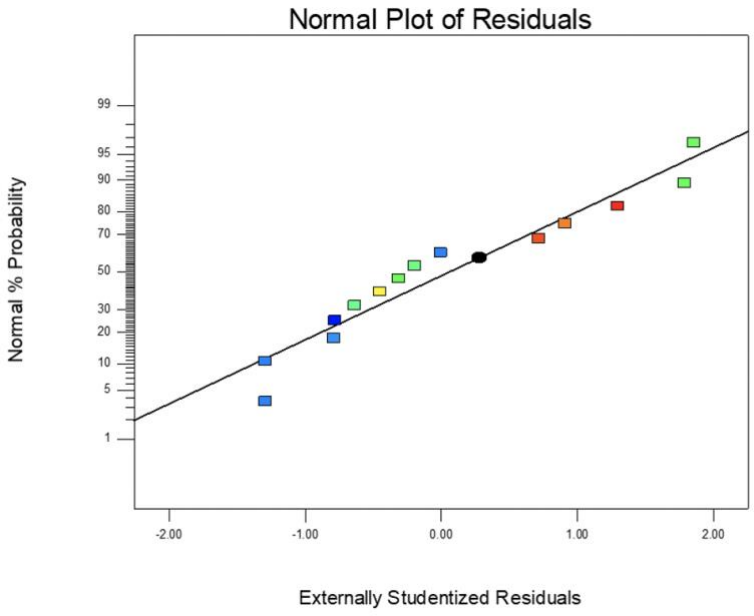
Normal Plot of Residuals
Normal % Probability
99
95
90
80
70
50
30
20
10
5
1
-2.00
-1.00
0.00
1.00
2.00
Externally Studentized Residuals

C.

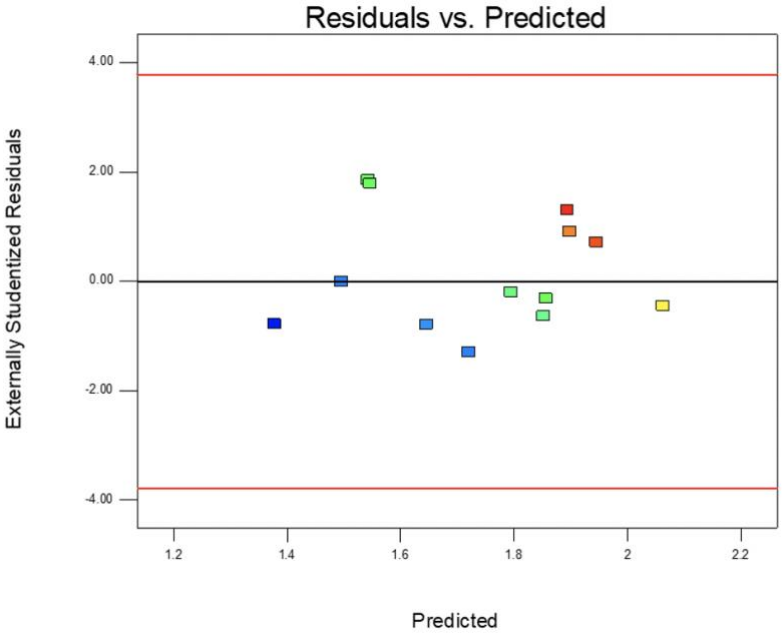
Residuals vs. Predicted
Externally Studentized Residuals
4.00
2.00
0.00
-2.00
-4.00
1.2
1.4
1.6
1.8
2
2.2
Predicted

D.

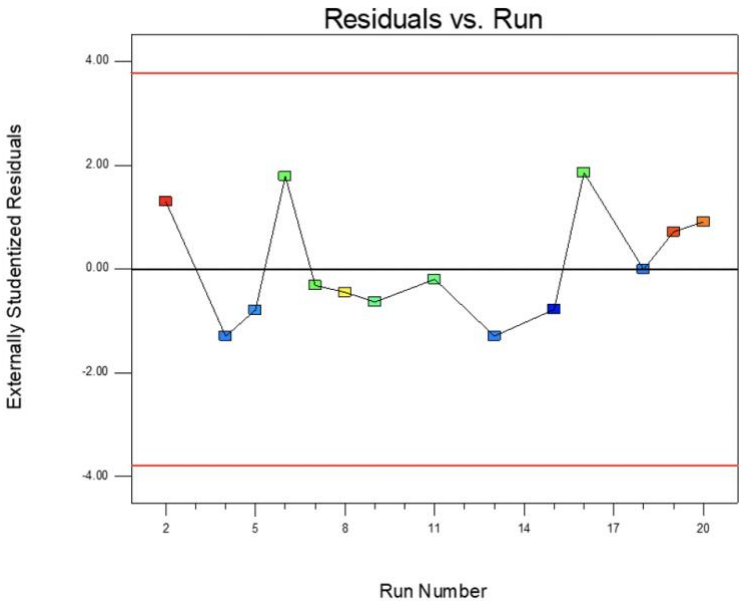
Residuals vs. Run
Externally Studentized Residuals
4.00
2.00
0.00
-2.00
-4.00
2
5
8
11
14
17
20
Run Number

E.

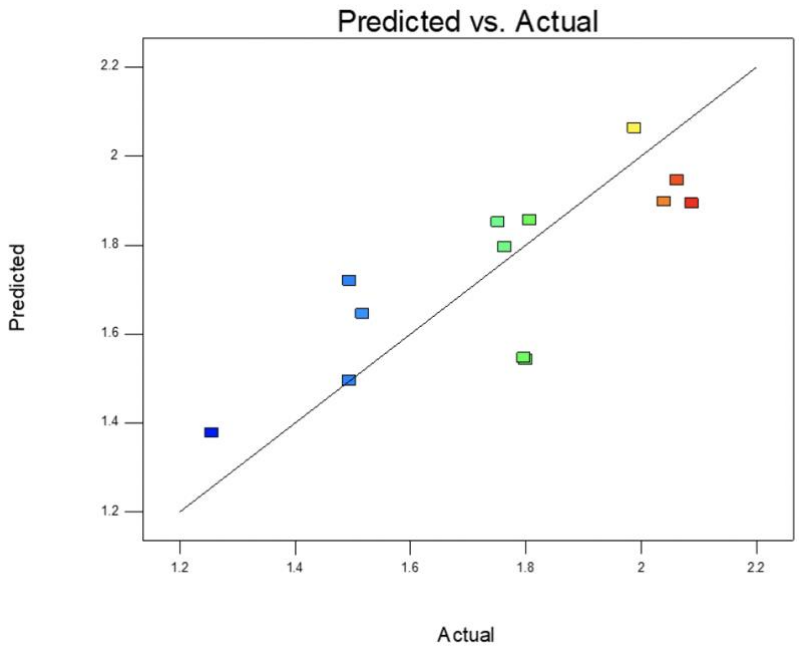
Predicted vs. Actual
Predicted
Actual
2.2
2
1.8
1.6
1.4
1.2
1.2
1.4
1.6
1.8
2
2.2

F.

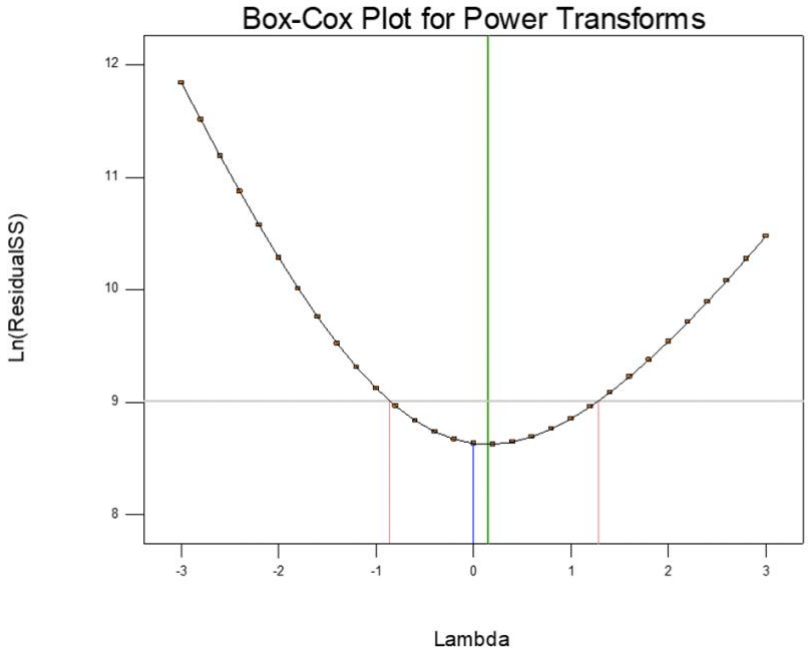
Box-Cox Plot for Power Transforms
Ln(ResidualSS)
Lambda
12
11
10
9
8
-3
-2
-1
0
1
2
3

G.

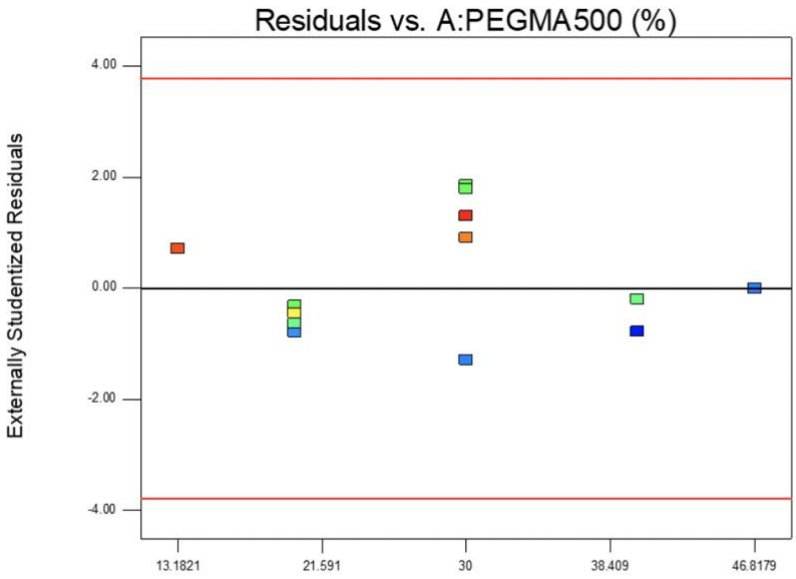
Residuals vs. A:PEGMA500 (%)
Externally Studentized Residuals
4.00
2.00
0.00
-2.00
-4.00
13.1821
21.591
30
38.409
46.8179

H.

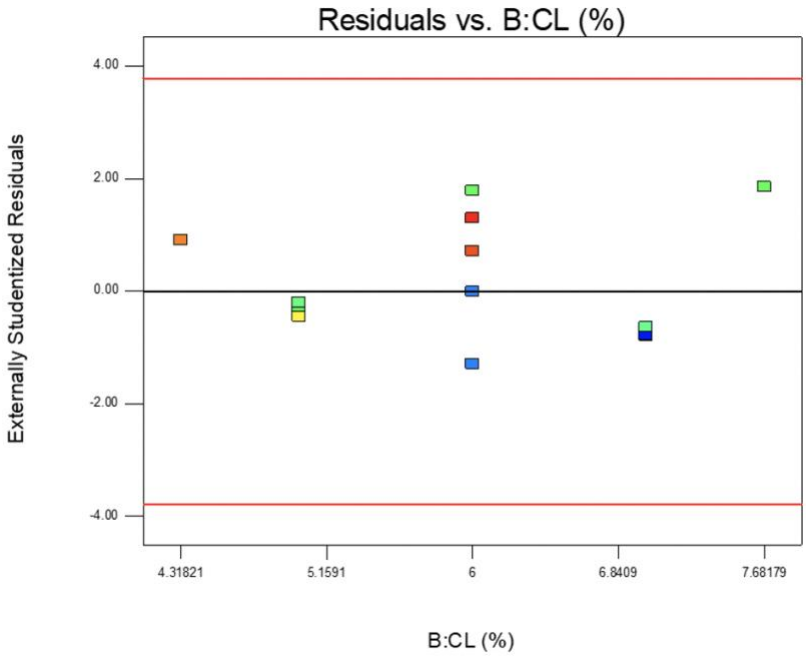
Residuals vs. B:CL (%)
Externally Studentized Residuals
4.00
2.00
0.00
-2.00
-4.00
4.31821
5.1591
6
6.8409
7.68179
B:CL (%)

I.

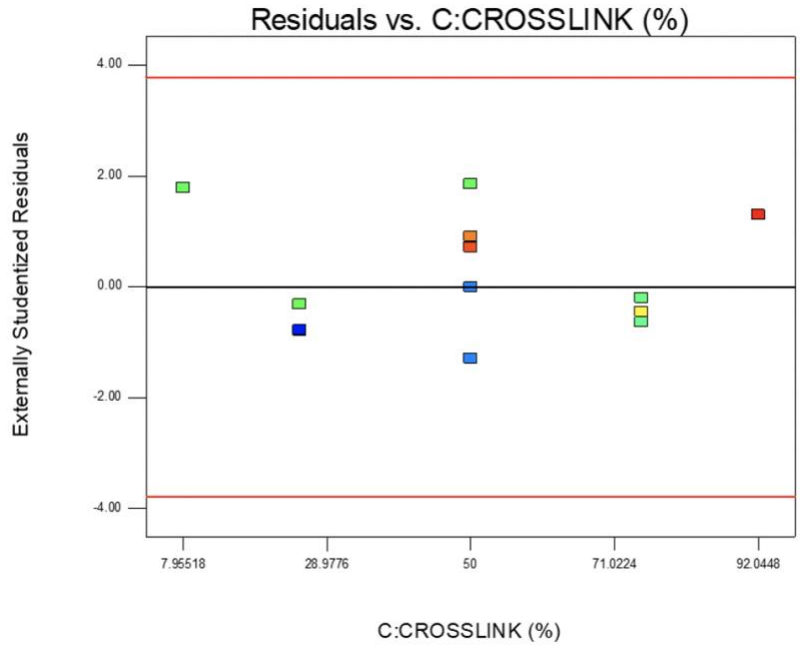
Residuals vs. C:CROSSLINK (%)
Externally Studentized Residuals
4.00
2.00
0.00
-2.00
-4.00
7.95518
28.9776
50
71.0224
92.0448
C:CROSSLINK (%)

J.

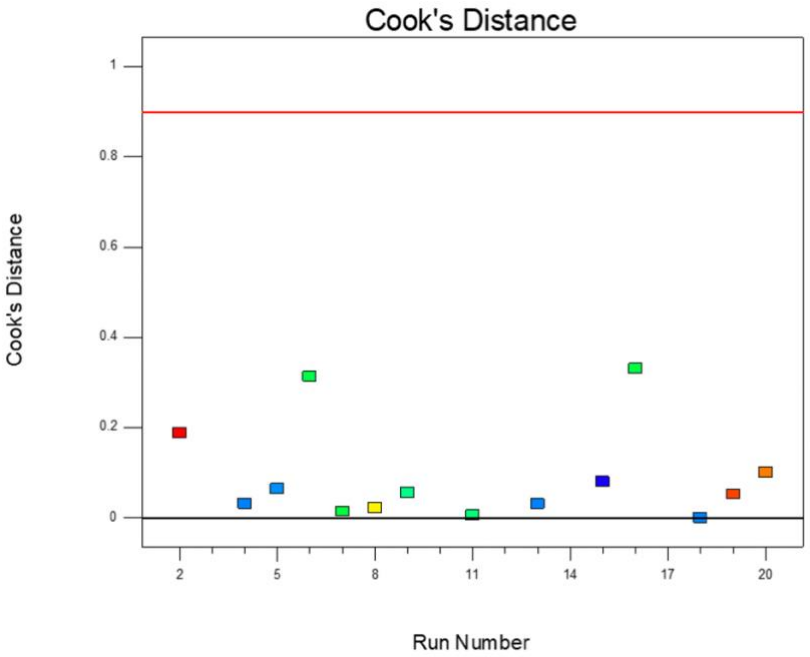
Cook's Distance
Cook's Distance
1
0.8
0.6
0.4
0.2
0
2
5
8
11
14
17
20
Run Number

K.

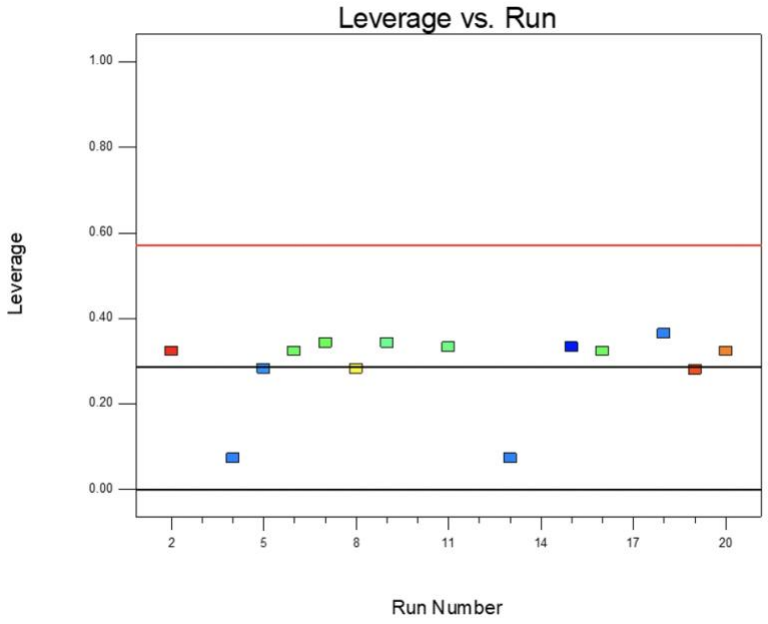
Leverage vs. Run
Leverage
1.00
0.80
0.60
0.40
0.20
0.00
2
5
8
11
14
17
20
Run Number

L.

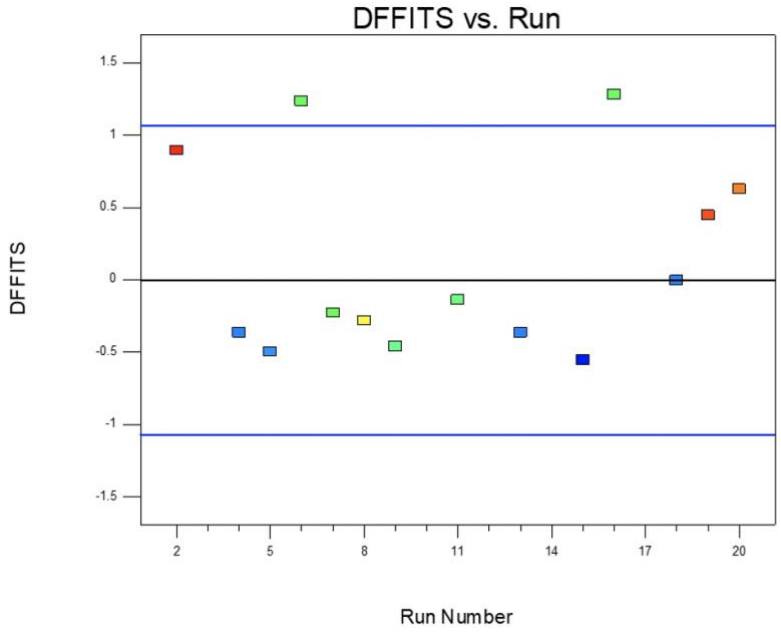
DFFITS vs. Run
DFFITS
1.5
1
0.5
0
-0.5
-1
-1.5
2
5
8
11
14
17
20
Run Number

M.

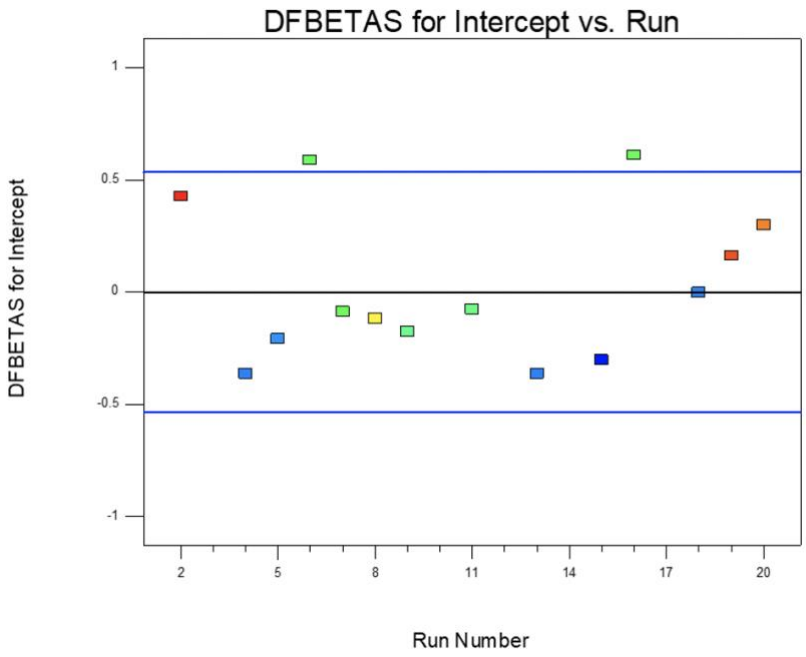

Figure 12. Surface map (A) and diagnostic plots (B-M) for CCD model used for formulation size optimization

Table 15. Tabular summary of model diagnostics for formulation size optimization

Response	3	Size			Transform:	Base 10 Log	Constant:	0.000	
Diagnostics Case Statistics									
					Internally	Externally		Influence on	
Run	Actual	Predicted			Studentized	Studentized	Cook's	Fitted Value	Standard
Order	Value	Value	Residual	Leverage	Residual	Residual	Distance	DFFITS	Order
15	1.26	1.38	-0.12	0.333	-0.797	-0.782	0.079	-0.552	4
4	1.49	1.72	-0.23	0.073	-1.251	-1.292	0.031	-0.363	20
13	1.49	1.72	-0.23	0.073	-1.251	-1.292	0.031	-0.363	15
18	1.49	1.50	-9.074E-004	0.364	-0.006	-0.006	0.000	-0.004	10
5	1.52	1.65	-0.13	0.282	-0.805	-0.790	0.064	-0.496	3
9	1.75	1.85	-0.100	0.343	-0.655	-0.635	0.056	-0.459	7
11	1.76	1.80	-0.032	0.333	-0.207	-0.197	0.005	-0.139	6
6	1.80	1.55	0.25	0.323	1.620	1.789	0.313	1.236 *	13
16	1.80	1.54	0.26	0.323	1.663	1.855	0.330	1.282 *	12
7	1.81	1.86	-0.050	0.343	-0.330	-0.315	0.014	-0.228	1
8	1.99	2.06	-0.074	0.282	-0.467	-0.448	0.022	-0.281	5
20	2.04	1.90	0.14	0.323	0.918	0.910	0.101	0.629	11
19	2.06	1.95	0.12	0.280	0.734	0.716	0.052	0.446	9
2	2.09	1.89	0.19	0.323	1.254	1.296	0.188	0.896	14

4.2.3 Selection of an optimal drug delivery system and validation of the CCD with Cal and PTX

Numerical optimization was used to obtain the optimal drug-loaded micelles. A desirability function was used to simultaneously optimize response by indicating a range for each independent variable within the experimental design. The limits for each response was assigned a minimum, maximum or target value. To allow flexibility in model predictions, a range for each response was indicated. The objectives of developing this drug delivery system were to minimize Cal toxicity by reducing free Cal in systemic circulation, extend the apparent biological half-life of Cal and PTX, and enhance their accumulation in the tumor. Based on preliminary experiments, we aimed at having no more than 25% of drugs released at 2 hr to control initial burst effect, and micelle size range of 40 -100 nm. The range for XL was set at 50-75%.

Even though PEGMA-500 confers stealth properties on nanoparticles and increases circulation time, its hydrophilicity reduces cellular uptake (Ruiz et al., 2013; Wang and Thanou, 2010). However, nanoparticle size and shape also strongly impact cellular uptake (Albanese et al., 2012; Zhang et al., 2015). We desired micelles with a size of 40-100 nm, because this is the optimal size for cellular uptake (Jiang et al., 2008; Lu et al., 2009; Yuan et al., 2010; Zhang et al., 2009). Nanoparticles within such a size range have the appropriate entropic and enthalpic properties that influence adhesion strength between the particles and cellular receptors (Yuan et al., 2010; Zhang et al., 2009). The optimal micelle was thus selected with 40 repeating units of PEGMA-500, 20 repeating units of HEMA and 7 repeating units of CPL along with 75% XL. The predicted average values of particle size, 2-hr drug release at pH 6 and 7.4 were 53 nm, 25% and 22%, respectively. The model was validated by performing confirmatory runs using the model-predicted optimal micelle composition, with co-encapsulation of Cal and PTX. The observed values for average micelle size was 51 nm. For PTX, 2-hour drug release at pH 6, 7.4 and in serum were 20%, 18% and 7%, respectively, and for Cal, 6%, 24% and 6% (**Table 16**). The observed responses correlated well with model-predicted response with biases between 3.7%-20%

highlighting the reliability of using the CCD model for formulation development (**Table 16**). The full drug release profile (**Fig. 13**) showed that the cumulative percentage of Cal and PTX released at pH 6, 7.4 and in serum were 42%, 58%, 58% and 80%, 80%, 76%, respectively after 120 h, demonstrating the sustained drug release characteristics of the optimal micelles.

Table 16. Model-predicted and observed outputs for PTX in optimal M-Cal/PTX

Optimal M-Cal/PTX	Predicted	Observed N=3 Mean + SD)	%Bias
PTX size (nm)	53	51 ± 2.7	3.7
2-hr Cumulative release (%)			
pH 6	25	20 ± 4.5	20
Ph 7.4	22	18 ± 3.3	18.2

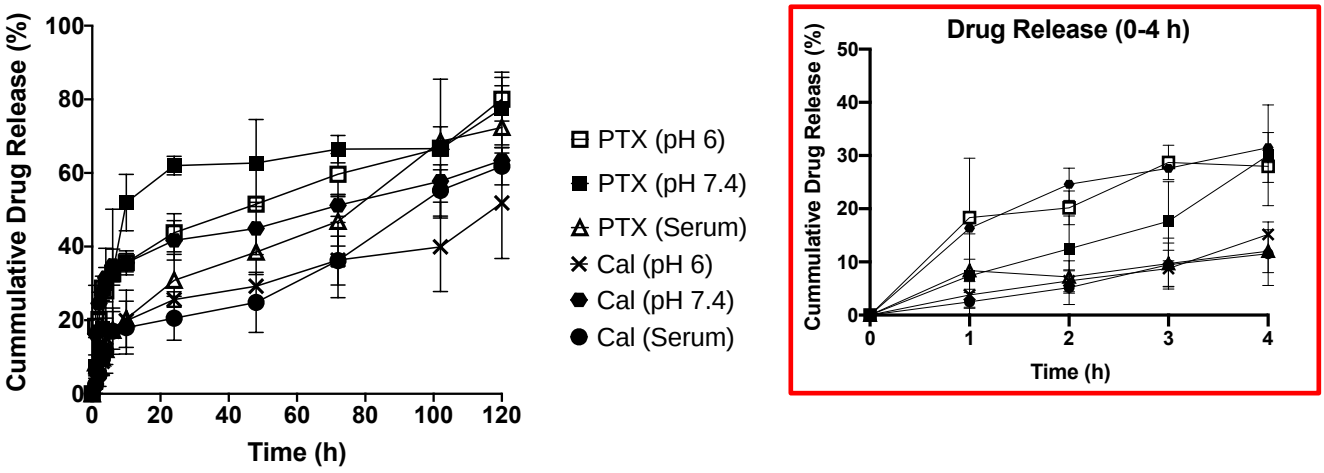

Figure 13. Drug release profiles of Cal and PTX from optimal M-Cal/PTX

Graph shows mean ± SD of 3 independent studies and an insert for 0-4 h

4.3 Characterization of optimal M-Cal/PTX

Micelle morphology, solution state-size, encapsulation efficiency, polydispersity index (PDI), zeta potential and the storage stability of optimal M-Cal/PTX were characterized.

4.3.1 NMR and TEM analyses

NMR analysis confirmed the structure of polymer used for micelle (**Figure 14A**) formation while TEM analysis of the optimal M-Cal/PTX showed spherical particles with the size range of 40-100 nm (**Figure 14B**). The shape and size distribution were consistent among the three independently prepared micelles

A

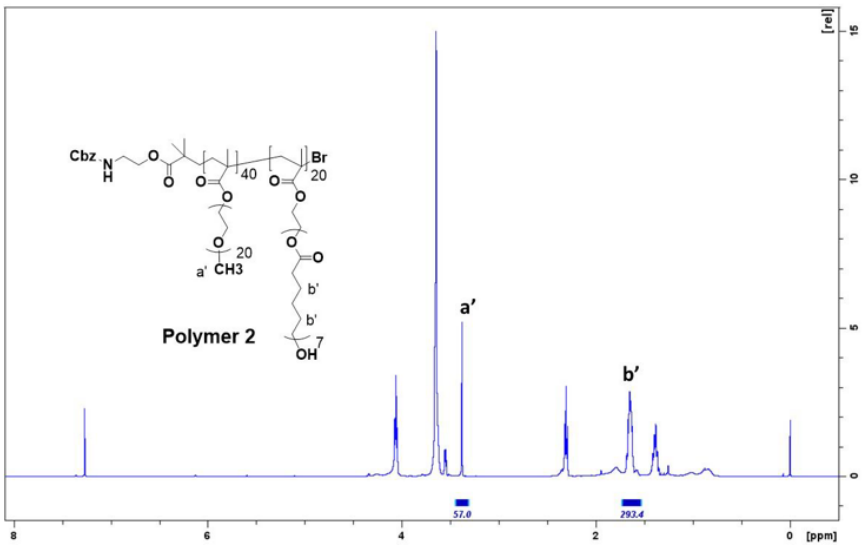

B

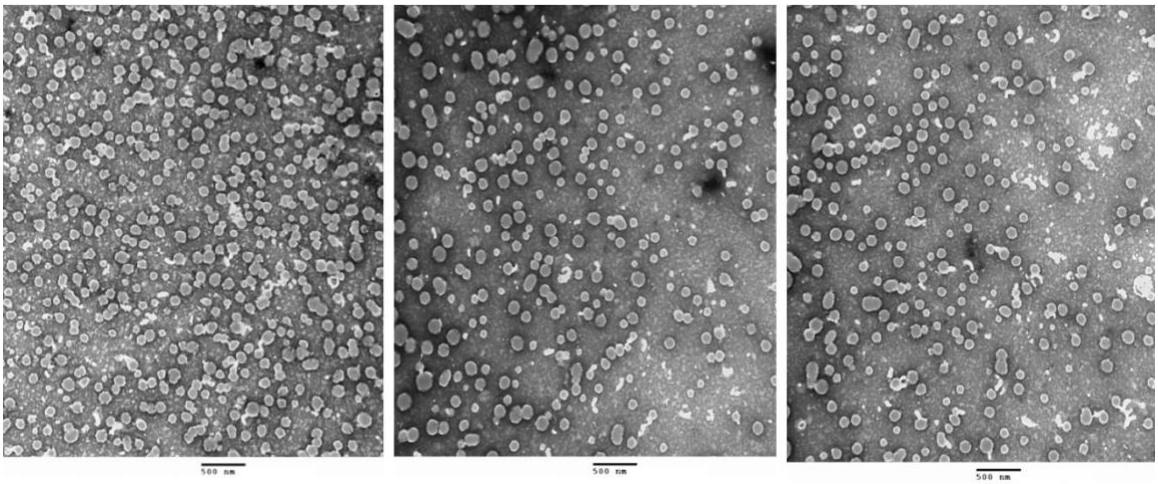

Figure 14. 1H-NMR spectrum of poly(OEG-MA)40-b-poly[HEMA-g-(ε-caprolactone)7]20 (polymer 2) (A) TEM (B) images of M-Cal/PTX at a scale of 500 nm and at 25,000X magnification (Images shown were from three sets of independently prepared M Cal/PTX). Hydrogen atoms and their corresponding peak integrations are marked by a' and b'.

4.3.2 Encapsulation efficiency of optimal M-Cal/PTX

A DOE approach was used to optimize the encapsulation efficiencies (EE) of Cal and PTX. The ratio of PTX to Cal (w/w) affected the encapsulation efficiencies of Cal, but to a lesser extent PTX (**Figure 15A and B**). In fact, the EE of PTX (**Figure 15B**) did not appreciably change with changing amounts of Cal. Unsurprisingly modeling efforts for PTX were insignificant due to the little change observed. The DOE modeling effort was therefore focused on modeling Cal EE accounting for its interaction with PTX. Generally, it was observed that increasing Cal amount resulted in decreased EE (**Figure 15A**). The response surface map (**Figure 16A**) and corresponding diagnostic plots for Cal EE (**Figure 15B-L)** are shown. A 5:1 PTX to Cal yielded a high PTX encapsulation efficiency of > 90% and a satisfactory encapsulation efficiency of >65% for Cal.

A. **B.**

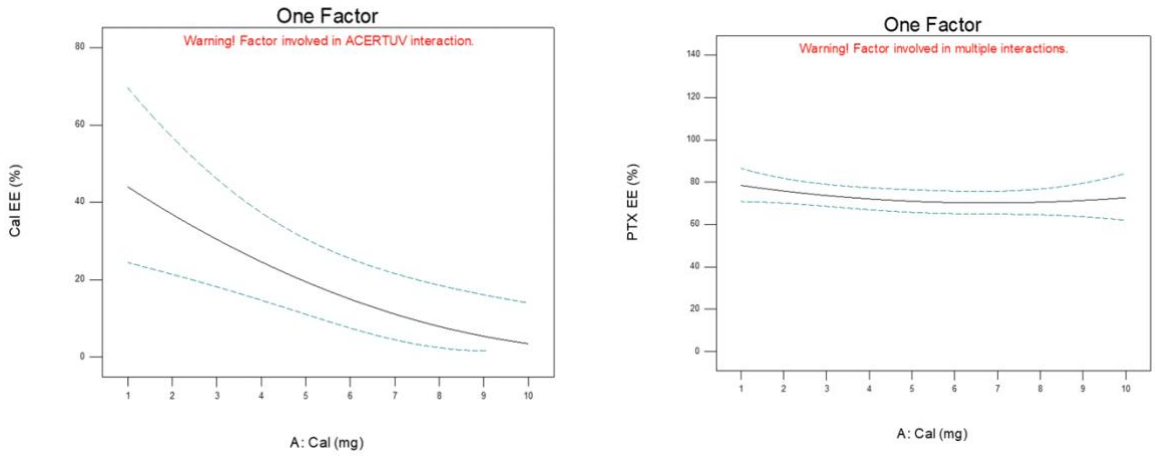

Figure 15. Effects of ratios of Cal and PTX on their encapsulation efficiencies.

A.

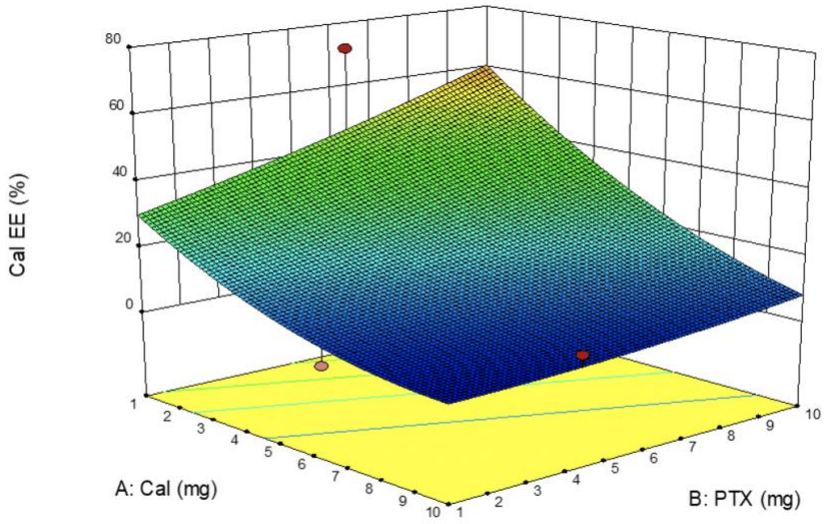
Cal EE (%)
80
60
40
20
0
A: Cal (mg)
1
2
3
4
5
6
7
8
9
10
B: PTX (mg)
1
2
3
4
5
6
7
8
9
10

B.

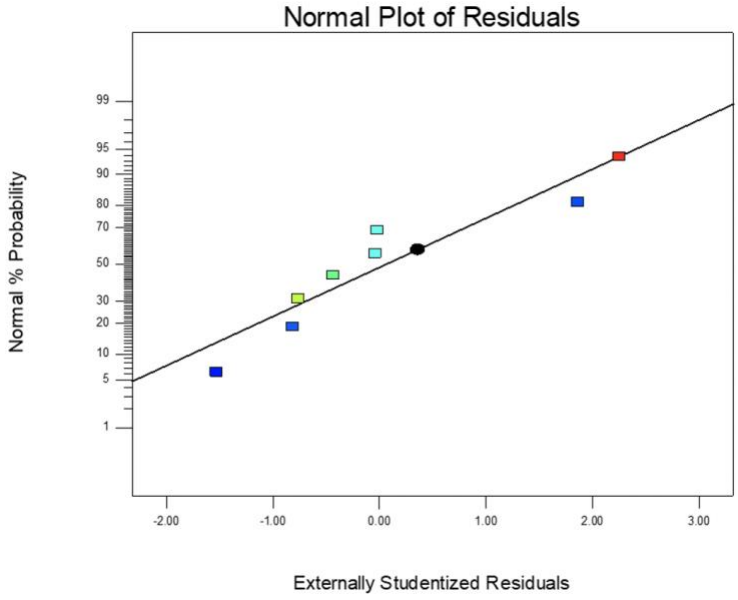
Normal Plot of Residuals
Normal % Probability
99
95
90
80
70
50
30
20
10
5
1
-2.00
-1.00
0.00
1.00
2.00
3.00
Externally Studentized Residuals

C.

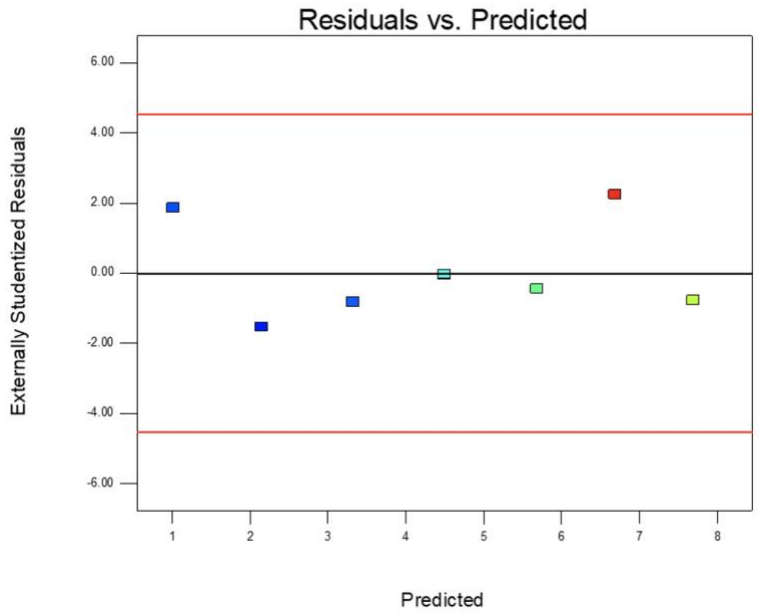
Residuals vs. Predicted
Externally Studentized Residuals
6.00
4.00
2.00
0.00
-2.00
-4.00
-6.00
1
2
3
4
5
6
7
8
Predicted

D.

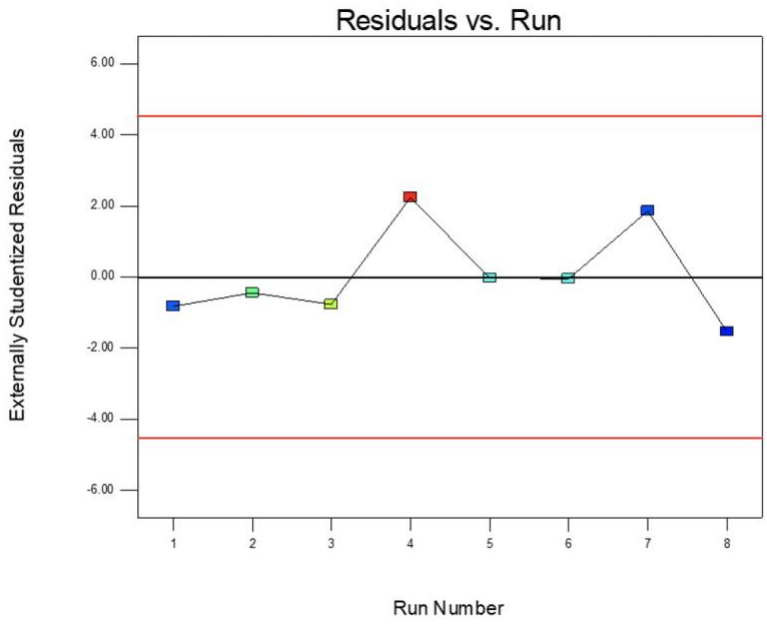
Residuals vs. Run
Externally Studentized Residuals
6.00
4.00
2.00
0.00
-2.00
-4.00
-6.00
1
2
3
4
5
6
7
8
Run Number

E.

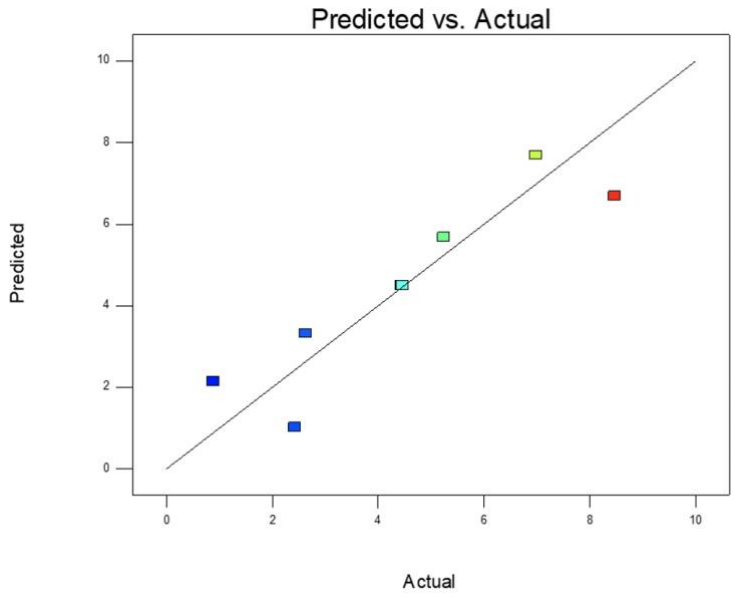
Predicted vs. Actual
Predicted
Actual
0
2
4
6
8
10

F.

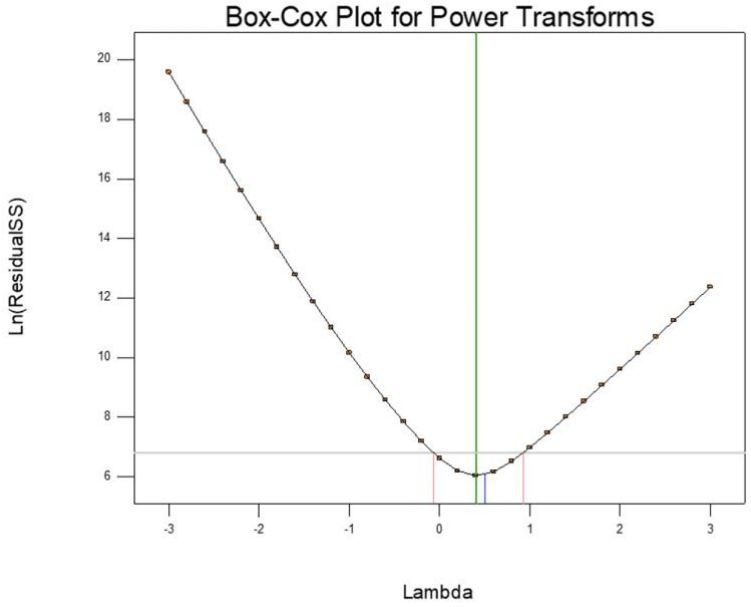
Box-Cox Plot for Power Transforms
Ln(ResidualSS)
Lambda
6
8
10
12
14
16
18
20
-3
-2
-1
0
1
2
3

G.

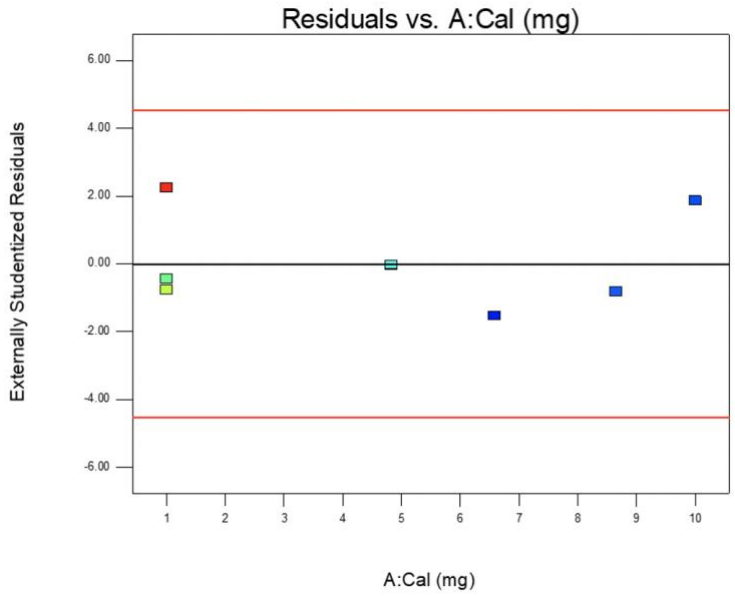
Residuals vs. A:Cal (mg)
Externally Studentized Residuals
6.00
4.00
2.00
0.00
-2.00
-4.00
-6.00
1
2
3
4
5
6
7
8
9
10
A:Cal (mg)

H.

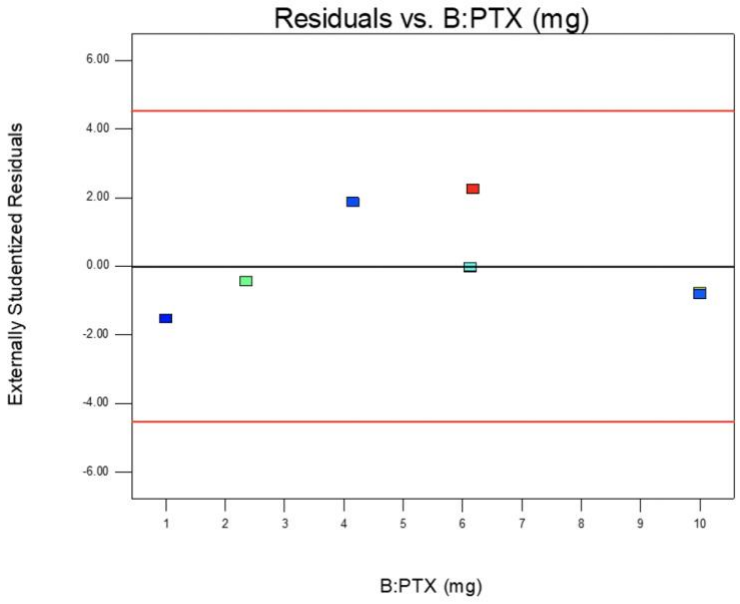
Residuals vs. B:PTX (mg)
Externally Studentized Residuals
6.00
4.00
2.00
0.00
-2.00
-4.00
-6.00
1
2
3
4
5
6
7
8
9
10
B:PTX (mg)

I.

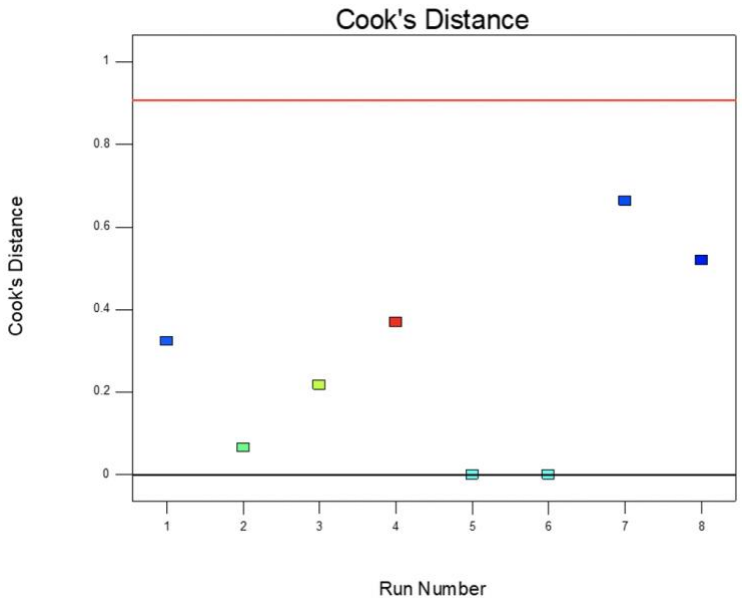
Cook's Distance
Cook's Distance
1
0.8
0.6
0.4
0.2
0
1
2
3
4
5
6
7
8
Run Number

J.

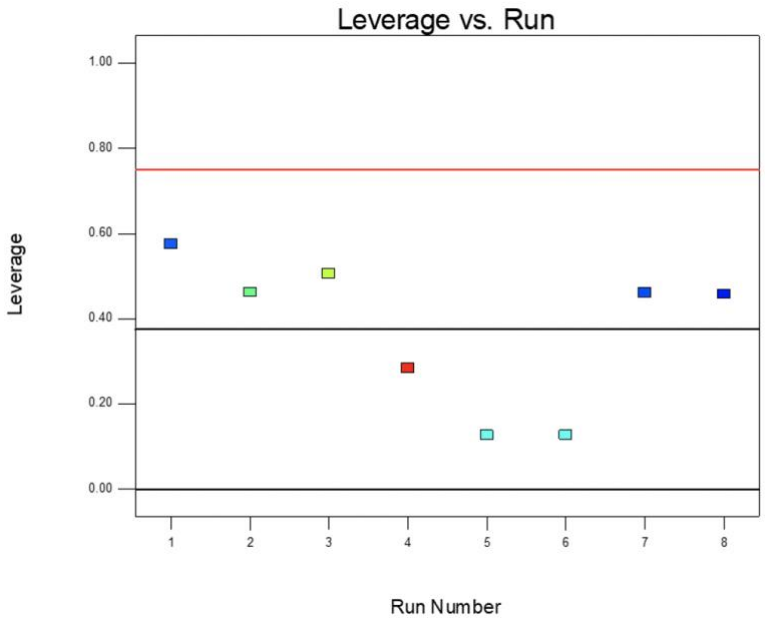
Leverage vs. Run
Leverage
1.00
0.80
0.60
0.40
0.20
0.00
1
2
3
4
5
6
7
8
Run Number

K.

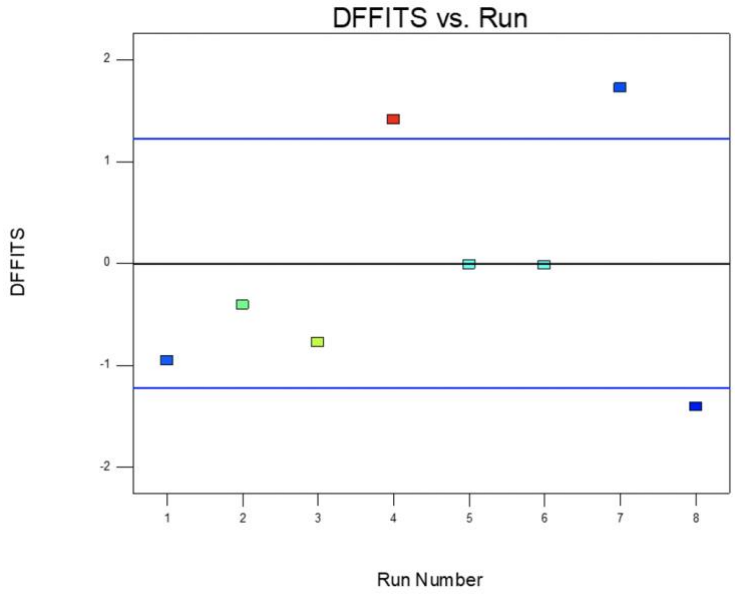

L.

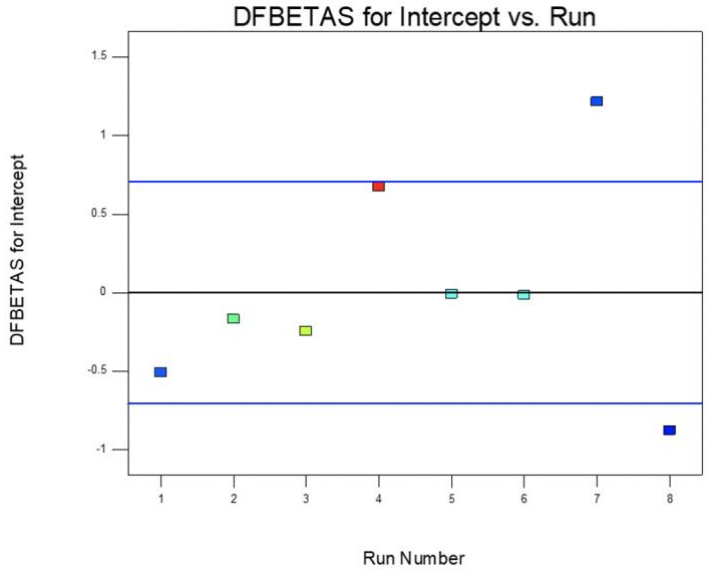

Figure 16. Surface map (A) and diagnostic plots (B-L) for CCD model used for the optimization of Cal encapsulation efficiency.

Table 17. Tabular summary of model diagnostics for Cal encapsulation optimization

Response	1	Cal EE			Transform	Square Root	Constant:	0.000	
Diagnostics Case Statistics									
					Internally	Externally		Influence on	
Run	Actual	Predicted			Studentized	Studentized	Cook's	Fitted Value	Standard
Order	Value	Value	Residual	Leverage	Residual	Residual	Distance	DFFITS	Order
8	0.88	2.15	-1.26	0.458	-1.359	-1.530	0.519	-1.406 *	1
7	2.43	1.02	1.41	0.461	1.525	1.865	0.664	1.725 *	3
1	2.63	3.32	-0.70	0.575	-0.847	-0.819	0.323	-0.952	8
6	4.44	4.49	-0.055	0.127	-0.046	-0.041	0.000	-0.016	4
5	4.46	4.49	-0.032	0.127	-0.027	-0.024	0.000	-0.009	5
2	5.24	5.69	-0.44	0.462	-0.478	-0.438	0.065	-0.406	2
3	6.99	7.69	-0.71	0.506	-0.798	-0.764	0.218	-0.774	7
4	8.47	6.69	1.78	0.284	1.671	2.250	0.368	1.415 *	6

4.3.2 Polydispersity index and zeta potential of optimal M-Cal/PTX

The size distribution of the optimized formulation, reflected by PDI measured by dynamic light scattering (DLS), was 0.249 ± 0.004 and a zeta potential of 0.006 ± 0.001V (N=3 independent batches). In general, particles with a PDI < 0.3 are considered uniformly dispersed(Das and Chaudhury, 2011)

4.3.3 Storage stability at 4ºC and 80ºC

The stability of M-Cal/PTX in storage is shown in **Figures 17** and **18**. Particle size and EE and PDI were measured over a 6-week period from micelles stored at 4°C (**Figure 17A**)

The micelle size and encapsulation efficiencies of both drugs were not appreciably changed over the 6-week period and also after 3 months when stored at -80 °C (**Figure 17B**) in 5% sucrose. The PDI measures were in short term (**Figure 18A**) as well as long term storage (**Figure 18B**). The PDI significantly increased from 0.249 to 0.255 after 1 week to 0.273 after 6-week storage (**Figure 18A**); nevertheless, still below the stable threshold PDI of 0.3. The optimized M-Cal/PTX formulation had a 75% crosslinking density and could be used within 6 weeks of storage at 4°C after preparation or up to 3 months in -80 °C freezer.

A.

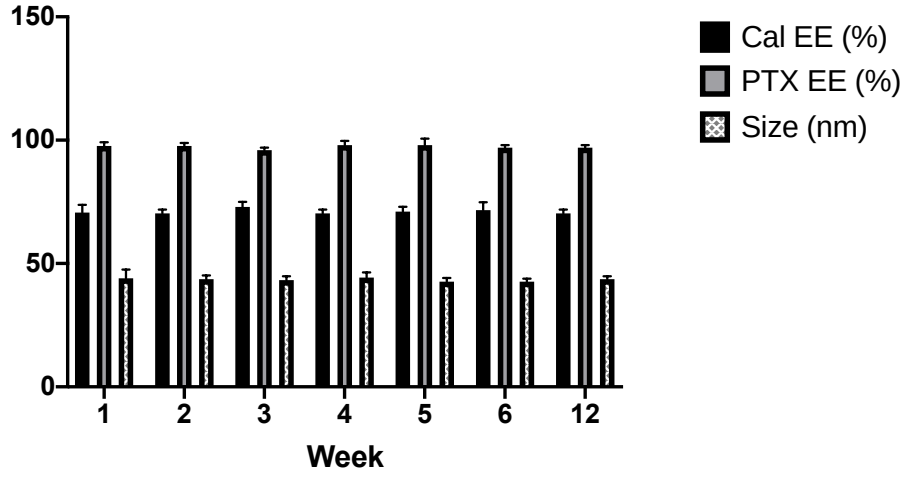

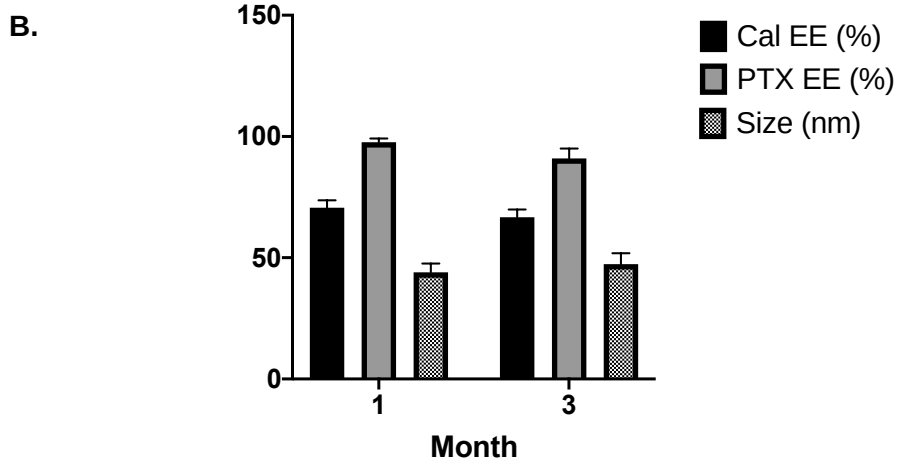

Figure 17. Storage stability of optimal M-Cal/PTX as measured by encapsulation efficiency (EE) and size at 4°C (A) and at -80°C (B). Data shows mean ± SD of measurements from 3 independently prepared batches

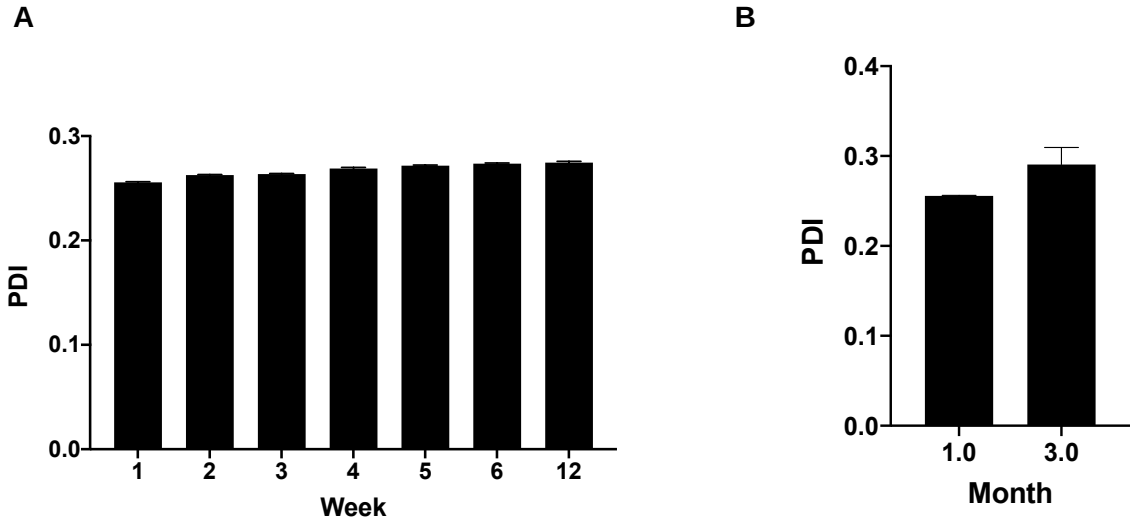

Figure 18. Polydispersity index (PDI) of M-Cal/PTX during short term (A) and long term (B) storage. Data shows mean ± SD of measurements from 3 independently prepared batches. * $p<0.05$ ($n = 3$).

4.3.4 Pharmacokinetic and biodistribution of optimal M-Cal/PTX in healthy mice and an orthotopic Kras^{G12D} mouse model of pancreatic cancer

4.3.4.1 Comparative PK between formulated and unformulated Cal and PTX in healthy mice

The pharmacokinetic (PK) profiles of Cal (from dosing free Cal, dissolved in 10% dimethyl acetamide), PTX (from free PTX, dissolved in 10% dimethyl acetamide), M-Cal, and M-PTX (from dosing M-Cal/PTX) in healthy C57BL/6 mice were constructed (**Figure. 19**).

The PTX and M-PTX profiles appeared similar with no statistical difference at any time point. However, while M-Cal could be measured up to 24 hours post dose, Cal could only be measured up to 6 hours post dose. In addition, the elimination phase of Cal appeared steeper than that in M-Cal.

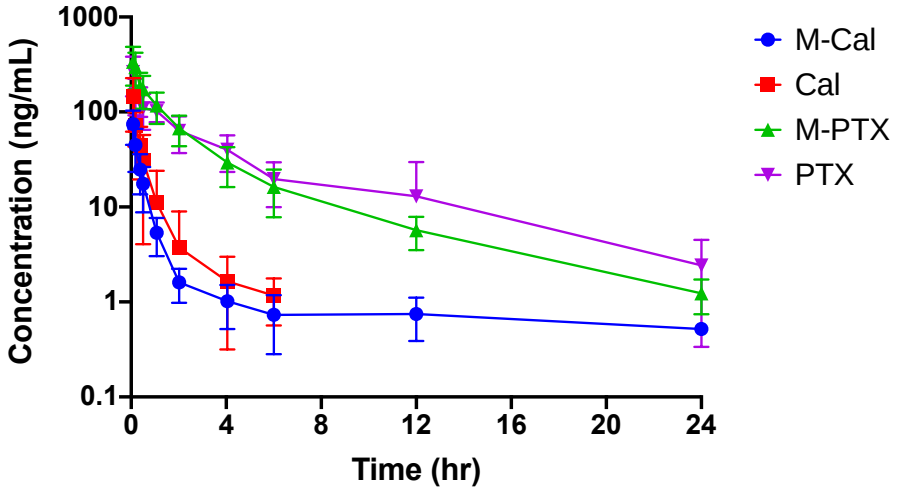

Figure 19. Mean Concentration-time profiles of Cal/PTX and M-Cal/PTX after a single IV bolus dose of 0.5 mg/kg Cal and 5 mg/kg PTX in healthy mice. Plots show mean +/- SD

Non-compartmental analysis (NCA) was done to estimate PK parameters for the formulated and unformulated groups in healthy mice. The terminal half-life for Cal in the M-Cal/PTX group is > 3x higher than in the Cal/PTX group while the micellar formulation reduced Cal AUC by > 2x (**Table 18**). Clearance (CL), volume of distribution (V_{ss}) and the mean resident time (MRT_{inf}) for

Cal in the M-Cal/PTX group were higher than in the Cal/PTX group. The differences were less pronounced for PTX. The terminal half-life for PTX in the M-Cal/PTX group was slightly higher than in the Cal/PTX group (**Table 18**). As was the observation for Cal, PTX AUC was lower in the M-Cal/PTX group compared with the Cal/PTX group. The CL, V_{ss} and MRT_{inf} for PTX in both groups were similar.

Table 18. Comparative PK parameters for M-Cal/PTX and free Cal/PTX

		M-Cal		**Cal**		**M-PTX**		**PTX**	
$t_{1/2}$	h	3.3*	(1.8)	0.9	(0.2)	4.5	(1.1)	3.4	(0.4)
AUC_{last}/D	h*(ng/mL)/(mg/kg)	71.6*	(22.6)	166.1	(117.2)	106.4	(30.4)	123.2	(41.4)
AUC_{INF}/D	h*(ng/mL)/(mg/kg)	79.3*	(29.9)	170.4	(120.7)	108.3	(30.2)	127.1	(44.3)
CL	L/h/kg	14.0*	(4.7)	7.6	(3.5)	9.9	(3.3)	8.7	(3.1)
MRT_{inf}	h	1.8*	(1.3)	0.7	(0.08)	3.5	(0.8)	3.6	(0.7)
V_{ss}	L/kg	10.2*	(10.5)	5.5	(2.30)	33.2	(8.8)	36.4	(7.2)

Data is presented as Mean (%CV) for N=4-5/group. *p<0.05.

4.3.4.2 Comparative PK for M-Cal/PTX between healthy and diseased mice

Healthy and $Kras^{G12D}$ PDAC mice were administered a single IV bolus dose of M-Cal/PTX and blood samples were taken at pre-defined time points to measure Cal and PTX concentrations. The mean concentration-time profiles of Cal and PTX are shown in **Figures 20A and B.** In healthy mice Cal was measurable up to 24 hr post single IV bolus dose but it was only measurable up to 30 min post single dose in diseased mice (**Figure 20A**). For PTX the initial concentrations between healthy and diseased animals were similar but PTX concentrations in the healthy animals were higher beyond 1 hr (**Figure 20B**). Non-compartmental analysis was used to understand the relative elimination and distribution kinetics of Cal and PTX in healthy and diseased mice. These analyses showed that Cal is rapidly cleared in diseased mice (>4x) than in healthy ones. Rapid CL in diseased mice resulted in a significantly shorter half-life in these animals (**Table 19**). In fact, the terminal half-life in healthy mice is > 16x longer than in the diseased ones. Unsurprisingly, the dose normalized Cmax AUC at the last dose and infinity were also lower in the diseased animals compared with the healthy ones. Both the

terminal volume of distribution (V_z) and volume of distribution at steady state (Vss) were higher in the diseased animals compared with the healthy ones (**Table 19**). Finally, the mean residence time (MRT) for Cal in healthy mice is > 3x longer than in the diseased ones. For PTX elimination half-life between the two groups were similar. However, both dose-normalized AUC_{last} and AUC_{inf} were higher in the healthy mice than the diseased counterparts. The CL and steady state volume of distribution was similar in both groups, but terminal volume of distribution ($V_{z)}$ was significantly higher in the diseased group compared with the healthy mice. Mean residence time for PTX is marginally longer in healthy animals compared with the diseased ones (**Table 19)**.

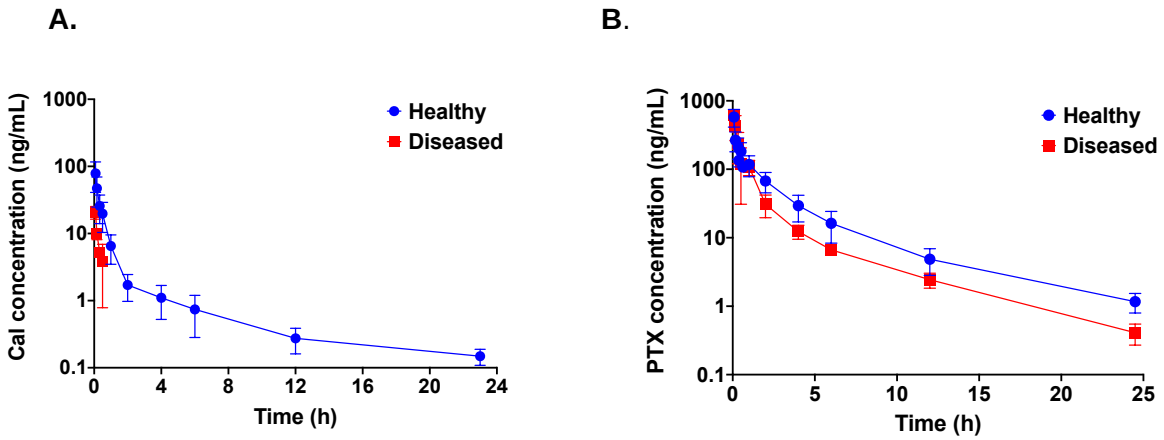

Figure 20. Comparative concentration-time profiles of Cal (A) and PTX (B) in healthy and diseased mice. Each data point represents the mean concentration with SD for N=5 for healthy group and N=3 for diseased group.

Table 19. Comparative PK parameters for Cal and PTX in healthy and diseased mice

Calcipotriol				
	Healthy		Diseased	
PK parameter	Mean (N=5)	%CV	Mean (N=3)	%CV
$t_{1/2}$ (hr)	2.51*	54.60	0.15	57.37
Cmax_D (kg*ng/mL/mg)	119.89*	29.44	40.99	21.73
$AUCl_{last}$_D (hr*kg*ng/mL/mg)	64.42*	31.84	11.76	19.09
AUC_{INF}_D (hr*kg*ng/mL/mg)	67.07*	30.62	13.85	28.83
Vz (L/kg)	53.92*	35.19	70.88	36.04
Vss (L/kg)	15.99*	59.64	36.79	23.27
CL (mL/hr/kg)	14.91*	26.36	72.2	33.96
MRT_{last} (hr)	0.72*	36.05	0.22	43.33
Paclitaxel				
	Mean (N=5)	%CV	Mean (N=3)	%CV
$t_{1/2}$ (hr)	4.58	20.97	4.66	26.24
Cmax_D (kg*ng/mL/mg)	65.80	45.94	121.48	12.58
AUC_{last}_D (hr*kg*ng/mL/mg)	106.51	27.90	72.71	11.97
AUC_{INF}_D (hr*kg*ng/mL/mg)	541.74	27.39	74.00	11.46
Vz (L/kg)	61	29.70	90.93	21.82
Vss (L/kg)	31.33	27.22	34.66	24.53
CL (mL/hr/kg)	9.22	32.32	13.51	10.77
MRTlast (hr)	2.95	25.07	2.07	11.86

*significantly different at $p < 0.05$

4.3.4.3 Biodistribution of M-Cal/PTX in Kras mouse model of PDAC

The time-course biodistribution of M-Cal and M-PTX (**Figure 21**) in a $Kras^{G12D}$ mouse model of PDAC were evaluated. The mean tumor Cal concentration was either marginally higher or similar at all time points evaluated except at the 12 hr (**Figure 21A**) when compared to the concentrations in the liver. However, the difference was statistically insignificant. Of the three organs evaluated, the spleen had the lowest Cal concentrations which was measurable up to 6 hr post single IV bolus dose. At the 24-hr mark post single IV bolus the concentrations of Cal from M-Cal/PTX and also from free Cal/PTX were compared. The tumor and liver concentrations of Cal from M-Cal/PTX were higher and statistically significant in the M-Cal/PTX group compared to free Cal/PTX group (**Figure 21B)**. In fact

Cal could not be measured in the tumors of mice that received free Cal/PTX at 24 hr post dose.

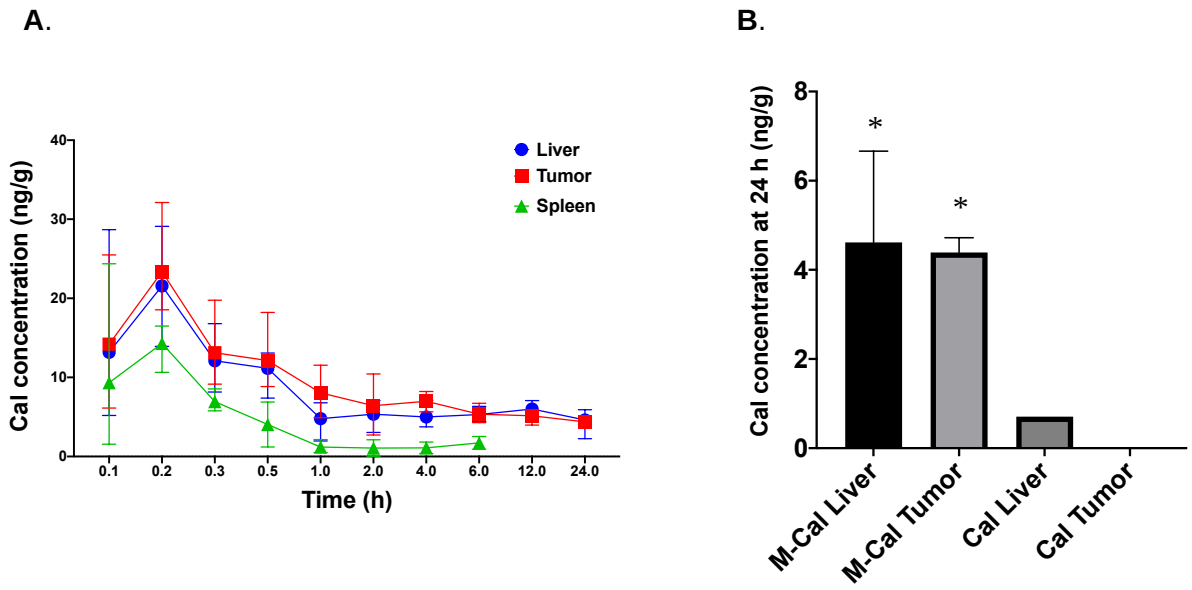

Figure 21. Biodistribution of Cal M-Cal/PTX and Cal/PTX in a Kras mouse model of PDAC. Data shows Mean and SD for N=3-4 per time point. (A) Concentration-time profile of Cal in liver, tumor and spleen and (B) Comparison of Cal concentration in various tissues at 24 hr between formulated and free drugs groups. *Statistically significant at $p < 0.05$ between formulated and unformulated groups.

The biodistribution of PTX was also evaluated. Of the three organs studied the concentrations of PTX in liver was highest up to the 6th hr post single dose, beyond which liver concentrations appeared similar to tumor concentrations (**Figure 22A**). Spleen concentrations of PTX were on a similar magnitude as tumor. At the 24-hr time point liver and tumor concentrations of PTX from M-Cal/PTX and free Cal/PTX were compared. Again, PTX concentrations in liver and tumor were significantly higher in the M-Cal/PTX group than in the free Cal/PTX group (**Figure 22B**). As was observed for Cal, PTX could not be measured in the tumors of mice that received free Cal/PTX at the 24-hr mark.

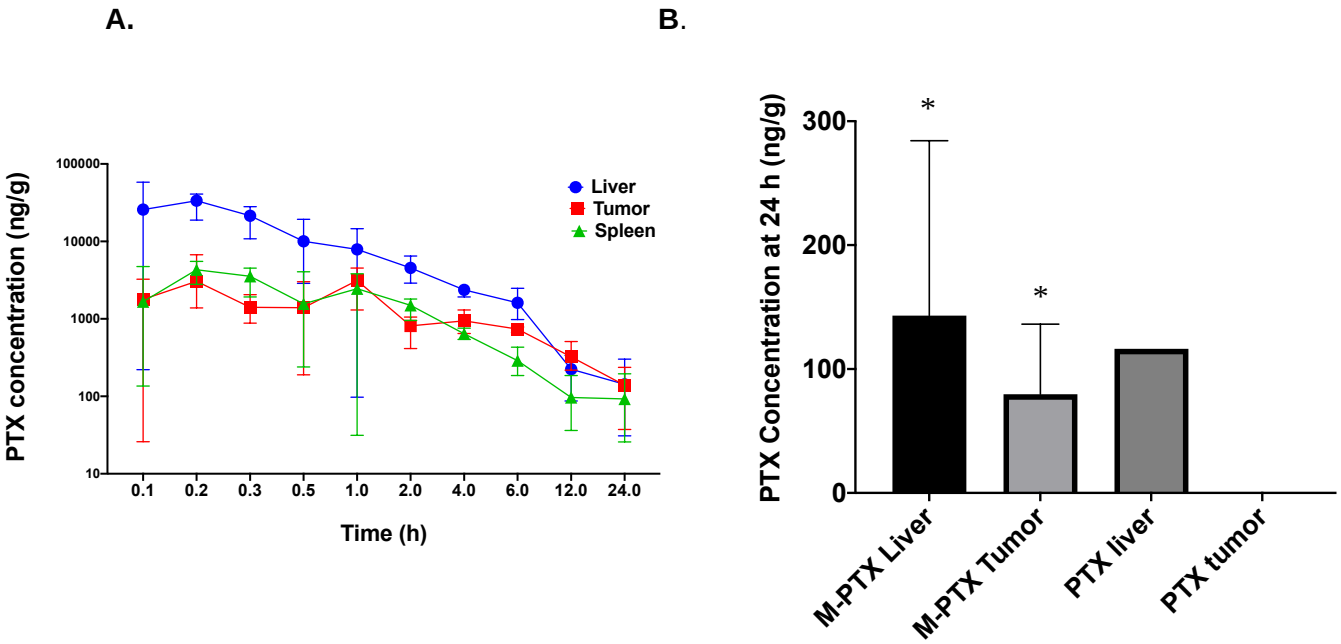

Figure 22. Biodistribution of PTX from M-Cal/PTX and Cal/PTX in a Kras mouse model of PDAC. Data shows Mean and SD for N=3-4 per time point. *statistically significant at $p < 0.05$ between formulated and unformulated groups.

4.3.4.4 Drug accumulation across different formulations of Cal and PTX

Accumulation of Cal and PTX from mono (M-Cal, M-PTX) and dual formulations (M-Cal/PTX) after multiple dose administration was also evaluated and compared with cremophor formulation of Cal and PTX (Crem-Cal+PTX), and Abraxane (ABX), a nano-albumin bound formulation of PTX. Equivalent does of Cal and PTX were administered IV across all groups for a total of 10 doses (0.5mg/kg Cal, 5 mg/kg PTX). These studies showed that either as mono formulation or dual formulation, using the micelle platform is superior in achieving tumor accumulation. All groups that received Cal either as the mono formulation (M-Cal), or as a physical mixture with PTX (M-Cal +M-PTX) or as a dual formulation (M-Cal/PTX) had significantly higher concentrations of Cal in the tumor when compared with the cremophor formulation of Cal. (**Figure 23A**). For PTX the dual formulated M-Cal/PTX had significantly higher concentrations of

PTX than all other groups (**Figure 23B**). Cal did not appear to accumulate in the tumor with increasing number of doses. The mean concentrations of Cal in the tumor from the first to the 10th dose were similar (**Figure 23C**). For PTX, the data suggests there might be accumulation. Mean tumor concentrations of PTX after the 2nd, 3rd 4th and 5th doses were higher than after dose 1. After the 10th dose the mean tumor PTX concentration was significantly higher (**Figure 23D**)

A.

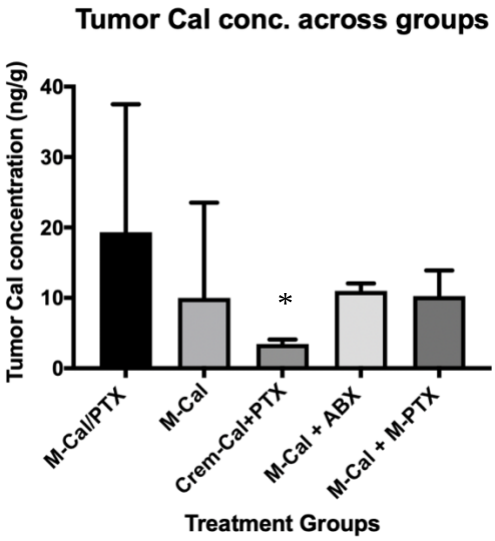

B.

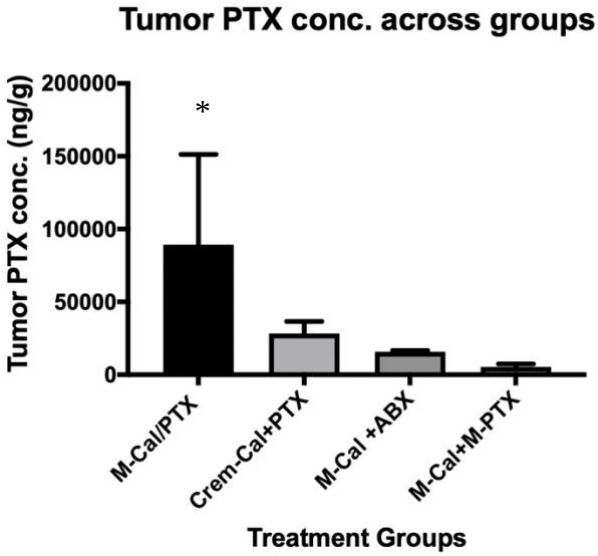

C.

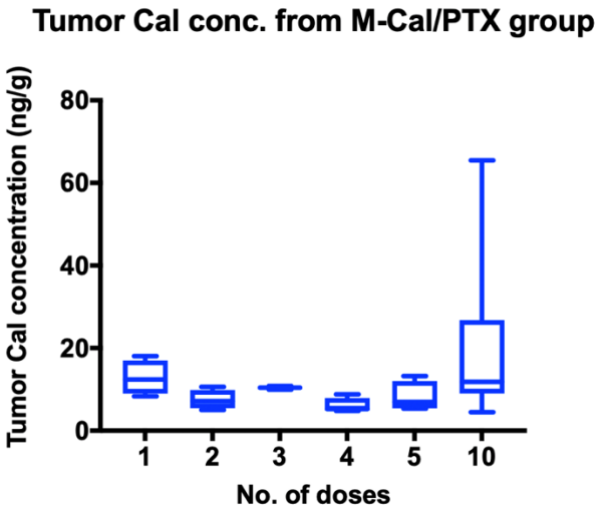

D.

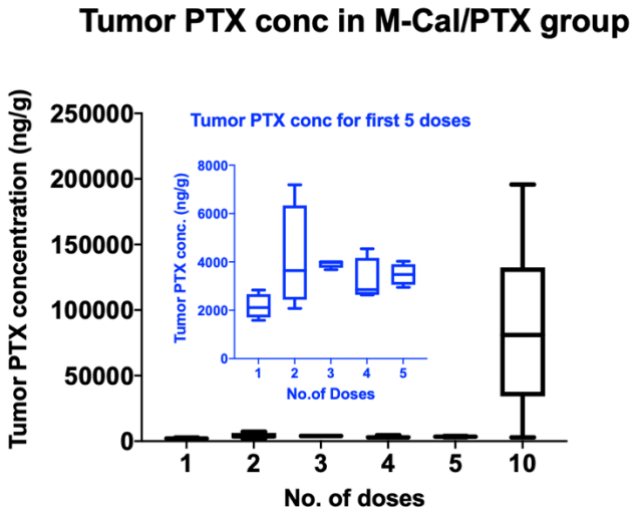

Figure 23. Comparative biodistribution of Cal and PTX across different formulations of Cal and PTX. N= 3-4 for each group. *Statistical significance between the difference in Crem-Cal +PTX vs other groups. **Statistical significance between PTX for M-Cal/PTX group and other groups, ABX=Abraxane, Crem-Cal+PTX = cremophor formulation of Cal and PTX, M-Cal + M-PTX = physical mixture of mono formulated Cal and PTX.

4.3.5. Simultaneous population PK modeling of Cal and it's metabolites MC1046 and MC1080

Cal is metabolized by CYP24 to the intermediate MC1046 which is further Metabolized by unknown enzyme, presumable CYP to form MC1080. To further understand the metabolic profile of Cal and differences in formulated and unformulated Cal, a population PK approach was used to simultaneously model Cal and its metabolites. Healthy mice were administered an IV bolus dose of formulated or unformulated Cal and PTX (0.5 mg/kg Cal, 5 mg/kg PTX). Blood samples were collected at predefined time points and analyte concentrations were measured. Modeling was done in NONMEM (v7.4) with PdxPOP (v5.2.2) as the graphics user interface. Post processing of model output was done in R Studio (v3.5.1 or later) and GraphPad Prism (v8 or later)

4.3.5.1 Pharmacokinetics of Cal and metabolites

The whole blood concentration-time plots for Cal, MC1046 and MC1080 were constructed for both the formulated and unformulated groups. The plots for all analytes are shown in **Figure 24A**. The PK profiles support the metabolism pathway for Cal. In both the formulated (**Figure 24B**) and unformulated (**Figure 24C**) groups, the profiles of Cal and MC1080 follow the same pattern with peak exposures at the earliest time point and then

gradually falling-consistent with what is expected for IV dosing. However, MC1080 has a PO-Like profile with peak concentration at 1 hr. This supports MC1080 being produced after MC1046. Formulated Cal group had lower peak concentrations than the unformulated group (**Figure 24D**), but Cal concentrations could be measured up to 24 hr post single dose in the formulated group while it could only be measured up to 6 hours in the unformulated group. While MC1046 profiles were similar for both groups (**Figure 24E**), MC1080 concentrations in the formulated group was higher from 5 min to 1 hr in the formulated group than in the unformulated group (**Figure 24F**). Beyond 2 hr, MC1080 concentration in the unformulated group was higher than in the formulated group.

A

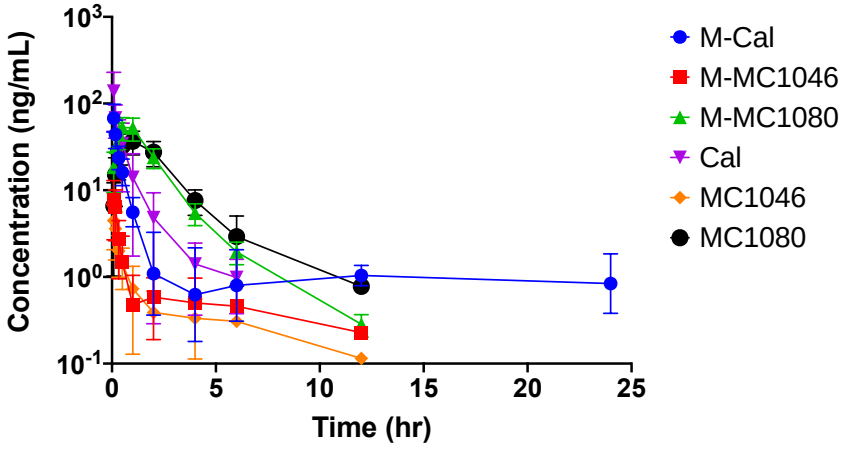

B

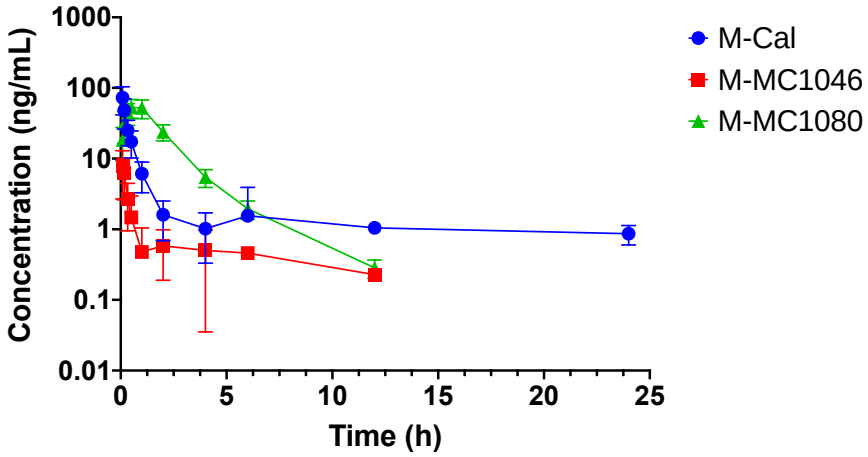
1000
100
10
1
0.1
0.01
Concentration (ng/mL)
0
5
10
15
20
25
Time (h)
M-Cal
M-MC1046
M-MC1080

C

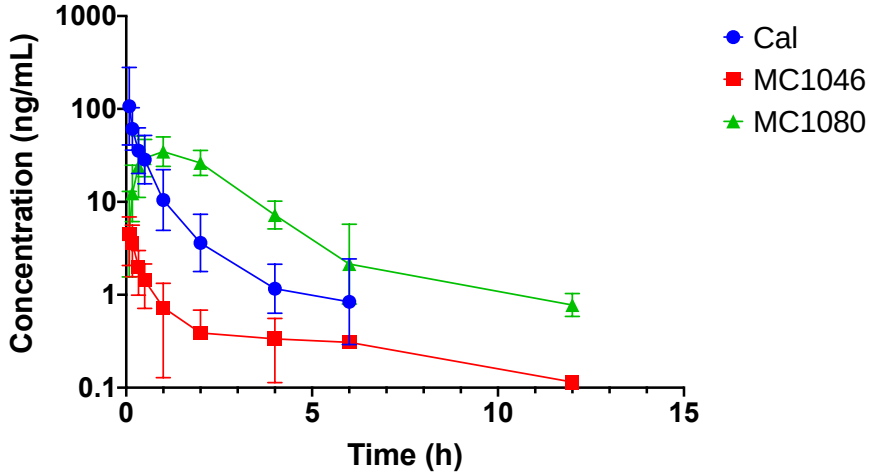
1000
100
10
1
0.1
Concentration (ng/mL)
0
5
10
15
Time (h)
Cal
MC1046
MC1080

D

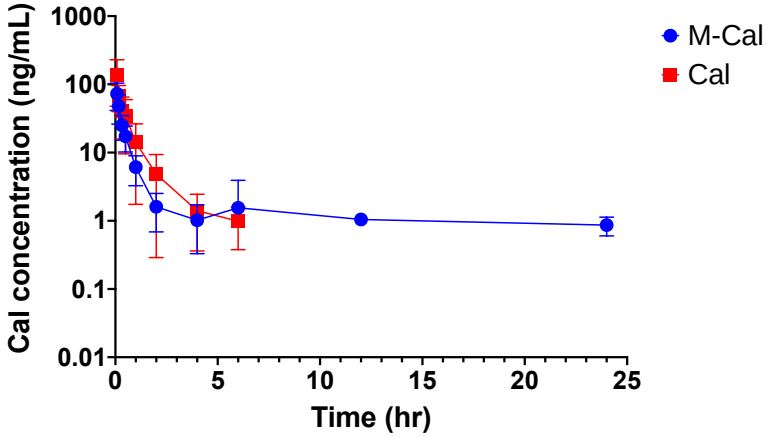
1000
100
10
1
0.1
0.01
Cal concentration (ng/mL)
0
5
10
15
20
25
Time (hr)
M-Cal
Cal

E.

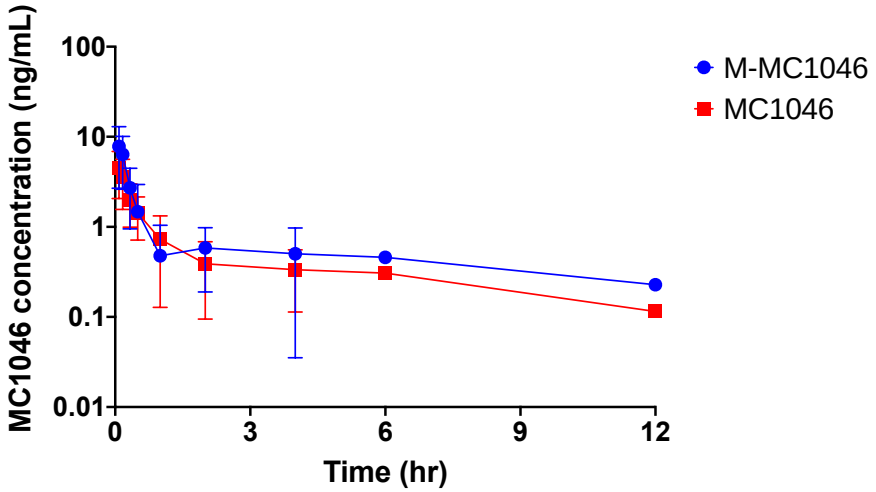

F.

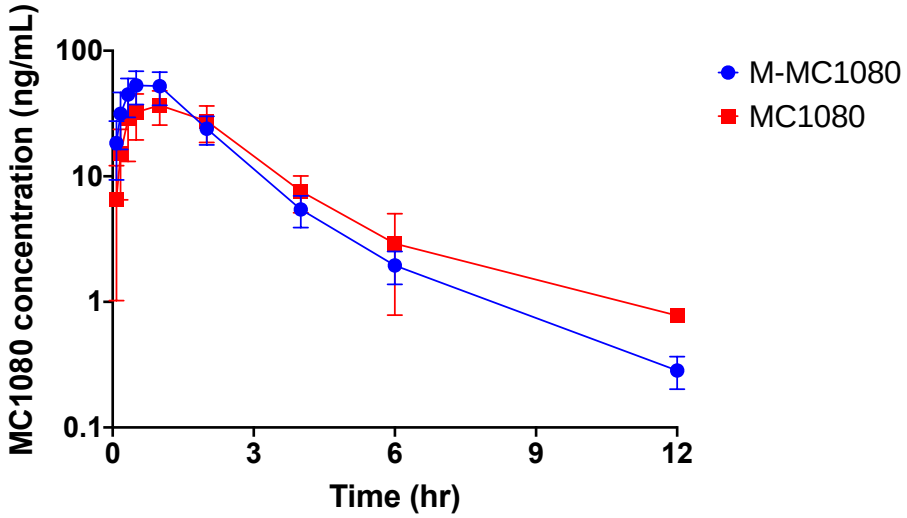

Figure 24. Concentration time profiles for formulated and unformulated Cal and its metabolites (A), formulated Cal and its metabolites (B), unformulated Cal and its metabolites (C), formulated and unformulated Cal (D), formulated and unformulated MC1046 (E), formulated and unformulated MC1080 (F). Data shows mean and SD for N=8 for formulated group and N=7 for unformulated group.

4.3.5.2 Simultaneous modeling of Cal, MC1040 and MC1080

A 3-compartment IV model was used to model the 3 analytes with each of the compartments designated a central compartment because all analytes were measured in blood. The total Cal CL (CLC) and fraction metabolized (FM) were estimated. From these, the fraction of Cal metabolized to MC1046 was calculated (CLCM) as well as fraction of Cal that is metabolized to other metabolites and/or eliminated by an alternative route (CLCB).

Similar terms were created for MC1046. Total MC1046 CL was denoted by CLC1 and the fraction of MC1046 metabolized denoted as FM1. From these, the fraction of MC1046 potentially metabolized by CYP24A1 to MC1080 (CLCM1) and fraction of MC1046 that is potentially metabolized by other enzymes and/or elimination route (CLCB1) were calculated. For MC1080 a total CL term was estimated (CLC2). Additive and proportional residual models were used.

The goodness of fits and diagnostic plots are shown in **Figure 25**.

From the model the total CL of Cal was estimated to be 13.1 L/h (**Table 20**). Also, the fraction of Cal metabolized to MC1046 by CYP24A1 was estimated to be about 23% while the fraction of MC1046 metabolized to MC1080 was estimated to be 94% (**Table 20**). The total clearance of MC1046 was estimated to be 46.7 L/hr. Also, the total CL of MC1080 was estimated to be 1 L/hr. Finally, the central volumes of distribution of Cal, MC1046 and MC1080 were estimated as 4.9, 1.5 and 1.1 L respectively (**Table 20**). Other derived parameters are summarized in **Table 20.**

The conversion rate of Cal to MC1046 was estimated to be 0.61 1/hr while that of MC1046 to MC1080 was higher, at 39.9 1/hr (**Table 20**).

For model qualification, the observation (OBS) versus population predicted (PRED) or Individual predictions (IPRED) plots (**Figures 25A and C**) showed very good model fits in both the formulated and unformulated groups. The same observation was made when the plots were separated by analyte (**Figures 25B and D**). The proportional weighting used in the model balanced the population weighted residuals vs PRED plot (**Figure 25E**) with most WRES between the acceptable +/- 2 deviation range. Finally, the tests for WRES normality showed no significant

deviation from this assumption (**Figures 25F and G**)

A.

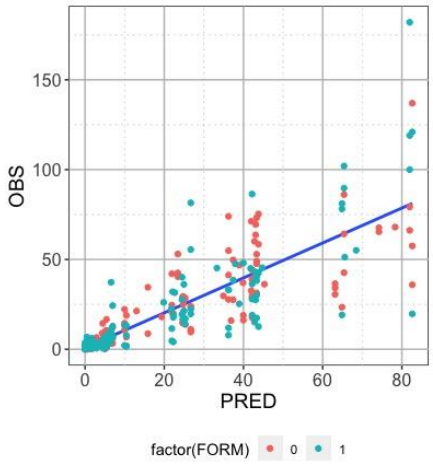

B.

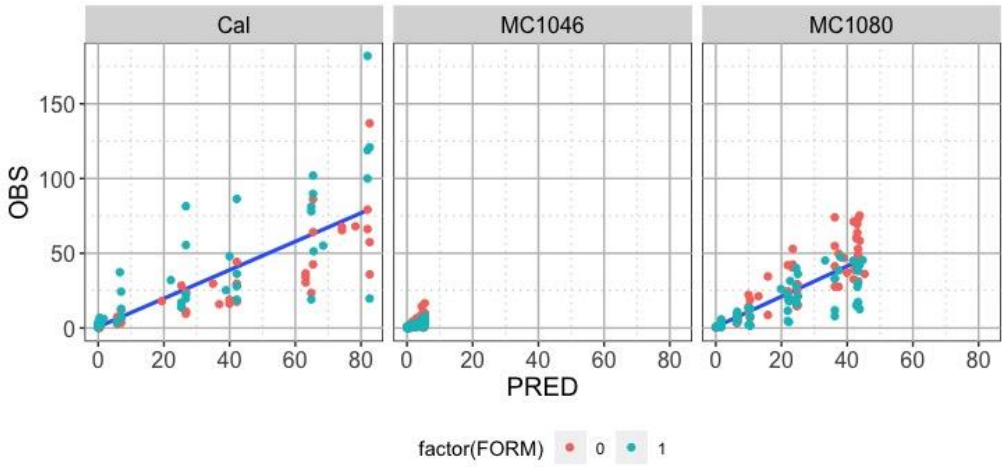

C.

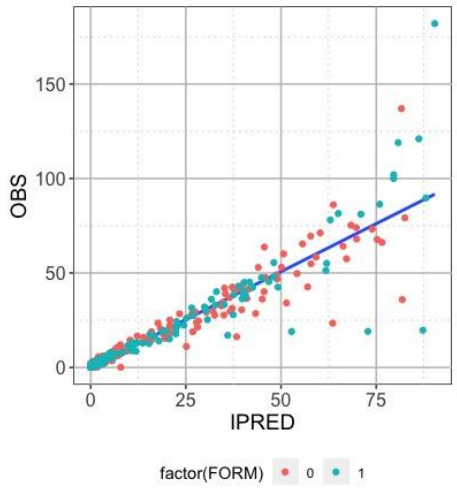
OBS
IPRED
0
25
50
75
0
50
100
150
factor(FORM)
0
1

D.

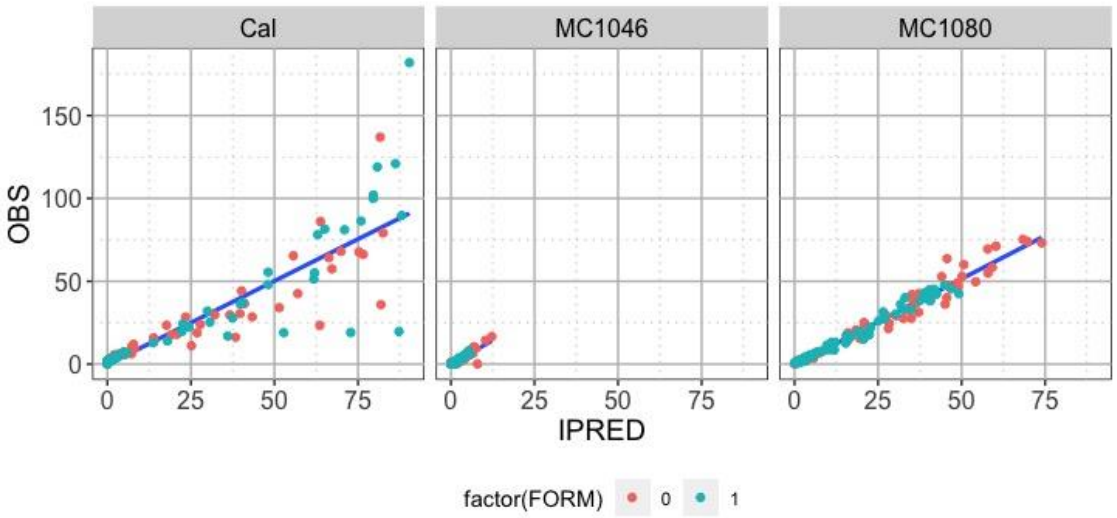
Cal
MC1046
MC1080
OBS
IPRED
0
25
50
75
0
50
100
150
factor(FORM)
0
1

E

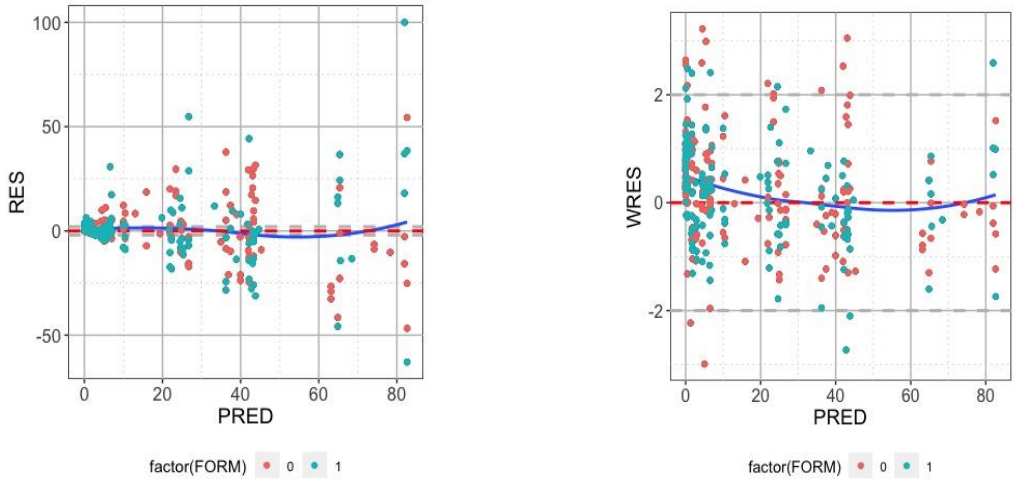
RES
PRED
WRES
PRED
factor(FORM) 0 1
factor(FORM) 0 1

F.

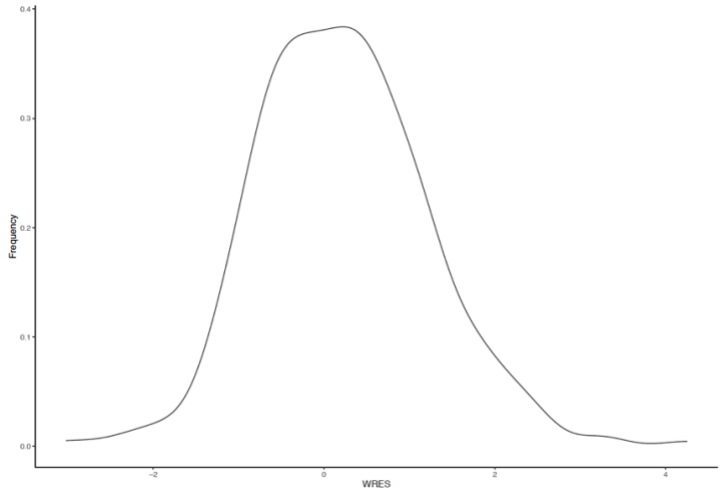
Frequency
WRES

G.

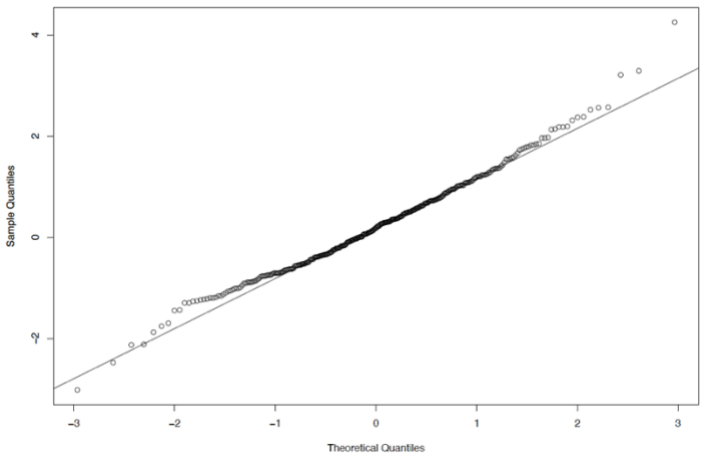
Sample Quantiles
Theoretical Quantiles

Figure 25. Observed vs PRED/IPRED for all analytes (A), Observed vs PRED/IPRED plotted by analyte (B, C), Residual vs PRED and WRES vs PRED (D), histogram of WRES (E) and theoretical vs observed quantiles for the WRES (F).

The population PK parameters are summarized in **Table 20**.

Table 20. Population PK parameters for Cal and its metabolites

Parameter	Description	Unit	Estimate	% RSE
CLC	Total Cal Clearance	L/hr	13.1	14
FM	Fraction of Cal metabolized to MC1046		0.23	8.68
CLCM	CYP24A1 clearance of Cal	L/hr	2.98	NA
CLCB	Other clearance of Cal	L/hr	10.1	NA
CLC1	Total clearance of MC1046	L/hr	46.7	9.29
FM1	Fraction of MC1046 metabolized to MC1080		0.941	0.49
CLCM1	Potential CYP24A1 clearance of MC1046	L/hr	43.9	NA
CLCB1	Other clearance of MC1046	L/hr	2.80	NA
CLC2	Total clearance of MC1080	L/hr	1	8.22
V1	Volume of distribution of Cal	L	4.90	11.5
V2	Volume of distribution of MC1046	L	1.10	35
V3	Volume of distribution of MC1080	L	1.50	11.3
K12	Rate of conversion of Cal to MC1046	1/hr	0.61	NA
K23	Rate of conversion of MC1046 to MC1080	1/hr	39.9	NA

4.3.5.3 Posthoc comparison of PK parameters between formulated and unformulated Cal

Posthoc analyses were done to compare the individual level PK parameters between formulated and unformulated groups. These analyses showed statistically different CYP24A1-mediated elimination between formulated and unformulated Cal (**Figure 26A**) with formulated Cal having a higher CL. Other CL terms for Cal are higher and statistically significant in the formulation group than in animals that received free Cal**.** For MC1046, almost all circulating metabolites was almost entirely eliminated through one enzyme, potentially CYP24A1. This elimination accounted for 94% of MC1046 elimination with very little elimination attributed to other routes and/or mechanism.

Additionally, this observation was consistent regardless of whether the animals received formulated or free Cal (**Figure 26B**).

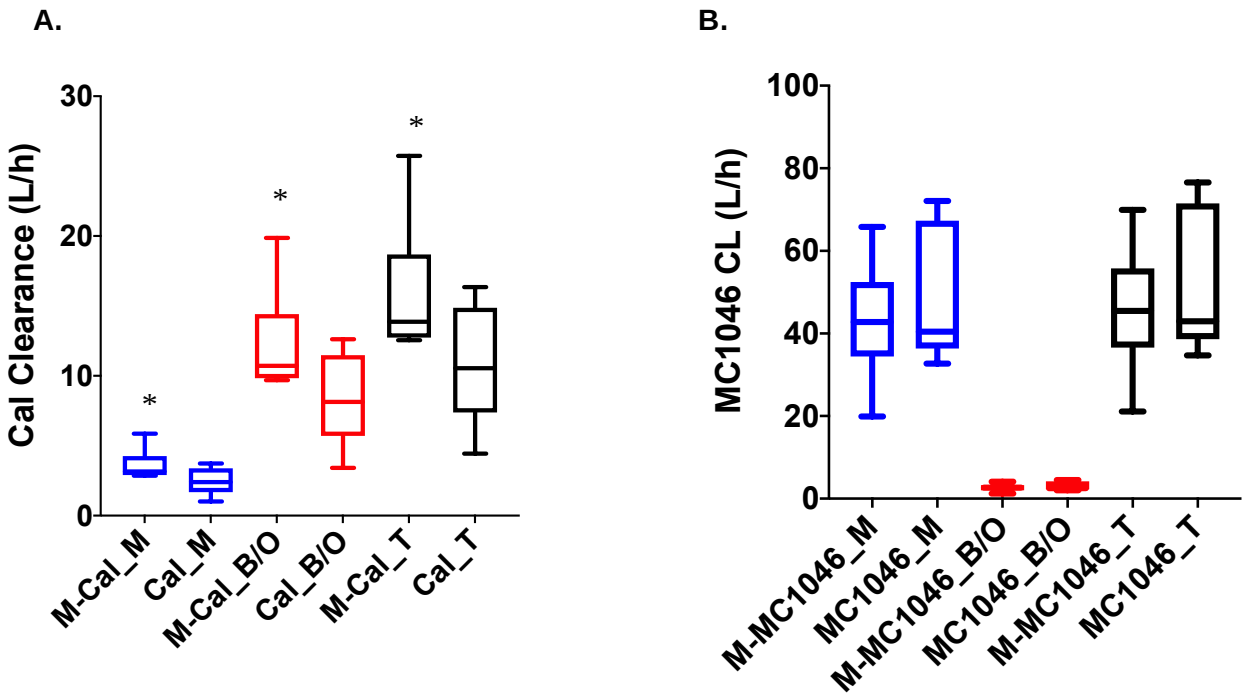

Figure 26. Model-predicted individual Clearance of Cal (A) and MC1046 (B)

The plots show the mean and SD for N=8 for the formulated and N=7 for the unformulated groups.

*statistical difference at $p < 0.05$ (parametric t-test with Welch's correction)

M-Cal_M and **Cal_M** represent CYP-24A1 elimination of formulated and unformulated Cal respectively.

M-Cal_B/O and **Cal_B/O** represent biliary and/or other mechanisms of elimination of formulated and unformulated Cal respectively.

M-Cal_T and **Cal_T** represent total clearance of formulated and unformulated Cal

M-MC1046 and **MC1046_M** represent Potential CYP24A1-mediated elimination of MC1046 from formulated and unformulated Cal respectively.

M-MC1046_B/O and **MC1046_B/O** represent biliary and/or other mechanisms of elimination of MC 1046 from formulated and unformulated Cal respectively.

M-MC1080_T and **MC1080_T** represent total clearance of MC1080 from formulated and unformulated Cal

The model suggested that MC1080 CL in the formulated and unformulated groups are similar (**Figure 27A**).

Finally, the model also showed that only about 23% of Cal is converted to MC1046, whereas almost all of MC1046 is converted to MC1080 (**Figure 27B**).

A. **B.**

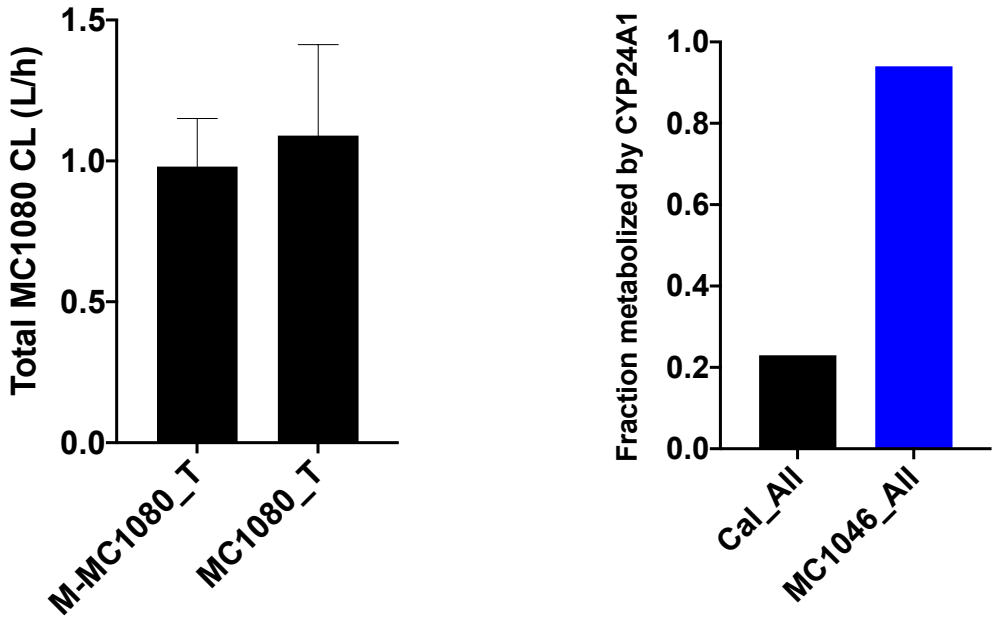

Figure 27. Model-predicted clearance for MC1080 (A) and the fraction of Cal and MC1040 elimination by CYP-mediated mechanism (B). Graphs show mean with SD for N=8 for the formulated group and N=7 for the unformulated group.

M-MC1080_T and **MC1080_T** represent clearance of MC1080 from formulated and unformulated Cal respectively.

4.3.6 Population PK modeling of formulated and unformulated Cal in healthy and diseased mice

To understand the population PK of Cal and PTX and establish the impact of relevant covariates on these, population PK modeling was used. Data from healthy animals that received either formulated or unformulated drugs, as well as those from diseased animals that received the formulated regimen were tested. The demographics of animals included in these analyses is summarized in **Table 21**.

Table 21. Demographics of animals used for population PK modeling

State of mice	Number of animals	Dose (mg/kg)	Formulated (M-Cal/PTX)	Unformulated Cal/PTX	No. of doses
Healthy	15	0.5 Cal, 5 PTX	8	6	1
Diseased	4	0.5 Cal, 5 PTX	4		1
	4	0.5 Cal, 5 PTX	4		2
	4	0.5 Cal, 5 PTX	4		3
	3	0.5 Cal, 5 PTX	3		4
	2	0.5 Cal, 5 PTX	2		5
	2	0.5 Cal, 5 PTX	2		10
Total	34		28	6	

4.3.6.1 Concentration-time profiles of Cal and PTX

After intravenous drug administration, whole blood samples were collected at pre-defined time points and the concentrations of analytes were measured using the previously described UPLC-MS/MS assay. The concentration time plots were constructed and shown in **Figure 28**.

A.

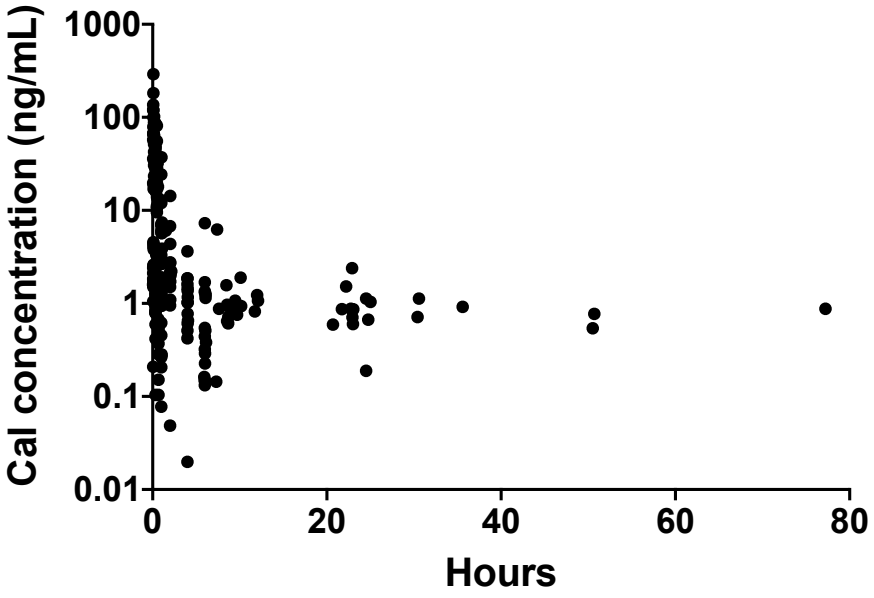

B.

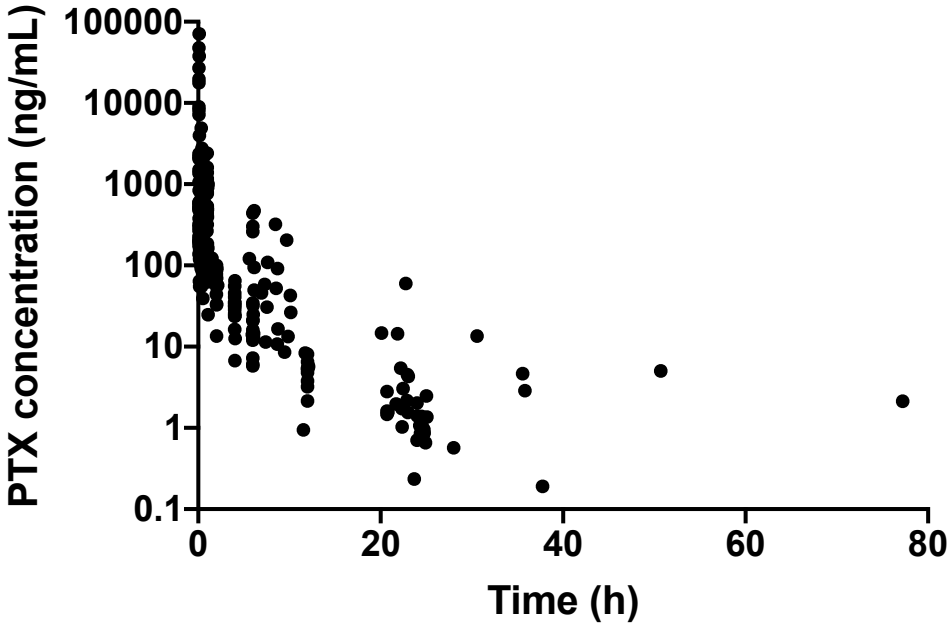

Figure 28. Concentration-time profiles of Cal and PTX. Individual data points are shown for N= 34

4.3.6.2 Population PK modeling of Cal

Calcipotriol showed a biexponential decay, hence a 2-compartement model was used as shown in the diagram below.

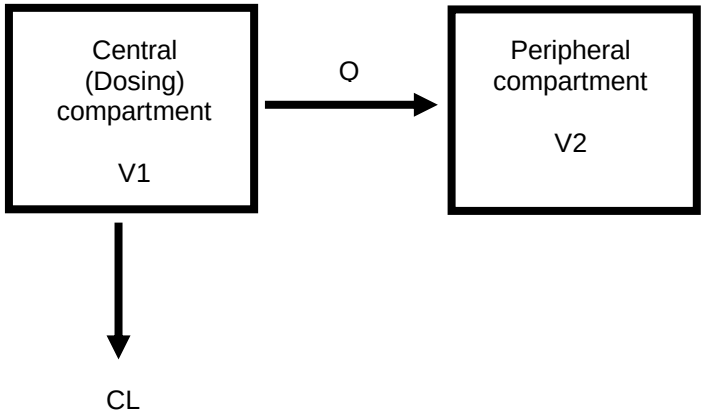

Figure 29. Two-compartment for Cal population PK modeling

V1: Central volume of distribution

V2: Peripheral volume of distribution

CL: Clearance of Cal from the central compartment

Q: Blood flow from central to peripheral compartments

A base model for Cal was constructed according to the formula

$$THETA_{i.} = TVTHETA \times EXP(ETA)_I \quad \text{..... Equation 1}$$

Where $THETA_i$ is the individual parameter

TVTHETA is the typical value of the parameter and

ETA is the inter-subject variation

The base model successfully converged with an objective function value (OFV) of 634.174. Stepwise covariate search identified disease status (STAT, 0= diseased and 1= healthy) and drug formulation (FORM, 0= formulated, 1= unformulated) as significant covariates and these were coded as shown in equation 2

$$TVTETHA = THETA(n-1) \times EXP(ETA)_I \times THETA(n)^{STAT} \times THETA(n+1)^{FORM} \quad \text{Equation 2}$$

Where THETA(n) and THETA(n+1) are the effects of health status (STAT) and formulation status (FORM) on the parameter THETA(n-1). Also, about 8% of the measurements were below the limit of quantification. Therefore, the M3 (Beal, 2001) method for modeling observations below the limit of quantification was applied. The addition of covariates lowered the OFV to 575.154 indicating these covariates were significant.

The PK parameters for the final model with covariates is shown in **Table 22**.

Table 22. Population PK parameters for calcipotriol

Parameter	Description	Unit	Estimate	% RSE
CL	Clearance	L/hr	14.29	22.4
V1	Central volume of distribution	L	450.33	3.62
Q	Blood flow from central to peripheral compartments	L	7.24	32.2
V2	Peripheral volume of distribution	L	85.63	33.3
STAT_CL	Effect of health status on clearance		0.57	36.1
FORM_CL	Effect of formulation on clearance		0.54	47.2
STAT_V1	Effect of health status on central volume of distribution		0.017	32.8
FORM_V1	Effect of formulation on central volume of distribution		0.704	28

The model showed that the diseased status of animals (STAT=0) resulted in Cal being cleared almost twice as fast as in the healthy counterparts (**Table 22**). The micellar formulation also had an impact on Cal CL according to the model predictions. Similar to the diseased status, Cal CL is two times higher in mice that received the formulated drug than the unformulated one. These covariates also had a significant impact on the central volume of distribution (V1) but to different extents. The impact of diseased status on Cal V1 was particularly significant with the model showing that diseased animals had a 58-fold increase in V1 compared to the healthy counterparts. Although significant but to a lesser extent, the micellar formulation also increased V1 for Cal by almost 1.5 times when compared with free Cal.

4.3.6.2.1 Model fits and diagnostic plots for Cal population PK model

Population PK modeling involves making statistical assumptions that must be met for the model to be considered valid. The observed (OBS) versus population prediction (PRED) showed the model was able to adequately predict OBS (**Figure 30A**). At the individual level (IPRED), where the inter-subject variation was accounted for, the model showed a good fit between OBS and IPRED (**Figure 30B**). Because the M3 method was applied, a normalized prediction distribution error (NPDE) versus PRED was evaluated instead of WRES vs PRED. Most of the residuals were between the acceptable +/- 2 S.D range showing the prediction weighting strategy employed was acceptable (**Figure 30C**). **Figures 30 C** and **D** evaluated the assumption of normality of the residuals in the model. Both figures showed no significant deviation from this assumption

A.

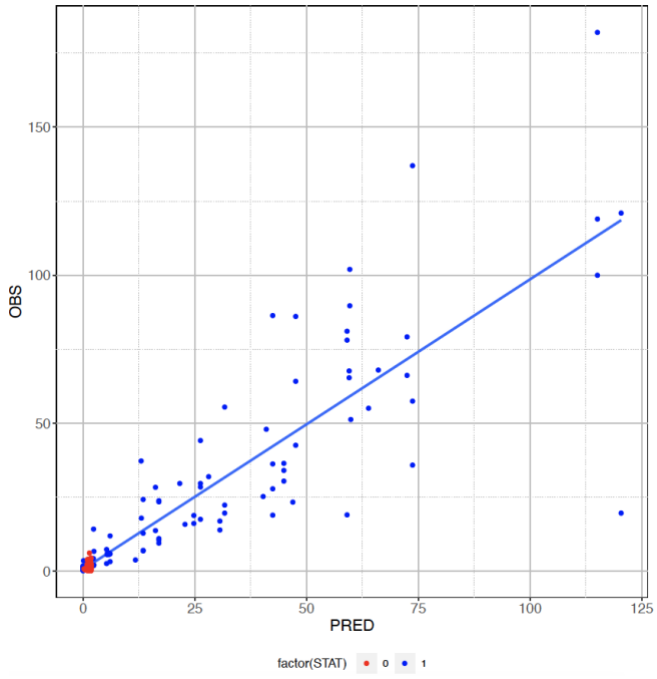

B.

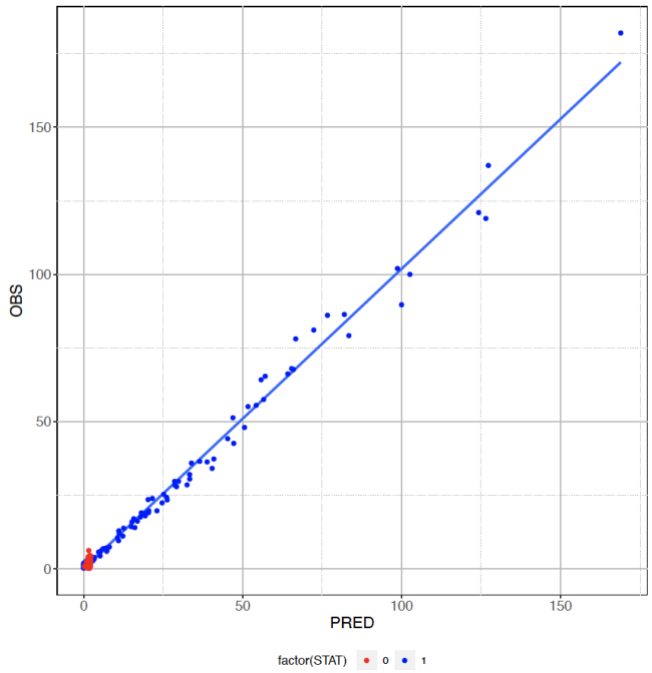

C.

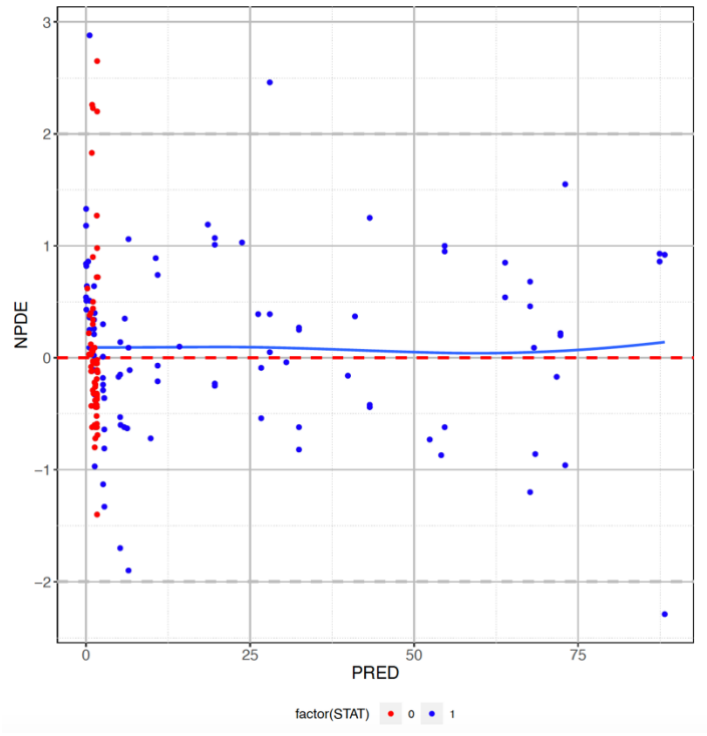
NPDE
PRED
factor(STAT) 0 1

D.

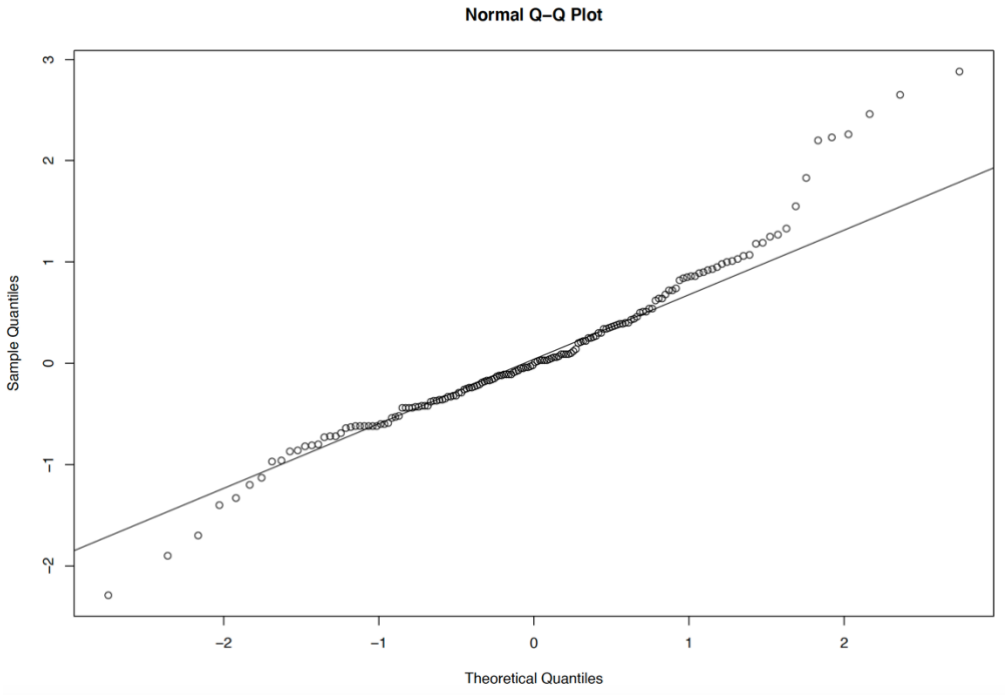
Normal Q–Q Plot
Sample Quantiles
Theoretical Quantiles

E.

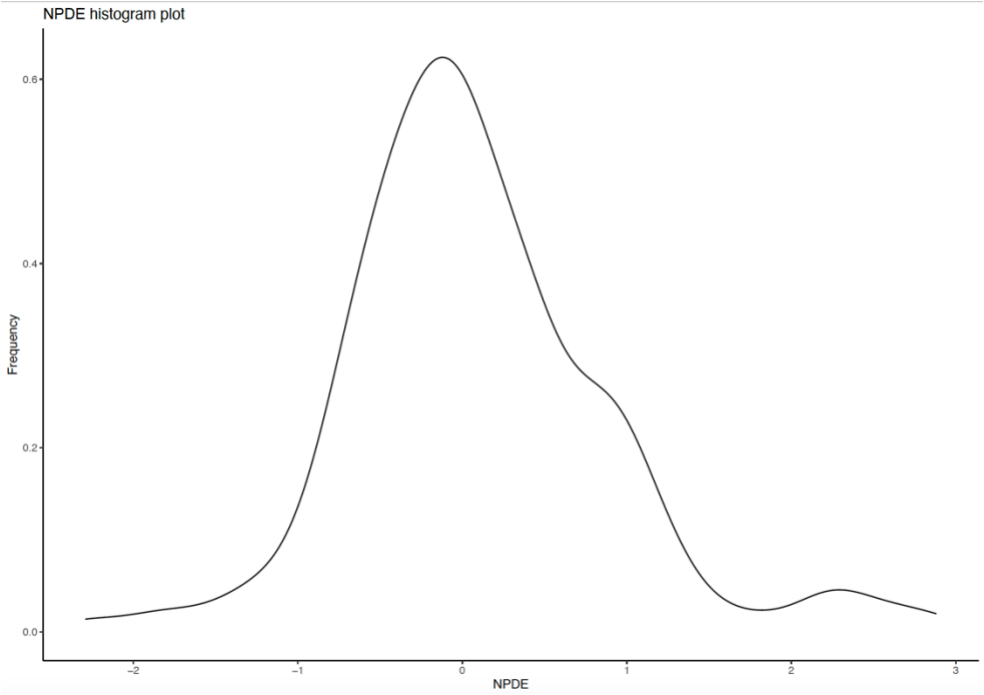

Figure 30. Observed vs PRED (A), Observed vs IPRED (B), NPDE vs PRED (C), theoretical vs observed quantiles for the WRES (D) and histogram of residuals (E) for Cal population PK model.

4.3.6.3 Population PK modeling of PTX

Similar to Cal, PTX showed biexponential concentration-time profile (**Figure 28B**) so a 2-compartment model was used as shown in **Figure 29**. The base model for PTX was constructed according to the formula in equation 1. Covariates were also introduced through a power model as shown in equation 2. The PK parameters for PTX are shown in **Table 23.** Model code is found in the Appendix.

Table 23. Population PK parameters of PTX

Parameter		Unit	Estimate	% RSE
CL	Clearance	L/hr	12.4	9.72
V1	Central volume of distribution	L	4.3	21.3
Q	Blood flow	L	3.5	19.8
V2	Peripheral volume of distribution	L	66.7	15.9
STAT_V1	Health status effect on V1		0.037	21.6

The model estimated PTX to have a clearance of 12.4 L/hr and a small central volume of distribution (V1) of 4.3 L while the peripheral volume of distribution (V2) was much larger at 66.7 L. Covariate analysis showed the diseased animals had a central volume of distribution that was 27-fold higher than the healthy counterparts for PTX.

4.3.6.3.1 Model fits and diagnostic plots for PTX population PK model

Model qualification was performed as for Cal. The observed (OBS) versus population prediction (PRED) showed the model was able to adequately predict OBS (**Figure 31A**). At the individual level (IPRED), where the inter-subject variation was accounted for, the model showed a good fit between OBS and IPRED (**Figure 31B**). The weighted residual (WRES) vs PRED plot showed the residuals were evenly balanced with most between the acceptable +/- 2 S.D range showing the prediction weighting strategy employed was acceptable (**Figure 31C**). **Figures 31 C** and **D** evaluated the assumption of normality of the residuals in the model. Both figures showed no significant deviation from this assumption

A.

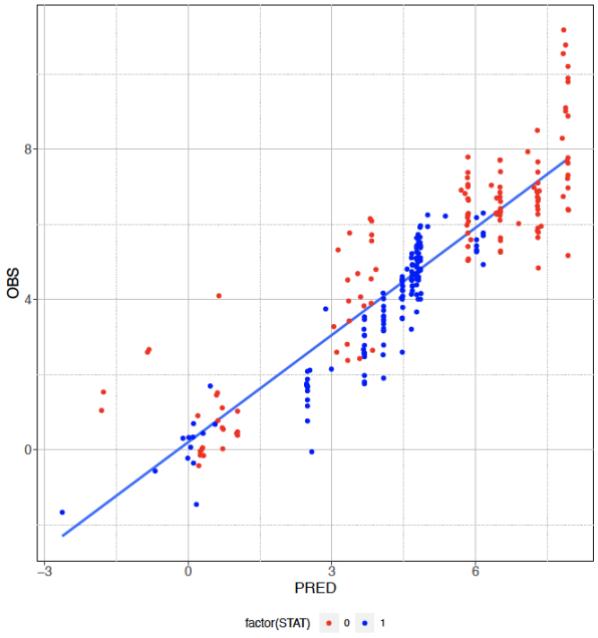

B.

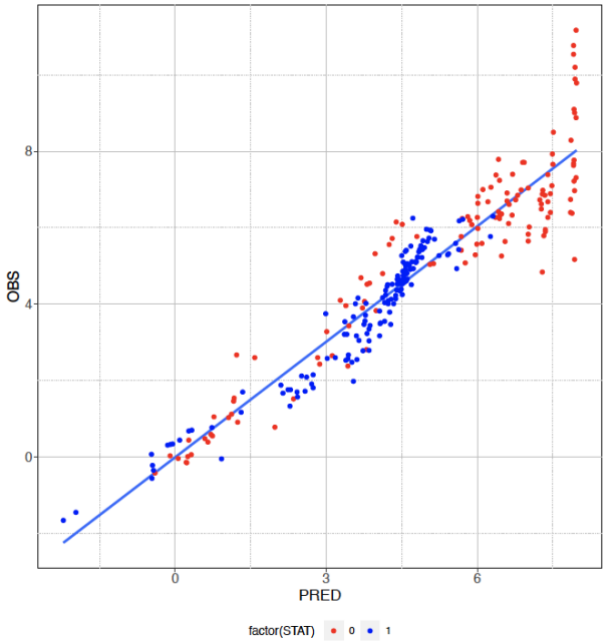
OBS
8
4
0
0
3
6
PRED
factor(STAT) 0 1

C.

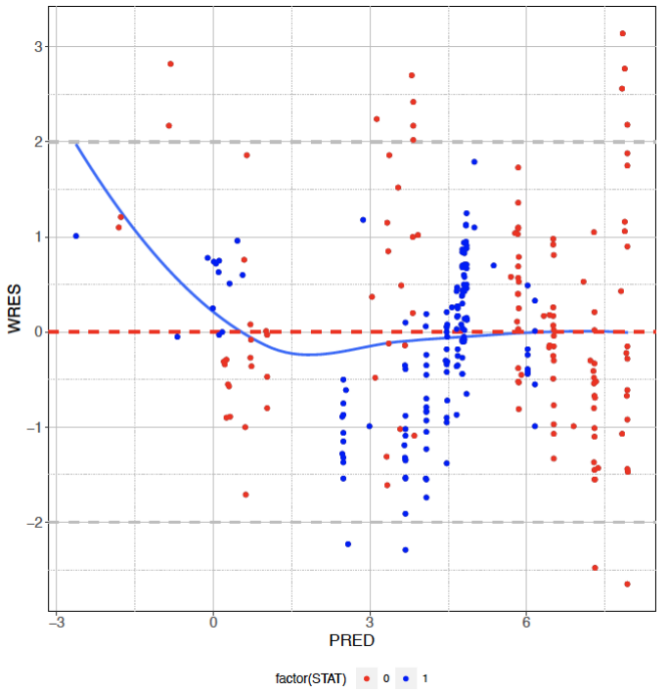
WRES
3
2
1
0
−1
−2
−3
0
3
6
PRED
factor(STAT) 0 1

C.

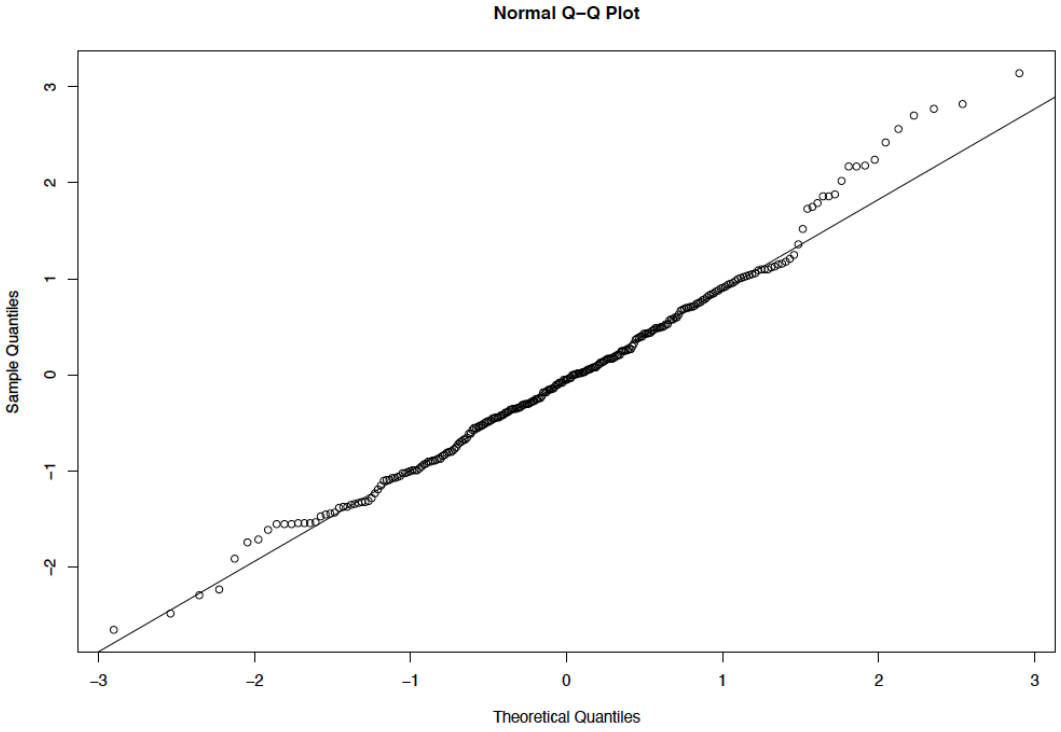
Normal Q–Q Plot
Sample Quantiles
Theoretical Quantiles
–3
–2
–1
0
1
2
3

D.

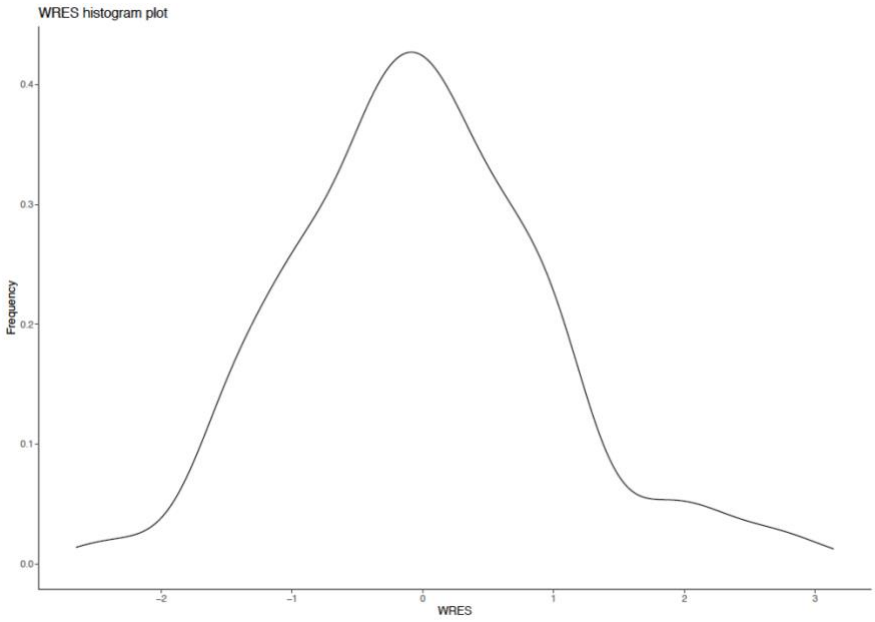
WRES histogram plot
Frequency
WRES
0.0
0.1
0.2
0.3
0.4

Figure 31. Observed vs PRED (A), Observed vs IPRED (B), WRES vs PRED (C), theoretical vs observed quantiles for the WRES (D) and histogram of residuals (E) for PTX population PK model.

4.3.7 Short-term efficacy and safety studies of M-Cal/PTX in an orthotopic Kras* mouse model of PDAC

The treatment benefits of M-Cal/PTX was evaluated in a mouse model of PDAC. Mice received IV doses of M-Cal/PTX. The dosing scheme used is summarized in **Figure 32.** The primary endpoints for this study were to assess the change in circulating stroma markers with M-Cal/PTX treatment and also tumor response to treatment as measured by T2-MRI. In addition, collection of PK samples was a secondary goal for the study. Considering the quantities of serum required for the measurement of circulating stroma markers, an innovative design was used. Thirty-two mice with palpable tumors were enrolled and these mice received M-Cal/PTX (0.5 mg/kg Cal and 5 mg/kg PTX). After each dosing event, four mice were randomly selected and from these PK samples were obtained at pre-defined time points. The PK-sampled mice were sacrificed 24 hours after dosing and the tissues including tumor were harvested. The remaining mice received the next dose followed by PK sampling and subsequent sacrifice of 4 mice 24 hr after the second dose as shown in the scheme. A 3-days on, 3 days off dosing design was used. Four mice from the M-Cal/PTX and sham groups were tagged, and their baseline, midpoint and end of study MRI measurements were taken to assess treatment impact on tumor size change. The animals that were imaged were not sampled for PK. Mono formulation of Cal (M-Cal), a mixture of mono-formulated Cal and mono-formulated PTX (M-Cal + M-PTX), a combination of M-Cal and Abraxane (M-Cal + ABX) and a cremophor formulation of Cal and PTX (Crem-Cal + PTX) were included as controls. Pharmacokinetic samples were not taken from the animals in the control groups.

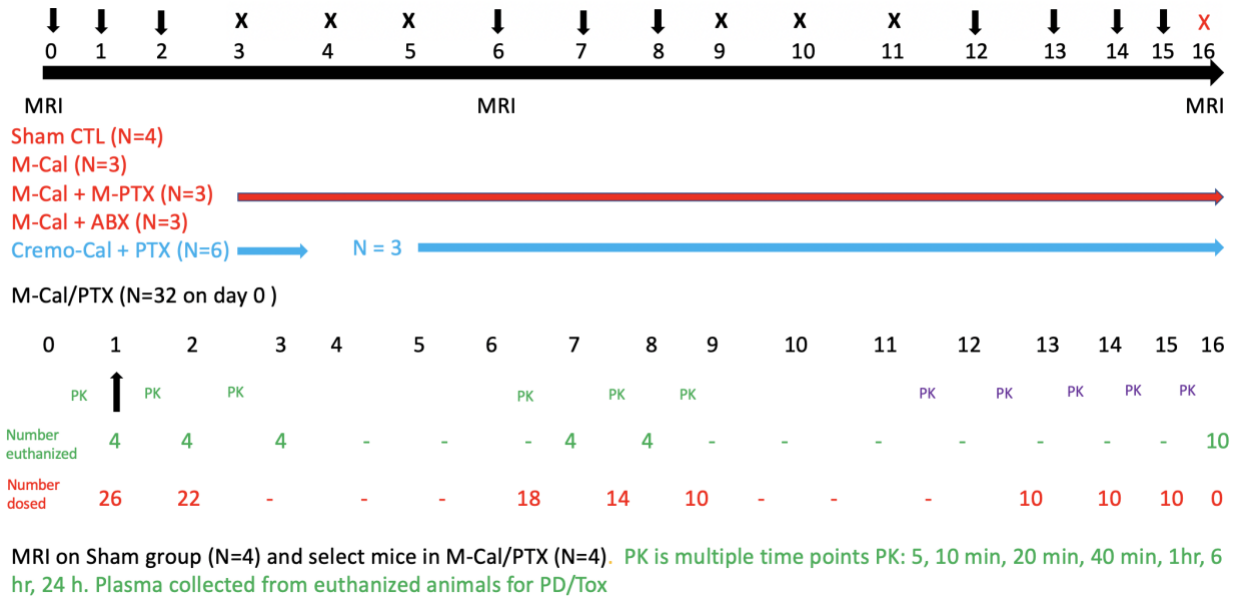

Figure 32. Schematic dosing scheme for the evaluation of short-term benefit of M-Cal/PTX in a mouse model of PDAC

4.3.7.1 M-Cal/PTX and blank micelles (sham) effects on tumor volume

The tumor size was measured by means of T2-MRI (**Figure 33**) and the corresponding volumetric quantifications were obtained (**Figure 34**).

Compared to the sham group, there was a 75% response in the M-Cal/PTX group. Two animals showed a moderate increase in their tumor volumes from day 7 while one had tumor shrinkage at days 7 and 14 **(Figure 34B)**. One animal in the M-Cal/PTX group had significant tumor progression. In the sham group, 75% of the study animals had significant tumor progression while one animal showed a moderate increase in the tumor volume **(Figure 34A)**.

4.3.7.2 M-Cal/PTX and blank micelles (sham) effects on circulating stroma markers

The effects of treatment on the circulating levels of TIMP1, TSP2 and MMP7 were evaluated by ELISA.

A.

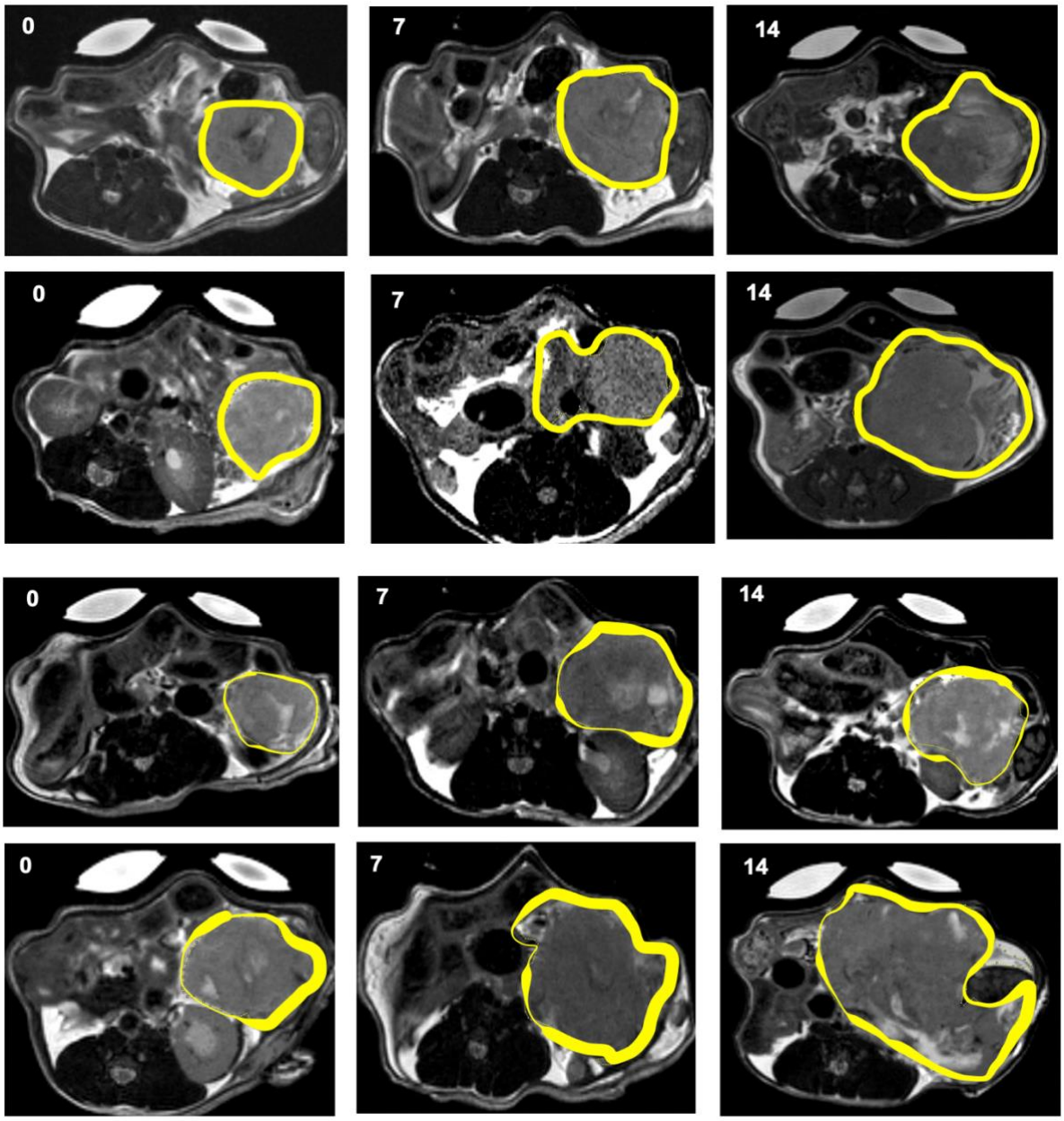

B.

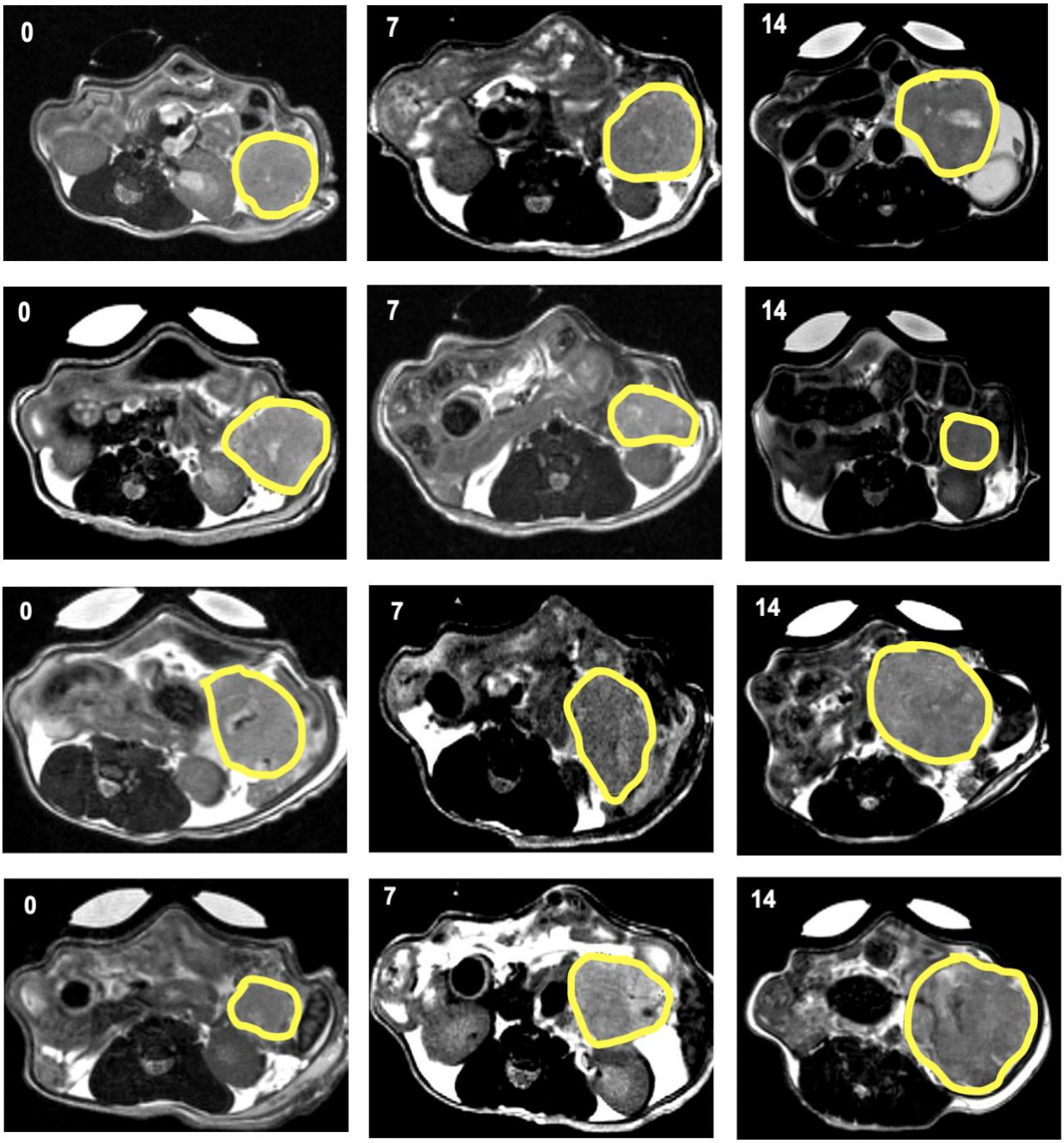

Figure 33. T2-MRI Measurements of PDAC tumors in sham (A) and M-Cal/PTX groups (B). Tumors were measured at baseline (day 0), midpoint (day 7) and on day 14.

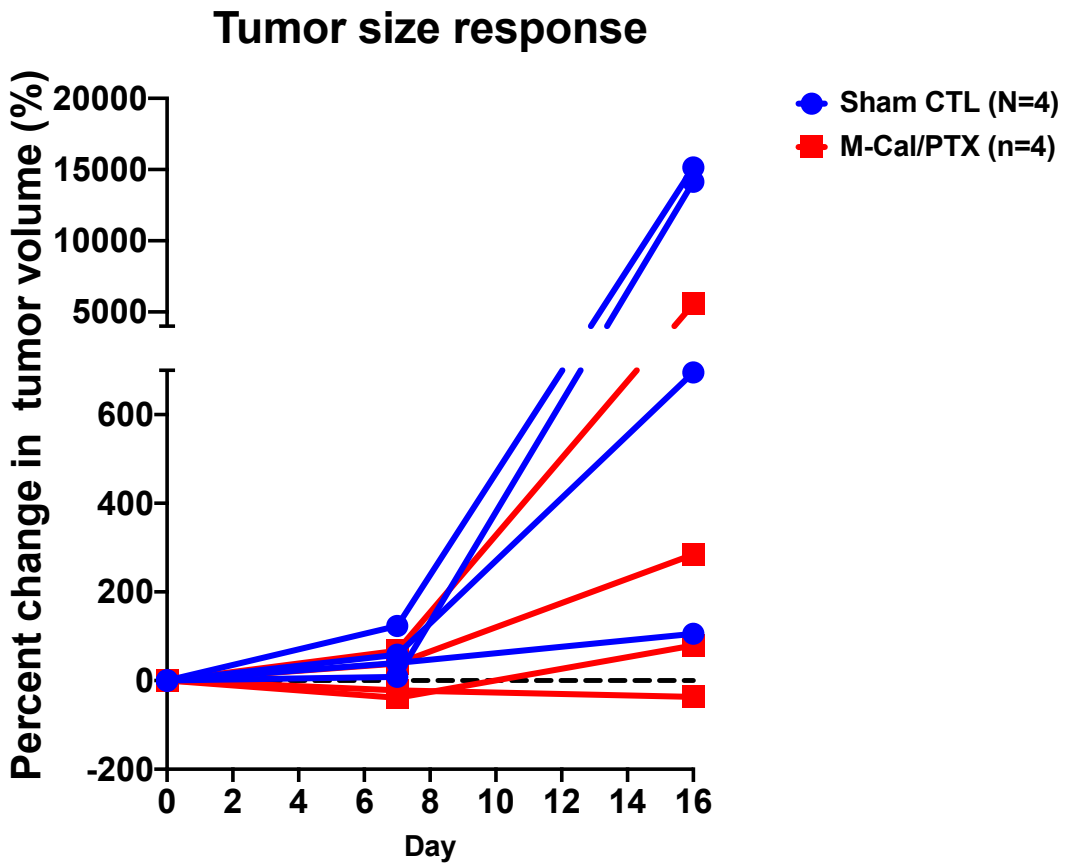

Figure 34. Change in tumor volumes with M-Cal/PTX (Red) and sham treatments (Blue)

4.3.7.3 M-Cal/PTX effects on circulating markers of stroma activity

The effects of M-Cal/PTX on circulating plasma markers of stroma activity were measured. For TIMP1 a delayed response was observed. Circulating TIMP1 levels remained high and similar to what was observed in the sham group after the first dose (**Figure 35A**). The levels remained high after the subsequent dose but started decreasing after the third dose although the decrease was statistically insignificant compared to day 1 observations. The mean TIMP1 levels continued to decrease after the 4th dose (day 7) while the levels remained very high in the sham group. Maximum TIMP1 decrease was achieved after the 10th dose with two subjects' measurements similar to what was observed in healthy mice (baseline).

Unlike TIMP1, the effects of M-Cal/PTX on circulating TSP2 levels was rapid. Reduction of TSP2

to baseline levels was achieved after the second dose and the levels remained low through the 10th dose (**Figure 35B).** Circulating TSP2 levels remained at dose 1 and dose 4 in the sham group.

The effects of treatment on MMP7 were also evaluated. MMP7 levels were elevated in the diseased animals compared with healthy ones (**Figure 35C)**. However, M-Cal/PTX did not impact the circulating levels of this marker after 10 doses.

A.

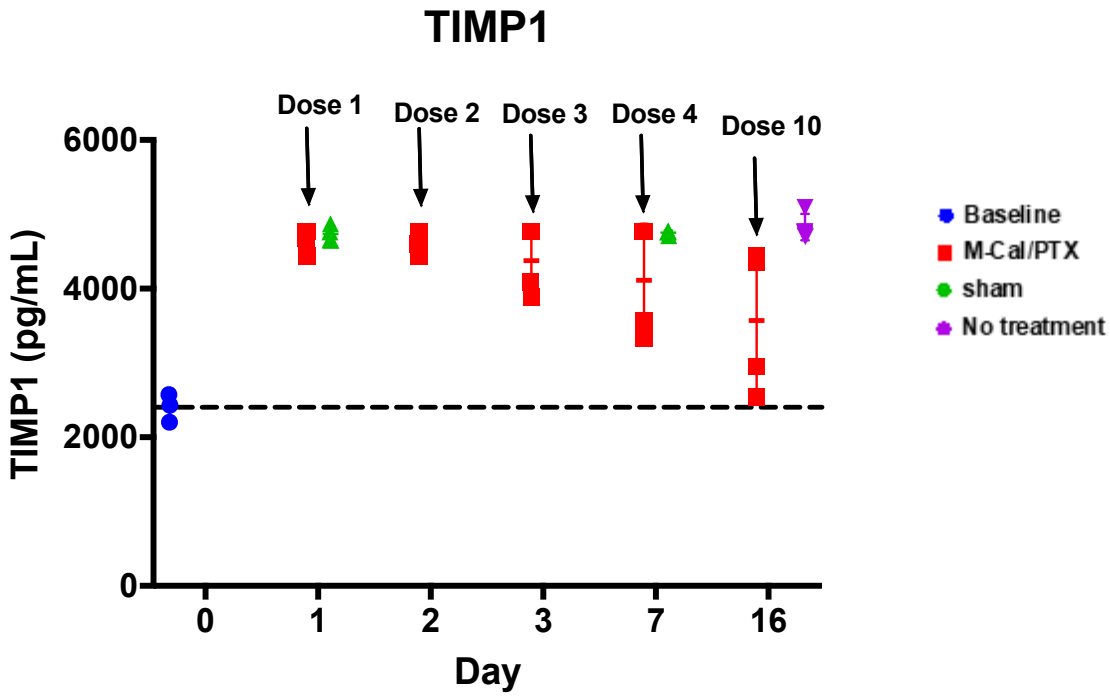

B.

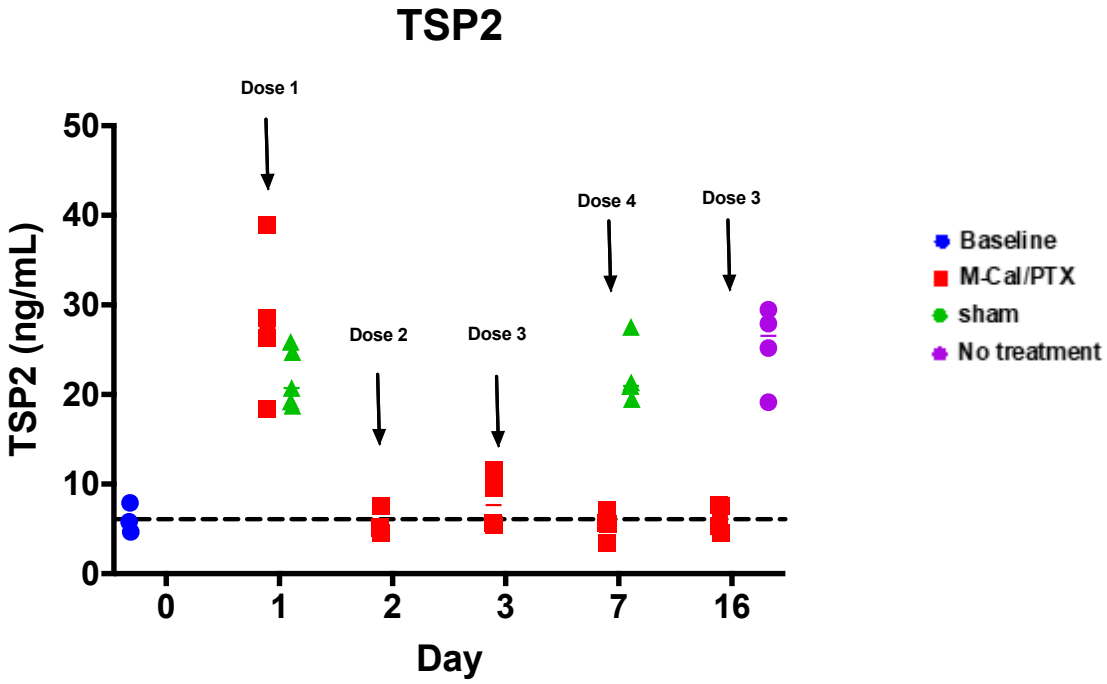

C.

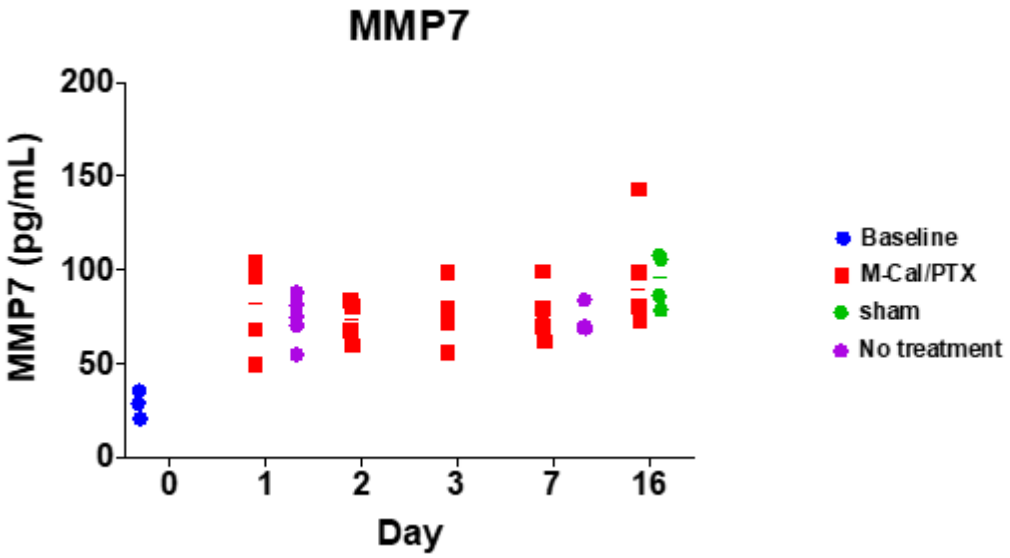

Figure 35. Treatment effects on circulating stroma markers TIMP1 (A), TSP2 (B) and MMP7 (C). Data shows individual measurements and the mean.

4.3.7.4 Effects of treatment on alpha-smooth muscle actin (α-SMA)

Alpha-smooth muscle is reliable marker molecular marker for stromal activity. The impact of M-Cal/PTX on this marker was evaluated. Compared with the sham group, M-Cal/PTX significantly decreased the expression of α-SMA in the tumor (**Figure 36A and B**). Mono-formulated Cal (M-Cal), a physical mixture of mono-formulated Cal in combination with mono-formulated PTX (M-Cal + M-PTX), and with abraxane (M-Cal + ABX) significantly reduced α-SMA expression except a cremophor formulation of Cal and PTX (crem-Cal + PTX) which also reduced α-SMA but was not statistically significant compared with the sham group, presumably because of the variation in response between the subjects.

A

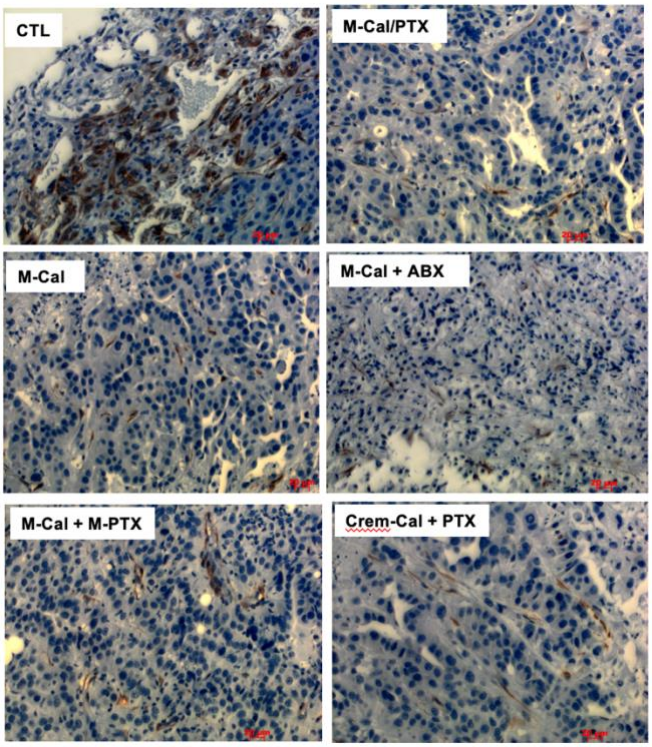

B.

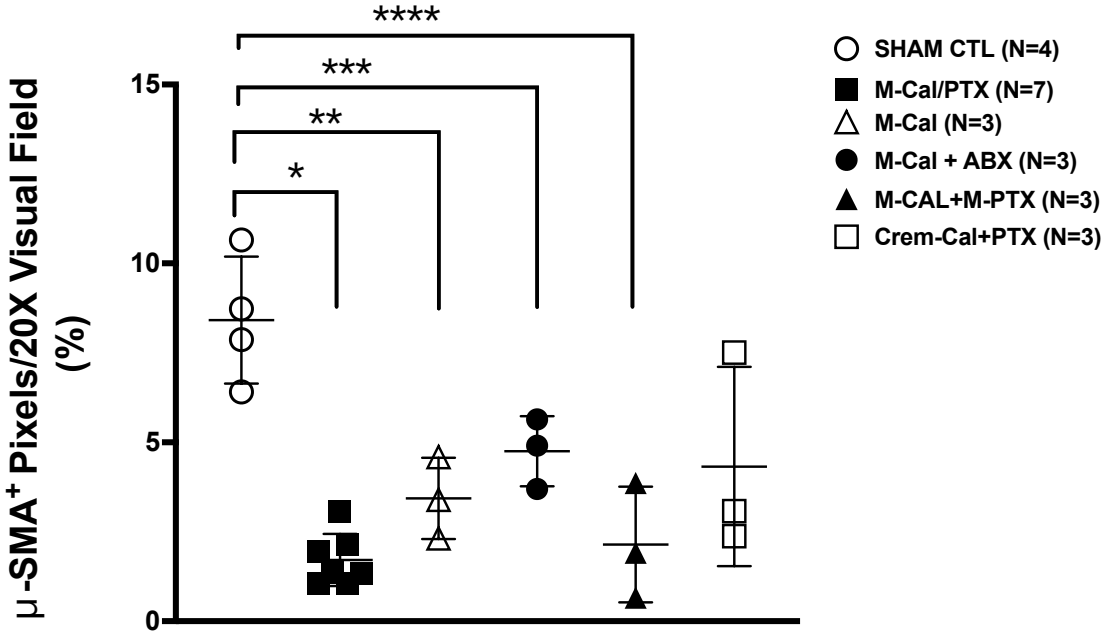

Figure 36. Effects of treatment on tumor α-SMA. Representative stains of tumor tissues are shown in A and the corresponding quantifications from 15-20 sections per tissue are shown in B. *, **, ***, ****Significantly different from sham group at $p < 0.05$

4.3.7.5 Effects of treatment on the cell proliferation marker Ki67 inhibition

Again, M-Cal/PTX significantly inhibited cell proliferation in the tumor compared with the sham group. This inhibition was more robust compared with the other control groups in which a response was observed that is M-Cal + M-PTX and M-Cal + ABX groups (**Figure 37A and B)**. The M-Cal and Crem-Cal+PTX groups did not inhibit the expression levels of Ki67.

A.

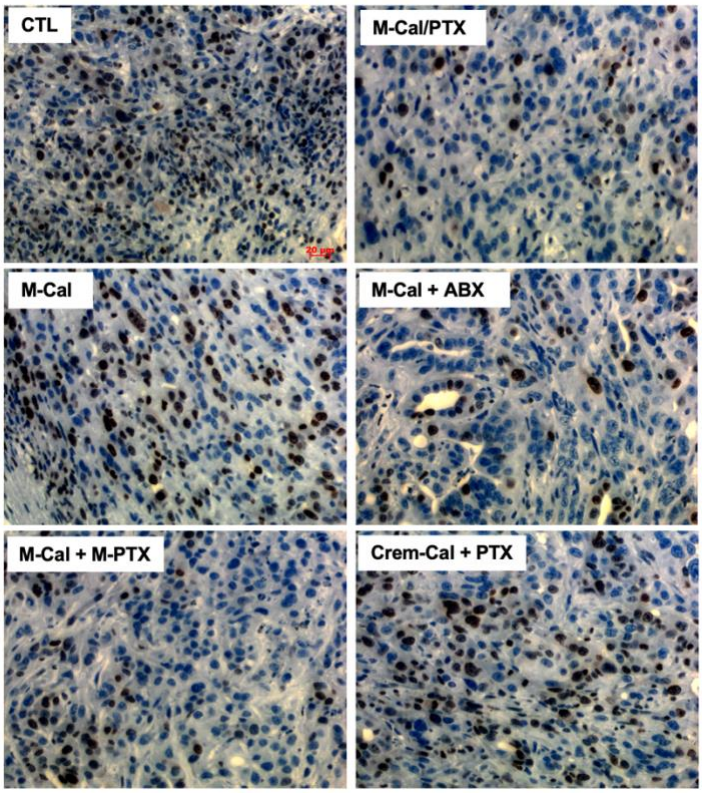
CTL
M-Cal/PTX
M-Cal
M-Cal + ABX
M-Cal + M-PTX
Crem-Cal + PTX

B.

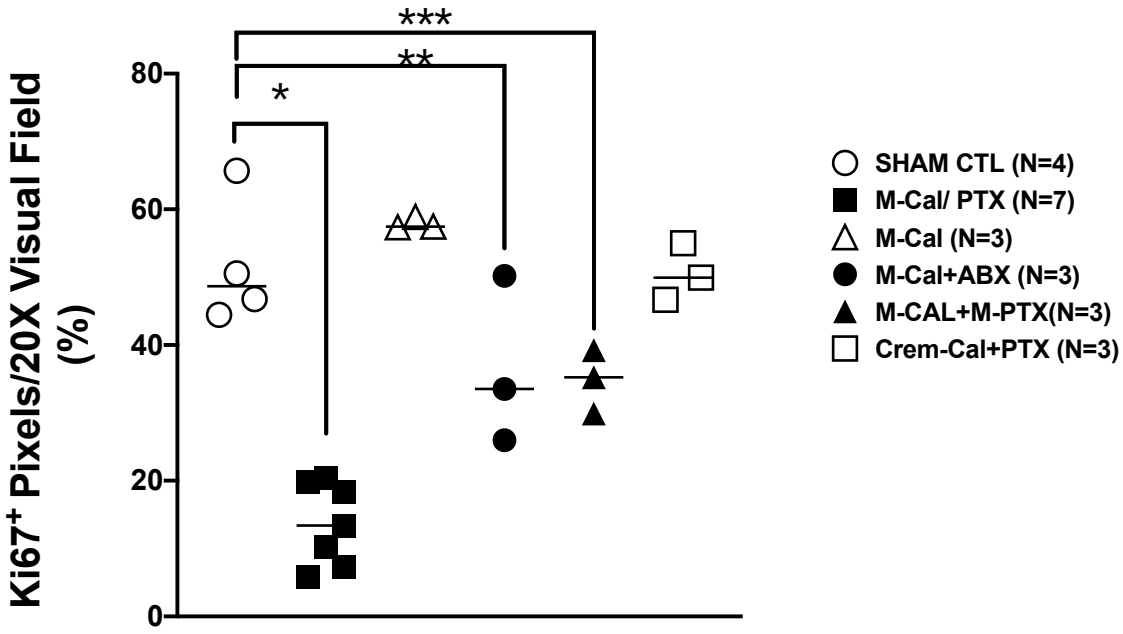
***
**
*
80
60
40
20
0
Ki67+ Pixels/20X Visual Field (%)
SHAM CTL (N=4)
M-Cal/ PTX (N=7)
M-Cal (N=3)
M-Cal+ABX (N=3)
M-CAL+M-PTX(N=3)
Crem-Cal+PTX (N=3)

Figure 37. Effects of treatment on tumor Ki67. Representative stains of tumor tissues are shown in A and the corresponding quantifications from 15-20 sections per tissue are shown in B. *, **, ***, Significantly different from sham group at $p < 0.05$

4.3.7.6 Effects of treatment on the matrix protein collagen

Compared with the sham group, M-Cal/PTX, M-Cal, M-Cal + M-PTX and M-Cal + ABX reduced the collagen expression levels in the tumor. All were significant except the M-Cal + ABX group when compared with the sham group (**Figure 38A and B)**.

A.

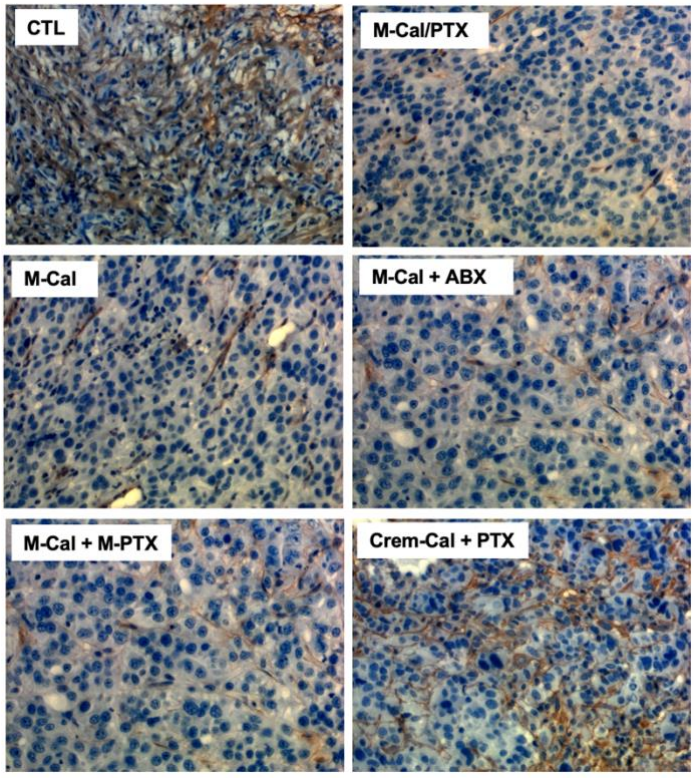

B.

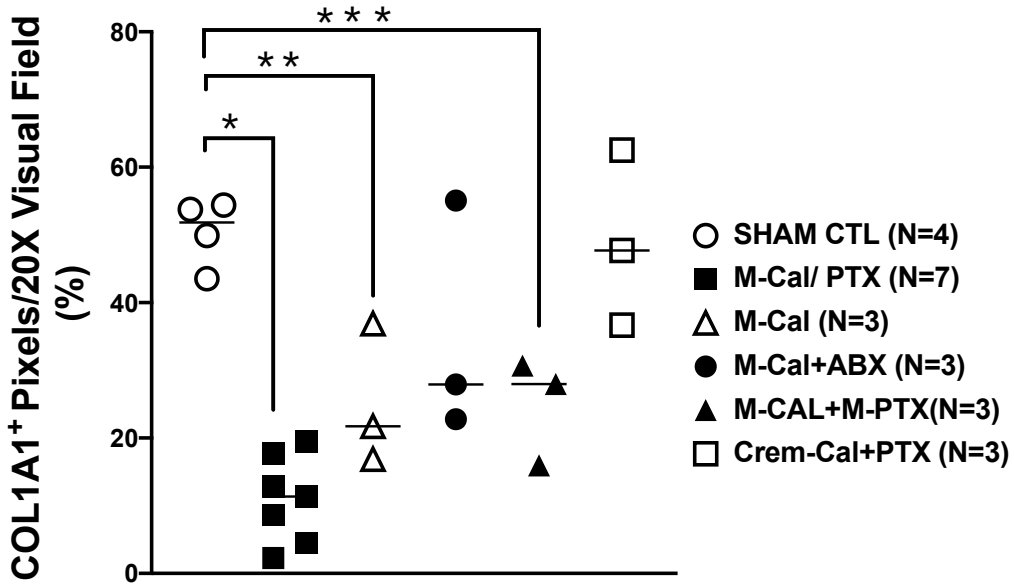

Figure 38. Effects of treatment on COL1A1. Representative stains of tumor tissues are shown in A and the corresponding quantifications from 15-20 sections per tissue are shown in B. *, **, ***, Significantly different from sham group at $p < 0.05$

4.3.7.7 Effects of treatment on body weight

Body weight changes in mice after treatment with M-Cal/PTX, M-Cal, M-Cal + M-PTX and M-Cal + ABX were similar to the sham group. However, significant body weight changes were observed in mice treated with Crem-Cal + PTX compared with the sham group (**Figure 39)**. For this group the body weight decreased from baseline value after dose administration and rebound with cessation. After the 10th dose the body weights of mice in this group decreased by as much as 13%.

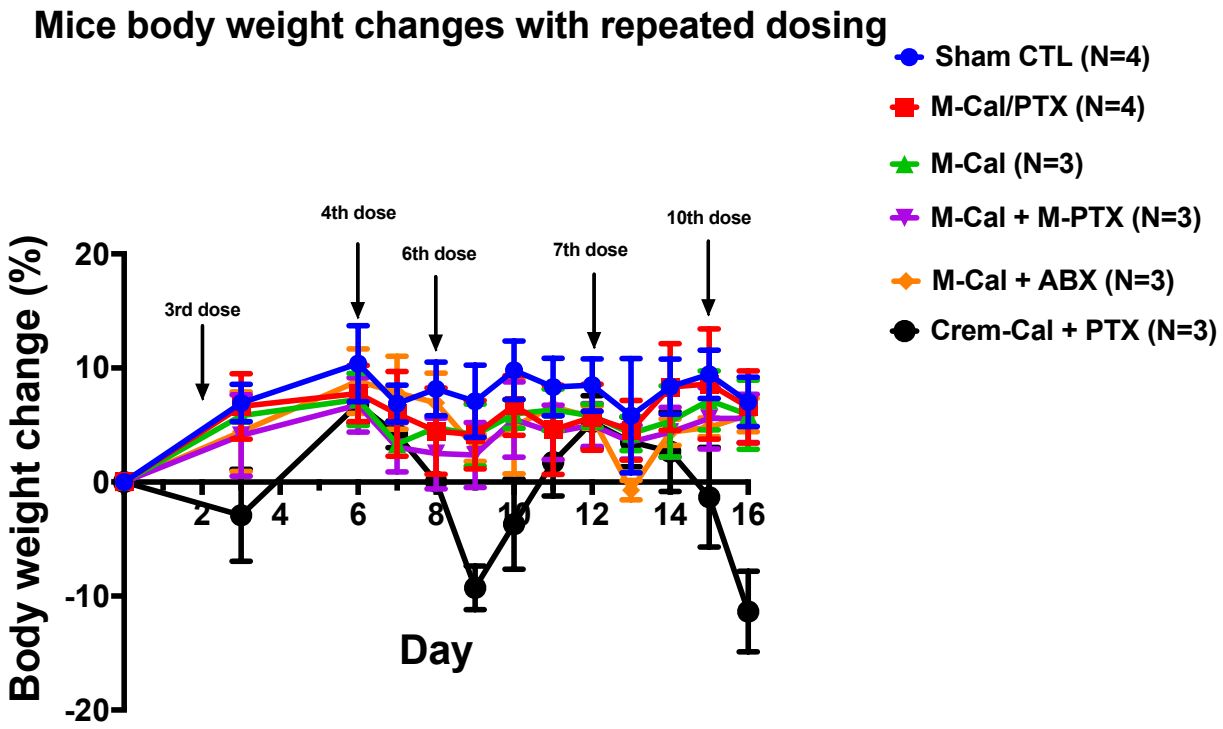

Figure 39. Body weight change with treatment. Plots show the mean weights and standard deviations

4.3.7.8 Effects of treatment on markers of organ health

Serum concentrations of albumin, alkaline phosphatase (ALP), alanine transferase (ALT), aspartate aminotransferase (AST), blood urea nitrogen (BUN), globulin and total protein were measured to assess liver and kidney functions after treatment (**Figure 40**). The range and median of observations are shown in this figure and statistical analyses were not performed because in most cases the data was from two animals.

Comparison of baseline albumin levels to day 3 and 16 levels post treatment showed there was overlap between the median levels at all time points for mice (compared with baseline) that received either the micelle or cremophor formulated regimen (**Figure 40A)**. While there was overlap with baseline levels for ALP for animals that received M-Cal/PTX 3 days post dose, the same was not observed for those in the cremophor formulation group (**Figure 40B).** On day 16 post treatment, ALP levels appeared lower when compared with baseline in both groups. For ALT and AST, there was overlap in the medians at all time points dose when compared with baseline (**Figures 40C and D**)**.** Blood Urea Nitrogen (BUN) levels at 3 days post treatment were higher than at baseline (**Figure 40E).** While the levels in the cremophor formulation group on day 16 overlapped with baseline, those in the M-Cal/PTX group remained high. Median globulin levels at day 3 post dose were similar to baseline levels but higher on day 16 post dose compared to the levels at baseline for both groups (**Figure 40F)**. Similar to Globulin, total protein levels were similar for both groups when compared to baseline on day 3 post dose, but higher on day 16 (**Figure 40G)**

A

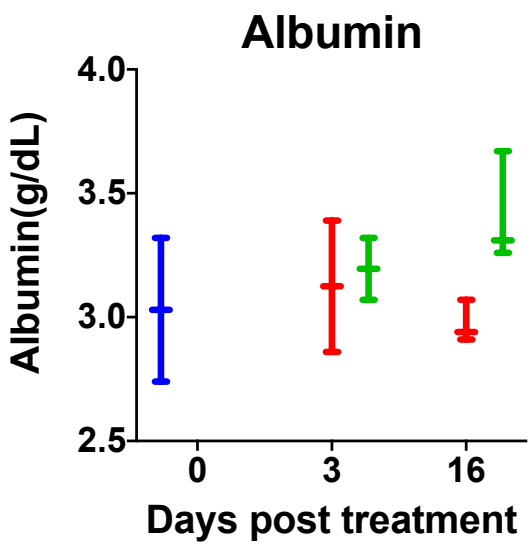
Albumin
Albumin(g/dL)
4.0
3.5
3.0
2.5
0
3
16
Days post treatment

B

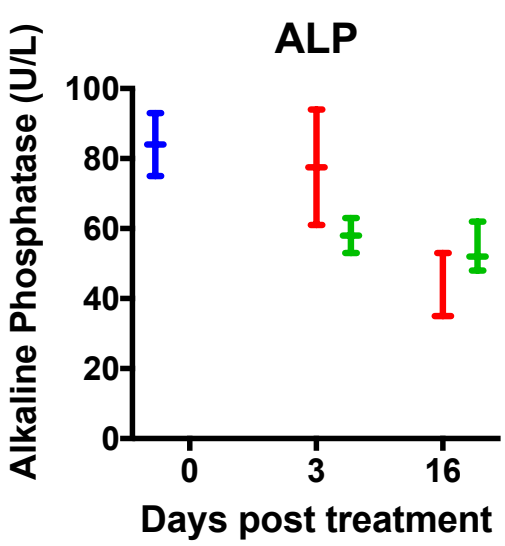
ALP
Alkaline Phosphatase (U/L)
100
80
60
40
20
0
0
3
16
Days post treatment

C

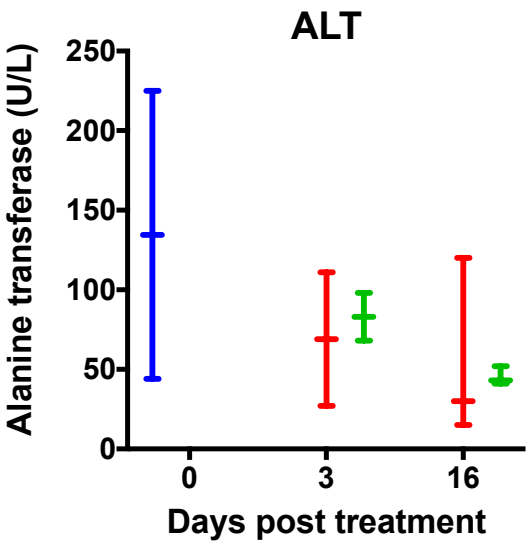
ALT
Alanine transferase (U/L)
250
200
150
100
50
0
0
3
16
Days post treatment

D

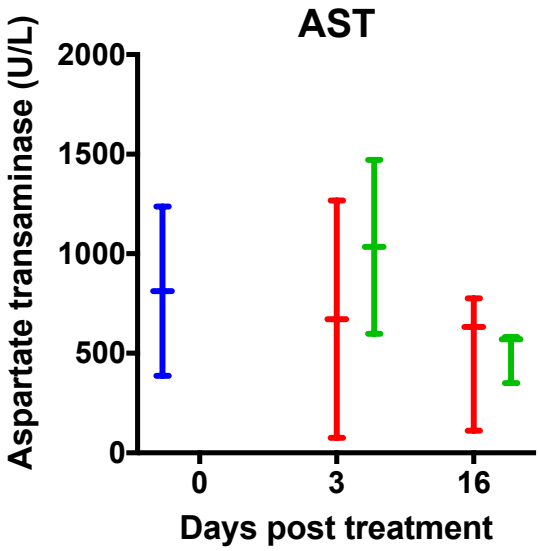
AST
Aspartate transaminase (U/L)
2000
1500
1000
500
0
0
3
16
Days post treatment

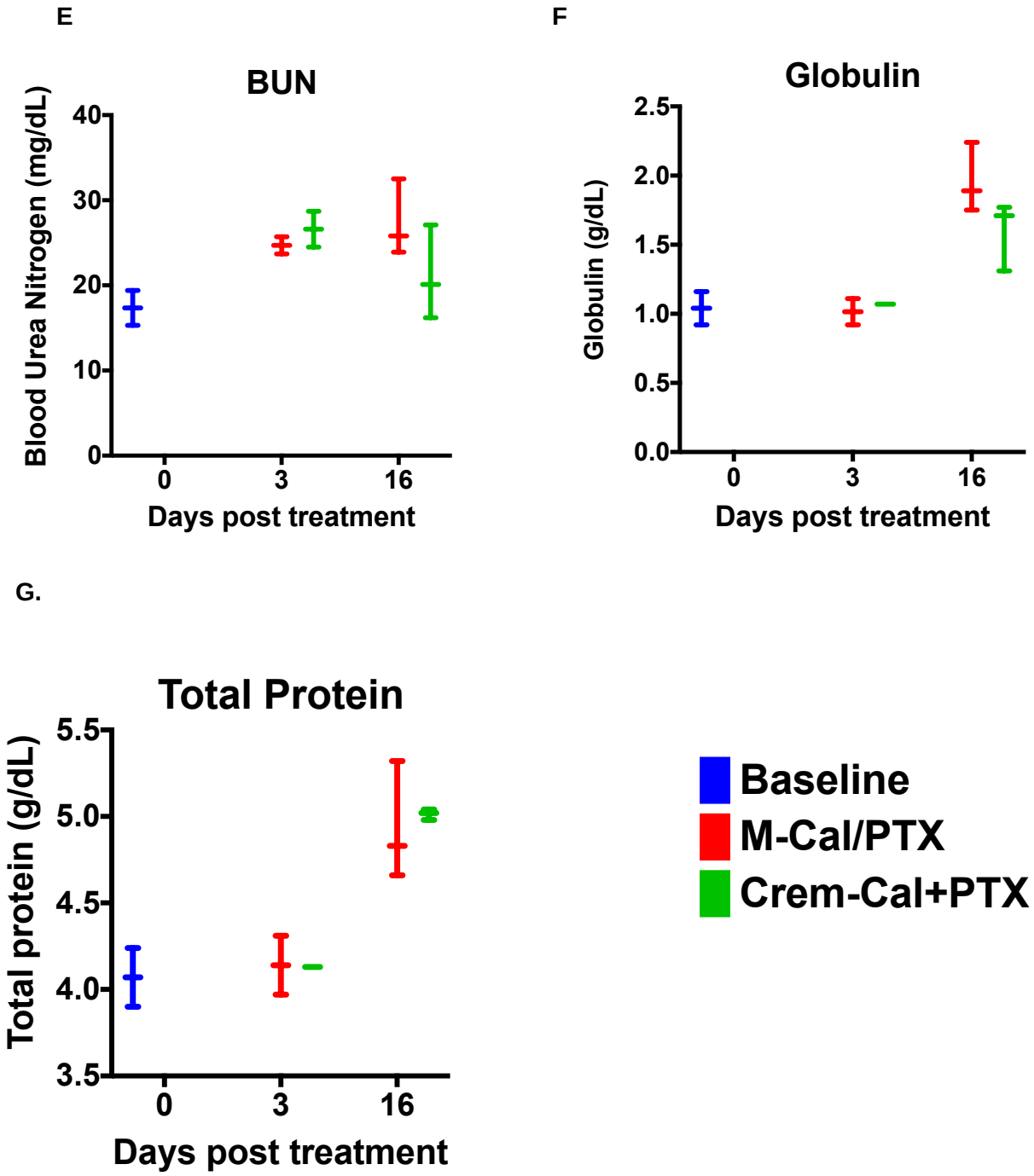

Figure 40. Treatment effect on organ specific toxicity including Albumin (A), ALP (B), ALT(C), ASP (D), BUN (E), Globulin (F) and total protein (G). Plots show the range of observations as well as the median.

4.3.7.9 Reverse phase protein array (RPPA)

Tumor samples were prepared and probed using the reverse phase protein array. RPPA is a high throughput method that allows probing multiple molecular targets in the same sample (Boellner and Becker, 2015). This technique could be used to target specific proteins or explore proteins that change with treatment and serve as the basis for identification of targets that could be used for diagnosis or monitoring response to treatment for a particular disease. A number of targets were probed, and comparisons made between the sham and M-Cal/PTX group, but no clear pattern could be observed. The heat maps are included in the supplementary material.

4.3.7.10 Survival studies

A survival study was conducted to estimate the treatment benefit in terms of overall survival. Animals that were administered M-Cal/PTX lived longest, with a median survival of 54 days followed by those that received mono-formulated Cal and abraxane (M-Cal + ABX). The M-Cal + ABX group had a median survival of 40 days. Animals that received only mono-formulated Cal (M-Cal) had a slight increase in the median survival days (29 days). Of all the groups, those that received sham had the lowest median survival of 24 days.

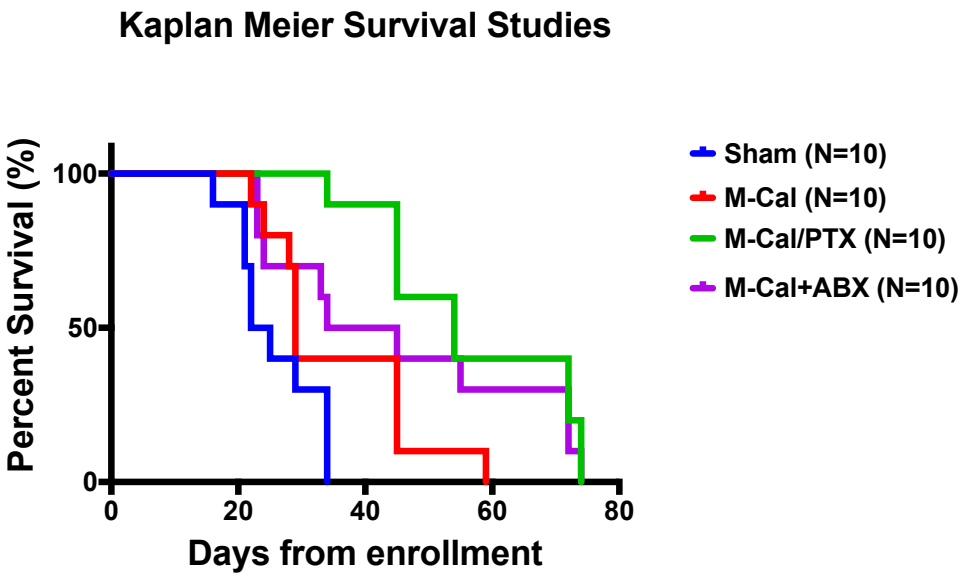

Treatment Group (Days)	Median Survival
Sham	24
M-Cal	29
M-Cal/PTX	54
M-Cal + ABX	40

Figure 41. Kaplan-Meier survival curves for mice survival after various treatments

4.3.8 A tumor growth inhibition model to describe tumor progression

Although overall survival (OS) remains the gold standard for assessing treatment effects in oncology, tumor progression serves as an early marker for assessing treatment benefit. A tumor growth inhibition model was developed to compare tumor metrics between the sham and M-Cal/PTX.

The tumor growth inhibition model is based on the work of Claret et. al. (Claret et al., 2016)

Tumor progression is modelled as

$$y_i\left(t_{ij}\right) = y_{0,i} \cdot \exp\left[KL_i\ t_{ij} - \frac{KD_i}{l_i} \cdot \left(1-e^{-\lambda_i \cdot t_{ij}}\right)\right] + e_{ij}$$

Where

y is the tumor size

KL is the tumor growth rate

y_0 is the tumor size at baseline

KD is the tumor growth inhibition rate

j is the observation of the individual i

λ is tumor resistance to treatment

From the tumor model, secondary parameters were derived including

$$ETS_i = \frac{y_{week\ x,\ l}}{y_{0,i}} \quad ETS = \text{early tumor shrinkage}$$

$$TTG_i = \frac{log(KD_i\lambda_i)-log(KL_i)}{\lambda_i}$$

TTG is the time to tumor growth

Baseline tumor size and treatment used as covariates power model with normalized covariate

4.3.8.1 Base model and covariate assessment

A base model was first constructed. Afterwards, baseline tumor size and treatment assignment (active or sham) were explored as covariates to further improve the model fits.

The relationship between the longitudinal covariate (baseline tumor size) and categorical (active treatment, or sham) with the inter-subject variation of the three estimated parameters was explored in order to eliminate any correlation that would confound the covariate relationship with the parameter (**Figure 42**). No relationship was discernable between the inter-subject variation and baseline tumor size (**Figures 42 A, B, C**) and treatment assignment (**Figures 42 D, E, F).**

The baseline tumor size and treatment assignment were therefore added as covariates on the parameters (Final model code in appendix)

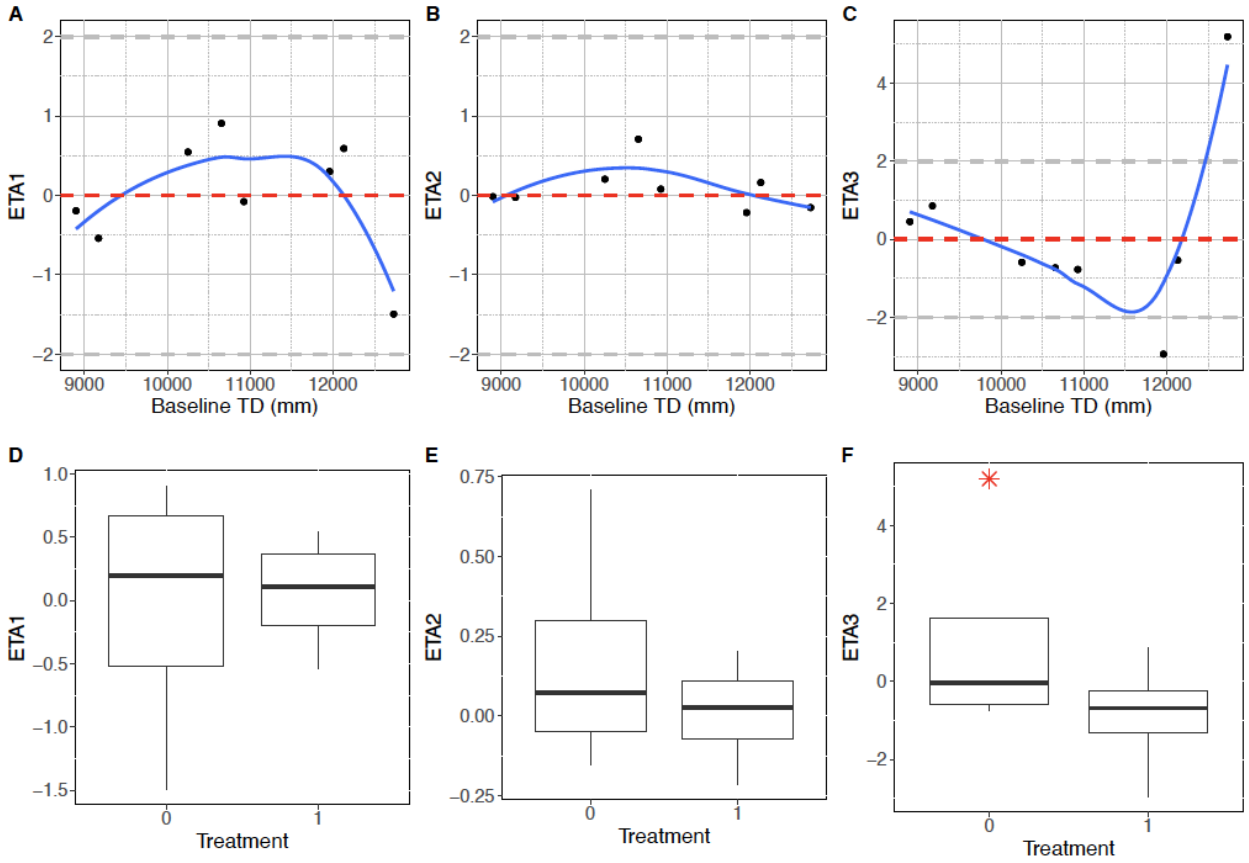

Figure 42. Relationship between baseline tumor size and inter-subject variation of tumor growth rate (A), tumor growth inhibition rate (B), resistance (C) as well as treatment assignment with tumor growth rate (D), tumor growth inhibition rate (E), resistance (F)

4.3.8.2 Tumor growth model fits and diagnostic plots

The final model yielded decent fits as shown by the OBS vs PRED as well as OBS vs IPRED plots (**Figure 43**).

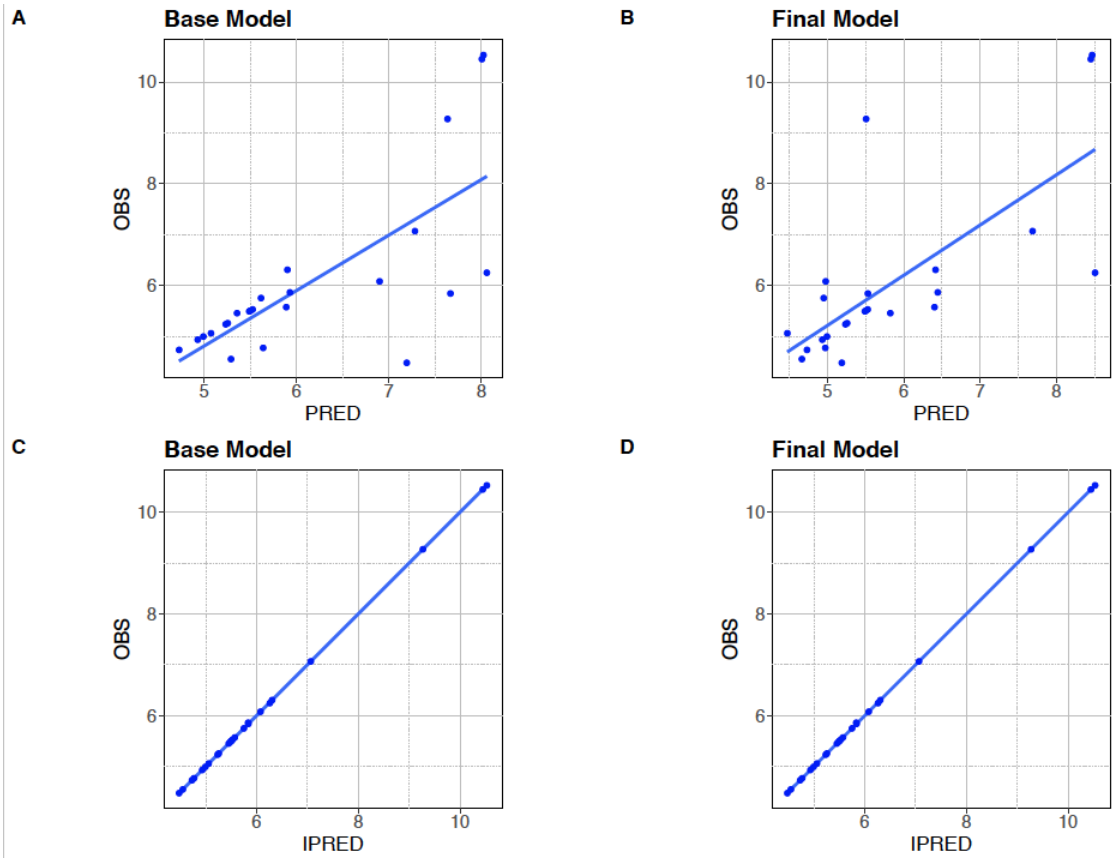

Figure 43. Goodness of fit plots for PDAC tumor growth model. Observed vs Population Predicted (A) and Individual predicted (B) for base model, observed vs population predicted (C) and individual predicted (D) for final model with covariates.

The residual plots showed no significant structural flaws in the model with most residuals within the acceptable +/- 2 standard deviation range (**Figure 44**).

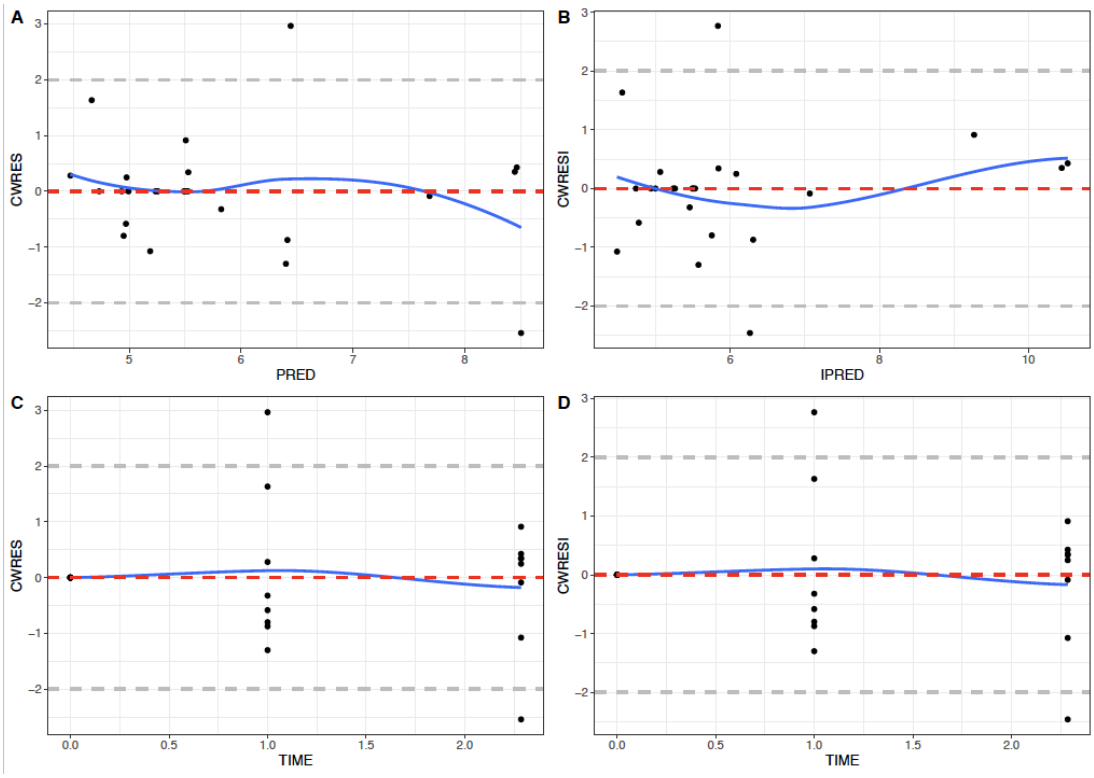

Figure 44. Conditional weighted residual vs population prediction (A), individual conditional weighted residual vs individual prediction (B), conditional weighted residual vs time (C) and individual conditional weighted residual vs time (D).

The time to tumor growth (TTG) and tumor size changes at weeks 1 and 2 were estimated from the model for the sham (0) and M-Cal/PTX (1) groups. The variability in time to tumor growth in the M-Cal/PTX group was higher than in the sham group (**Figure 45A**). The mean time to tumor growth in the M-Cal/PTX group is longer than in the sham group (0.6 weeks vs 0.4 weeks)

The response in M-Cal/PTX group was highly variable with TTG in some animals as long as 2 weeks. Additionally, the model showed the mean tumor size at week 1 and 2 was smaller in the M-Cal/PTX group than in the sham group (**Figure 45B)**.

A

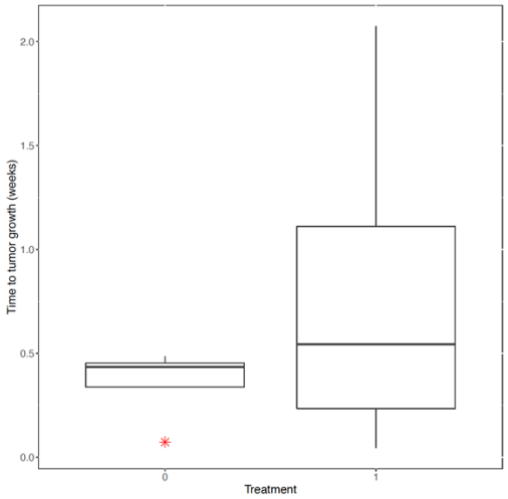

B

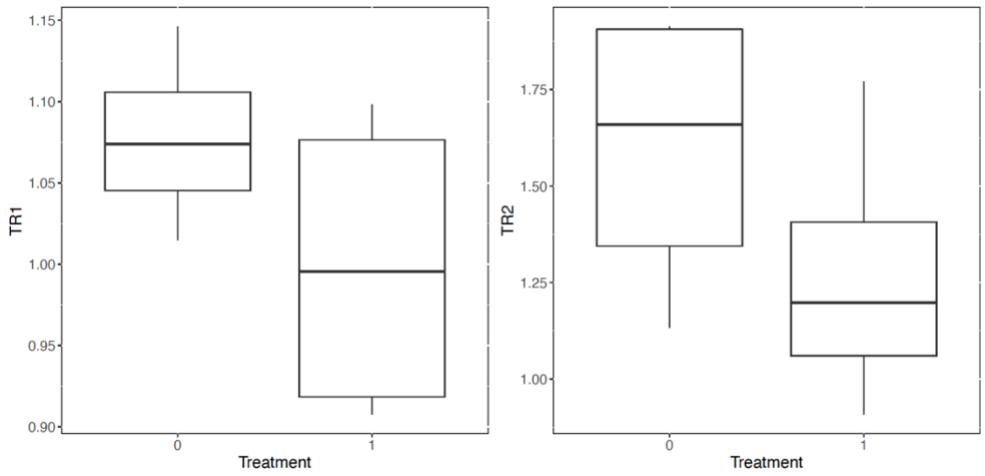

Figure 45. Time to tumor growth (A), tumor size change at week 1 (TR1, B) and 2 (TR2, B) for sham (0) and M-Cal/PTX (1) groups.

The mean tumor progression was simulated based on the model. The simulations showed the tumor growth trajectory in the M-Cal/PTX group is shallower than in the sham group where tumor growth is much steeper (**Figure 46**). The relative tumor growth profiles show M-Cal/PTX slowed tumor growth when compared with sham treatment.

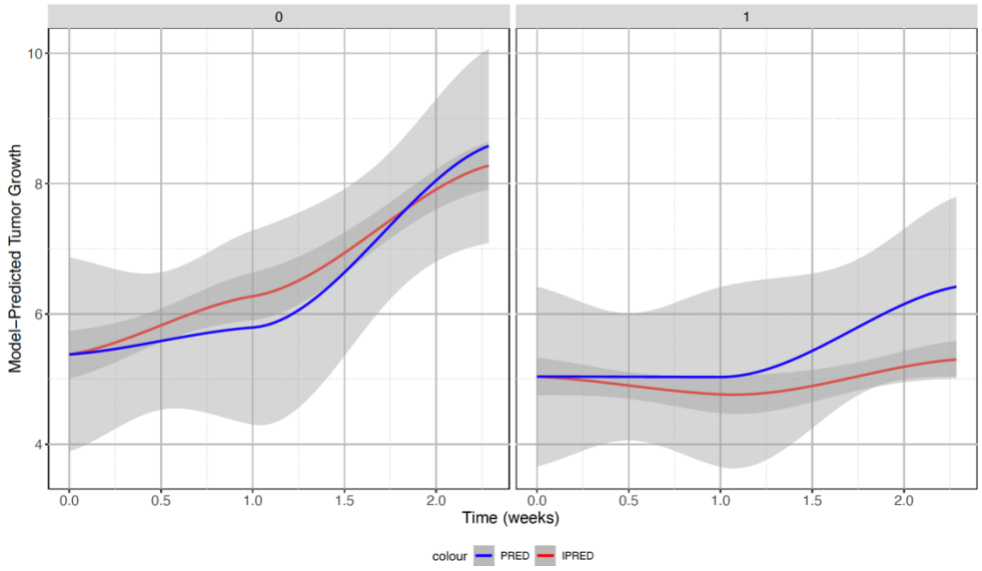

Figure 46. Mean model-predicted tumor progression between sham (0) and M-Cal/PTX (1) groups.

4.3.9 Exposure-response model to describe Cal effects on tumor stroma deactivation

An exposure response model was explored to see if exposure metrics could predict the extent of TIMP1 reduction in circulation. A linear regression model was developed for AUC and TIMP1 levels. No apparent relationship was observed between the two variables (**Figure 47**)

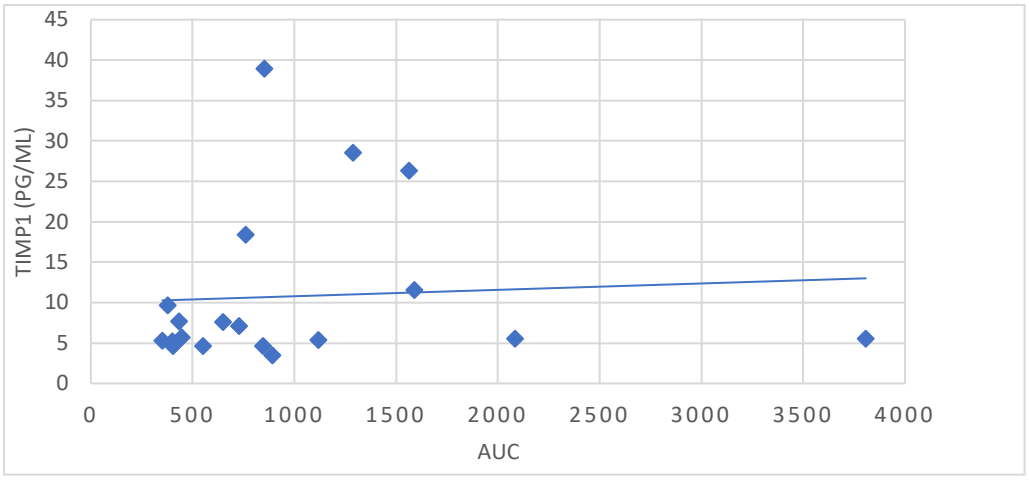

Figure 47. Relation between AUC and circulating TIMP1 levels in mouse blood

Chapter 5. Discussion and Conclusion

5.1. UPLC-MS/MS Assay for simultaneous quantifications of Cal and PTX in biomatrices

An accurate, robust and sensitive assay to measure Cal and PTX concentrations using minimal sample volume was required for successful completion of this study.

An IND-enabling assay was thus developed as well as validated and discussed herein.

Several LC-MS/MS methods for PTX quantification in plasma have been published and discussed (Posocco et al., 2018) with sensitivities ranging from 0.125 – 102.1 ng/mL. In urine, PTX assays with sensitivities between 2.50 -17.1 ng/mL have also been reported (Chang et al., 2004; Hendrikx et al., 2014; Mould et al., 2006). A conspicuous limitation in these assays is the volumes of samples required, ranging from 90 µL to 500 µL. In contrast, assays for Cal quantification are limited. To the best of our knowledge, only one fully-validated LC-MS/MS assay was in literature for quantifying Cal in the skin samples of pig, rat and mouse with sensitivities of 1, 0.5 and 40 ng/mL, respectively (Li et al., 2013). Another LC-MS/MS assay for quantifying Cal in rat plasma with LLOQ of 0.5 ng/mL was incompletely described (Hirabe et al., 2016) and could not measure the plasma concentration of Cal beyond 2 hours post intravenous dose. Although plasma samples are by far the biomatrix of choice in PK studies, attaining enough especially in longitudinal sampling of small animals like mice is often challenging. For the purpose of our studies, an assay was desired to measure Cal and PTX concentrations simultaneously in whole blood using minimal sample volume attainable from the mouse models of PDAC. An assay with additional capabilities to measure Cal and PTX in plasma gave the flexibility to extend the use of this assay in animals/subjects where handling plasma is easier or convenient. The objective of this study was to develop and validate an assay that could simultaneously measure concentrations of Cal and PTX in whole blood and plasma and demonstrate its application in monitoring Cal and PTX simultaneously in a preclinical pharmacokinetic study in rats. In choosing the parent-daughter pairs for analyte quantifications, daughter ions with the highest signal intensities were considered first. Although the 395.4 →133.1 m/z for Cal had the highest signal, this pair produced

chromatograms with a high baseline, making Cal quantifications at low concentrations unreliable. The 395.4 → 105.1 m/z for Cal was therefore chosen to monitor and quantify Cal (**Figure 4A).** For Cal-D4, 399.2 → 283.9 m/z was chosen because this pair was very stable and could be reliably used for Cal normalization (**Figure 4B).**

Another critical element of assay development to ensure maximum sensitivity is achieved is sample preparation. Perhaps the most straight forward approach to achieve decent sample purity is through protein crushing to remove matrix constituents that may impact assay sensitivity and reduce column lifespan. In some situations, this simple extraction procedure may be inadequate. In this study several extraction procedures including protein precipitation were attempted but, the highest analyte recoveries and reduced matrix effects were attained with the liquid-liquid extraction procedure. In choosing the solvents for extraction, careful consideration was given to the physicochemical properties of Cal and PTX (both very hydrophobic), as well as matrix components. An initial solvent mixture of methanol and water allowed efficient extraction of the hydrophobic analytes but also the water-soluble components in the blood. A further purification step was achieved with a mixture of hexane, isopropyl alcohol and dichloromethane in an optimal ratio as described in **section 3.2.1.3**. Initially, several solvents and solvent mixtures were explored including acetonitrile (ACN), ethyl acetate-isopropyl alcohol (1:1 v/v), hexane-dichloromethane (1:1 v/v) and a previously described hexane-dichloromethane-isopropyl alcohol (300:150:15 v/v/v) for calcipotriol extraction (Li et al., 2013). Although the hexane-dichloromethane-isopropyl alcohol combination yielded acceptable recovery, the peak shapes were not optimal, especially at low Cal and PTX concentrations. Additional solvent ratio tuning was explored with different solvent ratios, and we observed dichloromethane content of between 15-25% by volume and isopropyl alcohol content of 5-15% yielded desirable analyte recoveries, and optimal peak shapes. The final solvent mixture was therefore hexane-dichloromethane-isopropyl alcohol (150:15:5 v/v/v). This solvent mixture was critical to separating the hydrophobic agents from the water-soluble components of the blood to attain a clean sample.

5.2 Conclusion of UPLC-MS/MS assay

A validated UPLC MS/MS assay for simultaneous quantifications of Cal and PTX was developed. The assay required only 20 µL of whole blood or plasma with a short run time of 3.5 min. The sample preparation procedures resulted in clean samples for reliable measurements and extended column life. The assay satisfied validation requirements of the USA FDA, including accuracy, precision, acceptable recoveries and negligible matrix interference. The assay also confirmed the integrity of Cal and PTX under conditions of freeze/thawing, processing and storage and was successfully applied in multiple PK studies.

5.3 A design of experiment approach facilitates the development of micelles with pre-specified characteristics

Delivery of drugs to solid tumors is often a difficult endeavor. Most often, only a small fraction of the administered dose reaches its intended target, thereby necessitating dose increase which unsurprisingly leads to toxicity (Sriraman et al., 2014). From the site of administration to the target site, the drugs face multiple bio-barriers. Often, chemotherapeutic agents are administered IV, which allows complete distribution. Nonetheless, once in systemic circulation the drugs must overcome a number of barriers to get to the site of action. Some of these barriers include opsonization by blood proteins or the mononuclear phagocyte system (MPS) which result in rapid clearance of the drugs (Sriraman et al., 2014). Multifunctional drug delivery systems layered with specific attributes enable drugs to evade some of these clearance mechanisms (Sriraman et al., 2014). A micelle-based nanocarrier was developed to deliver Cal and PTX. Ideal nanocarriers should avoid clearance by MPS and also circulate long enough to ensure accumulation in the tumor, and modifying the carrier properties such as size, shape and charge could impact these characteristics (Patel, 1992; Zein et al., 2020). Using a design of experiment approach (DoE) the micelle size and shape were tuned to improve tumor accumulation of Cal and PTX and also extend the apparent biological half-lives of both drugs, especially Cal. DoE is a mathematical modeling paradigm that involves developing relationships between process variables and

response/output. Traditionally, at least in the area of drug development, this approach has been confined to optimizing process parameters (Gupta et al., 2015; Hejri et al., 2013; Zhang et al., 2013). Here, we extended its application to the selection of monomer units and degree of crosslinking in the synthesis of a polymeric drug delivery platform. Within the DoE domain, we used the central composite design (CCD) to establish a design space with a response surface, using fractional factorial designs with defined center and axial points to estimate the surface curvature. The formulation variable-dependent drug release characteristics were best described by a linear model at pH 6 and, and a quadratic model for the release characteristics at pH 7.4. A log-transformed linear model best described the impacts of formulation variables on the micelle size, as summarized in **Table 12.** In the optimized micelles the extent of drug release decreased with increasing amount of PEGMA-500 at pH 6 (**Figure 10A**). However, the opposite trend was observed at pH 7.4 (**Figure 11A).** Also**,** micelle size decreased with higher PEGMA-500 amount (**Figure 12A).** The decrease of nanoparticle size with increasing PEGMA-500, a capping agent, was anticipated, as it has long been recognized and discussed (Arulmozhi and Mythili, 2013). PEGMA-500, a long chain polymer with terminal hydroxy groups caps polymer growth by shielding and stabilizing the nanoparticle. As more PEGMA-500 is added, a greater amount of OEG groups are present to cap the end of particles, effectively reducing average size (Arulmozhi and Mythili, 2013). Since the first report of PEGylation for drug delivery (Abuchowski et al., 1977), this strategy has become a mainstay in drug formulation due to the unique stealth properties, resisting interaction with components of a biological matrix, usually blood (Suk et al., 2016). It is therefore no surprise that as the concentration of PEGMA-500 increases, the micelle stabilization increases, and the cumulative PTX release decreases. This mechanism of extending circulation times of drugs underlines the reason why PEGylation is widely used to formulate drugs when longer circulation is desired (Arturson et al., 1983; Tan et al., 1993).

Unlike PEGMA-500, as CPL increased, the cumulative release of PTX over 72 hr increased. The micelle size decreased with increasing CPL, with a negative correlation. CPL has widespread

applications in drug delivery for its biocompatibility, biodegradability and being generally recognized as safe (Zelenková et al., 2014). Additionally, CPL undergoes slow degradation in the body (Karuppuswamy et al., 2015; Seremeta et al., 2013; Woodruff and Hutmacher, 2010).

These properties make CPL suitable for drug delivery. It is expected to slow down drug release with increasing CPL amount, due to increased hydrophobic interaction between the polymeric matrix and the drug payloads. However, our observation was the opposite. We speculated that the interaction between CPL and other polymers might be the reason. CPL has excellent compatibility with other polymers in the formulation, including PEG, and therefore it is plausible the characteristics of this block of copolymer may change as it interacts with other ingredients. The compatibility of CPL with PEG makes it desirable when it is intended to control properties like degradation kinetics and hydrophilicity (Bilensoy et al., 2009; Payyappilly et al., 2015). The interaction between PEGMA-500 and CPL was indeed observed in our model to affect the PTX drug release at pH 7.4. This interaction was captured by the curvature for the surface response map from our CCD approach (**Figure 11A**), and the mathematical model suggested the impact of the interaction was dominated by PEGMA-500. Even though PEGMA-500 confers stealth properties on nanoparticles and increases circulation time, its hydrophilicity reduces cellular uptake (Ruiz et al., 2013; Wang and Thanou, 2010). However, nanoparticle size and shape also strongly impact cellular uptake (Albanese et al., 2012; Zhang et al., 2015). We desired micelles with a size of 40-100 nm, because this is the optimal size for cellular uptake (Jiang et al., 2008; Lu et al., 2009; Yuan et al., 2010; Zhang et al., 2009). Nanoparticles within such a size range have the appropriate entropic and enthalpic properties that influence adhesion strength between the particles and cellular receptors (Yuan et al., 2010; Zhang et al., 2009)

5.3.1 Summary of formulation optimization using central composite design

Herein, we developed a micellar drug delivery platform to encapsulate and deliver Cal and PTX simultaneously for the treatment of pancreatic cancer. A sustained release delivery system was desired to reduce the systemic exposure of Cal in the circulation, a potential solution to Cal-

associated toxicity. Additionally, micelles with a particle size < 100 nm were desired to improve tumor accumulation. The DOE approach was used to obtain the optimal delivery system with the size range of 40-100 nm which and sustained release of Cal and PTX.

5.4 A potential drug-drug interaction between Cal and PTX is possible

When combining drugs, especially small molecules drugs, the potential for drug-drug interaction between the drugs must be evaluated. Drug-drug interactions (DDIs) between drugs have the potential to reduce the efficacy of one or both drugs and also increase the incidence of adverse events due to excessive drug exposure. In fact, one of the major reasons for drug withdrawal from the market is DDI (Huang et al., 2008). With most cancer patients on multiple therapies, evaluating DDI potential in polypharmacy could not be overstated. PTX is a well-studied drug and its interactions with other agents are known, but its interaction with Cal has not been studied. The DDI potential between these two agents was therefore evaluated. The data suggested possible DDI liability between Cal and PTX. In the presence of PTX, Cal clearance was significantly higher, correlating with low exposure (**Table 10**). This observation has the potential to render Cal efficacy sub-optimal. The opposite was observed for PTX-in the presence of Cal, PTX clearance was significantly lower (**Table 10**). To the best of our knowledge this observation has never been reported. Considering Cal and PTX have different metabolic pathways, the involvement of metabolic enzymes in this potential DDI is unlikely. In a recent report, Tan et. al showed that calcipotriol had an inhibitory effect on the transport functions of MRP-1, P-gp and BCRP (Tan et al., 2018). Interestingly, PTX is a substrate of these efflux transporters. While the interaction of Cal and PTX at the transporter level is plausible, the contribution of each transporter is unclear. MRP1, located on the basolateral side effluxes drugs into the extracellular matrix while P-gp and BCRP efflux drugs from hepatocytes into the bile canaliculus for biliary excretion. Depending on which transporter has the highest affinity for Cal, the inhibitory effect of Cal could either lead to increased or decreased exposure for PTX. The results suggest Cal inhibition of BCRP and Pg-p might be stronger than MRP1 leading to increased exposure of PTX in the combination group.

5.4.1 Conclusion of Cal and PTX DDI study

The data shows that a potential DDI between Cal and PTX is likely because these agents share some transporters. However, the exact nature of this interaction and the contribution of each transporter is unknown and would warrant further investigation

5.5 Micelle formulated Cal and PTX (M-Cal/PTX) reduced Cal exposure and extended the half-lives

Among the vitamin D analogs, Cal is considered the least-hypercalcemia inducing. Nonetheless, significant toxicity has been associated with Cal systemic therapy in mice (Sherman et al., 2014). We postulated that Cal toxicity is possibly due to activating the vitamin D receptor in unwanted areas. Cal is an agonist of the vitamin D receptor (VDR), a ubiquitously expressed receptor found in a variety of tissues and controls the activity of several genes. Following activation, the VDR triggers a cascade of reactions that result in modifications in transcriptional output of several genes (Pike and Meyer, 2012).

Comparison of Cal exposure metrics in the formulated and unformulated groups demonstrated the benefits of the micellar formulation. Not only was the exposure (AUC_{last}/dose and AUC_{inf}/dose) halved in mice that received the formulated drugs compared to those that received the unformulated regimen, but the terminal half-life was also increased by more than 3-folds in the M-Cal/PTX group (**Table 18**). Earlier studies reported a half-life of between 4- 12 min for Cal in rats (Binderup et al., 2005; Kissmeyer and Binderup, 1991). However, our studies estimated unformulated Cal to have a half-life of 54 min (**Table 18)**. While the difference in animal species that were used in these studies might account for some of the difference, the apparent discrepancy is largely due to the inferior analytical methods that were used in the reported studies. Indeed, Kissmeyer and Binderup in the paper stated they were only able to measure the distribution phase of Cal, but not the emination phase. The assay used in our studies was vastly superior and was thus able to measure Cal in its terminal elimination phase. The difference

between PTX kinetics in the formulated and unformulated mice were less pronounced. A marginal increase in the half-life of PTX in the formulated compared to the unformulated group was estimated (**Table 18).** It is apparently clear that the micelle formulation resulted in an increased CL of both Cal and PTX. This is expected for nanoparticle-based formulations. It is widely believed that nanoparticle formulations which the body recognizes as foreign objects are adsorbed on the surface of circulating proteins. These proteins are essentially a tag on the nanoparticles marking them for opsonization which leads to aggregation and rapid CL from the blood stream (Moghimi et al., 2001; Owens and Peppas, 2006; Romberg et al., 2008; Vittaz et al., 1996). Despite the well-characterized unfavorable interaction between nanoparticles and host-cells, an extended half-life was achieved with this micellar platform. This was largely due to the surface characteristics of the micelles-the inert surface together with the crosslinking technology used likely ensured reduced interaction between the micelles and opsonin. Additionally, the crosslinking agents used effectively "trapped" the Cal and PTX within the micelles core to enable release over a longer period. Depending on context the downside to this technology is the overall reduced drug exposure. While this is advantageous for a drug like Cal whose exposure has to be controlled to minimize toxicity, the same couldn't be said for PTX. Ideally, maximum exposure of PTX would be pursued but within the context of co-delivering both drugs as was done in the study, a balance was required. As would be shown later, we were able to deliver enough PTX to effect tumor killing while keeping Cal levels low to minimize toxicity.

5.5.1 Conclusion of Cal and PTX PK in formulated and unformulated groups.

The sustained drug delivery platform developed to study Cal and PTX in pancreatic cancer performed as expected. Although CL was high, the half-lives of both Cal and PTX were extended. This extension of Cal half-life would make a once-a-day dosing possible. Also, Cal exposure was significantly reduced, and this is expected to lead to reduced safety events associated with Cal treatment.

5.6 Cal PK is substantially different in healthy vs diseased mice while PTX is essentially the same

Until now the PK of Cal after intravenous or dermal administration had only been characterized in healthy animals. However, it is known that sometimes drugs demonstrate differential PK when administered in healthy vs diseased subjects. Our studies demonstrated significant PK differences for Cal in healthy female C57BL/6 mice vs the diseased strain-that is those with orthotopically implanted $Kras^{G12D}$ cells in the pancreas. The oncogenic Kras mutation is present in about 90% of PDAC cases (Waters and Der, 2018), hence this disease model is widely used in preclinical PDAC studies. In this diseased model, we discovered that Cal half-life is significantly reduced in diseased animals compared to the healthy ones (**Table 19**). Unsurprisingly, an increased CL was also observed in the same group. This led to reduced drug exposure of Cal in diseased mice when compared with the heathy ones. Remarkably, the PK difference for PTX in diseased vs healthy animals was less (**Table 19**). Interestingly for PTX, while the dose normalized Cmax was higher in the diseased group compared with the healthy ones, the overall drug exposure as estimated by AUC_{last} and AUC_{inf} were lower in the diseased group. A population PK model identified disease status as a significant covariate for Cal PK. The model showed that Cal CL is at least doubled when administered to diseased mice (**Table 22**), a result consistent with the overall trend that was observed from the non-compartmental analyses. Changes in drug absorption due to gastrointestinal alterations, changes in plasma protein binding and thus free fraction of the drug and altered hepatic and renal CL due to disease are some of the disease-induced changes that impact drug PK that have been discussed. While no additional studies were done to elucidate what physiological process accounts for the differences in Cal PK between healthy and diseased animals, metabolism of vitamin D_3 could provide some insight

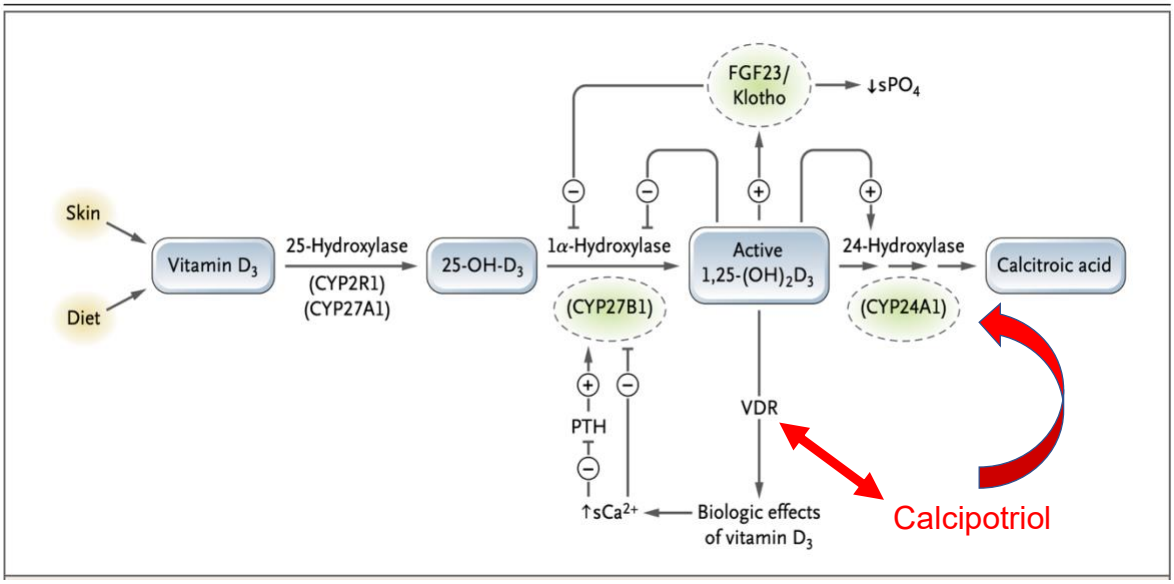

Figure 48: Metabolism of vitamin D_3 . Modified from (Schlingmann et al., 2011)

Once absorbed or ingested through dietary sources, Vitamin D is activated through 25-hydroxylation in the liver to form 25-hydroxyvitamin D_3. The 25-hydroxy moiety of vitamin D_3 is further hydroxylated to form the active 1,25-dihydroxyvitamin D_3 which exerts the biological effects after binding to the vitamin D receptor. The circulating levels of active vitamin D_3 is under tight control through a variety of mechanisms including calcium sensing and FGF23/Klotho. Also, active vitamin D_3 can exert an inhibitory effect on its production by inhibiting the 1α – hydroxylase which activates inactive vitamin D_3 to the active form, or by activating the expression of CYP24A1 which catalyzes the 24-hydroxylkation of active vitamin D to calcitroic acid, its metabolite. Sherman et al., reported increased expression of VDR in human pancreatic stellate cells in patients with cancer vs those without (Sherman et al., 2014). Considering the high affinity of Cal for VDR, it is conceivable that binding of Cal to the overexpressed VDR in diseased group "tricked" the animal's active vitamin D control mechanism to believe there was too much vitamin D, thereby resulting in increased metabolism of active vitamin D by CYP24A1, for which Cal is also a substrate. This potentially could explain why Cal elimination is higher in the diseased group vs healthy ones.

5.6.1 Summary of Cal and PTX in healthy vs diseased mice

We revealed for the first time that differential PK exists for Cal in healthy vs diseased animals, and less so for PTX. Cal elimination is exacerbated in diseased animals when compared to the healthy ones. Although the reasons for this difference is unknown, it is possible that changes in VDR expression in heathy vs diseased mice might be an underlying factor.

5.7 Cal to MC1046 conversion accounts for about a quarter of total Cal clearance

Till date, the metabolic profile of Cal had only been evaluated in *in vitro* settings. Considering the potential toxicity associated with Cal therapy, a full understanding of its disposition, as well as the enzymes and organs mediating its elimination is warranted. Like most drugs, hepatic metabolism of vitamin D analogs have been reported (Jones et al., 2006). Two hepatic CYP-enzymes have been reported to potentially mediate Cal metabolism-namely CYP24A1 and possibly CYP27B. The conversion of Cal to MC1046 is mediated by CYP24A1 but the products of CYP27B are unclear. Initial metabolic studies of Cal in hepatoma and keratinocyte cell models suggested modification of Cal at the C-24 position, consistent with what was also observed in a broken cells system (Masudata et al., 1994; Sørensen et al., 1990). Further, in a Chinese hamster lung V79 host cell expressing individual CYP, the host cell showed no metabolism in the absence of CYP24. However, once transfected with CYP24, a full spectrum of Cal metabolites were observed (Jones et al., 2006). Our study added further insights into the metabolic profile of Cal and MC1046. Although MC1046 and MC1080 have been reported as the two major metabolites of Cal (Huovinen et al., 2019; Kissmeyer and Binderup, 1991), the model showed that only about a quarter of Cal (23%) is converted to MC1046 by CYP24A1. This suggests that besides MC1046, other metabolites directly produced from Cal metabolism may be present. Indeed, Huovinen and colleagues (Huovinen et al., 2019) identified at least 5 metabolites of Cal in synovial and mesenchymal stromal cell cultures, but were unsuccessful in measuring these metabolites of Cal in PK studies conducted in sheep. Not only does this study succesfully quantify two of the identified metabolites *iv vivo* for the first time, it also revealed that the metabolites of Cal not

considered major could potentially account for up to 75% of Cal metabolism. In their assesment, Huovinen and colleagues noted that other metabolites were present, but their structures could not be established. Interestingly, they noted that although the metabolic profile of Cal was similar in synovial and mesenchymal stromal cells, CYP24A1 transcripts were only presented in the mesenchymal cells.

Their observation leaves room for the interpretation that another enzyme, other than CYP24A1 might be capable of metabolizing Cal. This enzyme could possibly be CY27B which has also been reported to metabolize Cal. In any case, our results are in alignment with published literature and also shows that a significant portion of Cal is eliminated through mechanisms that have not been fully investigated yet. Unlike Cal, MC1046 appeared to be predominantly metabolized by one enzyme to its major metabolite MC1080. The contribution of another enzyme and/or pathway cannot be ruled out, but this would likely account for a small portion of MC1046 elimination (**Table 20)**. Unsurprisingly, the calculated rate of MC1046 conversion to MC1080 was high, compared with the conversion of Cal to MC1046 (**Table 20).**

5.7.1 Summary of Calcipotriol metabolic profile

Using a modeling approach, we provided further evidence for the metabolic profile of Cal. We showed that while Cal metabolism is mediated by CY24A1, this path only accounts for about 25% of administered Cal. Possibly, CYP24A1 could also catalyze Cal metabolism to other metabolites, or an entirely different enzyme might be involved, possibly CYP27B. We also for the first-time described the fate of the immediate metabolite, MC1046 once it is produced. Our work showed that unlike the parent, this intermediate might be predominantly metabolized by one enzyme.

5.8 The micellar formulation facilitates tumor accumulation of Cal and PTX

Polymeric nanoparticles continue to be of interest to many researchers because of their potential utility in numerous settings. Within the context of drug delivery, polymeric nanoparticles continue to generate interest because of the potential to tune their properties for different applications. Considering the barrier posed by solid tumors to drug delivery, we sought to tune the size of M-

Cal/PTX to obtain optimal tumor accumulation. Our data showed the optimal M-Cal/PTX achieved this goal. At the 24-hr mark post single IV bolus dose, significant amounts of Cal (**Figure 21B**) and PTX (**Figure 22B**) were measured in the tumors. These results confirmed the micellar drug delivery platform facilitated tumor accumulation. The shape and size are two physical characteristics of nanoparticles that play crucial roles in tumor uptake (Batist, 2007). Nanoparticles face several bio-barriers while in circulation. A major barrier to tumor uptake is the body's immune response which considers the formulation platform a foreign body. However, tuning the particle size and shape can provide stealth allowing the particles to circulate longer and accumulate in desired areas through the "Enhanced Permeability and Retention" (EPR) effect (Batist, 2007; Lasic and Papahadjopoulos, 1995). Nanoparticles of size greater than 200 nm do not generally extravasate into tumor (Nagayasu et al., 1999). Also, shapes of nanoparticles dictate their interactions with membranes and circular shapes are favored for tumor accumulation (Nagayasu et al., 1999). A combination of these factors possibly contributed to the enhanced uptake of Cal and PTX encapsulated in the M-Cal/PTX system.

5.8.1 Summary of M-Cal/PTX distribution

The results show tuning M-Cal/PTX size to enhance tumor accumulation is possible. M-Cal/PTX enhanced tumor accumulation of both Cal and PTX. Compared to abraxane, a nano-albumin formulation of PTX, the mean tumor concentrations of PTX in ice that received M-Cal/PTX was higher than in those that received abraxane. The enhanced tumor accumulation is expected to translate into enhanced therapeutic benefit.

5.9 M-Cal/PTX showed better treatment benefits, as well as reduced impact on body weight change

Treatment outcomes for PDAC remain dire despite the advancement in our knowledge of the disease. PK and biodistribution studies of M-Cal/PTX suggested this formulated combination regimen could potentially be an effective treatment option for PDAC. Here direct evidence for the anti-tumor activity of M-Cal/PTX is discussed. 75% of test animals that received M-Cal/PTX had

a favorable response in their tumor measurements (**Figure 34**). For the placebo group, ¼ of the animals had a favorable response. Although the response in the placebo group was unexpected, it was not totally surprising. An immune competent strain of mice was used for these studies. It is possible the immune system may have contributed to the unexpected response in the mouse that received placebo. Nonetheless, the difference in treatment response between the two groups is clear. Genetic approaches have been used to deplete CAFs resulting in varying degrees of success (Lee et al., 2014; Özdemir et al., 2014; Rhim et al., 2014). The general consensus now is that over-depleting the tumor stroma actually leads to more aggressive cancer phenotypes because some elements of the stroma have a tumor restraining function (Rhim et al., 2014). Against this backdrop, a strategy that maintains a balance between stroma excess and depletion is favored. Pharmacological reprogramming of the stroma through the activation of VDR appears to be a good strategy as our results show. Cal normalization of the of the stroma, as evidenced by reduced expression levels of α – SMA (**Figure 36**) and COL1A1(**Figure 38**) enabled tumor infiltration by cytotoxic T lymphocytes as well as chemotherapy (PTX) to achieve the observed anti-tumor effect. The results suggested that using the micelle-formulated combination is superior for stromal modulation because a cremophor formulation of Cal and PTRX achieved impressive, albeit inferior results with a larger variation in subject response (**Figure 36**). Indeed, unformulated Cal achieved similar results in a study reported by Sherman and colleagues (Sherman et al., 2014). However, in that same study, the authors reported clinical signs of abdominal ascites, severe cachexia, significant weight loss and in some cases complete animal inactivity due to Cal toxicity. Body weight measurements in our study recapitulated some of those results where animals that received the cremophor formulation of Cal and PTX had larger fluctuations in their body weight after each cycle of treatment (**Figure 39**). With each cycle of treatment, the body weight fluctuations got worse. Compared with the cremophor-formulation group, animals that received micelle-formulated Cal either alone or in combination with PTX or ABX did not experience significant body weight changes. In fact, the mean body weight changes were positive

in these groups (**Figure 37**). This provides direct evidence that although both formulated and unformulated Cal may modulate the stroma, the micelle-formulated Cal had a better safety profile. As discussed earlier, this is because the drug delivery technology controls Cal exposure and also facilitates accumulation in the tumor, thereby reducing unwanted activation of VDR outside of the tumor.

The body weight fluctuations in the cremophor formulation did not appear to be correlated with any specific changes in the liver and kidney as assessed by the liver and kidney function tests. On the contrary, the liver and kidney function tests were generally consistent between M-Cal/PTX and cremophor formulation groups (**Figure 40**). Overall, no significant organ safety flags were identified in both groups.

Another direct evidence of the antitumor effect of M-Cal/PTX is in the robust reduction of Ki67, a tumor cell proliferation marker (**Figure 37**). Unlike micelle formulated Cal and PTX, the cremophor formulation did not result in the reduction of tumor cell proliferation. This is consistent with the inability of this formulation to deliver sufficient PTX into the tumor as demonstrated in **Figure 23B**. Interestingly, co-formulated Cal and PTX (M-Cal/PTX) and a physical mixture of the mono-formulated agents (M-Cal + M-PTX) both showed significant inhibitory effect on tumor cell proliferation when compared to sham group, although the former did better. This result is unsurprising because the size range of the mono and co-formulated agents were similar. This result opens up the possibility for flexibility in terms of dose modification in the micelle formulated group. A disadvantage for co-formulating Cal and PTX is the limitation it puts on the range of doses that could be tested. To achieve decent co-encapsulation of both agents, a balance has to be attained in the weights of drugs that are loaded. Mono-formulating the drugs and administering them as a physical mixture opens up the possibility to encapsulate even higher amounts of the drugs as single agents. A potential limitation for this strategy will be the volume of mixture that could be administrated at a time. Physically mixing the drugs will increase the volume of solution, and in the context of IV administration, this could be problematic.

One of the reasons for the seeming lack of progress in PDAC is the lack of reliable blood markers which could be easily measured to diagnose or assess treatment effect in PDAC (Resovi et al., 2018). Till date, only CA19.9 is approved by the US FDA to detect and monitor PDAC. However clinical utility of this marker is limited due to insufficient specificity and sensitivity. Additionally, CA19.9 is not expressed in some PDAC patients and has been shown to have different expression patterns in different races and sexes. (Korc, 2007). Resovi and colleagues identified 3 biomarkers- TIMP1, TSP2 and MMP7 with the potential to be used as a panel to assess treatment benefit. This panel of stroma-related biomarkers had better sensitivity and specificity in discriminating different stages of PDAC and was successfully applied to both mice and human samples (Resovi et al., 2018). These biomarkers were measured in this study and the insights are discussed here. In the $Kras^{G12D}$ model, TIMP1 and TSP2 changed with M-Cal/PTX treatment but MMP7 did not (**Figure 35**). Of the markers that responded to treatment, different response profiles were observed. TSP2 responded almost immediately to treatment while a delayed response was observed for TIMP1 (**Figures 35A and B**). Reductions in TIMP1 and TSP2 levels with M-Cal/PTX treatment provided further evidence that this treatment was able to reduce stroma content. Because PTX is not known to be stroma to be a stroma-modulator, these effects were attributed to Cal.

A tumor growth model was developed to further understand disease progression in the sham and M-Cal/PTX groups. The metrics derived from the model added further evidence of the potential of M-Cal/PTX to modulate tumor growth. Simulations showed M-Cal/PTX disease slowed disease progression compared with sham treatment (**Figure 46**). Mathematical models of tumor growth have gained increased utility in recent years (Vaghi et al., 2020). This is primarily because data from the gold standard of treatment assessment, overall survival, often takes a long time to be obtained. There is a desire to obtain information early on that will inform which subjects are benefitting from treatment, or those that would have to go off-treatment. Tumor growth metrics from these models could be used as covariates to predict progression

free survival (PFS) or overall survival (OS). Although tumor growth metrics were estimated in this study, they were not used to predict OS because the same set of animals were not used in the tumor growth measurement and survival studies.

A separate survival study was conducted to estimate treatment effect on mice survival. Results from this study confirmed that M-Cal/PTX was indeed able to extend the median survival of tumor-bearing mice. Animals in the M-Cal/PTX group out-lived those in the comparator groups, that is sham, M-Cal, M-Cal + ABX groups (**Figure 41**).

Compared with the sham group, M-Cal treatment extended the median survival of mice by 5 days. This is in line with studies that showed vitamin D analogs like Cal have inhibitory activities on various cancer cell lines including pancreatic cancer (Arensman et al., 2015; Emanuelsson et al., 2018). While a positive signal was observed for Cal monotherapy, the study also demonstrated this response is weak. Calcipotriol in combination with other agents would make better alternatives.

5.9.1 Exploratory reverse phase protein array

Exploratory studies were conducted with tumor biopsies with the goal to identify potential proteins or signaling patterns that might be relevant to PDAC. No specific changes were observed in the heat maps from sham and M-Cal/PTX treated groups. RPPA is a procedure that is very sensitive to the quality and expression of proteins. Due to circumstances that could not be controlled, the samples were stored longer than would have been ideal. This could potentially explain why no meaningful changes were observed.

5.9.2 Summary of efficacy and safety studies

The data showed that M-Cal/PTX is a promising regimen for PDAC. Compared to the sham and other treatment groups, M-Cal/PTX reduced stroma-related markers, shrunk or inhibited tumor growth and extended the median survival of tumor-bearing mice.

6.0 Study conclusions

Pancreatic cancer remains an unmet health challenge that needs to be addressed. Targeting the stroma and tumor compartments has been shown to be a viable strategy for PDAC treatment due to the inter-play between the two compartments. The goal of this study was to develop a drug delivery vehicle to safely and effectively deliver Cal, a stroma modulator as well as PTX, an anti-cancer agent.

To enable such studies, a reliable and more sensitive assay to measure Cal and PTX was required. We developed and validated an LC-MS/MS assay that was able to measure Cal and PTX up to 24-hr post single iv bolus dose. The assay was sensitive, reliable and was used to measure Cal, metabolites of Cal and PTX in various samples. Further, a polymeric micellar delivery system was developed and optimized using the central composite design. The micelle extended the half-lives of Cal and PTX and reduced the exposure of Cal. The reduction in Cal exposure and extension of biological half-lives improved the efficacy and safety profiles of the combination regimen.

In this study, we discovered for the first time a potential DDI between Cal and PTX. Co-administering Cal with PTX resulted in faster Cal CL whereas the CL was lower for PTX compared with when the drugs were administered alone. Further population PK analysis revealed differential PK for Cal between healthy and diseased mice. We observed faster Cal CL and lower exposure in disease mice than in the heathy ones. Covariate analysis revealed disease status is a significant covariate on Cal CL, and we postulated that the CL is faster in diseased animals due to overexpressed CYP24A1, the enzyme primarily responsible for Cal elimination. Our studies also provided further evidence for the metabolic profile of Cal as previously reported. We concluded that CYP24A1-mediated metabolism of Cal only contributes to 23% of total Cal CL. Contributions from another enzyme/process, possibly CYP27 cannot be ruled out. In contrast MC1046 is primarily metabolized by one enzyme to MC1080 accounting for 94% of total MC1080 CL. In our efficacy studies, M-Cal/PTX showed promising results. It reduced circulating levels of

TIMP1 and TSP2-markers of stroma content. The formulated regimen also significantly inhibited the expression of α –SMA and COL1A1, providing further evidence that the combination regime modulated tumor stroma. Tumor cell and tumor growth were also significantly inhibited by this regimen and in the survival studies, M-Cal/PTX prolonged the survival of tumor-bearing mice, more than any of the comparator treatments that were tested. Treatment with M-Cal/PTX did not lead to any marked changes in body weight showing the delivery vehicle reduced toxicity that is often associated with Cal treatment. We finally hypothesized that in the combination treatment of PDAC with Cal and MPTX, Cal deactivated CAFs, and in so doing enabled the re-activation of T-cells which release tumor cell-killing cytokines (**Figure 49**). Together with the direct anticancer activity of PTX, M-Cal/PTX inhibited tumor growth that led to the prolongation of survival in tumor-bearing mice

Overall, these studies provided evidence for further development of this regimen for PDAC treatment.

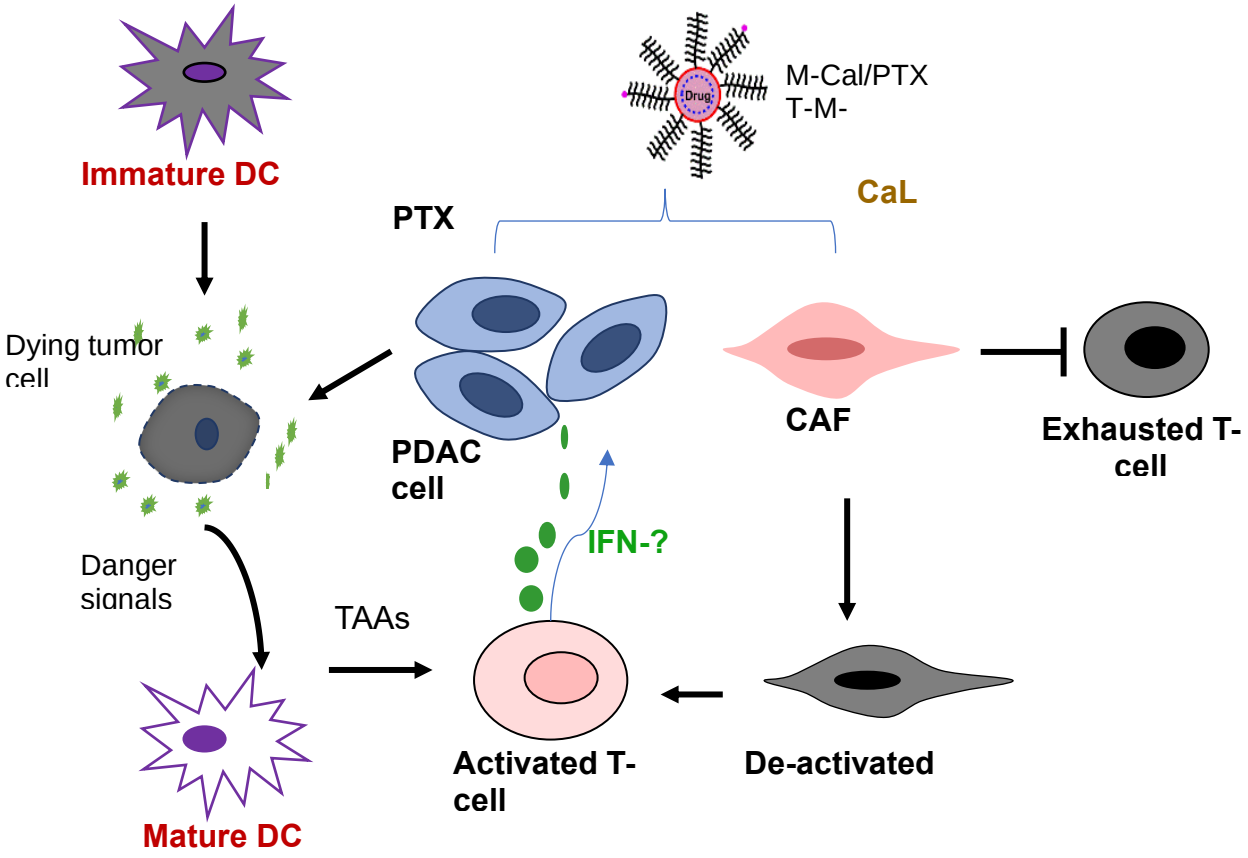

Figure 49. Graphical abstract for the proposed mechanism of action of M-Cal/PTX

References

Abbassi, R., Schmid, R.M., 2019. Evolving Treatment Paradigms for Pancreatic Cancer. Visc. Med. 35, 362–372. https://doi.org/10.1159/000503797

Abuchowski, A., McCoy, J.R., Palczuk, N.C., van Es, T., Davis, F.F., 1977. Effect of covalent attachment of polyethylene glycol on immunogenicity and circulating life of bovine liver catalase. J. Biol. Chem. 252, 3582–3586.

Albanese, A., Tang, P.S., Chan, W.C.W., 2012. The Effect of Nanoparticle Size, Shape, and Surface Chemistry on Biological Systems. Annu. Rev. Biomed. Eng. 14, 1–16. https://doi.org/10.1146/annurev-bioeng-071811-150124

Andersen, D.K., Andren-Sandberg, Å., Duell, E.J., Goggins, M., Korc, M., Petersen, G.M., Smith, J.P., Whitcomb, D.C., 2013. Pancreatitis-diabetes-pancreatic cancer: Summary of an NIDDK-NCI workshop. Pancreas 42, 1227–1237. https://doi.org/10.1097/MPA.0b013e3182a9ad9d

Anderson, K.G., Stromnes, I.M., Greenberg, P.D., 2017. Obstacles Posed by the Tumor Microenvironment to T cell Activity: A Case for Synergistic Therapies. Cancer Cell 31, 311–325. https://doi.org/10.1016/j.ccell.2017.02.008

Apte, M. V., Haber, P.S., Applegate, T.L., Norton, I.D., McCaughan, G.W., Korsten, M.A., Pirola, R.C., Wilson, J.S., 1998. Periacinar stellate shaped cells in rat pancreas: Identification, isolation, and culture. Gut 43, 128–133. https://doi.org/10.1136/gut.43.1.128

Arensman, M.D., Nguyen, P., Kershaw, K.M., Lay, A.R., Ostertag-Hill, C.A., Sherman, M.H., Downes, M., Liddle, C., Evans, R.M., Dawson, D.W., 2015. Calcipotriol targets LRP6 to inhibit wnt signaling in pancreatic cancer. Mol. Cancer Res. https://doi.org/10.1158/1541-7786.MCR-15-0204

Arturson, P., Laakso, T., Edman, P., 1983. Acrylic microspheres in vivo IX: Blood elimination kinetics and organ distribution of microparticles with different surface characteristics. J. Pharm. Sci. 72, 1415–1420. https://doi.org/10.1002/jps.2600721213

Arulmozhi, K.T., Mythili, N., 2013. Studies on the chemical synthesis and characterization of lead oxide nanoparticles with different organic capping agents. AIP Adv. 3. https://doi.org/10.1063/1.4858419

Awaji, M., Singh, R.K., 2019. Cancer-associated fibroblasts' functional heterogeneity in pancreatic ductal adenocarcinoma. Cancers (Basel). 11, 1–14. https://doi.org/10.3390/cancers11030290

Balachandran, V.P., Łuksza, M., Zhao, J.N., Makarov, V., Moral, J.A., Remark, R., Herbst, B., Askan, G., Bhanot, U., Senbabaoglu, Y., Wells, D.K., Cary, C.I.O., Grbovic-Huezo, O., Attiyeh, M., Medina, B., Zhang, J., Loo, J., Saglimbeni, J., Abu-Akeel, M., Zappasodi, R., Riaz, N., Smoragiewicz, M., Larkin Kelley, Z., Basturk, O., Gönen, M., Levine, A.J., Allen, P.J., Fearon, D.T., Merad, M., Gnjatic, S., Iacobuzio-Donahue, C.A., Wolchok, J.D., Dematteo, R.P., Chan, T.A., Greenbaum, B.D., Merghoub, T., Leach, S.D., Johns, A.L., Scott Mead, R., Gill, A.J., Chang, D.K., McKay, S.H., Chantrill, L.A., Chin, V.T., Chou, A., Humphris, J.L., Pajic, M., Steinmann, A., Arshi, M., Drury, A., Froio, D., Morgan, A., Timpson, P., Hermann, D., Vennin, C., Warren, S., Pinese, M., Wu, J., Pinho, A. V., Tucker, K., Andrews, L., Samra, J.S., Arena, J., Pavlakis, N., High, H.A., Mittal, A., Biankin, A. V., Bailey, P., Martin, S., Musgrove, E.A., Jones, M.D., Nourse, C., Jamieson, N.B., Stoita, A., Williams, D., Spigelman, A., Waddell, N., Pearson, J. V., Patch, A.M., Nones, K., Newell, F., Mukhopadhyay, P., Addala, V., Kazakoff, S., Holmes, O., Leonard, C., Wood, S., Xu, C., Grimmond, S.M., Hofmann, O., Wilson, P.J., Christ, A., Bruxner, T., Asghari, R., Merrett, N.D., Pavey, D., Das, A., Goodwin, A., Cosman, P.H., Ismail, K., O'connor, C., Cooper, C.L., Grimison, P., Kench, J.G., Sandroussi, C., Lam, V.W., McLeod, D., Nagrial, A.M., Kirk, J., James, V., Texler, M., Forest, C., Epari, K.P., Ballal, M., Fletcher, D.R., Mukhedkar, S., Zeps, N., Beilin, M., Feeney, K., Nguyen, N.Q., Ruszkiewicz, A.R., Worthley, C., Chen, J., Brooke-Smith, M.E., Papangelis, V., Clouston, A.D., Martin, P., Barbour, A.P., O'rourke, T.J., Fawcett, J.W., Slater, K., Hatzifotis, M., Hodgkinson, P.,

Nikfarjam, M., Eshleman, J.R., Hruban, R.H., Wolfgang, C.L., Hodgin, M., Scarpa, A., Lawlor, R.T., Beghelli, S., Corbo, V., Scardoni, M., Bassi, C., 2017. Identification of unique neoantigen qualities in long-term survivors of pancreatic cancer. Nature 551, S12–S16. https://doi.org/10.1038/nature24462

Balli, D., Rech, A.J., Stanger, B.Z., Vonderheide, R.H., 2017. Immune cytolytic activity stratifies molecular subsets of human pancreatic cancer. Clin. Cancer Res. 23, 3129–3138. https://doi.org/10.1158/1078-0432.CCR-16-2128

Batist, G., 2007. Cardiac safety of liposomal anthracyclines. Cardiovasc. Toxicol. 7, 72–74. https://doi.org/10.1007/s12012-007-0014-4

Beal, S.L., 2001. Ways to fit a PK model with some data below the quantification limit. J. Pharmacokinet. Pharmacodyn. https://doi.org/10.1023/A:1012299115260

Bi, S., Wang, Y., Guan, J., Sheng, X., Meng, J., 2014. Three new Jurassic euharamiyidan species reinforce early divergence of mammals. Nature 514, 579–584. https://doi.org/10.1038/nature13718

Bierie, B., Moses, H.L., 2006. Tumour microenvironment - TGFB: The molecular Jekyll and Hyde of cancer. Nat. Rev. Cancer 6, 506–520. https://doi.org/10.1038/nrc1926

Biffi, G., Oni, T.E., Spielman, B., Hao, Y., Elyada, E., Preall, J., Tuveson, D.A., 2020. HHS Public Access. https://doi.org/10.1158/2159-8290.CD-18-0710.IL-1-induced

Bilensoy, E., Sarisozen, C., Esendağli, G., Doğan, A.L., Aktaş, Y., Şen, M., Mungan, N.A., 2009. Intravesical cationic nanoparticles of chitosan and polycaprolactone for the delivery of Mitomycin C to bladder tumors. Int. J. Pharm. 371, 170–176. https://doi.org/10.1016/j.ijpharm.2008.12.015

Binderup, L., Binderup, E., Godtfredsen, W.O., Kissmeyer, A.M., 2005. Development of New Vitamin D Analogs. Vitam. D 2, 1489–1510. https://doi.org/10.1016/B978-012252687-9/50088-7

Binderup, L., Bramm, E., 1988. Effects of a novel vitamin D analogue MC 903 on cell

proliferation and differentiation in vitro and on calcium metabolism in vivo. Biochem. Pharmacol. https://doi.org/10.1016/0006-2952(88)90177-3

Boellner, S., Becker, K.-F., 2015. Reverse Phase Protein Arrays—Quantitative Assessment of Multiple Biomarkers in Biopsies for Clinical Use. Microarrays. https://doi.org/10.3390/microarrays4020098

Brace, R.A., 1981. Progress toward resolving the controversy of positive vs negative interstitial fluid pressure. Circ. Res. 49, 281–297. https://doi.org/10.1161/01.RES.49.2.281

Brahmer, J.R., Tykodi, S.S., Chow, L.Q.M., Hwu, W.-J., Topalian, S.L., Hwu, P., Drake, C.G., Camacho, L.H., Kauh, J., Odunsi, K., Pitot, H.C., Hamid, O., Bhatia, S., Martins, R., Eaton, K., Chen, S., Salay, T.M., Alaparthy, S., Grosso, J.F., Korman, A.J., Parker, S.M., Agrawal, S., Goldberg, S.M., Pardoll, D.M., Gupta, A., Wigginton, J.M., 2012. Safety and Activity of Anti–PD-L1 Antibody in Patients with Advanced Cancer. N. Engl. J. Med. https://doi.org/10.1056/nejmoa1200694

Brand, R.E., Nolen, B.M., Zeh, H.J., Allen, P.J., Eloubeidi, M.A., Goldberg, M., Elton, E., Arnoletti, J.P., Christein, J.D., Vickers, S.M., Langmead, C.J., Landsittel, D.P., Whitcomb, D.C., Grizzle, W.E., Lokshin, A.E., 2011. Serum biomarker panels for the detection of pancreatic cancer. Clin. Cancer Res. https://doi.org/10.1158/1078-0432.CCR-10-0248

Burris, H.A., Moore, M.J., Andersen, J., Green, M.R., Rothenberg, M.L., Modiano, M.R., Cripps, M.C., Portenoy, R.K., Storniolo, A.M., Tarassoff, P., Nelson, R., Dorr, F.A., Stephens, C.D., Von Hoff, D.D., 1997. Improvements in survival and clinical benefit with gemcitabine as first- line therapy for patients with advanced pancreas cancer: A randomized trial. J. Clin. Oncol. 15, 2403–2413. https://doi.org/10.1200/JCO.1997.15.6.2403

Canon, J., Rex, K., Saiki, A.Y., Mohr, C., Cooke, K., Bagal, D., Gaida, K., Holt, T., Knutson, C.G., Koppada, N., Lanman, B.A., Werner, J., Rapaport, A.S., San Miguel, T., Ortiz, R., Osgood, T., Sun, J.R., Zhu, X., McCarter, J.D., Volak, L.P., Houk, B.E., Fakih, M.G., O'Neil, B.H., Price, T.J., Falchook, G.S., Desai, J., Kuo, J., Govindan, R., Hong, D.S.,

Ouyang, W., Henary, H., Arvedson, T., Cee, V.J., Lipford, J.R., 2019. The clinical KRAS(G12C) inhibitor AMG 510 drives anti-tumour immunity. Nature 575, 217–223. https://doi.org/10.1038/s41586-019-1694-1

Capello, M., Cappello, P., Linty, F.C., Chiarle, R., Sperduti, I., Novarino, A., Salacone, P., Mandili, G., Naccarati, A., Sacerdote, C., Beghelli, S., Bersani, S., Barbi, S., Bassi, C., Scarpa, A., Nisticò, P., Giovarelli, M., Vineis, P., Milella, M., Novelli, F., 2013. Autoantibodies to Ezrin are an early sign of pancreatic cancer in humans and in genetically engineered mouse models. J. Hematol. Oncol. https://doi.org/10.1186/1756-8722-6-67

Chan, A., Prassas, I., Dimitromanolakis, A., Brand, R.E., Serra, S., Diamandis, E.P., Blasutig, I.M., 2014. Validation of biomarkers that complement CA19.9 in detecting early pancreatic cancer. Clin. Cancer Res. https://doi.org/10.1158/1078-0432.CCR-14-0289

Chang, Q., Yin, O.Q.., Chow, M.S.., 2004. Liquid chromatography–tandem mass spectrometry method for the determination of tranexamic acid in human plasma. J. Chromatogr. B 805, 275–280. https://doi.org/10.1016/j.jchromb.2004.03.013

Claret, L., Zheng, J., Mercier, F., Chanu, P., Chen, Y., Rosbrook, B., Yazdi, P., Milligan, P.A., Bruno, R., 2016. Model-based prediction of progression-free survival in patients with first-line renal cell carcinoma using week 8 tumor size change from baseline. Cancer Chemother. Pharmacol. https://doi.org/10.1007/s00280-016-3116-5

Collisson, E.A., Sadanandam, A., Olson, P., Gibb, W.J., Truitt, M., Gu, S., Cooc, J., Weinkle, J., Kim, G.E., Jakkula, L., Feiler, H.S., Ko, A.H., Olshen, A.B., Danenberg, K.L., Tempero, M.A., Spellman, P.T., Hanahan, D., Gray, J.W., 2011. Subtypes of pancreatic ductal adenocarcinoma and their differing responses to therapy. Nat. Med. https://doi.org/10.1038/nm.2344

Dahan, L., Phelip, J.M., Le Malicot, K., Williet, N., Desrame, J., Volet, J., Petorin, C., Malka, D., Rebischung, C., Aparicio, T., Lecaille, C., Rinaldi, Y., Turpin, A., Bignon, A.L., Bachet, J.-B., Seitz, J.F., Lepage, C., Francois, E., 2018. FOLFIRINOX until progression,

FOLFIRINOX with maintenance treatment, or sequential treatment with gemcitabine and FOLFIRI.3 for first-line treatment of metastatic pancreatic cancer: A randomized phase II trial (PRODIGE 35-PANOPTIMOX). J. Clin. Oncol. https://doi.org/10.1200/jco.2018.36.15_suppl.4000

Das, S., Chaudhury, A., 2011. Recent advances in lipid nanoparticle formulations with solid matrix for oral drug delivery. AAPS PharmSciTech 12, 62–76. https://doi.org/10.1208/s12249-010-9563-0

De Wever, O., Westbroek, W., Verloes, A., Bloemen, N., Bracke, M., Gespach, C., Bruyneel, E., Mareel, M., 2004. Critical role of N-cadherin in myofibroblast invasion and migration in vitro stimulated by colon-cancer-cell-derived TGF-β or wounding. J. Cell Sci. 117, 4691–4703. https://doi.org/10.1242/jcs.01322

Dhir, M., Zenati, M.S., Hamad, A., Singhi, A.D., Bahary, N., Hogg, M.E., Zeh, H.J., Zureikat, A.H., 2018. FOLFIRINOX Versus Gemcitabine/Nab-Paclitaxel for Neoadjuvant Treatment of Resectable and Borderline Resectable Pancreatic Head Adenocarcinoma. Ann. Surg. Oncol. 25, 1896–1903. https://doi.org/10.1245/s10434-018-6512-8

Ducreux, M., Cuhna, A.S., Caramella, C., Hollebecque, A., Burtin, P., Goéré, D., Seufferlein, T., Haustermans, K., Van Laethem, J.L., Conroy, T., Arnold, D., 2015. Cancer of the pancreas: ESMO Clinical Practice Guidelines for diagnosis, treatment and follow-up. Ann. Oncol. https://doi.org/10.1093/annonc/mdv295

Duffy, M.J., Sturgeon, C., Lamerz, R., Haglund, C., Holubec, V.L., Klapdor, R., Nicolini, A., Topolcan, O., Heinemann, V., 2009. Tumor markers in pancreatic cancer: A European Group on Tumor Markers (EGTM) status report. Ann. Oncol. https://doi.org/10.1093/annonc/mdp332

Dufort, C.C., Delgiorno, K.E., Hingorani, S.R., 2016. Mounting Pressure in the Microenvironment: Fluids, Solids, and Cells in Pancreatic Ductal Adenocarcinoma. Gastroenterology 150, 1545-1557.e2. https://doi.org/10.1053/j.gastro.2016.03.040

Ebrahimi, S., Hosseini, M., Shahidsales, S., Maftouh, M., Ferns, G.A., Ghayour-Mobarhan, M., Hassanian, S.M., Avan, A., 2017. Targeting the Akt/PI3K Signaling Pathway as a Potential Therapeutic Strategy for the Treatment of Pancreatic Cancer. Curr. Med. Chem. 24, 1321–1331. https://doi.org/10.2174/0929867324666170206142658

Elyada, E., Bolisetty, M., Laise, P., Flynn, W.F., Courtois, E.T., Burkhart, R.A., Teinor, J.A., Belleau, P., Biffi, G., Lucito, M.S., Sivajothi, S., Armstrong, T.D., Engle, D.D., Yu, K.H., Hao, Y., Wolfgang, C.L., Park, Y., Preall, J., Jaffee, E.M., Califano, A., Robson, P., Tuveson, D.A., 2019. Cross-species single-cell analysis of pancreatic ductal adenocarcinoma reveals antigen-presenting cancer-associated fibroblasts. Cancer Discov. 9, 1102–1123. https://doi.org/10.1158/2159-8290.CD-19-0094

Emanuelsson, I., Wikvall, K., Friman, T., Norlin, M., 2018. Vitamin D Analogues Tacalcitol and Calcipotriol Inhibit Proliferation and Migration of T98G Human Glioblastoma Cells. Basic Clin. Pharmacol. Toxicol. https://doi.org/10.1111/bcpt.13007

Erdogan, B., Webb, D.J., 2017. Cancer-associated fibroblasts modulate growth factor signaling and extracellular matrix remodeling to regulate tumor metastasis. Biochem. Soc. Trans. https://doi.org/10.1042/BST20160387

Feig, C., Jones, J.O., Kraman, M., Wells, R.J.B., Deonarine, A., Chan, D.S., Connell, C.M., Roberts, E.W., Zhao, Q., Caballero, O.L., Teichmann, S.A., Janowitz, T., Jodrell, D.I., Tuveson, D.A., Fearon, D.T., 2013. Targeting CXCL12 from FAP-expressing carcinoma-associated fibroblasts synergizes with anti-PD-L1 immunotherapy in pancreatic cancer. Proc. Natl. Acad. Sci. U. S. A. https://doi.org/10.1073/pnas.1320318110

Fukunaga, A., Miyamoto, M., Cho, Y., Murakami, S., Kawarada, Y., Oshikiri, T., Kato, K., Kurokawa, T., Suzuoki, M., Nakakubo, Y., Hiraoka, K., Itoh, T., Morikawa, T., Okushiba, S., Kondo, S., Hiroyuki, K., 2004. CD8+tumor-infiltrating lymphocytes together with CD4+tumor-infiltrating lymphocytes and dendritic cells improve the prognosis of patients with pancreatic adenocarcinoma. Pancreas 28, 26–31. https://doi.org/10.1097/00006676-

200401000-00023

Goonetilleke, K.S., Siriwardena, A.K., 2007. Systematic review of carbohydrate antigen (CA 19-9) as a biochemical marker in the diagnosis of pancreatic cancer. Eur. J. Surg. Oncol. https://doi.org/10.1016/j.ejso.2006.10.004

Guo, S., Contratto, M., Miller, G., Leichman, L., Wu, J., 2017. Immunotherapy in pancreatic cancer: Unleash its potential through novel combinations. World J. Clin. Oncol. https://doi.org/10.5306/wjco.v8.i3.230

Gupta, B., Poudel, B.K., Tran, T.H., Pradhan, R., Cho, H.J., Jeong, J.H., Shin, B.S., Choi, H.G., Yong, C.S., Kim, J.O., 2015. Modulation of Pharmacokinetic and Cytotoxicity Profile of Imatinib Base by Employing Optimized Nanostructured Lipid Carriers. Pharm. Res. 32, 2912–2927. https://doi.org/10.1007/s11095-015-1673-7

Haas, M., Siveke, J.T., Schenk, M., Lerch, M.M., Caca, K., Freiberg-Richter, J., Fischer von Weikersthal, L., Kullmann, F., Reinacher-Schick, A., Fuchs, M., Kanzler, S., Kunzmann, V., Ettrich, T.J., Kruger, S., Westphalen, C.B., Held, S., Heinemann, V., Boeck, S., 2018. Efficacy of gemcitabine plus erlotinib in rash-positive patients with metastatic pancreatic cancer selected according to eligibility for FOLFIRINOX: A prospective phase II study of the ‘Arbeitsgemeinschaft Internistische Onkologie.’ Eur. J. Cancer 94, 95–103. https://doi.org/10.1016/j.ejca.2018.02.008

Hanahan, D., Weinberg, R.A., 2011. Hallmarks of cancer: The next generation. Cell. https://doi.org/10.1016/j.cell.2011.02.013

Hejri, A., Khosravi, A., Gharanjig, K., Hejazi, M., 2013. Optimisation of the formulation of β-carotene loaded nanostructured lipid carriers prepared by solvent diffusion method. Food Chem. 141, 117–123. https://doi.org/10.1016/j.foodchem.2013.02.080

Hendrikx, J.J.M.A., Rosing, H., Schinkel, A.H., Schellens, J.H.M., Beijnen, J.H., 2014. Combined quantification of paclitaxel, docetaxel and ritonavir in human feces and urine using LC-MS/MS. Biomed. Chromatogr. 28, 302–310. https://doi.org/10.1002/bmc.3021

Hidalgo, M., 2011. Pancreatic Cancer : Pancreatic Cancer : Overview. Lancet 378, 1605–1617.

Hingorani, S.R., Harris, W.P., Beck, J.T., Berdov, B.A., Wagner, S.A., Pshevlotsky, E.M., Tjulandin, S.A., Gladkov, O.A., Holcombe, R.F., Korn, R., Raghunand, N., Dychter, S., Jiang, P., Shepard, H.M., Devoe, C.E., 2016. Phase Ib study of PEGylated recombinant human hyaluronidase and gemcitabine in patients with advanced pancreatic cancer. Clin. Cancer Res. https://doi.org/10.1158/1078-0432.CCR-15-2010

Hirabe, M., Tokuda, T., Hosomi, A., Amano, T., Okamoto, T., Nakamura, H., 2016. Calcium effects and systemic exposure of vitamin D 3 analogues after topical treatment of active vitamin D 3 -containing ointments in rats. Eur. J. Pharmacol. 788, 98–103. https://doi.org/10.1016/j.ejphar.2016.06.028

Hobaus, J., Thiem, U., M. Hummel, D., Kallay, E., 2012. Role of Calcium, Vitamin D, and the Extrarenal Vitamin D Hydroxylases in Carcinogenesis. Anticancer. Agents Med. Chem. https://doi.org/10.2174/18715206130105

Hou, Y.C., Chao, Y.J., Hsieh, M.H., Tung, H.L., Wang, H.C., Shan, Y.S., 2019. Low cd8+ t cell infiltration and high pd-l1 expression are associated with level of cd44+/cd133+ cancer stem cells and predict an unfavorable prognosis in pancreatic cancer. Cancers (Basel). 11. https://doi.org/10.3390/cancers11040541

Huang, H., Brekken, R.A., 2019. The next wave of stroma-targeting therapy in pancreatic cancer. Cancer Res. 79, 328–330. https://doi.org/10.1158/0008-5472.CAN-18-3751

Huang, S.M., Strong, J.M., Zhang, L., Reynolds, K.S., Nallani, S., Temple, R., Abraham, S., Al Habet, S., Baweja, R.K., Burckart, G.J., Chung, S., Colangelo, P., Frucht, D., Green, M.D., Hepp, P., Karnaukhova, E., Ko, H.S., Lee, J.I., Marroum, P.J., Norden, J.M., Qiu, W., Rahman, A., Sobel, S., Stifano, T., Thummel, K., Wei, X.X., Yasuda, S., Zheng, J.H., Zhao, H., Lesko, L.J., 2008. Drug interactions/review: New era in drug interaction evaluation: US Food and Drug Administration update on CYP enzymes, transporters, and the guidance process. J. Clin. Pharmacol. https://doi.org/10.1177/0091270007312153

Huizing, M.T., Keung, A.C.F., Rosing, H., Van der Kuij, V., Ten Bokkel Huinink, W.W., Mandjes, I.M., Dubbelman, A.C., Pinedo, H.M., Beijnen, J.H., 1993. Pharmacokinetics of paclitaxel and metabolites in a randomized comparative study in platinum-pretreated ovarian cancer patients. J. Clin. Oncol. https://doi.org/10.1200/JCO.1993.11.11.2127

Hwang, R.F., Moore, T., Arumugam, T., Ramachandran, V., Amos, K.D., Rivera, A., Ji, B., Evans, D.B., Logsdon, C.D., 2008. Cancer-associated stromal fibroblasts promote pancreatic tumor progression. Cancer Res. https://doi.org/10.1158/0008-5472.CAN-07-5714

Iqbal, J., Ragone, A., Lubinski, J., Lynch, H.T., Moller, P., Ghadirian, P., Foulkes, W.D., Armel, S., Eisen, A., Neuhausen, S.L., Senter, L., Singer, C.F., Ainsworth, P., Kim-Sing, C., Tung, N., Friedman, E., Llacuachaqui, M., Ping, S., Narod, S.A., 2012. The incidence of pancreatic cancer in BRCA1 and BRCA2 mutation carriers. Br. J. Cancer 107, 2005–2009. https://doi.org/10.1038/bjc.2012.483

Jacobetz, M.A., Chan, D.S., Neesse, A., Bapiro, T.E., Cook, N., Frese, K.K., Feig, C., Nakagawa, T., Caldwell, M.E., Zecchini, H.I., Lolkema, M.P., Jiang, P., Kultti, A., Thompson, C.B., Maneval, D.C., Jodrell, D.I., Frost, G.I., Shepard, H.M., Skepper, J.N., Tuveson, D.A., 2013. Hyaluronan impairs vascular function and drug delivery in a mouse model of pancreatic cancer. Gut 62, 112–120. https://doi.org/10.1136/gutjnl-2012-302529

Janssen, Q.P., Buettner, S., Suker, M., Beumer, B.R., Addeo, P., Bachellier, P., Bahary, N., Bekaii-Saab, T., Bali, M.A., Besselink, M.G., Boone, B.A., Chau, I., Clarke, S., Dillhoff, M., El-Rayes, B.F., Frakes, J.M., Grose, D., Hosein, P.J., Jamieson, N.B., Javed, A.A., Khan, K., Kim, K.P., Kim, S.C., Kim, S.S., Ko, A.H., Lacy, J., Margonis, G.A., McCarter, M.D., McKay, C.J., Mellon, E.A., Moorcraft, S.Y., Okada, K.I., Paniccia, A., Parikh, P.J., Peters, N.A., Rabl, H., Samra, J., Tinchon, C., Van Tienhoven, G., Van Veldhuisen, E., Wang-Gillam, A., Weiss, M.J., Wilmink, J.W., Yamaue, H., Homs, M.Y.V., Van Eijck, C.H.J., Katz, M.H.G., Groot Koerkamp, B., 2019. Neoadjuvant FOLFIRINOX in Patients with Borderline

Resectable Pancreatic Cancer: A Systematic Review and Patient-Level Meta-Analysis. J. Natl. Cancer Inst. 111, 782–794. https://doi.org/10.1093/jnci/djz073

Jiang, W., Kim, B.Y.S., Rutka, J.T., Chan, W.C.W., 2008. Nanoparticle-mediated cellular response is size-dependent. Nat. Nanotechnol. 3, 145–150. https://doi.org/10.1038/nnano.2008.30

Jones, G., Byford, V., West, S., Masuda, S., Ibrahim, G., Kaufmann, M., Knutson, J.C., Strugnell, S., Mehta, R., 2006. Hepatic activation and inactivation of clinically-relevant vitamin D analogs and prodrugs. Anticancer Res.

Joyce, J.A., Fearon, D.T., 2015. T cell exclusion, immune privilege, and the tumor microenvironment. Science (80-.). https://doi.org/10.1126/science.aaa6204

Kang, X., Lin, Z., Xu, M., Pan, J., Wang, Z. wei, 2019. Deciphering role of FGFR signalling pathway in pancreatic cancer. Cell Prolif. 52. https://doi.org/10.1111/cpr.12605

Karuppuswamy, P., Reddy Venugopal, J., Navaneethan, B., Luwang Laiva, A., Ramakrishna, S., 2015. Polycaprolactone nanofibers for the controlled release of tetracycline hydrochloride. Mater. Lett. 141, 180–186. https://doi.org/10.1016/j.matlet.2014.11.044

Kissmeyer, A.M., Binderup, L., 1991. Calcipotriol (MC 903): Pharmacokinetics in rats and biological activities of metabolites. A comparative study with 1,25(OH)2D3. Biochem. Pharmacol. 41, 1601–1606. https://doi.org/10.1016/0006-2952(91)90160-7

Knutson, J.C., LeVan, L.W., Valliere, C.R., Bishop, C.W., 1997. Pharmacokinetics and systemic effect on calcium homeostasis of 1α-24-dihydroxyvitamin D2 in rats. Comparison with 1α,25-dihydroxyvitamin D2, calcitriol, and calcipotriol. Biochem. Pharmacol. https://doi.org/10.1016/S0006-2952(97)00004-X

Korc, M., 2007. Pancreatic cancer-associated stroma production. Am. J. Surg. https://doi.org/10.1016/j.amjsurg.2007.05.004

KRAGBALLE, K., BECK, H.I., SØGAARD, H., 1988. Improvement of psoriasis by a topical vitamin D3 analogue (MC 903) in a double-blind study. Br. J. Dermatol.

https://doi.org/10.1111/j.1365-2133.1988.tb03204.x

Lai, E., Puzzoni, M., Ziranu, P., Pretta, A., Impera, V., Mariani, S., Liscia, N., Soro, P., Musio, F., Persano, M., Donisi, C., Tolu, S., Balconi, F., Pireddu, A., Demurtas, L., Pusceddu, V., Camera, S., Sclafani, F., Scartozzi, M., 2019. New therapeutic targets in pancreatic cancer. Cancer Treat. Rev. 81, 101926. https://doi.org/10.1016/j.ctrv.2019.101926

Lasic, D.D., Papahadjopoulos, D., 1995. Liposomes revisited. Science (80-.). 267, 1275–1276. https://doi.org/10.1126/science.7871422

Le, D.T., Durham, J.N., Smith, K.N., Wang, H., Bartlett, B.R., Aulakh, L.K., Lu, S., Kemberling, H., Wilt, C., Luber, B.S., Wong, F., Azad, N.S., Rucki, A.A., Laheru, D., Donehower, R., Zaheer, A., Fisher, G.A., Crocenzi, T.S., Lee, J.J., Greten, T.F., Duffy, A.G., Ciombor, K.K., Eyring, A.D., Lam, B.H., Joe, A., Kang, S.P., Holdhoff, M., Danilova, L., Cope, L., Meyer, C., Zhou, S., Goldberg, R.M., Armstrong, D.K., Bever, K.M., Fader, A.N., Taube, J., Housseau, F., Spetzler, D., Xiao, N., Pardoll, D.M., Papadopoulos, N., Kinzler, K.W., Eshleman, J.R., Vogelstein, B., Anders, R.A., Diaz, L.A., 2017. Mismatch repair deficiency predicts response of solid tumors to PD-1 blockade. Science (80-.). 357, 409–413. https://doi.org/10.1126/science.aan6733

Lee, J.J., Perera, R.M., Wang, H., Wu, D.C., Liu, X.S., Han, S., Fitamant, J., Jones, P.D., Ghanta, K.S., Kawano, S., Nagle, J.M., Deshpande, V., Boucher, Y., Kato, T., Chen, J.K., Willmann, J.K., Bardeesy, N., Beachy, P.A., 2014. Stromal response to Hedgehog signaling restrains pancreatic cancer progression. Proc. Natl. Acad. Sci. U. S. A. https://doi.org/10.1073/pnas.1411679111

Li, X., Wang, J., Li, G., Lin, C., Zhang, X., Sun, Y., Yang, Y., Gu, J., 2013. Evaluation of calcipotriol transdermal permeation through pig, rat and mouse skin using liquid chromatography-tandem mass spectrometry. Biomed. Chromatogr. 27, 1714–1719. https://doi.org/10.1002/bmc.2984

Lu, F., Wu, S.H., Hung, Y., Mou, C.Y., 2009. Size effect on cell uptake in well-suspended,

uniform mesoporous silica nanoparticles. Small 5, 1408–1413. https://doi.org/10.1002/smll.200900005

Macherla, S., Laks, S., Naqash, A.R., Bulumulle, A., Zervos, E., Muzaffar, M., 2018. Emerging role of immune checkpoint blockade in pancreatic cancer. Int. J. Mol. Sci. 19, 1–12. https://doi.org/10.3390/ijms19113505

Makohon-Moore, A.P., Matsukuma, K., Zhang, M., Reiter, J.G., Gerold, J.M., Jiao, Y., Sikkema, L., Attiyeh, M.A., Yachida, S., Sandone, C., Hruban, R.H., Klimstra, D.S., Papadopoulos, N., Nowak, M.A., Kinzler, K.W., Vogelstein, B., Iacobuzio-Donahue, C.A., 2018. Precancerous neoplastic cells can move through the pancreatic ductal system. Nature 561, 201–205. https://doi.org/10.1038/s41586-018-0481-8

Masudata, S., Strugnell, S., Calverley, M.J., Makin, H.L.J., Kremer, R., Jones, G., 1994. In vitro metabolism of the anti-psoriatic vitamin D analog, calcipotriol, in two cultured human keratinocyte models. J. Biol. Chem. https://doi.org/10.1016/s0021-9258(17)37614-7

Matyjaszewski, K., Xia, J., 2001. Atom transfer radical polymerization. Chem. Rev. https://doi.org/10.1021/cr940534g

Moffitt, R.A., Marayati, R., Flate, E.L., Volmar, K.E., Loeza, S.G.H., Hoadley, K.A., Rashid, N.U., Williams, L.A., Eaton, S.C., Chung, A.H., Smyla, J.K., Anderson, J.M., Kim, H.J., Bentrem, D.J., Talamonti, M.S., Iacobuzio-Donahue, C.A., Hollingsworth, M.A., Yeh, J.J., 2015. Virtual microdissection identifies distinct tumor- and stroma-specific subtypes of pancreatic ductal adenocarcinoma. Nat. Genet. 47, 1168–1178. https://doi.org/10.1038/ng.3398

Moghimi, S.M., Hunter, A.C., Murray, J.C., 2001. Long-circulating and target-specific nanoparticles: Theory to practice. Pharmacol. Rev.

Mokdad, A.A., Minter, R.M., Zhu, H., Augustine, M.M., Porembka, M.R., Wang, S.C., Yopp, A.C., Mansour, J.C., Choti, M.A., Polanco, P.M., 2017. Neoadjuvant therapy followed by resection versus upfront resection for resectable pancreatic cancer: A propensity score matched analysis. J. Clin. Oncol. 35, 515–522. https://doi.org/10.1200/JCO.2016.68.5081

Monsarrat, B., Royer, I., Wright, M., Cresteil, T., 1997. Biotransformation of taxoids by human cytochromes P450: Structure-activity relationship. Bull. Cancer.

Moore, M.J., Cox, T.F., Valle, J.W., Palmer, D.H., Mcdonald, A.C., Carter, R., Tebbutt, N.C., Dervenis, C., Glimelius, B., Scarfe, A.G., Middleton, M.R., Halloran, C.M., Lerch, M.M., Rawcliffe, C.L., Verbeke, C.S., Campbell, F., Bu, M.W., 2012. Effect of Adjuvant Chemotherapy With Fluorouracil Plus Folinic Acid or Gemcitabine. Jama 308, 147–156.

Moore, M.J., Goldstein, D., Hamm, J., Figer, A., Hecht, J.R., Gallinger, S., Au, H.J., Murawa, P., Walde, D., Wolff, R.A., Campos, D., Lim, R., Ding, K., Clark, G., Voskoglou-Nomikos, T., Ptasynski, M., Parulekar, W., 2007. Erlotinib plus gemcitabine compared with gemcitabine alone in patients with advanced pancreatic cancer: A phase III trial of the National Cancer Institute of Canada Clinical Trials Group. J. Clin. Oncol. 25, 1960–1966. https://doi.org/10.1200/JCO.2006.07.9525

Mould, D.R., Fleming, G.F., Darcy, K.M., Spriggs, D., 2006. Population analysis of a 24-h paclitaxel infusion in advanced endometrial cancer: A gynaecological oncology group study. Br. J. Clin. Pharmacol. 62, 56–70. https://doi.org/10.1111/j.1365-2125.2006.02718.x

Nagayasu, A., Uchiyama, K., Kiwada, H., 1999. The size of liposomes: A factor which affects their targeting efficiency to tumors and therapeutic activity of liposomal antitumor drugs. Adv. Drug Deliv. Rev. 40, 75–87. https://doi.org/10.1016/S0169-409X(99)00041-1

Niyaz, M., Khan, M.S., Wani, R.A., Shah, O.J., Mudassar, S., 2020. Sonic Hedgehog Protein is Frequently Up-Regulated in Pancreatic Cancer Compared to Colorectal Cancer. Pathol. Oncol. Res. 26, 551–557. https://doi.org/10.1007/s12253-018-00564-2

Norman, A.W., 2008. From vitamin D to hormone D: Fundamentals of the vitamin D endocrine system essential for good health. Am. J. Clin. Nutr. https://doi.org/10.1093/ajcn/88.2.491s

Norton, J., Foster, D., Chinta, M., Titan, A., Longaker, M., 2020. Pancreatic cancer associated fibroblasts (CAF): Under-explored target for pancreatic cancer treatment. Cancers (Basel). 12, 1–18. https://doi.org/10.3390/cancers12051347

Oettle, H., Neuhaus, P., Hochhaus, A., Hartmann, J.T., Gellert, K., Ridwelski, K., Niedergethmann, M., Zülke, C., Fahlke, J., Arning, M.B., Sinn, M., Hinke, A., Riess, H., 2013. Adjuvant chemotherapy with gemcitabine and long-term outcomes among patients with resected pancreatic cancer: The CONKO-001 randomized trial. JAMA - J. Am. Med. Assoc. 310, 1473–1481. https://doi.org/10.1001/jama.2013.279201

Okada, K.I., Hirono, S., Kawai, M., Miyazawa, M., Shimizu, A., Kitahata, Y., Ueno, M., Hayami, S., Yamaue, H., 2017. Phase i study of nab-paclitaxel plus gemcitabine as neoadjuvant therapy for borderline resectable pancreatic cancer. Anticancer Res. 37, 853–858. https://doi.org/10.21873/anticanres.11389

Olive, K.P., Jacobetz, M.A., Davidson, C.J., Gopinathan, A., McIntyre, D., Honess, D., Madhu, B., Goldgraben, M.A., Caldwell, M.E., Allard, D., Frese, K.K., DeNicola, G., Feig, C., Combs, C., Winter, S.P., Ireland-Zecchini, H., Reichelt, S., Howat, W.J., Chang, A., Dhara, M., Wang, L., Rückert, F., Grützmann, R., Pilarsky, C., Izeradjene, K., Hingorani, S.R., Huang, P., Davies, S.E., Plunkett, W., Egorin, M., Hruban, R.H., Whitebread, N., McGovern, K., Adams, J., Iacobuzio-Donahue, C., Griffiths, J., Tuveson, D.A., 2009. Inhibition of Hedgehog signaling enhances delivery of chemotherapy in a mouse model of pancreatic cancer. Science (80-.). https://doi.org/10.1126/science.1171362

Owens, D.E., Peppas, N.A., 2006. Opsonization, biodistribution, and pharmacokinetics of polymeric nanoparticles. Int. J. Pharm. https://doi.org/10.1016/j.ijpharm.2005.10.010

Özdemir, B.C., Pentcheva-Hoang, T., Carstens, J.L., Zheng, X., Wu, C.C., Simpson, T.R., Laklai, H., Sugimoto, H., Kahlert, C., Novitskiy, S. V., DeJesus-Acosta, A., Sharma, P., Heidari, P., Mahmood, U., Chin, L., Moses, H.L., Weaver, V.M., Maitra, A., Allison, J.P., LeBleu, V.S., Kalluri, R., 2014. Depletion of carcinoma-associated fibroblasts and fibrosis induces immunosuppression and accelerates pancreas cancer with reduced survival. Cancer Cell. https://doi.org/10.1016/j.ccr.2014.04.005

Patel, H.M., 1992. Serum opsonins and liposomes: Their interaction and opsonophagocytosis.

Crit. Rev. Ther. Drug Carrier Syst.

Payyappilly, S.S., Panja, S., Mandal, P., Dhara, S., Chattopadhyay, S., 2015. Organic solvent-free low temperature method of preparation for self assembled amphiphilic poly(ε-caprolactone)-poly(ethylene glycol) block copolymer based nanocarriers for protein delivery. Colloids Surfaces B Biointerfaces 135, 510–517. https://doi.org/10.1016/j.colsurfb.2015.07.075

Pelzer, U., Schwaner, I., Stieler, J., Adler, M., Seraphin, J., Dörken, B., Riess, H., Oettle, H., 2011. Best supportive care (BSC) versus oxaliplatin, folinic acid and 5-fluorouracil (OFF) plus BSC in patients for second-line advanced pancreatic cancer: A phase III-study from the German CONKO-study group. Eur. J. Cancer 47, 1676–1681. https://doi.org/10.1016/j.ejca.2011.04.011

Phillips, P.A., McCarroll, J.A., Park, S., Wu, M.J., Pirola, R., Korsten, M., Wilson, J.S., Apte, M. V., 2003. Rat pancreatic stellate cells secrete matrix metalloproteinases: Implications for extracellular matrix turnover. Gut 52, 275–282. https://doi.org/10.1136/gut.52.2.275

Pihlak, R., Valle, J.W., Mcnamara, M.G., 2017. Oncotarget 73240 www.impactjournals.com/oncotarget Germline mutations in pancreatic cancer and potential new therapeutic options. Oncotarget 8, 73240–73257.

Pike, J.W., Meyer, M.B., 2012. The Vitamin D Receptor: New Paradigms for the Regulation of Gene Expression by 1,25-Dihydroxyvitamin D 3. Rheum. Dis. Clin. North Am. 38, 13–27. https://doi.org/10.1016/j.rdc.2012.03.004

Pike, J.W., Meyer, M.B., 2010. The vitamin D receptor: New paradigms for the regulation of gene expression by 1,25-dihydroxyvitamin D3. Endocrinol. Metab. Clin. North Am. https://doi.org/10.1016/j.ecl.2010.02.007

Polireddy, K., Chen, Q., 2016. Cancer of the pancreas: Molecular pathways and current advancement in treatment. J. Cancer 7, 1497–1514. https://doi.org/10.7150/jca.14922

Portal, A., Pernot, S., Tougeron, D., Arbaud, C., Bidault, A.T., De La Fouchardière, C., Hammel,

P., Lecomte, T., Dréanic, J., Coriat, R., Bachet, J.B., Dubreuil, O., Marthey, L., Dahan, L., Tchoundjeu, B., Locher, C., Lepère, C., Bonnetain, F., Taieb, J., 2015. Nab-paclitaxel plus gemcitabine for metastatic pancreatic adenocarcinoma after Folfirinox failure: An AGEO prospective multicentre cohort. Br. J. Cancer 113, 989–995. https://doi.org/10.1038/bjc.2015.328

Posocco, B., Buzzo, M., Follegot, A., Giodini, L., Sorio, R., Marangon, E., Toffoli, G., 2018. A new high-performance liquid chromatography-tandem mass spectrometry method for the determination of paclitaxel and 6α-hydroxy-paclitaxel in human plasma: Development, validation and application in a clinical pharmacokinetic study. PLoS One. https://doi.org/10.1371/journal.pone.0193500

Provenzano, P.P., Cuevas, C., Chang, A.E., Goel, V.K., Von Hoff, D.D., Hingorani, S.R., 2012. Enzymatic Targeting of the Stroma Ablates Physical Barriers to Treatment of Pancreatic Ductal Adenocarcinoma. Cancer Cell. https://doi.org/10.1016/j.ccr.2012.01.007

Puré, E., Lo, A., 2016. Can targeting stroma pave the way to enhanced antitumor immunity and immunotherapy of solid tumors? Cancer Immunol. Res. https://doi.org/10.1158/2326-6066.CIR-16-0011

Rahib, L., Smith, B.D., Aizenberg, R., Rosenzweig, A.B., Fleshman, J.M., Matrisian, L.M., 2014. Projecting cancer incidence and deaths to 2030: The unexpected burden of thyroid, liver, and pancreas cancers in the united states. Cancer Res. 74, 2913–2921. https://doi.org/10.1158/0008-5472.CAN-14-0155

Ren, C., Chen, Y., Han, C., Fu, D., Chen, H., 2014. Plasma interleukin-11 (IL-11) levels have diagnostic and prognostic roles in patients with pancreatic cancer. Tumor Biol. https://doi.org/10.1007/s13277-014-2459-y

Resovi, A., Bani, M.R., Porcu, L., Anastasia, A., Minoli, L., Allavena, P., Cappello, P., Novelli, F., Scarpa, A., Morandi, E., Falanga, A., Torri, V., Taraboletti, G., Belotti, D., Giavazzi, R., 2018. Soluble stroma-related biomarkers of pancreatic cancer. EMBO Mol. Med.

https://doi.org/10.15252/emmm.201708741

Rhim, A.D., Oberstein, P.E., Thomas, D.H., Mirek, E.T., Palermo, C.F., Sastra, S.A., Dekleva, E.N., Saunders, T., Becerra, C.P., Tattersall, I.W., Westphalen, C.B., Kitajewski, J., Fernandez-Barrena, M.G., Fernandez-Zapico, M.E., Iacobuzio-Donahue, C., Olive, K.P., Stanger, B.Z., 2014. Stromal elements act to restrain, rather than support, pancreatic ductal adenocarcinoma. Cancer Cell 25, 735–747. https://doi.org/10.1016/j.ccr.2014.04.021

Romberg, B., Hennink, W.E., Storm, G., 2008. Sheddable coatings for long-circulating nanoparticles. Pharm. Res. https://doi.org/10.1007/s11095-007-9348-7

Rosen, C.J., Adams, J.S., Bikle, D.D., Black, D.M., Demay, M.B., Manson, J.A.E., Murad, M.H., Kovacs, C.S., 2012. The nonskeletal effects of vitamin D: An endocrine society scientific statement. Endocr. Rev. https://doi.org/10.1210/er.2012-1000

Rowinsky, E.K., Eisenhauer, E.A., Chaudhry, V., Arbuck, S.G., Donehower, R.C., 1993. Clinical toxicities encountered with paclitaxel (TAXOL®), in: Seminars in Oncology.

Rowinsky, E.K., Onetto, N., Canetta, R.M., Arbuck, S.G., 1992. Taxol: The first of the taxanes, an important new class of antitumor agents. Semin. Oncol. https://doi.org/10.5555/uri:pii:009377549290034X

Royal, R.E., Levy, C., Turner, K., Mathur, A., Hughes, M., Kammula, U.S., Sherry, R.M., Topalian, S.L., Yang, J.C., Lowy, I., Rosenberg, S.A., 2010. Phase 2 trial of single agent ipilimumab (Anti-CTLA-4) for locally advanced or metastatic pancreatic adenocarcinoma. J. Immunother. https://doi.org/10.1097/CJI.0b013e3181eec14c

Ruiz, A., Salas, G., Calero, M., Hernández, Y., Villanueva, A., Herranz, F., Veintemillas-Verdaguer, S., Martínez, E., Barber, D.F., Morales, M.P., 2013. Short-chain PEG molecules strongly bound to magnetic nanoparticle for MRI long circulating agents. Acta Biomater. 9, 6421–6430. https://doi.org/10.1016/j.actbio.2012.12.032

Sahin, I.H., Iacobuzio-Donahue, C.A., Oreilly, E.M., 2016. Molecular signature of pancreatic

adenocarcinoma: An insight from genotype to phenotype and challenges for targeted therapy. Expert Opin. Ther. Targets 20, 341–359. https://doi.org/10.1517/14728222.2016.1094057

Sano, M., Driscoll, D.R., DeJesus-Monge, W.E., Quattrochi, B., Appleman, V.A., Ou, J., Zhu, L.J., Yoshida, N., Yamazaki, S., Takayama, T., Sugitani, M., Nemoto, N., Klimstra, D.S., Lewis, B.C., 2016. Activation of WNT/β-Catenin Signaling Enhances Pancreatic Cancer Development and the Malignant Potential Via Up-regulation of Cyr61. Neoplasia (United States) 18, 785–794. https://doi.org/10.1016/j.neo.2016.11.004

Schiff, P.B., Fant, J., Horwitz, S.B., 1979. Promotion of microtubule assembly in vitro by taxol [19]. Nature. https://doi.org/10.1038/277665a0

Schiff, P.B., Horwitz, S.B., 1981. Taxol Assembles Tubulin in the Absence of Exogenous Guanosine 5'-Triphosphate or Microtubule-Associated Proteins. Biochemistry. https://doi.org/10.1021/bi00514a041

Schiff, P.B., Horwitz, S.B., 1980. Taxol stabilizes microtubules in mouse fibroblast cells. Proc. Natl. Acad. Sci. U. S. A. https://doi.org/10.1073/pnas.77.3.1561

Schlingmann, K.P., Kaufmann, M., Weber, S., Irwin, A., Goos, C., John, U., Misselwitz, J., Klaus, G., Kuwertz-Bröking, E., Fehrenbach, H., Wingen, A.M., Güran, T., Hoenderop, J.G., Bindels, R.J., Prosser, D.E., Jones, G., Konrad, M., 2011. Mutations in CYP24A1 and Idiopathic Infantile Hypercalcemia . N. Engl. J. Med. https://doi.org/10.1056/nejmoa1103864

Schwarz, L., Vernerey, D., Bachet, J.B., Tuech, J.J., Portales, F., Michel, P., Cunha, A.S., 2018. Resectable pancreatic adenocarcinoma neo-adjuvant FOLF(IRIN)OX-based chemotherapy - a multicenter, non-comparative, randomized, phase II trial (PANACHE01-PRODIGE48 study). BMC Cancer 18, 1–14. https://doi.org/10.1186/s12885-018-4663-4

Seremeta, K.P., Chiappetta, D.A., Sosnik, A., 2013. Poly(e{open}-caprolactone), Eudragit® RS 100 and poly(e{open}-caprolactone)/Eudragit® RS 100 blend submicron particles for the

sustained release of the antiretroviral efavirenz. Colloids Surfaces B Biointerfaces 102, 441–449. https://doi.org/10.1016/j.colsurfb.2012.06.038

Sherman, M.H., Yu, R.T., Engle, D.D., Ding, N., Atkins, A.R., Tiriac, H., Collisson, E.A., Connor, F., Van Dyke, T., Kozlov, S., Martin, P., Tseng, T.W., Dawson, D.W., Donahue, T.R., Masamune, A., Shimosegawa, T., Apte, M. V., Wilson, J.S., Ng, B., Lau, S.L., Gunton, J.E., Wahl, G.M., Hunter, T., Drebin, J.A., O'Dwyer, P.J., Liddle, C., Tuveson, D.A., Downes, M., Evans, R.M., 2014. Vitamin D receptor-mediated stromal reprogramming suppresses pancreatitis and enhances pancreatic cancer therapy. Cell 159, 80–93. https://doi.org/10.1016/j.cell.2014.08.007

Sørensen, H., Blnderup, L., Calverley, M.J., Hoffmeyer, L., Andersen, N.R., 1990. In vitro metabolism of Calcipotriol (MC 903), a vitamin D analogue. Biochem. Pharmacol. https://doi.org/10.1016/0006-2952(90)90039-N

Sriraman, S.K., Aryasomayajula, B., Torchilin, V.P., 2014. Barriers to drug delivery in solid tumors. Tissue Barriers. https://doi.org/10.4161/tisb.29528

Stolzenberg-Solomon, R.Z., Hayes, R.B., Horst, R.L., Anderson, K.E., Hollis, B.W., Silverman, D.T., 2009. Serum vitamin D and risk of pancreatic cancer in the prostate, lung, colorectal, and ovarian screening trial. Cancer Res. https://doi.org/10.1158/0008-5472.CAN-08-2694

Stolzenberg-Solomon, R.Z., Jacobs, E.J., Arslan, A.A., Qi, D., Patel, A. V., Helzlsouer, K.J., Weinstein, S.J., McCullough, M.L., Purdue, M.P., Shu, X.O., Snyder, K., Virtamo, J., Wilkins, L.R., Yu, K., Zeleniuch-Jacquotte, A., Zheng, W., Albanes, D., Cai, Q., Harvey, C., Hayes, R., Clipp, S., Horst, R.L., Irish, L., Koenig, K., Le Marchand, L., Kolonel, L.N., 2010. Circulating 25-hydroxyvitamin D and risk of pancreatic cancer: Cohort Consortium Vitamin D Pooling Project of Rarer Cancers. Am. J. Epidemiol. https://doi.org/10.1093/aje/kwq120

Stolzenberg-Solomon, R.Z., Vieth, R., Azad, A., Pietinen, P., Taylor, P.R., Virtamo, J., Albanes, D., 2006. A prospective nested case-control study of vitamin D status and pancreatic cancer risk in male smokers. Cancer Res. https://doi.org/10.1158/0008-5472.CAN-06-1876

Suk, J.S., Xu, Q., Kim, N., Hanes, J., Ensign, L.M., 2016. PEGylation as a strategy for improving nanoparticle-based drug and gene delivery HHS Public Access Graphical abstract. Adv Drug Deliv Rev 99, 28–51. https://doi.org/10.1016/j.addr.2015.09.012

Sun, C., Rosendahl, A.H., Ansari, D., Andersson, R., 2011. Proteome-based biomarkers in pancreatic cancer. World J. Gastroenterol. https://doi.org/10.3748/wjg.v17.i44.4845

Tan, J.S., Butterfield, D.E., Voycheck, C.L., Caldwell, K.D., Li, J.T., 1993. Surface modification of nanoparticles by PEO/PPO block copolymers to minimize interactions with blood components and prolong blood circulation in rats. Biomaterials 14, 823–833. https://doi.org/10.1016/0142-9612(93)90004-L

Tan, K.W., Sampson, A., Osa-Andrews, B., Iram, S.H., 2018. Calcitriol and Calcipotriol Modulate Transport Activity of ABC Transporters and Exhibit Selective Cytotoxicity in MRP1-overexpressing Cells. Drug Metab. Dispos. 46, 1856–1866. https://doi.org/10.1124/dmd.118.081612

Tempero, M.A., Klimstra, D., Berlin, J., Hollingsworth, T., Kim, P., Merchant, N., Moore, M., Pleskow, D., Wang-Gillam, A., Lowy, A.M., 2013. Changing the way we do business: Recommendations to accelerate biomarker development in pancreatic cancer. Clin. Cancer Res. https://doi.org/10.1158/1078-0432.CCR-12-2745

Tod, J., Jenei, V., Thomas, G., Fine, D., 2013. Tumor-stromal interactions in pancreatic cancer. Pancreatology 13, 1–7. https://doi.org/10.1016/j.pan.2012.11.311

Townsend, K., Evans, K.N., Campbell, M.J., Colston, K.W., Adams, J.S., Hewison, M., 2005. Biological actions of extra-renal 25-hydroxyvitamin D-1α-hydroxylase and implications for chemoprevention and treatment, in: Journal of Steroid Biochemistry and Molecular Biology. https://doi.org/10.1016/j.jsbmb.2005.06.004

Uesaka, K., Boku, N., Fukutomi, A., Okamura, Y., Konishi, M., Matsumoto, I., Kaneoka, Y., Shimizu, Y., Nakamori, S., Sakamoto, H., Morinaga, S., Kainuma, O., Imai, K., Sata, N., Hishinuma, S., Ojima, H., Yamaguchi, R., Hirano, S., Sudo, T., Ohashi, Y., 2016. Adjuvant

chemotherapy of S-1 versus gemcitabine for resected pancreatic cancer: a phase 3, open-label, randomised, non-inferiority trial (JASPAC 01). Lancet 388, 248–257. https://doi.org/10.1016/S0140-6736(16)30583-9

Vaccaro, V., Sperduti, I., Milella, M., 2011. FOLFIRINOX versus gemcitabine for metastatic pancreatic cancer. N. Engl. J. Med. 365, 768–769. https://doi.org/10.1056/NEJMc1107627

Vaghi, C., Rodallec, A., Fanciullino, R., Ciccolini, J., Mochel, J.P., Mastri, M., Poignard, C., Ebos, J.M.L., Benzekry, S., 2020. Population modeling of tumor growth curves and the reduced Gompertz model improve prediction of the age of experimental tumors. PLoS Comput. Biol. https://doi.org/10.1371/journal.pcbi.1007178

Van Mackelenbergh, M.G., Stroes, C.I., Spijker, R., Van Eijck, C.H.J., Wilmink, J.W., Bijlsma, M.F., Van Laarhoven, H.W.M., 2019. Clinical trials targeting the stroma in pancreatic cancer: A systematic review and meta-analysis. Cancers (Basel). 11, 1–23. https://doi.org/10.3390/cancers11050588

Vittaz, M., Bazile, D., Spenlehauer, G., Verrecchia, T., Veillard, M., Puisieux, F., Labarre, D., 1996. Effect of PEO surface density on long-circulating PLA-PEO nanoparticles which are very low complement activators. Biomaterials. https://doi.org/10.1016/0142-9612(95)00322-3

Von Ahrens, D., Bhagat, T.D., Nagrath, D., Maitra, A., Verma, A., 2017. The role of stromal cancer-associated fibroblasts in pancreatic cancer. J. Hematol. Oncol. 10, 1–8. https://doi.org/10.1186/s13045-017-0448-5

Wang, M., Thanou, M., 2010. Targeting nanoparticles to cancer. Pharmacol. Res. 62, 90–99. https://doi.org/10.1016/j.phrs.2010.03.005

Waters, A.M., Der, C.J., 2018. KRAS: The critical driver and therapeutic target for pancreatic cancer. Cold Spring Harb. Perspect. Med. https://doi.org/10.1101/cshperspect.a031435

Whatcott, C.J., Han, H., Posner, R.G., Hostetter, G., Von Hoff, D.D., 2011. Targeting the tumor microenvironment in cancer: Why hyaluronidase deserves a second look. Cancer Discov.

1, 291–296. https://doi.org/10.1158/2159-8290.CD-11-0136

Whitney, A.R., Diehn, M., Popper, S.J., Alizadeh, A.A., Boldrick, J.C., Relman, D.A., Brown, P.O., 2003. Individuality and variation in gene expression patterns in human blood. Proc. Natl. Acad. Sci. U. S. A. https://doi.org/10.1073/pnas.252784499

Wiernik, P.H., Schwartz, E.L., Strauman, J.J., Dutcher, J.P., Lipton, R.B., Paietta, E., 1987. Phase I Clinical and Pharmacokinetic Study of Taxol. Cancer Res.

Wolfe, A.R., Prabhakar, D., Yildiz, V.O., Cloyd, J.M., Dillhoff, M., Abushahin, L., Alexandra Diaz, D., Miller, E.D., Chen, W., Frankel, W.L., Noonan, A., Williams, T.M., 2020. Neoadjuvant-modified FOLFIRINOX vs nab-paclitaxel plus gemcitabine for borderline resectable or locally advanced pancreatic cancer patients who achieved surgical resection. Cancer Med. 9, 4711–4723. https://doi.org/10.1002/cam4.3075

Wong, K.M., Horton, K.J., Coveler, A.L., Hingorani, S.R., Harris, W.P., 2017. Targeting the Tumor Stroma: the Biology and Clinical Development of Pegylated Recombinant Human Hyaluronidase (PEGPH20). Curr. Oncol. Rep. 19. https://doi.org/10.1007/s11912-017-0608-3

Woodruff, M.A., Hutmacher, D.W., 2010. The return of a forgotten polymer - Polycaprolactone in the 21st century. Prog. Polym. Sci. 35, 1217–1256. https://doi.org/10.1016/j.progpolymsci.2010.04.002

Yachida, S., Jones, S., Bozic, I., Antal, T., Leary, R., Fu, B., Kamiyama, M., Hruban, R.H., Eshleman, J.R., Nowak, M.A., Velculescu, V.E., Kinzler, K.W., Vogelstein, B., Iacobuzio-Donahue, C.A., 2010. Distant metastasis occurs late during the genetic evolution of pancreatic cancer. Nature. https://doi.org/10.1038/nature09515

Yao, W., Maitra, A., Ying, H., 2020. Recent insights into the biology of pancreatic cancer. EBioMedicine 53, 102655. https://doi.org/10.1016/j.ebiom.2020.102655

Ying, H., Dey, P., Yao, W., Kimmelman, A.C., Draetta, G.F., Maitra, A., Depinho, R.A., 2016. Genetics and biology of pancreatic ductal adenocarcinoma. Genes Dev. 30, 355–385.

https://doi.org/10.1101/gad.275776.115

Yuan, H., Li, J., Bao, G., Zhang, S., 2010. Variable nanoparticle-cell adhesion strength regulates cellular uptake. Phys. Rev. Lett. 105, 1–4. https://doi.org/10.1103/PhysRevLett.105.138101

Yvon, A.M.C., Wadsworth, P., Jordan, M.A., 1999. Taxol suppresses dynamics of individual microtubules in living human tumor cells. Mol. Biol. Cell. https://doi.org/10.1091/mbc.10.4.947

Zein, R., Sharrouf, W., Selting, K., 2020. Physical Properties of Nanoparticles That Result in Improved Cancer Targeting. J. Oncol. https://doi.org/10.1155/2020/5194780

Zeitz, U., Weber, K., Soegiarto, D.W., Wolf, E., Balling, R., Erben, R.G., 2003. Impaired insulin secretory capacity in mice lacking a functional vitamin D receptor. FASEB J. https://doi.org/10.1096/fj.02-0424fje

Zelenková, T., Fissore, D., Marchisio, D.L., Barresi, A.A., 2014. Size control in production and freeze-drying of poly-ε-caprolactone nanoparticles. J. Pharm. Sci. 103, 1839–1850. https://doi.org/10.1002/jps.23960

Zhang, S., Gao, H., Bao, G., 2015. Physical Principles of Nanoparticle Cellular Endocytosis. ACS Nano 9, 8655–8671. https://doi.org/10.1021/acsnano.5b03184

Zhang, S., Li, J., Lykotrafitis, G., Bao, G., Suresh, S., 2009. Size-dependent endocytosis of nanoparticles. Adv. Mater. 21, 419–424. https://doi.org/10.1002/adma.200801393

Zhang, W., Li, X., Ye, T., Chen, F., Sun, X., Kong, J., Yang, X., Pan, W., Li, S., 2013. Design, characterization, and in vitro cellular inhibition and uptake of optimized genistein-loaded NLC for the prevention of posterior capsular opacification using response surface methodology. Int. J. Pharm. 454, 354–366. https://doi.org/10.1016/j.ijpharm.2013.07.032

Zhao, J., Wang, H., Hsiao, C.H., Chow, D.S.L., Koay, E.J., Kang, Y., Wen, X., Huang, Q., Ma, Y., Bankson, J.A., Ullrich, S.E., Overwijk, W., Maitra, A., Piwnica-Worms, D., Fleming, J.B., Li, C., 2018a. Simultaneous inhibition of hedgehog signaling and tumor proliferation

remodels stroma and enhances pancreatic cancer therapy. Biomaterials 159, 215–228. https://doi.org/10.1016/j.biomaterials.2018.01.014

Zhao, J., Xiao, Z., Li, T., Chen, H., Yuan, Y., Wang, Y.A., Hsiao, C.H., Chow, D.S.L., Overwijk, W.W., Li, C., 2018b. Stromal Modulation Reverses Primary Resistance to Immune Checkpoint Blockade in Pancreatic Cancer. ACS Nano. https://doi.org/10.1021/acsnano.8b02481

Appendix

1. Population PK modeling of Cal and metabolites model code

```
;Model Desc: Cal parent-metabolites modeling with formulation as covariate
;Project Name: cal_par_mets
;Project ID: NO PROJECT DESCRIPTION

;Model Desc: Cal parent-metabolites modeling with formulation as covariate

$PROBLEM Cal Parent-metabolites model ;3-comp IV dosing
$DATA Cal_par_met.csv  IGNORE = C
$INPUT C,ID,TIME,AMT,DV,CMT,FORM, TYPE, EVID, FLG

$SUB ADVAN7 TRANS1
$MODEL

   NCOMPARTMENTS=3
   COMP=(CAL)          ;CENTRAL COMPARTMENT FOR CAL
   COMP=(MC1040)       ;CENTRAL COMPARTMENT FOR M1(MC1040)
   COMP=(MC1080)       ;CENTRAL COMPARTMENT FOR M2 (MC1080)

$PK

   CLC=THETA(1)*EXP(ETA(1))         ;Total Cal CL, FORM=0 is micelle and FORM=1 is free
drugs
   FM = THETA(2)                    ; Fraction of Cal Metabolized
   CLCM = CLC*FM                     ; CYP24A1 CL of Cal
   CLCB = CLC*(1-FM)                  ; Other CL of Cal

   CLC1 = THETA(3)*EXP(ETA(2))            ;Total Cl of MC1046
   FM1 = THETA(4)                    ; Fraction of MC1046 Metabolized
   CLCM1 = CLC1*FM1                     ; CYP? CL of MC1046
   CLCB1 = CLC1*(1-FM1)                  ; Other CL of MC1046

   CLC2 = THETA(5)*EXP(ETA(3))               ;Total Cl of MC1080


   V1=THETA(6)*EXP(ETA(4))
   V2= THETA(7)*EXP(ETA(5))
   V3= THETA(8)*EXP(ETA(6))

   K12 = CLCM/V1
   K10 = CLCB/V1

   K23 = CLCM1/V2
   K20 = CLCB1/V2

   K30 = CLC2/V3
```

```
   S1=V1/1000
   S2=V2/1000
   S3=V3/1000

$ERROR

   C1=A(1)/V1
   C2=A(2)/V2
   C3=A(3)/V3
   IPRED= F
   W=IPRED
   ;W=SQRT(THETA(9)**2 + (THETA(10)*IPRED)**2)
   IRES = DV-IPRED
   IWRES = IRES/W

    IND1=0
    IND2=0
    IND3=0
    IF (CMT.EQ.1) IND1=1
    IF (CMT.EQ.2) IND2=1
    IF (CMT.EQ.3) IND3=1

    Y2=F*(1+ERR(3))+ ERR(4)
    Y1=F*(1+ERR(1))+ ERR(2)
    Y3=F*(1+ERR(5))+ ERR(6)
    Y=Y2*IND2+Y1*IND1+Y3*IND3


$THETA

   (0, 15)        ;[TOTAL Cal CL]
   (0, 0.8, 1)    ;[FRACTION OF Cal Metabolized]
   (0, 35)        ;[TOTAL MC1046 CL]
   (0, 0.95, 1)   ;[FRACTION OF MC1046 Metabolized]
   (0, 5)        ;[TOTAL MC1080 CL]
   (0, 3)        ;[V OF CAL]
   (0, 2)        ;[V OF MC1046]
   (0, 1.5)      ;[V OF MC1080]
   ;(0, 0.2)      ;[Effect of formulation Total Cal CL]


$OMEGA
  0.02
  0.03
  0.04
  0.02
  0.04
  0.04


$SIGMA
```

0.16
0.04
0.04
0.06
0.03
0.02

;$MSF=cal_par_met.MSF
$ESTIMATION METHOD=1 INTER NOTBT NOOBT SORT NOSBT MAXEVAL=999999 MSFO=cal_par_met.MSF POSTHOC
;$EST MAXEVAL=999999 METHOD=1 LAPLACIAN INTER PRINT=5 MSFO=cal_par_met.MSF POSTHOC
$COVARIANCE PRINT =E UNCONDITIONAL;MATRIX=R
$TABLE NOPRINT ONEHEADER
ID TIME CMT MDV IPRED FORM CWRES ETA1 ETA2 ETA3 ETA4 ETA5 ETA6 CLC FM CLC1 FM1 CLC2 V1 V2 V3 K12 K10 K23 K20 K30 FILE=cal_par_met.tab

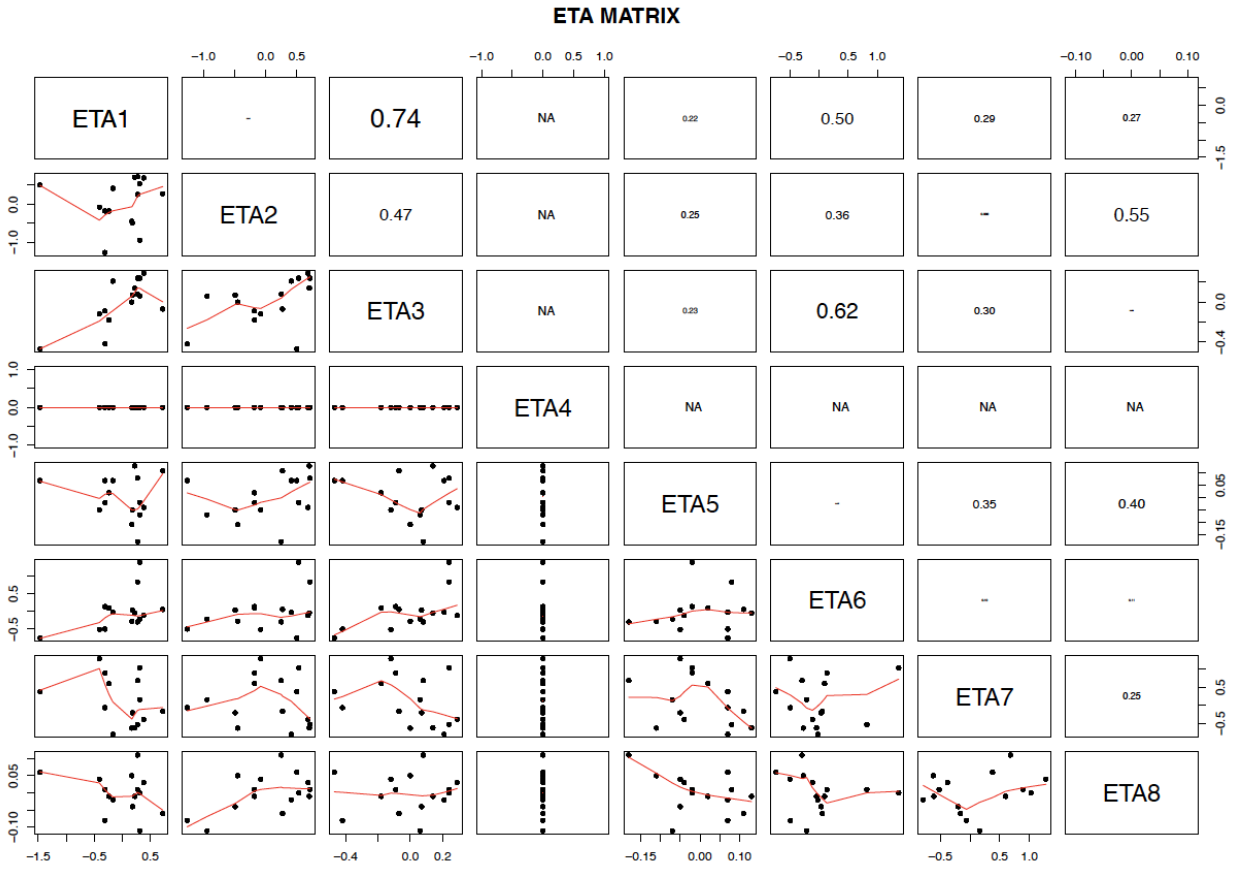

Figure S1: Eta-matrix for Calcipotriol Parent-metabolites model

Model Code for Cal Population PK model

```
;Model Desc: Cal popPK model for Dx and healthy with COV
;Project Name: cal_poppk_all
;Project ID: NO PROJECT DESCRIPTION

;Model Desc: Cal popPK model for Dx and healthy with COV
$PROB Cal pop for All with Cov
$INPUT C ID TIME AMT DV=ODV LNDV CMT FORM MDV EVID TYPE STAT FLG
$DATA Cal_popPK_healthyDx.csv IGNORE = C
$SUBROUTINES ADVAN3 TRANS4

$PK
    MU_1 = THETA(1)
    MU_2 = THETA(2)
    MU_3 = THETA(3)
    MU_4 = THETA(4)



    CL   = THETA(5)**STAT*THETA(6)**FORM*EXP(MU_1 + ETA(1))
    V1   = THETA(7)**STAT*THETA(8)**FORM*EXP(MU_2 + ETA(2))
    Q    = EXP(MU_3 + ETA(3))
    V2   = EXP(MU_4 + ETA(4))
    S1   = V1/1000

$ERROR


  LOQ = 0.5
  IPRED = F
  W=SQRT(THETA(9)**2 + (THETA(10)/IPRED)**2)
  DUM = (LOQ-IPRED)/(W*IPRED)
  CUMD=PHI(DUM)
  IF(FLG.EQ.0)THEN  ; non BQL values
  F_FLAG=0
  Y = F*(1+W*ERR(1))
  ENDIF
  IF(FLG.EQ.1)THEN ; BQL values
  F_FLAG=1
  Y=CUMD
  ENDIF

$THETA
  (0.000001, 2)      ;[CL]
```

```
  (0.000001, 4)     ;[V1]
  (0.000001, 5)     ;[Q]
  (0.000001, 3)     ;[V2]
  (0.000001, 2)     ;[STAT ON CL]
  (0.000001, 0.2)   ; [FORM ON CL]
  (0, 0.5)          ;[STAT ON V1]
  (0, 0.1)          ;[FORM ON V1]
  (0.000001, 0.5)
  (0.000001, 0.2)


$OMEGA ;BLOCK(4)
  0.1  ;0.04   ;[P]
  0.1  ;[F]
  0.04   ;[P]
  0.01  ;[F]


$SIGMA
  1 FIXED   ;[P]

$EST METHOD=IMP LAPLACE INTERACTION AUTO=1 SLOW PRINT=5 RANMETHOD=S2

;$SIM (5469) ONLY SUB=100

$COV MATRIX=R PRINT=E UNCONDITIONAL

$TABLE ID TIME AMT TYPE FORM STAT DV PRED IPRED WRES NPDE ETA1 ETA2 ETA3
ETA4 NOAPPEND ONEHEADER ESAMPLE=1000
                                        FILE=Cal_HealthyDx.tab NOPRINT

;$TABLE IND ID AMT TIME EVID TYPE FORM STAT ETA1 ETA2 ETA3 ETA4  ONEHEADER
NOPRINT NOAPPEND FILE=run1cov.tab
```

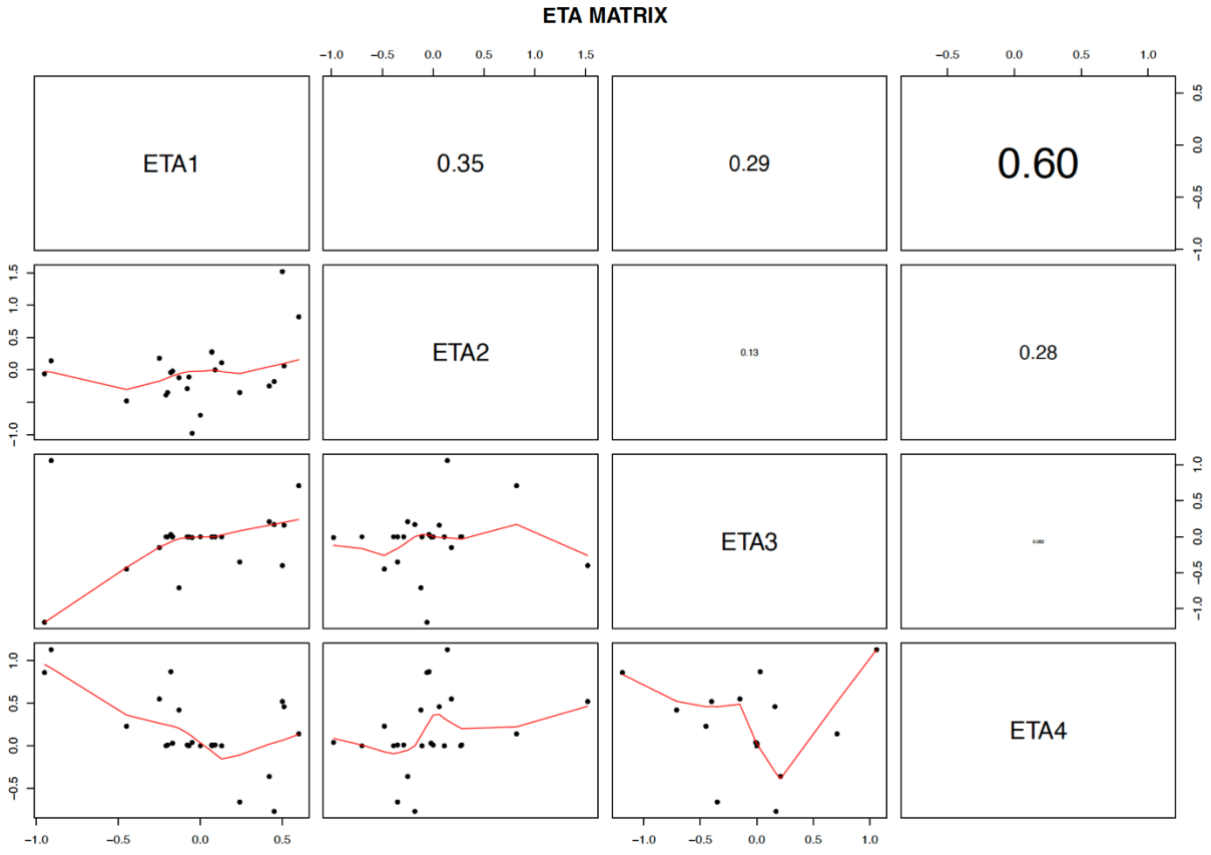

Figure S2. Eta-matrix for Cal population PK model

Model Code for PTX population Model

```
;Model Desc: NO MODEL DESCRIPTION
;Project Name: ptx_pop_model
;Project ID: NO PROJECT DESCRIPTION

;Model Desc: NO MODEL DESCRIPTION
;DESC PTX pop model

$PROB RUN# PTX_base_mod
$INPUT C ID TIME AMT ODV DV CMT MDV EVID TAD FORM STAT
$DATA Datptx4.CSV IGNORE=C
$SUBROUTINES ADVAN3 TRANS4
$PK

   TVCL = THETA(1)
    CL=   TVCL*EXP(ETA(1))

    TVV1 = THETA(2)*THETA(5)**STAT
    V1=TVV1*EXP(ETA(2))

    TVQ=  THETA(3)
    Q=TVQ*EXP(ETA(3))

    TVV2=THETA(4)
    V2=TVV2*EXP(ETA(4))
    S1=V1/1000

$ERROR

  IPRED = LOG(F)

   W = THETA(6)*IPRED
   IRES = DV-IPRED
   IWRES = IRES/W
   Y = IPRED + W*EPS(1) + EPS(2)

$THETA
  (0.00001, 2)     ;[LNCL]
  (0.00001, 4)     ;[LNV1]
  (0.00001, 2)     ;[LNQ]
  (0.00001, 5)     ;[LNV2]
  (0, 0.5)         ;[STAT ON V1]
  (0.00001, 0.3)

$OMEGA
  0.01 ;[P] INTERIND VAR IN CL
```

```
  0.03  ;0 FIX ;[P] INTERIND VAR IN V1
  0.4  ;FIX ;[P] INTERIND VAR IN Q
  0.01 ;[P] INTERIND VAR IN V2

$SIGMA

  0.04  ;0.04  ;[P] PROPORTIONAL COMPONENT
  0.02  ;[A] ADDITIVE COMPONENT

;$MSFI
$EST METHOD=1 INTER NOTBT NOOBT SORT NOSBT MAXEVAL=999999
MSF=PTX_base_mod.msf PRINT=15 POSTHOC

$COVARIANCE MATRIX=R PRINT=E UNCONDITIONAL

;$SIMULATION ONLYSIM (9283745)
$TABLE ID TIME TAD FORM STAT CWRESI CWRES PRED IPRED ETA1 ETA2 ETA3 ETA4
NOPRINT ONEHEADER FILE=PTX_base_mod.TAB

$SCAT DV VS PRED UNIT
$SCAT (RES WRES) VS PRED
$SCAT DV VS IPRED
```

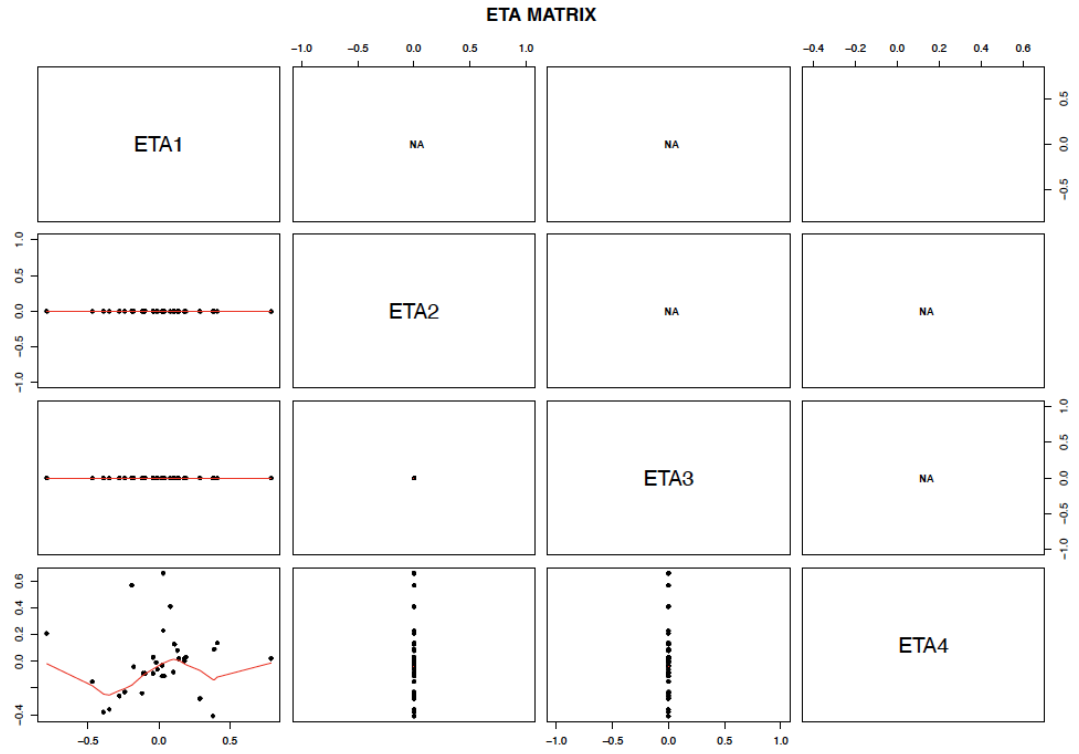

Figure S3: Eta-matrix for PTX population PK model

Model code for the tumor growth inhibition model

```
;Model Desc: Tumor Growth Inhibition model_all with covariates
;Project Name: tgi
;Project ID: NO PROJECT DESCRIPTION

;Model Desc: Tumor Growth Inhibition model_all with covariates
$PROB RUN# TGI
$INPUT C ID TRT DAY TIME OBSLD BSLD ODV DV=LNDV LD EVID
$DATA TGI.CSV IGNORE=C
$SUBROUTINES ADVAN13 TOL=12
$MODEL COMP=TUMOR
$PK

   TVKL = LOG(THETA(1)/52)*(LD/10840.2)**THETA(6)*THETA(7)**TRT ; PowerModel with
Normalized Covariate
       ;TVKL = LOG(THETA(1)/52)+THETA(6)*LOG(LD/10840.2)*TRT*LOG(THETA(7)) ; Log-
Transformed PowerModel with Normalized Covariate
   MU_1 = TVKL
   KL = EXP(MU_1 + ETA(1))


   TVKD = LOG(THETA(2)/52)*(LD/10840.2)**THETA(8)*THETA(9)**TRT
      ;TVKD = LOG(THETA(1)/52)+THETA(8)*LOG(LD/10840.2)*TRT*LOG(THETA(9))
   MU_2 = TVKD
   KD = EXP(MU_2 + ETA(2))


   TVLAM = LOG(THETA(3)/52)*(LD/10840.2)**THETA(10)*THETA(11)**TRT
     ;TVLAM = LOG(THETA(1)/52)+THETA(10)*LOG(LD/10840.2)*TRT*LOG(THETA(11))
   MU_3 = TVLAM
   LAM = EXP(MU_3 + ETA(3))

   A_0(1) = BSLD


$DES

  ;y(t)= y(0)exp[kL.t-(kD.treatment/lam)(1-exp(-lam.t))]
  ;dy/dt = [kL.t-kD/lam Treatment(exp(-lam t))]y(t)

  DADT(1) = (KL-KD*EXP(-LAM*T))*A(1)

$ERROR
```

```
  IPRED = A(1)
  W = SQRT(THETA(4)**2*IPRED**2+THETA(5)**2)
  Y = IPRED + W*ERR(1) ;+ ERR(2)
  IWRES = (DV-IPRED)/W

  TTG = (LOG(LAM*KD)-LOG(KL))/LAM


  W1 = BSLD*EXP(KL*1-(KD/LAM)*(1-EXP(-LAM*1)))
  W2 = BSLD*EXP(KL*2.28571-(KD/LAM)*(1-EXP(-LAM*2.28571)))
  TR1 = W1/BSLD
  TR2 = W2/BSLD

$THETA
  (0, 0.140) ;[KL]
  (0, 1.6);[KD]
  (0, 4) ;[LAM]
  (0, 0.081)  ;[PROP ERROR]
   (0, 0.04)  ; [ADD ERROR]
   (0, 0.001) ;KL~LD
   (0, 0.001) ;KL~TRT
   (0, 0.001) ;KD~LD
   (0, 0.001) ;KD~TRT
   (0, 0.001) ;LAM~LD
   (0, 0.001) ;LAM~TRT
$OMEGA
  2.348 ;[P] INTERIND VAR ON KL
  0.842 ;[P] INTERIND VAR ON KD
  0 FIX ;[P] INTERIND VAR ON LAM

$SIGMA
 ;1 FIXED
 0.04
 ;0.2

$ESTIMATION METHOD=1 INTER NOTBT NOOBT SORT NOSBT MAXEVAL=999999
MSF=TGI.msf PRINT=15 POSTHOC
;$ESTIMATION METHOD=0 NOTBT NOOBT SORT NOSBT SIG=4 MAXEVAL=999999
MSF=TGI.msf PRINT=15

;$EST METHOD=IMP AUTO=1 SLOW PRINT=5 RANMETHOD=S2
$COV
$TABLE NOPRINT FILE=TGI.TAB ONEHEADER ID TRT LD TIME TTG KL KD LAM W1 W2
TR1 TR2 ETA1 ETA2 ETA3 IPRED CPREDI PRED CPRED CWRESI CWRES

;$TABLE NOPRINT FILE=TGI_cov.TAB ONEHEADER ID TRT TIME PRED KL KD LAM
```

Figure S4. Overlaid observed, population predicted and individual predicted values for tumor growth model